Collective nuclear motion at finite temperature investigated with fission reactions induced by ^{238}U at 1 A·GeV on deuterium

Jorge Pereira Conca

6th July 2004

Jose F. Benlliure Anaya, Profesor Titular
de la **Universidad de Santiago de Compostela**,

CERTIFICO: que la memoria titulada **"Collective nuclear motion at finite temperatures investigated in fission reactions induced by ^{238}U at 1 A·GeV on deuterium"**, ha sido realizada por **Jorge Pereira Conca** bajo mi dirección en el **Departamento de Física de Partículas** de esta Universidad, y constituye la Tesis que presenta para optar al grado de **Doctor en Ciencias Físicas**.

Santiago de Compostela, Mayo de 2004

Prof. Jose F. Benlliure Anaya **Jorge Pereira Conca**

Contents

Introduction

Nuclei represent nowadays a remarkable example of quantum many-body systems wherein macroscopic and microscopic phenomena are manifested at the same level. These objects are made up of small constituents, the nucleons, that are held together through the strong interaction. Analysis of single particle interactions from a quantum-mechanical point of view gave rise to the so-called shell model [Fer74]. However, there are many indications that nuclear phenomena do not consist only in single-particle excitations, but also in collective motion where many nucleons move coherently. Thus, instead of describing the nucleus by its 3A internal degrees of freedom it is convenient to introduce new macroscopic coordinates that are better suited to describe the collective nature of nuclei. The simplest model that followed such approach was the liquid-drop model [Wei30], which considers the nucleus as a fluid drop influenced by proton Coulomb repulsion. A more sophisticated model that deals with both collective and single-particle phenomena is the unified model of Bohr and Mottelson [Boh98].

A noteworthy example of nuclear phenomenon wherein collective and internal motions are manifested is the deexcitation of hot nuclei produced in a nuclear reaction. At moderate energies, this process is mediated by the competition between the scission of the nucleus, referred to as fission, and the evaporation of light particles:

The description of the fission process is based upon the dependence of the nuclear potential $V(X)$ on a particular collective (macroscopic) degree of freedom: the fission coordinate X [1]. By considering the dependence of the surface energy and Coulomb repulsion on deformation [Coh63, Nix65, Coh72] it is possible to identify the so-called saddle point X_{sad}, beyond which the fission degree of freedom becomes unbound, leading to fission decay. In this way, the evolution of the nucleus along the fission coordinate constitutes an example of large-amplitude collective motion where many nucleons move coherently with well defined phases. Other types of small-amplitude collective motion linked to the existence of bound macroscopic degrees of freedom are rotations, surface vibrations and giant resonances. Besides these collective phenomena, internal (microscopic) motion can be observed experimentally in single-particle processes such as the evaporation of nucleons from the nuclear surface. Therefore, the competition between fission and evaporation occurring in the deexcitation of hot nuclei constitutes an interesting process which

---

[1] This coordinate is defined by a set of deformation parameters used to describe the evolution of the nuclear shapes during the fission process [Eis88].

manifests the macroscopic-microscopic dichotomy of the nucleus.

An equivalent phenomena that reflects the internal and collective nature of classical matter is the motion of hot honey under the influence of the gravity force. The slow dripping of honey from a spoon is governed by the competition between the surface tension and the gravity force: this fluid will hang suspended at the border of the spoon unless the gravity force overcomes the surface tension, which normally occurs for sufficiently large deformations. The dripping of honey can be favored by other collective motions like rotations and vibrations of the spoon. The overall process is very similar to nuclear fission, where Coulomb repulsion acts in the same manner as the gravity force does on honey. As far as internal degrees of freedom are concerned, the evaporation of honey from the surface of a drop is equivalent to the evaporation of light particles from the surface of a nucleus.

In the same way, the motion of hot honey and the competition of evaporation and fission decay modes in nuclear matter reflects the interplay of the macroscopic and microscopic degrees of freedom from two different perspectives. However, the relative size of nuclei with respect to their nucleonic constituents raises serious questions regarding the interplay of internal and collective degrees of freedom. Indeed much effort has been invested in nuclear science, both theoretically and experimentally to understand the microscopic origin of the collective motions and their viscous coupling to the internal degrees of freedom.

Motivated by these ideas, the present work aims to investigate the presence of collective motion in hot nuclei by analyzing the fission and evaporation residue productions in the spallation of ^{238}U at 1 A·GeV on deuterium. The experimental results used in this analysis include the production cross sections and kinematical properties of fission residues, measured in the present work and the production of evaporation residues, measured by E. Casarejos [Cas01]. From this analysis, it was possible to investigate the role of small-amplitude motion (rotations and vibrations) on the survival probability against fission, as well as the viscous coupling of large-amplitude motion (fission) with the internal degrees of freedom of the hot nucleus.

The major advantage in the use of spallation reactions arises from the fast interaction between the projectile and target which leads, after a thermalization stage, to a distribution of excited pre-fragments with small deformations and low angular momenta. The analysis of the deexcitation processes is thus simplified by the rather constrained initial conditions of the decaying systems. Furthermore, the high-fissilities of uranium-like pre-fragments and the high energies induced by the interaction with the deuterium facilitates the investigation of the fission mechanism and its competition to evaporation over a wide range of fissioning nuclei and excitation energies.

Apart from this motivation, there is renewed interest in spallation reactions for several reasons: First, they have a wide range of applications as neutron sources in material science or nuclear technology (Accelerator Driven Systems). Second, they also make possible the production of intense Radioactive Nuclear Beams (RNB). Third, these reactions provide valuable information in many different Astrophysical phenomena related to nuclear abundances from fundamental nucleosynthesis processes (r-, rp-processes,...).

The reaction ^{238}U+d belongs to a campaign of measurements of spallation reactions performed at the *Gessellschaft für Schwerionenforschung* GSI (Darmstadt, Germany) in collaboration with the *Institute de Physique Nuclèaire* IPN (Orsay, France), the *Commissariat à l'Energie Atomique* DAPNIA/SPhN (Saclay, France), the *Centre d'Etudes Nuclèaires* CEN-BG (Bordeaux, France) and the *Universidade de Santiago de Compostela* USC (Santiago de Compostela, Spain). The experimental program included the spallation of ^{208}Pb, ^{238}U, ^{56}Fe and ^{60}Ni on proton and deuteron at different energies.

The present dissertation completes the analysis of the experimental data measured in this campaign, which were presented in previous publications [Enq01, Enq02, BeA01, Tai03, Ber03, Cas01]. The work is organized as follows: In chapter 1, the fundamental ideas underlying the deexcitation processes occurring in spallation reactions and the presence of collective motion are described. Chapter 2 includes a detailed description of the experimental setup employed to measure the residue productions of ^{238}U(1 A·GeV)+d. Then, chapters 3 and 4 are dedicated to the experimental results, including both the analysis of the kinematical properties of fission residues and their production cross sections. Finally, in chapter 5, the signatures of collective motion extracted from the measurements are analyzed in detail.

Chapter 1

Collective and intrinsic excitations at finite temperature

From a theoretical point of view, the competition among the different decay modes of a hot nucleus results from the evolution of the system over the available phase-space defined by internal and collective degrees of freedom. One of the simplest approaches for developing this idea consists in assuming that the many internal degrees of freedom of the nucleus are acting as a thermostat with which the collective degrees of freedom are in thermal equilibrium at a given temperature. The deexcitation of the nucleus follows then from the statistical weight of the phase-space configurations associated with each decay mode. Besides this statistical approach, other models exist that consider explicitly the phase-space evolution of the system before reaching equilibrium. Such an approach results in a description of the dynamical coupling between the internal and collective degrees of freedom through viscosity.

This chapter provides a general survey of the underlying considerations of these two models regarding the treatment of collective motion. The different experimental approaches used to investigate collective motion in nuclear reactions are also discussed with paying special attention to spallation reactions.

1.1 Statistical models

According to the statistical model, the probability of a given decay channel j of a thermalized compound nucleus with neutron number N, proton number Z and excitation energy E is given by:

$$W_j(N,Z,E) = \frac{\Gamma_j(N,Z,E)}{\sum_k \Gamma_k(N,Z,E)} \tag{1.1}$$

where Γ_j is the decay width associated with the corresponding channel.

As was mentioned above, the two canonical nuclear decay modes that govern the deexcitation process of an excited nucleus are particle evaporation and fission. The statistical evaporation formalism [Wei37, Wei50, Hau52, Gad92] is based upon the detailed balance principle to connect initial and final states of the decaying nucleus. In its simplest form, the decay width associated with the evaporation of a particle i is described in terms of the statistical weight of the phase-space volume associated with the initial and final states [Mor73]:

$$\Gamma_i = \frac{1}{2\pi\rho_c(E)} \frac{4m_i}{\pi\hbar^2} \int_0^{E-S_i-B_i} \sigma_{inv}\rho_i(X)(E - B_i - S_i - X)dX \tag{1.2}$$

where m_i is the mass of the emitted particle, S_i is the separation energy, B_i is the Coulomb barrier for charged particles and σ_{inv} is the cross-section associated with the inverse process. For a given energy E, the statistical weight of the initial and final states are given by the level densities of the compound nucleus ρ_c and the evaporation residue ρ_i.

The statistical description of the fission decay makes use of the transition-state model [Boh39], in which the compound nucleus regime and the fission regime are separated by a given point in phase space, the so-called saddle point [1]. The decay rate is identified with the phase-space flux across this point in the fission direction X and can be written as [Mor73]:

$$\Gamma_f^{BW} = \frac{1}{2\pi\rho_c(E)} \int_0^{E} \rho_f(X) \cdot P(E - B_f - X)dX \tag{1.3}$$

being ρ_f the level density of transition states of the fissioning nucleus in the saddle-point configuration, B_f the height of the fission barrier and $P(E - B_f - X)$ the quantum mechanical probability of penetrating the barrier.

Within equations 1.2 and 1.3 derived from statistical arguments, all the physical information concerning the nucleus at the saddle point and after particle emission is condensed in the level density. The simplest form of this quantity was deduced on the basis of the Fermi-gas model [Bet36, Lan65] which considers the nucleus as a system of non-interacting fermions occupying equidistant non-degenerate single particle levels. Its expression can be calculated on the basis of the grand partition function [Eri60, Gad92] as:

$$\rho(E) = \frac{\pi}{12} \frac{e^{2\sqrt{aE}}}{a^{1/4}E^{5/4}} \tag{1.4}$$

where E is the excitation energy of the system and a is the level density parameter [Bab70] in units of MeV^{-1}. This expression can be generalized to account for the angular momentum J of the nucleus, according to:

$$\rho(E, J) = \frac{1}{2} \frac{2J + 1}{\sqrt{2\pi}\sigma^3} e^{-\frac{J(J+1)}{2\sigma^2}} \rho(E) \tag{1.5}$$

where σ^2 is the spin cut-off factor given by:

$$\sigma^2 = \frac{\Im T}{\hbar^2} \tag{1.6}$$

---

[1] An attempt to extend the transition-state formalism to particle evaporation was carried out by Swiatecki [Swi83] on the basis of a canonical version of the model.

being $\Im$ the moment of inertia of the nucleus and T the nuclear temperature.

The little physics contained in this expression, beyond the Pauli principle, limits its application to rather high energies. At lower energies, the detailed structure of the single particle levels close to the Fermi energy surface are known to have a strong influence on the level densities [Hui72, Ign75a]. At present, numerous models exist that account for these effects both from microscopic [Mor72, Sch82] and phenomenological [Gai91, Jun98] points of view. A detailed discussion of their main considerations is beyond the scope of this work; we will limit ourselves to mention that for the present analysis we have used the phenomenological approach described in reference [Jun98]. The details of this formulation will be discussed in chapter 5.

Until now, the physical considerations underlying the derivation of the level density involved only the intrinsic nuclear degrees of freedom. The peculiar nature of collective motion of excited nuclei and their coupling to the intrinsic degrees of freedom substantially complicates the calculation of the shape and volume of the phase space which controls the statistical decay processes [Mor73]. Motivated by the analogy with molecular physics, where collective rotational bands and phonon vibrational excitations are coupled to electronic excitations, Bjornholm, Bohr and Mottelson [Bjo73] calculated the contribution of collective motion to the level density from the symmetry types of the nuclear shapes. Following an adiabatic formalism, in which the internal and collective degrees of freedom are completely decoupled to each other, these authors expressed the total level density $\rho(E)$ by:

$$\rho(E) = K_{coll}(E) \cdot \rho_{int}(E) \tag{1.7}$$

where $\rho_{int}(E)$ is the level density of the internal excitations (equation 1.4) and $K_{coll}(E)$ represents the collective enhancement factor.

For nuclei with well defined rotational symmetry-breaking, such as fissioning nuclei with highly deformed saddle points or nuclei with ground state deformations, the factor $K_{coll}(E)$ arises from the appearance of rotational bands above the intrinsic single-particle levels. In the case of axial and mirror symmetry, this factor was estimated to be proportional to the spin cutoff parameter $\sigma_\perp^2$ [Bjo73, Hui74a], given by:

$$K_{rot} \propto \sigma_\perp^2 = \frac{\Im_\perp T}{\hbar^2} \tag{1.8}$$

where $\Im_\perp$ is the rigid-body moment of inertia around an axis perpendicular to the nuclear symmetry axis and T is the temperature. This formalism leads to enhancements of the total level density by a factor of 10-100 at low energies. By contrast, the collective motion associated with near spherical nuclei is analyzed on the basis of low frequency vibrational modes of shell oscillation. For those nuclei which are known to be good vibrators, the factor $K_{coll}(E)$ can be calculated from the statistical sum of harmonic modes of vibration [Bjo73], given by:

$$K_{vib} = \left[1 - exp\left(-\frac{n\hbar\omega}{T}\right)\right]^g \tag{1.9}$$

where $n\hbar\omega$ stands for the nth-vibrational mode and $g = 2\lambda + 1$ is the degeneracy factor associated with a shape vibration of multiple order λ. Although this equation yields values of K_{vib} up to one order of magnitude lower than K_{rot}, further studies of the level density based on the production cross sections of fissioning actinides [Jun98] demonstrated that this factor led to a general overestimation of the level density for nuclei near a closed shell. Moreover, the transition from K_{vib}, for near spherical nuclei, to K_{rot}, for deformed nuclei, seemed a bit too abrupt, specially in regions of moderate deformation, where the collective character (rotational or vibrational) was not well defined. The failure of equation 1.9 was attributed to the assumed harmonic behavior of nuclear vibrations which is only valid for very few cases. Indeed, the transition from spherical to deformed shapes is accompanied by an increase of the anharmonic character of the shape vibrational modes [Bjo73]. An alternative formulation of the problem was proposed by Junghans et al. [Jun98] on the basis of a phenomenological approach, which assumes a gradual transformation of the rigid rotor moment of inertia (used to describe the rotational collective enhancement at large deformations) to an irrotational flow moment of inertia (for near spherical nuclei) more appropriate to describe vibrations. This model has been used to analyze our experimental results, as will be discussed in chapter 5.

Finally, since collective motion originates from the coherent superposition of a few higher-lying single particle excitations, a question arises regarding the reduction of the internal level density $\rho_{int}(E)$ at high energies, which is not included in the present formalism. The answer lies in the rapid increase of $\rho_{int}(E)$ with excitation energy: the inclusion of spurious higher-lying internal levels will not significantly affect the large values of $\rho_{int}(E)$ found at high energies. On the other hand, the appearance of collective states have a strong influence in the phase space available at low energies, for which the contribution from the single particle states is rather small. At high energies, the fluctuations in the deformation of the nucleus due to the single particle motion becomes so large that the collective and internal degrees of freedom begin to mix, leading to an absorption of the collective states into the intrinsic level density [Mor73]. The damping of K_{coll} was theoretically estimated by Hansen and Jensen, on the basis of the one-shell SU(3) model [Han83] and further analyzed by Junghans et al. [Jun98]. Details of that work will be discussed in chapter 5.

1.2 Dynamical models

The statistical model is reasonably successful in describing the competition of fission and evaporation at moderate energies, especially where the ratio Γ_f/Γ_{ev} is concerned. However, measurements of pre-scission particle emission revealed an enhanced neutron multiplicity as compared to those predicted by the statistical model [Hil81, Gav81]. This result was later interpreted as a signature of the time needed by the system to populate the phase-space configurations above the saddle point. According to this idea, the competition between the two deexcitation processes is ruled by the dynamical coupling between collective and internal degrees of freedom, which leads to the final thermal equilibrium assumed in the statistical model. Moreover, this coupling might damp the fission motion of the compound nucleus from the ground-state configurations to the scission point, giving rise to a general enlargement of the fission times.

A theoretical description of the deexcitation mechanisms which considers the interplay between the microscopic and macroscopic nature of the process is formulated in terms of stochastic transport equations [Wei80]. Such an approach simplifies enormously the microscopic calculations based on the time-dependent Hatree-Fock method (TDHF) [Mor91, Neg78]. In transport theories, the fission degree of freedom X is thought to be merged into a heat bath constituted by the internal motion of the single particles' degrees of freedom x_i. The deexcitation process is then described by solving the equation of motion associated to X, whose lagrangian can be written in a general way as follows:

$$L(X,\dot{X},x_i,\dot{x}_i) = L_{macro}(X,\dot{X}) + L_{micro}(x_i,\dot{x}_i) + L_{inter}(X,\dot{X},x_i,\dot{x}_i) \qquad (1.10)$$

where the term $L_{macro}(X,\dot{X})$ depends on the macroscopic potential associated with the fission coordinate $V(X)$ (see figure 1.1), $L_{micro}(x_i,\dot{x}_i)$ stands for the microscopic motion of the nucleus that constitutes the heat bath and $L_{inter}(X,\dot{X},x_i,\dot{x}_i)$ corresponds to the interaction between the internal x_i and collective X degrees of freedom. By assuming that the internal motion of the nucleus is determined by the fluctuations of the constituent nucleons and that the coupling between X and x_i is linear in first approximation, one gets the one-dimensional Langevin equation for the fission coordinate X [Fro98, Abe96]:

$$M(X)\ddot{X} = \frac{\partial}{\partial X}V(X) - \gamma(X)\dot{X} + \sqrt{D(X)}f(t) \qquad (1.11)$$

with

$$\langle f(t), f(t')\rangle = 2\delta(t-t') \qquad (1.12)$$

and $M(X)$ the inertia associated with the fission degree of freedom.

The first right-hand term of equation 1.11 corresponds to the drift force associated with the macroscopic potential which governs the evolution of X in absence of internal degrees of freedom [2], whereas the second and third terms correspond to the friction and diffusion forces, respectively. The friction coefficient $\gamma(X)$ weights the damping of the collective motion due to its coupling with the internal degrees of freedom; it is related to the reduced dissipation coefficient by $\beta(X) = \gamma(X)/M(X)$. The diffusion force is given by the product of the stochastic variable $f(t)$, which represents the sum of the motions of the internal nucleons, and the diffusion coefficient $D(X)$. The latter is related to the temperature of the system and the reduced dissipation coefficient according to the dissipation theorem:

$$D(X) = TM(X)\beta(X) \qquad (1.13)$$

---

[2] Because the compound nucleus is hot, the driving force is given by the liquid drop part of the free energy F. This quantity corresponds to the macroscopic potential with a thermodynamical correction that depends on the temperature and the level density parameter a ($F(T,X) = V(X) - aT^2$).

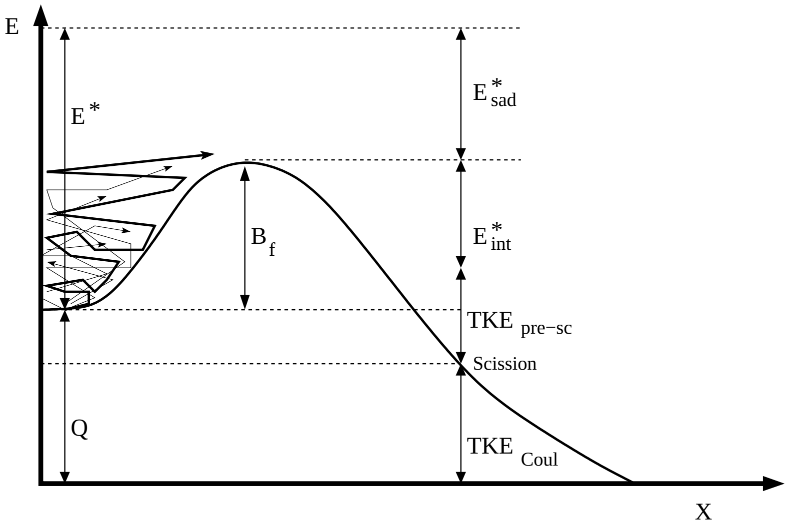

Figure 1.1: *Schematic representation of the macroscopic potential V(X) as a function of the fission degree of freedom. The initial excitation energy of the heat bath* E^**, the Q-value associated to the fission decay, the fission barrier* B_f *and the excitation energy above it* E^*_{sad} *are shown. At the end of the process the potential energy from saddle to scission is partly transformed into internal excitation energy* E^*_{int} *and collective energy that leads to the pre-scission kinetic energy* TKE_{pre-sc}*. The remaining kinetic energy of the two fission fragments arise from Coulomb repulsion* TKE_{Coul}*.*

which follows from the common origin of the friction and diffusion forces on the coupling between the collective degree of freedom and the heat bath.

Equation 1.12 establishes that the effects of the internal motion on the collective degree of freedom at a time t are not affected by those at the earlier times $t' < t$, i.e, they are not time-correlated. Such a condition corresponds to a Markovian process in which the "microscopic time" t_{micro} needed by the heat bath to reach equilibrium is much shorter than the "macroscopic time" t_{macro} required for the collective variable X to vary significantly. Hereafter, we will consider that the slow evolution of the fission degree of freedom fulfills this condition.

According to equations 1.11 and 1.13, the reduced dissipation coefficient $\beta(X)$ governs the collective fission motion of the compound nucleus, from its ground-state configuration toward a highly deformed shape at the scission point. The whole process is schematically illustrated in figure 1.1 and can be described as follows:

In the beginning of the process, all the excitation energy of the system E^* is absorbed by the heat bath of the compound nucleus, in thermal equilibrium with temperature T [3], whereas the collective degree of freedom (fission coordinate) remains "bound" in the ground state of the macroscopic potential $V(X)$ by the drift

---

[3] The temperature T can be deduced for instance from the Fermi-gas relation $T = \sqrt{E^*/a}$; where a is the level density parameter.

force term of equation 1.11. Due to the coupling between X and the heat bath, the internal motion of the system induces a fluctuating drift force, -proportional to the temperature T and the dissipation $\beta(X)$- that produces a "rising" stochastic motion of the fission degree of freedom X toward the saddle point. At the same time, this collective motion is partly damped by the friction force depending on the coefficient $\beta(X)$ and $\dot{X}$. Beyond the saddle point, fission turns out to be an irreversible process, though it is still delayed by the damping of the friction force. According to this, dissipation affects the fission process in several aspects: First, it is the quantity responsible for the collective thermal fluctuations that result in the fission decay process (diffusion). Secondly, it hinders this process by damping the collective motion toward the saddle point and beyond it. Third, it delays the entire fission motion from the ground-state configuration to the scission point.

The main difference between the dynamical approach and the statistical picture is that the former considers explicitly the evolution of the trajectories of the fissioning system over the phase-space volume between the ground state and the saddle point (see figure 1.1). From a qualitative point of view, this formulation leads to the following conclusions:

1. The collective trajectories shown in figure 1.1 need an average time to reach the saddle point, after which the quasiestationary flow will cross this point. That means that the statistical approach, in which all the phase-space is available, is only valid after a transient time.
2. The friction of the collective motion with the heat bath reduces the average number of trajectories that reach the saddle point and consequently the quasi-estationary flow across the saddle point will be lower than in a pure statistical model.
3. The damping of the fission motion, from the ground-state configuration to the scission point gives rise to an enlargement of the fission times.

A quantitative analysis of the dynamics of the deexcitation process was formulated in terms of the Fokker-Planck equation (FPE) [Kra40, Gra83, Hof83], which corresponds to the integral version of the Langevin equation, provided the Markovian condition is fulfilled. The use of the Fokker-Planck equation enables the study of the time-dependent probability distribution $W(X, \dot{X}, t)$ of collective trajectories as a function of X and its canonically conjugate momentum $\Pi = \dot{X}/M$, instead of solving equation 1.11 for different trajectories. By assuming the inertia and reduced dissipation coefficient to be constant quantities independent on the fission degree of freedom X, the FPE can be expressed by:

$$\frac{\partial W}{\partial t} = \left[-\frac{\partial}{\partial X}\dot{X} + \frac{\partial}{\partial \dot{X}}\left(\beta\dot{X} - \frac{1}{M}\frac{\partial}{\partial X}V(X) \right) + \frac{\beta T}{M}\frac{\partial^2}{\partial \dot{X}^2} \right] W \tag{1.14}$$

As was demonstrated in reference [Jur04a], the requirement of a constant mass inertia M can be fulfilled by choosing an appropriate coordinate system that defines the collective degree of freedom X. Although, this method provides a formal argument to support the approximation of a constant inertia, it does not justify the use of a constant dissipation coefficient. Several studies of the dependency of β upon the nuclear deformation suggest that this quantity remains rather constant along the fission path, at least until the saddle point is reached, whereas it might vary significantly at larger deformations [Fro93, ChP02]. According to this argument it is necessary to make the distinction between fission motion involving small shape distortions, e.g. between the ground-state configuration and the saddle point, and fission motion at high deformations beyond the saddle point:

On the one hand, the study of the fission probability, or equivalently the fission lifetime τ_f involves collective motion up to the saddle point ($X < X_{sad}$). Consequently, the assumption of a deformation-independent dissipation coefficient β in equation 1.14 has no major influence on the final result. On the other hand, as will be seen later, in order to account for the high pre-scission neutron multiplicities it is necessary to describe the entire fission motion, including deformations beyond the saddle point. Under this conditions, the value of β which defines the damping from saddle to scission might vary significantly with respect to the value at small deformations.

The first attempt to provide a dynamical description of the fission probability was carried out by Kramers [Kra40] who calculated the stationary probability current above the saddle point by making use of the time-independent Fokker-Planck equation. According to this author, the stationary solution of the FPE leads to a reduction of the fission width calculated by Bohr and Wheeler [Boh39] (equation 1.3) by the so-called Kramers' factor:

$$K = \sqrt{1+\gamma^2} - \gamma^2 \tag{1.15}$$

where γ is related to the reduced dissipation coefficient defined by:

$$\gamma = \frac{\beta}{2\omega_0} \tag{1.16}$$

being ω_0 the frequency of an inverted oscillator potential that simulates the fission barrier at the saddle point.

The time-dependent solution of equation 1.14 was numerically calculated by Grangé, Jun-Qing and Weidenmüller [Gra80, Gra83]. By using the conservation law for the probability current, these authors related the fission lifetime τ_f to the time-integrated escape rate across the saddle-point. The resulting time-dependent fission width $\Gamma_f(t)$ increases smoothly from zero value, at t=0, to an asymptotic value given by the Bohr and Wheeler fission width corrected by the Kramers factor. This delay of the fission probability is related to the average time needed by the collective trajectories shown in figure 1.1 to reach the saddle point. The transient time τ_{tr} was then formally defined as the time needed by $\Gamma_f(t)$ to reach 90% of its asymptotic value; its dependence upon the dissipation coefficient β is rather complicated. In particular, there is a critical value of β (frequently referred to as critical damping)

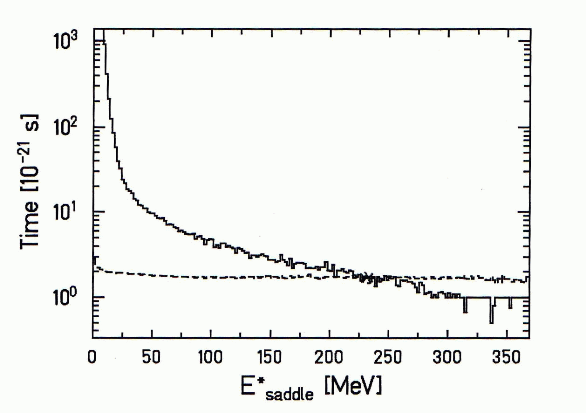

Figure 1.2: *Energy dependence of the average statistical decay time* $\langle\tau_{sta}\rangle$ *(solid line) compared to the average transient time* $\langle\tau_{tr}\rangle$ *(dashed line). The calculations were done for the reaction* ^{238}*U(1 A·GeV)+Pb with* β*=2×10*^{21} *s*$^{-1}$ *by B. Jurado [Jur04b].*

for which the transient time reaches a minimum value. It corresponds to the case where the diffusion and friction terms in equation 1.11, connected by the dissipation theorem, lead to the fastest possible population of the phase-space at the saddle point.

The suppression of the fission probability during the transient time τ_{tr} favors the deexcitation of the nucleus by evaporation of light particles leading to enhanced pre-scission neutron multiplicities [Gra80, Gra83]. The experimental observation of the delay of the fission process due to transient effects depends very much on the excitation energy of the nucleus. Figure 1.2 compares the mean value of the transient time $\langle\tau_{tr}\rangle$ (dashed line), calculated by B. Jurado et al. [Jur04b] for the reaction ^{238}U(1 A·GeV)+^{208}Pb, with the average statistical decay time $\langle\tau_{sta}\rangle$ (solid line) for the compound nuclei. As can be seen, at low energies τ_{sta} is much longer than τ_{tr} and consequently the delay of the fission process due to transient effects can not be observed. However, as the excitation energy increases beyond ~200 MeV, the transient time becomes larger than the statistical time, leading to a reduction of the fission width compared to that predicted by the statistical model, accompanied by an increment of the pre-scission neutron multiplicities. Therefore, transient effects will only be experimentally observed for excitation energies near or above 150 MeV [Jur04b]. Below this value, dissipation might still affect the data by reducing the fission width according to the Kramers factor, although this effect is less dramatic than the total suppression of fission during the transient time.

The dynamical description of the fission probability considers explicitly the collective fission motion at small deformations, from the ground-state configuration toward the saddle point. The reduced fission widths with respect to the statistical values causes an increase of the pre-saddle neutron multiplicities. Furthermore, as soon as the compound nucleus surmounts the fission barrier, it evolves irreversibly up to the scission point, where the compound system splits into two fragments (see figure 1.1). During this descent, the excited nucleus can still evaporate few neutrons that will then contribute to the total pre-scission neutron multiplicities. These post-saddle emissions are favored by the damping of the fission motion at these larger deformations. According to this idea, Grangé et al. [Gra86, Bha86] considered that the neutron emission prior to fission should be related to the fission time at scission τ_{sc}, which can be obtained as the sum of the fission lifetime at the saddle point τ_f (discussed above) and the saddle-to-scission time τ_{ssc}:

$$\tau_{sc} = \tau_f + \tau_{ssc} \tag{1.17}$$

The latter has been calculated by H. Hofmann and J.R. Nix [Hof83] by integrating the density of probability $n(X)$ given by the Kramer's stationary solution, normalized to the current probability $j(X)$, from the saddle point X_{sad} to the scission point X_{sc}, assuming an average constant dissipation coefficient γ:

$$\tau_{ssc} = \int_{X_{sad}}^{X_{sc}} dX \frac{n(X)}{j(X)} = \left[\left(1+\gamma^2\right)^{1/2} + \gamma\right] \tau_{ssc}^0 \tag{1.18}$$

The factor τ_{ssc}^0 refers to the non-dissipative saddle-to-scission time, which is calculated using the analytical expression:

$$\tau_{ssc}^0 = \frac{2}{\omega_0} R\left(\sqrt{\Delta V/T}\right) \tag{1.19}$$

where

$$R(z) = \int_0^z e^{y^2} dy \int_y^\infty e^{-x^2} dx \tag{1.20}$$

is a function studied and tabulated by Rosser [Ros48]; ΔV is the potential energy difference between the saddel point and the scission point and T is the nuclear temperature (details of this formulation can be found in appendix E). The value of γ in equation 1.18 corresponds to the average dissipation at large deformations, between saddle and scission points, and therefore can differ significantly with respect to the value used to describe the fission probability. According to this, the comparison of the values of dissipation required to describe the fission width $\Gamma_f(t)$ and the saddle-to-scission time τ_{ssc} could be used to analyze the possible deformation dependence of dissipation. These investigations are of fundamental interest for determining the underlying mechanism which define the dissipation of nuclear matter: According to the two-body theory [Neg78, Car86, Dav76, Wer81], dissipation remains rather constant at different deformations, while Dependant strongly on the temperature of the nucleus. By contrast, one-body mechanisms [Blo78, Fel87, Car86] predict very high values of dissipation that vary significantly with deformation.

1.3 Experimental investigations of collective motion

Collective motion in nuclear reactions has been extensively studied in the last decades by means of different experimental approaches. They were focused on the presence and nature of rotations and vibrations (small-scale motions) and the damping of large-scale fission motion due to the friction with the nuclear heat bath. In the following we briefly summarize the main considerations of these investigations.

Small-scale collective motion

Small-scale collective nuclear motion is manifested by the appearance of collective rotational and vibrational states above the intrinsic single particle levels. The presence of such levels at low energies has been investigated in nuclear spectroscopy by analyzing the transitions between excited states according to their spin, parity and excitation energy pattern (see for instance the review article of Alder et al. [Ald56]). This method is only applicable at rather low energies, close to the yrast line, where the nuclear levels are well separated.

At higher energies, where the levels are overlapped, the appearance of collective excitations can be inferred from their influence on the statistical properties of nuclei. As was discussed in section 1.1, the presence of rotations and vibrations leads to an enhancement of the intrinsic level density about 10-100. Consequently, collective excitations can be detected by comparing the measured level density $\rho(E)$ with that calculated from the single-particle excitations $\rho_{int}(E)$.

At present, the most abundant information on level densities comes from the counting of low-lying levels and from neutron resonances. This technique has been extensively exploited to investigate shell and collective effects on nuclei at different deformations. The analysis of neutron resonance spacing led to rather controversial results: On the one hand, Huizenga et al. [Hui74a, Hui74b] found that the experimentally measured level densities of deformed nuclei with $50 < A < 250$ could only be reproduced with numerical calculations when the collective enhancement was included. On the other hand, Kataria et al. [Kat78] found that such collective effects were not required when calculating the level density on the basis of their prescriptions.

The comparison of the decay rates of different deexcitation channels was also used to investigate the relative level densities associated with the configuration of each decay channel. For instance, the competition between the emission of different evaporated particles can be written from their respective decay widths [Mor73]:

$$\frac{\Gamma_i}{\Gamma_j} \propto \frac{\rho(E - B_i - S_i)}{\rho(E - B_j - S_j)} \tag{1.21}$$

Thus, by measuring this quantity it is possible to relate the level densities of neighboring nuclei with similar properties.

The application of this method for nuclei decaying by fission is specially interesting for investigating structural effects at different deformations since it relates the level densities of similar nuclei with very different configurations: the daughter evaporation nucleus in its ground-state deformation and the deformed fissioning father nucleus at the saddle point. The level density of the former is very sensitive to the presence of shell effects and collective excitations that arise mainly from vibrational and rotational motions at different deformations. By contrast, the shell effects of the fissioning father nucleus at the saddle point are expected to be small, while its large deformations favors the presence of rotational bands. According to this, the measurement of the fission probabilities can be exploited to investigate collective motion at saddle and ground-state deformations of neighbor nuclei.

Measurements of fission probabilities were undertaken for nuclei around ^{208}Pb [Mor72, Ign85, Mor95] at excitation energies above 20 MeV. These results could be equally reproduced either by neglecting any structural effect [Hui72, Mor95] or by including shell effects and collective excitations [Ign79a, Ign85, Ilj92]. These rather opposite conclusions could not be clarified due to the high fission barriers involved, which favor the washing out of collective effects at high excitation energies.

In contrast to this, the fission barriers of nuclei around the neutron shell N=126 are expected to be small and offer then the possibility for investigating shell and collective effects of near magic nuclei at low energies. The productions of these nuclei in fusion reactions are expected to be enhanced due to the shell stabilization around N=126 [Ver84, Sah85]. However, measurements of evaporation residues around ^{216}Th have revealed a normal production, which was interpreted as a lack of stabilization against fission due to the influence of collective excitations [Ign83, Sch84]. An understanding of these effects is crucial for the synthesis of superheavy nuclei, as discussed in reference [Zub02].

Collective rotational and vibrational enhancement of the level density has been intensively analyzed by A. Junghans et al. [Jun98] on the basis of measured evaporation cross sections for actinides and heavy pre-actinides produced in the reaction ^{238}U on Cu at 950 A·MeV. In this work, the damping of the collective motion with nuclear temperature has been also investigated.

Dynamics of large-scale fission motion

Dissipation of nuclear matter has been investigated in the past from the transfer of energy between the collective and internal degrees of freedom in the fission process. For instance, part of the collective energy can be reconverted into internal excitation energy E^*_{int}, during the descent from saddle to scission with the subsequent reduction of the collective pre-scission kinetic energy (TKE_{pre-sc}) (see figure 1.1). Thus, dissipation beyond the saddle point can be directly investigated by measuring the total kinetic energy at scission TKE [Hin92, HiH92], or indirectly by analyzing the internal excitation energy transferred to the nascent fission fragments, e.g. by measuring the disappearance of odd-even effects of the fission fragments at low energies [Gon91, Rej00].

An extended method to investigate dissipation of the fission motion is based on the measurement of pre- and post-scission neutrons [Hil92] or GDR γ-ray [Pau94] multiplicities of hot rotating nuclei produced in fusion-fission reactions. The observed high pre-scission multiplicities with respect to the predictions of the statistical model were interpreted as an evidence of the longer fission times due to dissipation. These observables have been combined with measurements of the fission probabilities P_f or survival probabilities against fission $1 - P_f$ in order to investigate the deformation-dependence of dissipation: whereas the fission cross sections provide information on dissipation up to the saddle point, pre-scission multiplicities are sensitive to the entire range of deformations, from the compound configuration to the scission point. Fröbrich et al. [Fro93] analyzed the pre-scission neutron multiplicities and fission probabilities with one-dimensional Langevin calculations coupled to statistical codes. These authors found that the experimental observables could only be reproduced with a deformation-dependent dissipation coefficient described by a constant value $\beta = 2$ Zs^{-1} [4], at small deformations, and a linear increase with deformation when the necking of the fissioning nucleus starts to set in. This deformation-dependent β was interpreted as a signature of two-body dissipation for compact shapes and the onset of one-body dissipation at larger deformations. Later, G. Chaudhuri and S. Pal [ChP02] investigated the pre-scission neutron multiplicities of several fusion-fission compound nuclei with their one-body chaos-weighted wall formula (CWWF) [ChP01]. The reduced dissipation coefficients obtained from this formula, with respect to the original wall formalism, coincided with the value suggested by Fröbrich et al. [Fro93] for nuclei with small deformations. However, the same formula was not able to reproduce the pre-scission multiplicities of very heavy compound nuclei, dominated by saddle-to-scission emissions. This was interpreted as a possible signature of increasing values of the dissipation coefficients beyond the saddle point.

Alternatively, other authors [Dio00, Sha00, Dio01] have tried to investigate dissipation at small and large deformations by separating the pre-saddle and the saddle-to-scission components of the GDR γ-ray spectra with the use of the CASCADE code [But91]. N.P. Shaw et al. [Sha00] analyzed the γ-ray GDR spectra of ^{240}Cf at different energies in order to investigate a possible temperature-dependence of dissipation. The major advantage of this system is that the measured pre-scission γ-rays were dominated by the saddle-to-scission component due to the vanishing fission barriers at relatively low angular momenta. The experimental results could be reproduced over the entire range of energies with a constant value of $\gamma = 2$, inside the saddle point, and of $\gamma = 5 - 10$ between saddle and scission [5]. This temperature independent behavior, combined with the large value of γ, was interpreted by these authors as a signature of one-body dissipation mechanism.

As mentioned, the observables discussed above are normally investigated from excited rotating nuclei produced in fusion-fission reactions. The interpretation of the experimental results requires the use of dynamical codes that describe the formation of the compound nucleus and its deexcitation along the fission process. The main uncertainty of this type of analysis arises from the very large angular momenta of the rotating nuclei, which may lead to vanishing fission barriers, and the contribution of the fast fission and quasifission component to the measured data. Under this conditions it is rather complicated to establish the initial conditions of the compound

---

[4] 1 Zs^{-1}=1$\times$10^{21} s^{-1}

[5] By making use of equation 1.16 and assuming $\omega_0 \simeq 1$ Zs^{-1}, these values of γ correspond to a value of $\beta \simeq 4$ Zs^{-1} inside the saddle point, and of $\beta \simeq 10 - 20$ Zs^{-1} beyond this point.

nucleus, leading to significant uncertainties that preclude a precise determination of the viscosity parameter. A detailed discussion of this and other shortcomings associated with these experimental approaches are presented in reference [Jur02].

Collective motion induced by spallation reactions

In the present work, we have investigated the collective nuclear motion in hot nuclei by analyzing the relative productions of fission and evaporation residues in the spallation reaction ^{238}U at 1 A·GeV on deuterium. As was described above, the competition between these two decay modes is strongly influenced by the presence of collective rotational and vibrational motion, as well as by the damping of the fission motion. This experimental approach has been extensively used in the last decade to investigate small-scale collective motion [Jun98] and the onset of dissipation [Ign95, Ben02, Jur04b, Jur04c] at small deformation.

The major advantage of the use of spallation reactions induced with Uranium on deuterium lies on the particular initial conditions of the decaying compound nuclei. According to the two-step formalism [Ser47], the fast interaction between the light and heavy reaction partners and the subsequent thermalization of the intermediate projectile-like pre-fragments result in a distribution of excited compound nuclei characterized by rather low angular momentum, small shape distortions [Jon97] and a wide range of excitation energies. Under these conditions, the study of collective motion in excited compound nuclei is simplified by several reasons:

1. The small shape distortions and angular momenta of the projectile-like pre-fragments make it possible to apply the Grangé and Weidenmüller formalism [Gra80, Gra83], which assumes small initial deformations.
2. The high energies induced by the collision of the uranium projectile with the deuterium target offer optimum conditions to analyze transient effects in the fission motion.
3. The relative small fission barriers of actinides and heavy pre-actinides provide an scenario to investigate the onset of rotational and vibrational motion at low excitation energies.

The experimental observables analyzed in the present work include the production cross sections of fission and evaporation residues and the velocities of the fission fragments. As will be discussed in chapter 5, these observables will provide insight into different aspects of collective nuclear motion:

The role of dissipation at small deformations could be investigated from the productions of fission and evaporation residues. The damping of the fission motion up to the saddle point is manifested by the hindrance of the fission process, or complementary by the enhancement of the evaporation cross sections. The low-energy evaporation residues, in the region of actinides and heavy pre-actinides were thus used to deduce the value of β from the Kramers factor. Moreover, the productions of fission and light evaporation residues at higher energies provided insight into the transient effects of the time-dependent fission probability. Apart from this, the velocities of the fission residues, defined at the scission point, were combined with the production cross sections in order to investigate the fission process beyond the saddle point. From this analysis we could study the role of dissipation at deformations beyond the saddle point.

In addition to this, the production cross sections of high-fissile actinides and heavy pre-actinides are very sensitive to small-scale collective motion. Therefore, this observable was also used to investigate the role of rotational and vibrational excitations upon the survival probability against fission for these nuclei and their damping with excitation energy.

Chapter 2

Experimental technique

In the present work, the fission resides produced in the reaction ^{238}U (1 A·GeV) on deuterium were studied by measuring their isotopic production cross sections and kinematics. The complexity of these measurements, along with the specific features of the reaction required very specific experimental conditions:

First, the isotopic production cross sections can only be determined after a clean separation and identification of the reaction product. While this requirement is easily fulfilled for light ions, it is a significant challenge for the heavy nuclei produced in the present reaction. Secondly, the yield and velocity measurements of each nucleus must be determined prior to any radioactive decay, in order to prevent the mixing of the nuclear properties of the father and daughter nuclei. Finally, the production rates must be high enough to keep the statistical uncertainties as low as possible.

According to these constraints, the best experimental choice is to perform the nuclear reaction in inverse kinematics, in such a way that the produced projectile-like fragments are emitted forward and can then be analyzed with an in-flight magnetic separator. At present, the only experimental facility which offers the possibility of employing this technique to study relativistic heavy-ion reactions is the GSI in Darmstadt, Germany (see figure 2.1). The SIS synchrotron can accelerate the ^{238}U projectiles up to an energy of 1 A·GeV with intensities of the order of 10^8 ions/s.

In the present experiment, after its extraction, the beam was monitored on the Secondary Electron Transmission Monitor (SEETRAM) and focused onto the liquid-deuterium target. Most of the projectile-like fragments left the target forward-emitted, and those with angular emittance smaller than the angular acceptance of the Fragment Separator (FRS) could then be analyzed. The ion-optical characteristics of this separator, together with its precise detection equipment, guarantied the unambiguous separation and identification of the selected reaction products according to their mass and atomic numbers. Furthermore, the time needed to measure the productions yields and velocities was of the order of 150 ns, avoiding losses due to radioactive decays. In addition to this, the limited angular acceptance of the apparatus enabled the identification of the different reaction mechanisms from their kinematics.

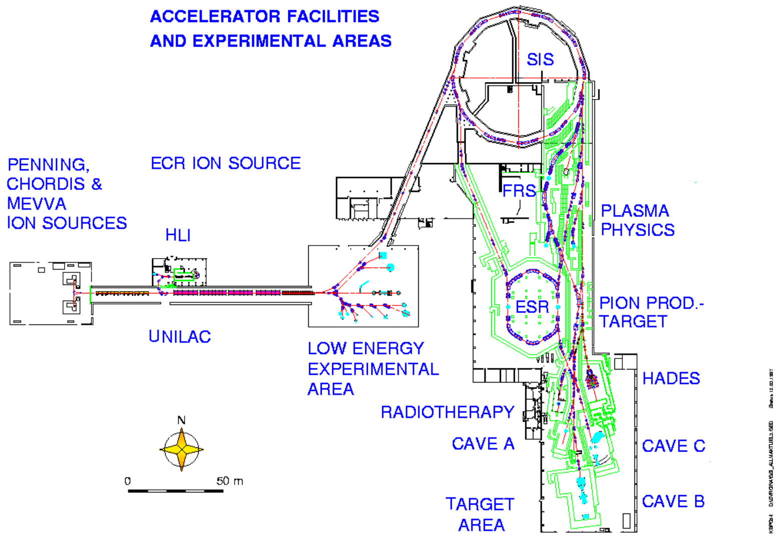

Figure 2.1: *Schematic view of the GSI facilities. The ion sources deliver the ions which are accelerated in the UNILAC and then injected into the SIS synchrotron. After being re-accelerated, the primary beam is driven to the FRS or to other experimental areas.*

2.1 The accelerator facility and the detection setup

This section is intended to provide a general introduction to the experimental facility employed to study the present reaction, beginning with a brief description of the technical aspects concerning the preparation and acceleration of the primary beam. The second part focuses on the general characteristics of the Secondary Electron Transmission Monitor (SEETRAM). The third part concerns the deuterium target and the importance of using a liquid system. The section ends with a brief summary of the technical aspects of the FRS, including the standard detection equipment.

2.1.1 Accelerator system

The study of the nuclear reaction ^{238}U (1 A·GeV)+d in inverse kinematics can only be done with an accelerator facility capable of delivering the U-beam at such high energies. Furthermore, the very high degree of precision required by the experiment relies in part on a high beam quality. An example of this is the fact that the resolution achieved by a separator depends strongly on the beam emittance in the target. Thus, during the acceleration process, the transversal beam emittance must be kept as low as possible. In addition, as will be discussed later, the operation mode of the ion sources and the charge state injectors are critical for making the high energies and intensities demanded by the experiment feasible.

The accelerator facility at GSI, responsible for the production of the ^{238}U beam, consists of three different stages [Acc95]: the ion source, the linear accelerator UNILAC and the heavy ion synchrotron SIS.

First the uranium ions, used as beam particles, were generated and extracted from the ion sources, located in the North and South injectors at the beginning of the beam path. In these sources, a high-current gas discharge bombarded the selected atoms to ionize them as efficiently as possible. The generated ions were then extracted and pre-accelerated through a potential difference of up to 2.2×10^5 volts.

The first stage of the UNILAC is made up of a Wideröe accelerator. It consists of four electrode structures, each containing about 130 accelerating electrodes with an inverting-polarity frequency of 27 MHz. Some of the electrodes also contain magnetic lenses to guide the beam along the 30-meter-long axis of the accelerator. The accelerated ions passed through a supersonic gas beam in order to strip off more electrons. At the end of the process, the uranium ions acquired an energy of 1.4 A·MeV and a charge state of around 28+ (28 electrons had been stripped off). This additional ionization was necessary in order to reach the desired final energy using the length of the linear accelerator.

The second stage of the UNILAC acceleration consists of a 55-meter-long Alvarez structure containing four tanks, each of which is 13 m long and has 150 drift tubes. The polarity between the drift tubes electrodes is reversed with a frequency of 108 MHz (four times faster than in the Wideröe structure), delivering the beam at 11.6 A·MeV.

Finally, a third stage consisting of fifteen single resonators made it possible to adjust the ion speed by accelerating or decelerating the ion beam over a range from 2 to 18 A·MeV. The beam was then injected into the SIS over a period of about 100 μs.

The last stage of the acceleration process concerns the synchrotron ring accelerator SIS [Ste92]. The ring consists of 12 identical cells placed consecutively along a circumference perimeter of 216 meters. Each cell contains two dipoles, a focusing quadrupole triplet and a set of sextupoles to correct chromatic aberrations. A thin carbon foil, situated at the entrance of the accelerator was used to increase the charge state of the uranium beam from 28+ to 73+ to reach high energies more efficiently. In order to provide a stable beam, this charge state was kept constant during the acceleration and thus, an extremely high vacuum of up to 10^{-10} torr was needed to avoid the stripping of bound electrons due to collisions with gas molecules. Two radio-frequency structures, situated diametrically opposite each other on the ring, accelerated the beam on each revolution by means of a potential difference of 1.5×10^5 volts. As the speed of the beam was increased with each revolution, the frequency of the two structures rose from 800 kHz to 5.6 MHz.

The maximum energies of the SIS are determined by its maximum magnetic bending power of 18 Tm, which corresponds to about 1 A·GeV for ^{238}U^{73+}. After acceleration, the beam was driven to the experimental area through the extraction beam line. A slow extraction mode was used in the present experiment, which kept

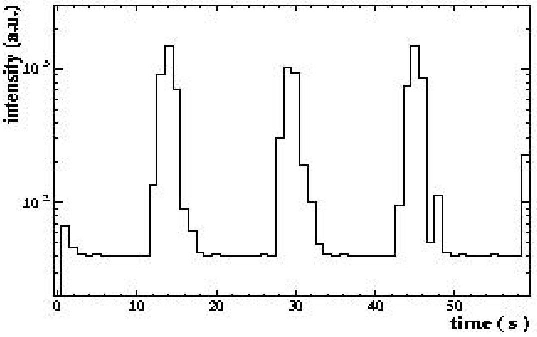

Figure 2.2: *Time profile structure of the beam measured during the present experiment. The beam spills have a length of about 6 seconds over a cycle of* ∼*15 seconds.*

the beam emittance low and led to a typical time structure of a few seconds (see figure 2.2).

Transversal beam emittances were measured in the past with the help of the FRS, as described in reference [Ste92]. Typical values were determined from the standard deviations of the position and angular distributions $\epsilon = \pi\sigma_{position}\sigma_{angle}$, are $\epsilon_{xx'} = (1.8 \pm 0.1)\pi$ mm·mrad and $\epsilon_{yy'} = (4.0 \pm 0.2)\pi$ mm·mrad, with beam widths of 3.0 mm in x and 3.9 mm in y. In addition to this, the beam momentum spread $\delta p = \Delta p/p$ is kept below 10^{-3} during the entire experiment.

The acceleration system employed at GSI also provides the very high intensities necessary to investigate the most exotic reaction products. In the present experiment, the uranium beam reached maximum intensities of up to 10^9 particles/spill, which are below the space-charge limit of SIS.

2.1.2 Beam monitor

As mentioned in the beginning of this chapter, the main goal of the present experiment was the measurement of the production cross sections of the reaction induced by the uranium projectile. Thus, in order to normalize the measured yields, the intensity of the primary beam, i.e. the number of projectiles impinging on the target, must be monitored before the reaction takes place. This monitor must fulfill specific conditions: First, it must withstand very high intensities of the order of 10^8 ions/s without saturating, which implies a linear response as a function of beam intensity. Secondly, it must preserve the high quality of the beam without disturbing its low emittance. Finally, the reaction rate of beam particles with the atoms of the monitor must be kept as low as possible.

According to these requirements, the heavy-ion beam intensities delivered by the SIS were measured by means of secondary-electron transmission monitor (SEETRAM) [Ann85]. An schematic view of this detector is shown in figure 2.3.

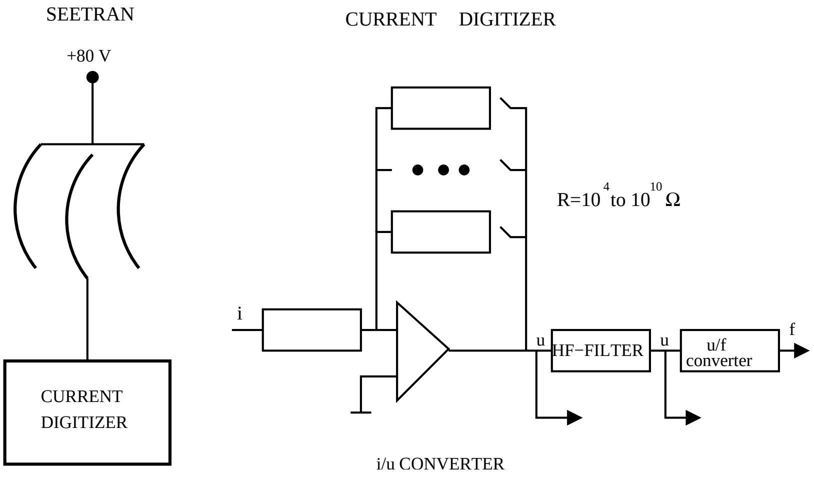

Figure 2.3: *Schematic view of the SEETRAM detector (Left) and the current digitizer (Right).*

The monitor consists of three aluminum foils of 10 μm thickness, mounted on rings of 11.5 cm diameter placed perpendicular to the beam. With this thickness the nuclear reaction rate in the detector was kept below 0.1%. The aluminum foils are slightly curved to minimize mechanical vibrations due to the passage of the primary beam. The inner foil is completely insulated from the rest of the detector and connected to the ground, whereas the outer ones are connected to a voltage of +80 V.

The passage of the beam particles through the inner foil of the detector may release some electrons close to the surface. These electrons are collected by the outer foils under the influence of the potential difference. A current digitizer connected to the central layer measures the resulting positive current. Additionally, the black currents in the monitor produce a constant background signal which must be subtracted from the total counting. The current digitizer transforms the input current into a voltage signal. The relation between the input and output signals depends on the sensitivity of the monitor. Up to seven levels can be selected by properly adjusting a resistance within the range 10^4-10^{10} Ω, which provides an output signal of 1 V from an input current that varies from 10^4 to 10^{10} A. The resulting voltage signals are then filtered, digitized and accumulated in a scaler as *seetram units*. In addition, the fast analogue output of the signal can be used as a monitor for measuring the extraction profile.

In order to determine the intensities of the primary beam, it was necessary to calibrate the voltage signals recorded by the monitor. The calibration [JuS02] was done by comparing the SEETRAM signals with a self-calibrated ionization chamber, which registered the number of beam particles at rather low intensities. The calibration curve obtained in the present experiment was fitted to a linear

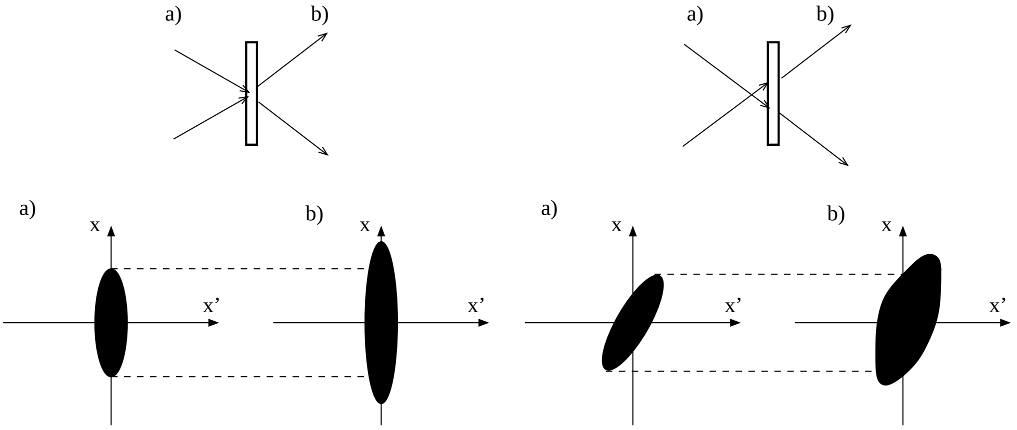

Figure 2.4: *Phase-space diagram showing the evolution of transversal emittance (surface of the black ellipse) of the beam passing through the target. Left: beam focused on the target. Right: beam focused on a point in front of the target. In this latter case, the growth of the emittance due to angular straggling is much more pronounced than in the former case.*

function [1], providing a calibration factor of 290.3(29) particles per SEETRAM unit, which was also used for high intensities since no saturation effects were observed. According to this, the number of beam particles N_{proj} were obtained from:

$$N_{proj} = N_{seet} \cdot f \cdot 10^{10} \cdot S \tag{2.1}$$

where N_{seet} is the number of seetram units, f is the calibration factor, and S is the sensitivity.

The SEETRAM detector was used continuously during the entire experiment to monitor the beam profile and to count the number of incident projectile beams. This number was accumulated in a scaler and later plotted as a function of time as shown in figure 2.2. The total number of SEETRAM units N_{seet}, obtained by integration of this spectra, include the quasi-constant offset of black currents induced in the detector. Such background signals had to be subtracted in order to obtain the actual number of seetram units produced by the passage of the beam particles.

2.1.3 Cryogenic deuterium target

After accelerated, the ions were driven to the production target through a beam line, which consists of different magnetic elements. Two dipole magnets, placed in front of the target keep the beam centered, whereas a quadrupole triplet guarantees a good focalization. This enables to preserve the low transversal emittance of the beam by minimizing its expansion due to angular straggling in the target (see figure 2.4).

---

[1] The linear response of the detector was verified by comparing the voltage signals of the SEETRAM with the intensity of the primary beam, measured at SIS with a beam transformer [Ree90]. The root-mean-square deviation of the data from a linear fit was 17×10^{-14} A.

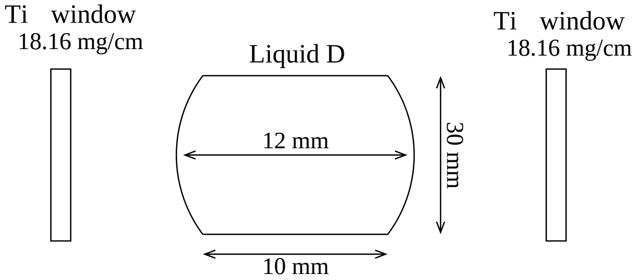

Figure 2.5: *Schematic representation of the deuterium target surrounded by the titanium windows.*

Two current grid detectors, placed in front of and behind the target serve to monitor the beam at the beginning of the experiment, in order to control its width and position in the target.

The liquid deuterium target [Che96] is a cylinder 1 cm in length and 3 cm in diameter, surrounded by 20 μm titanium foils and by five aluminum-coated mylar layers at each side of the beam line for protecting the beam line vacuum in case of rupture of the target cell. The liquefaction of deuterium was produced by cooling the system with a closed-circuit refrigerator setup. In order to protect the system against explosions due to leaks of oxygen into the target cell, a 57 liter storage tank at 1.05 bar pressure was connected to the system. At that pressure the liquefaction of deuterium occurs at a temperature of around 20 K. The whole setup (target+cryogenic system) is located 69 cm from the entrance of the FRS.

The target thickness used in the present experiment was found as a compromise between a maximized production of fragments and low secondary reaction rate. The total number of target nuclei is often expressed in terms of number of nuclei per unit of area:

$$N_T = N_A \cdot \frac{\rho_T \cdot l_T}{A_T} \tag{2.2}$$

Herein, N_A is the Avogadro's number, l_T is the length of the deuterium target in the beam direction, $\rho_T = 162$ mg/cm^3 its density and $A_T = 2.01$ the mass number. As can be seen in figure 2.5, the target windows were curved outward during the cooling of the system due to the pressure differences between the vacuum chamber and the target cell, leading to a transversal dependence of the target length l_T in the beam direction.

Since the accuracy of the final cross sections depends on a precise knowledge of l_T, a specific experiment was performed to measure its transversal dependence [Mus99]. The target thickness was found to vary from 10 mm at the borders to 12.35 mm at the central axis. Moreover, the central axis of the target was shifted by -2 mm with respect to the beam axis, with a thickness of 12.32 mm at that position, which corresponds to the nominal value of l_T. In order to estimate the error in assuming a constant target thickness, we determined the fraction of beam particles that lay within a region of the target with a thickness variation of less than a certain value.

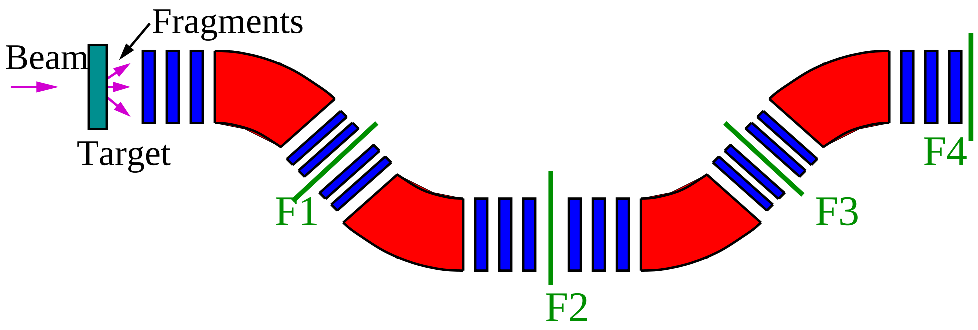

Figure 2.6: *Layout of the FRS at GSI showing the most important magnetic elements. Quadrupoles are placed before and after each dipole to define the ion-optic conditions at each image plane as well as to maximize the transmission through the spectrometer. Sextupoles behind the dipoles are not included in the figure; they correct second-order aberrations.*

Assuming a spherical profile of the target windows and a shift of the beam axis of -2 mm respect to the central axis of the target, we found that such a region can be parameterized by the curve:

$$x = \pm\sqrt{R^2 - (y - y_0)^2} \tag{2.3}$$

where $x(y)$ represents the thickness of the target as a function of the vertical displacement in figure 2.5, $R = 15$ mm and $y_0 = -2$ mm is the shift of the beam axis. The fraction of beam particles which lay within this region is given by:

$$\left(\frac{1}{\sigma\sqrt{2\pi}}\right) \cdot \int_{y_{min}}^{y_{max}} dy \cdot e^{-\frac{y^2}{2\sigma^2}} \int_{-x}^{+x} dx \cdot e^{-\frac{x^2}{2\sigma^2}} \tag{2.4}$$

where y_{min} and y_{max} correspond to the values for which the target thickness varies less than a certain value, and σ=1.06 mm is the width of the Gaussian distribution of the beam particles. According to this formalism, all the beam particles distributed over a beam spot of $\sqrt{6}\sigma$=2.7 mm have a target variation of less than 2%. A final uncertainty of 3% resulted from the contribution of this error and the uncertainties associated with the method used in the experiment (1%) and the density variation due to temperature fluctuations (0.2%) [Mus99].

2.1.4 Magnetic spectrometer: the Fragment Separator

The FRS is an achromatic zero-degree in-flight separator [Gei92], which consists of four 30^0 dipoles and a set of quadrupoles and sextupoles, all grouped in four independent stages (see figure 2.6). Its high resolving power of 1500 determined for an emittance of 20π mm·mrad and a beam spot of 2.7 mm was necessary to analyze heavy-ions with maximum magnetic rigidity values of 18 Tm. A vacuum line, separated from the high vacuum of the SIS by a titanium window, traverses

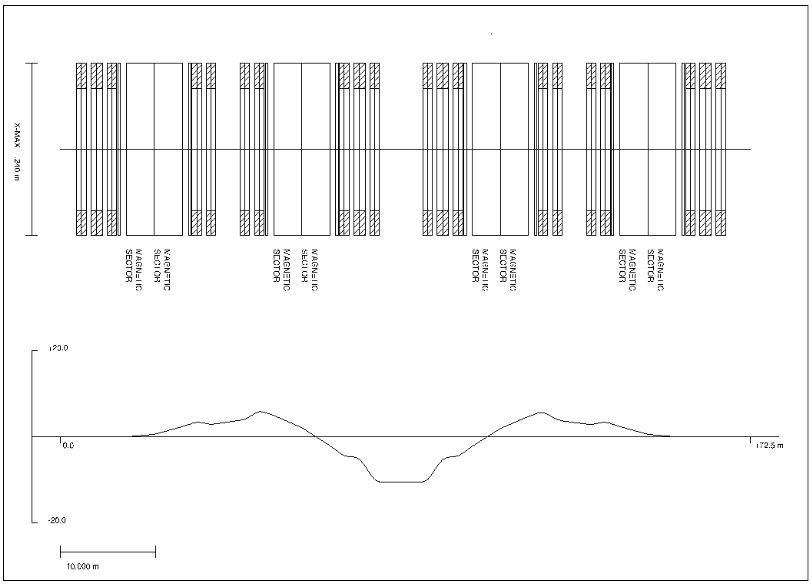

Figure 2.7: *Transversal x-position of a charged particle traversing the FRS with a momentum deviation of 1% with respect to that of a centred particle. The particle traverses the second image plane (the dispersive plane) at a transversal position of x= -6.8 cm demonstrating that maximum dispersion is reached at this image plane. This dispersion is canceled by that of the second stage, so that the overall separator is achromatic. The figure corresponds to a calculation done with the GICO code [Gico] for a beam emittance of* 20π *mm·mrad and a beam spot of 2.7 mm.*

the device from the entrance to the exit along a distance of 70 m. Its transversal apertures range from ±10 cm to ±18 cm, horizontally and from ±5 cm to ±15 cm vertically. These geometrical constraints, together with the ion-optical properties of the device result in a momentum and angular acceptance of about ±1.5% and ±15 mrad, respectively. The 18 Tm maximum magnetic rigidity accepted by the spectrometer is constrained by the curvature radius of ∼11 m, for each 30^0-dipole, and its maximum magnetic field of 1.6 T, achieved with non-superconducting technologies. The fields are controlled by Hall probes, with a precision and stability of about 10^{-4} T. Each magnetic element was properly field-mapped in order to provide realistic input parameters for the ion-optical codes [Gico, Iwa97].

Figure 2.6 shows the four independent stages of the FRS, each consisting of one triplet of quadrupoles, one dipole, one pair of quadrupoles and one sextupole. The four stages are placed consecutively, one after the other as shown. The free regions between each stage are referred to as $S1$, $S2$, $S3$ and $S4$.

Quadrupole magnets in front of the dipoles define the emittance of the transmitted ions. The horizontal component of this emittance must be enlarged to properly cover the field volume of the dipole magnets, whereas the vertical component must be kept low in order to minimize the vertical gap of the dipole and thus reduce its price. The quadrupoles following the dipoles determine the first-order focusing con-

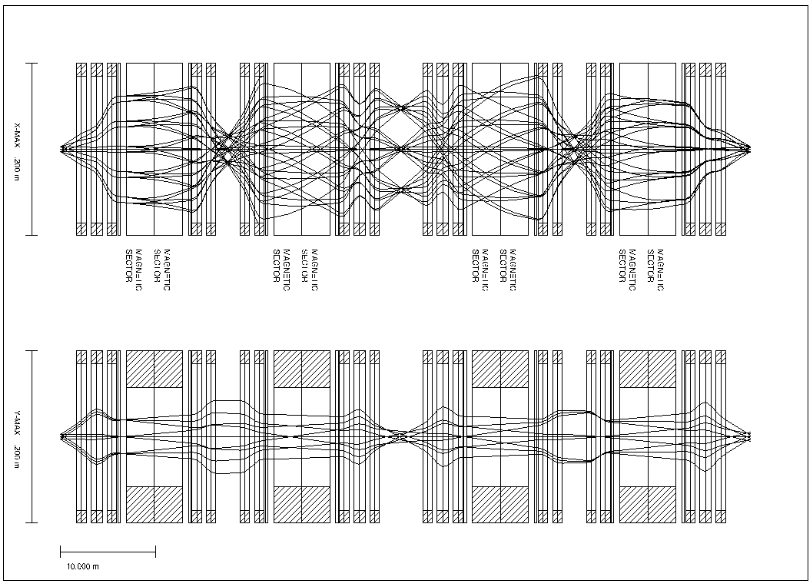

Figure 2.8: *Transversal x and y positions (upper and lower panel) of the particle trajectories that entered into the FRS with different angles and momenta. The figure corresponds to a calculation done with the GICO [Gico] code for a beam emittance of* 20π *mm·mrad and a beam spot of 2.7 mm.*

ditions at each image plane, referred to as $F1$, $F2$, $F3$ and $F4$. The dispersion of the first and second dipoles reaches a maximum value of -6.8 cm/% at the second image plane (refered to as the dispersive plane). This dispersion is exactly canceled by that of the third and fourth dipoles, so that the overall system is achromatic at the final image plane (achromatic plane). This is schematically illustrated in figure 2.7 where the trajectory of a particle with a momentum deviation of 1% is shown.

The figure shows that the achromatic condition is realized at the final image plane by requiring that both the position and the angle of the traversing particles are independent (to first order) of the momentum spread of the incident beam, i.e. $(x|\delta p)_{F4} = (x'|\delta p)_{F4} = 0$ [2]. Moreover, the parallel trajectory of the particle at the second image plane result from the requirement that the angle of the transmitted ions at this plane does not depend on the momentum deviation of the beam at the entrance of the FRS $(x'|\delta p)_{F2} = 0$. The second-order chromatic aberrations of the ion-optic of each stage were corrected by placing sextupoles in front of and behind each dipole magnet. The fields of these sextupoles are relatively low in order to prevent third and higher order aberrations. Sextupoles are also used to correct the momentum dependence of the positions of the second and fourth image planes. Figure 2.8 summarizes the ion-optics of the FRS by showing the trajectories of the particles entering the FRS with different angles and momenta.

The dipoles split the trajectories of the particles with different momentum values:

---

[2] Henceforth we will use the notation of Brown [Bro70].

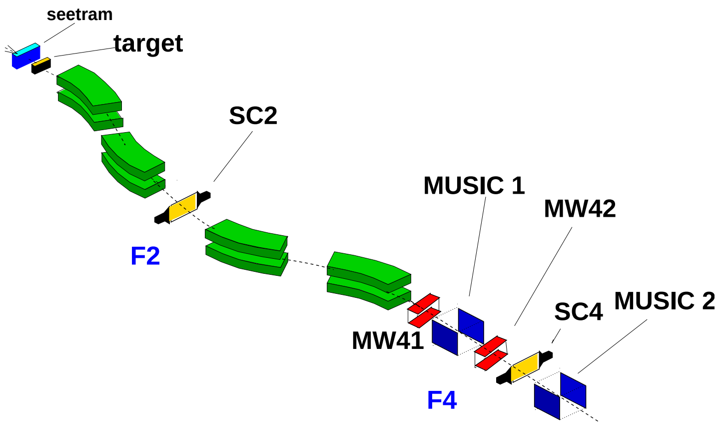

Figure 2.9: *Layout of the FRS with its standard detection equipment.*

Particles with momentum deviations of ±1% traverse the second image plane at ±6.8 cm. Moreover, it is also seen that the condition of point-to-point images in the x direction is required at all four image planes, while the same is only required in the y direction at $F2$ and $F4$.

2.1.5 Standard detection equipment

Figure 2.9 shows the FRS with its standard detection equipment. The ^{238}U primary beam, monitored with the SEETRAM hits the deuterium target at 1 A·GeV. The resulting fission residues were then measured with the FRS standard detection equipment. The plastic scintillators $SC2$ and $SC4$, placed at the second and fourth image planes were used to determine the horizontal $x-$deflection of the transmitted nuclei. Moreover, they measure the time-of-flight of the transmitted nuclei from F2 to F4. The ionization chambers $MUSIC$, placed at the end of the FRS, were used to determine the energy lost by the nuclei in their gas volume. Finally, the two multiwires $MW41$ and $MW42$ at the end of the FRS were used for the tracking measurement.

The multiwire chambers

Apart from the two final multiwire detectors shown in figure 2.9, another four multiwire chambers were used during the experiment to center the beam transversally along the FRS. These detectors were specifically designed to withstand the high intensities of the primary beam and to provide precise measurements of the transversal positions in x and y direction. In order to achieve a complete tracking of the central trajectory, they were installed at the four image planes of the FRS: MW11 and MW31 are mounted at S1 and S3, respectively, while MW21 and MW22 are installed at a distance of 1111 mm and 2222 mm upstream from the intermediate focal plane. The exact location of MW41 and MW42 at the final image plane was adjusted to provide a precise tracking of the transmitted reaction products. All the chambers, with the exception of MW42 are housed in hermetic containers and shielded from the vacuum by two 100 μm titanium foils. MW42 uses a 25 μm thick Kapton window to separate the gas volume from the surrounding air. The wire-structure of the chambers introduces transversal inhomogeneities which can spoil the achromatic of the FRS. Therefore, during the measurements of the reaction products, the multiwires at S1, S2 and S3 were removed.

Each chamber has five parallel planes, connected to different potentials depending on the range of charges covered by the measurements. According to reference [Ste91], for nuclei above ^{40}Ar, only the last three planes are important for determining the transversal positions of the traversing ions [3]. The central plane is the anode, consisting of 20 μm tungsten wires separated from each other by a distance of 2 mm. The first and third planes (x and y planes) are the cathode electrodes, made of 50 μm tungsten wires with a pitch of 1 mm. The wires of the x and y planes are vertical and horizontal respectively, and they are connected to delay lines. Each side of the line feeds the stop input of a TDC, while the start signal is provided by the anode wires. The central anode is connected to a high voltage which must be properly adjusted depending on the nuclei to be measured. The readout planes x and y are on ground. These three planes are housed in a container filled with a gas mixture of Argon, CO_2 and alcohol at atmospheric pressure.

When a nucleus passes through the multiwire, it leaves a track of ionized atoms and electrons, which migrate to the closest wire of the anode. The negative anode signal induces a positive signal on the adjacent cathode wires in the x and y direction, which then passes through the left and right (up and down) side of the delay line. The time difference between the arrival of the start signal of each TDC from the anode and the stop signal from each side of the line provides a measurement of the left and right (up and down) position of the traversing nucleus: x_R, x_L, y_U and y_D. These four signals are then used to determine the exact positions x and y, according to:

$$x_{MW}(mm) = a_x \cdot (x_L - x_R) + b_x \tag{2.5}$$

and

$$y_{MW}(mm) = a_y \cdot (y_U - y_D) + b_y \tag{2.6}$$

where a_x, a_y, b_x and b_y were determined from an independent calibration made with a radioactive source finger. Moreover, the sums $x_R + x_L$ and $y_U + y_D$ should be a constant proportional to the total length of the delay line and can thus be used to discriminate good events from multi-hit events.

The positions covered by these detectors ranges from -100 mm (left) to 100 mm (right). Moreover the final resolution achieved with these detectors was about 1 mm, which is sufficient to preserve the high resolution of the separator.

---

[3] The first two planes constitute a planar electrode structure called preamplification gap, which is used to amplify the electron avalanche generated by the passage of light ions. For nuclei above ^{40}Ar this amplification is no longer needed and thus, the pregap should be switched off.

The plastic scintillators

From an experimental point of view, the high-resolving power of the FRS needed to separate and identify heavy ions, required very precise characteristics of the plastic scintillators: First, they have to provide a fast and precise event-by-event measurement of the positions and time-of-flight of transmitted ions. Secondly, they must preserve the high ion-optical quality of the magnetic system; any non-uniformity in their thickness, specially in the dispersive plane, would lead to differences in the energy loss of the traversing ions which deteriorates the achromatism and consequently the ion-optical resolution. In order to fulfill these requirements, a detector system consisting of two fast scintillator detectors has been developed [Vos95]. The two plastic scintillators $SC2$ and $SC4$, shown in figure 2.9 are made of a plastic material (BC420) characterized by a high light output and a fast signal rise time (0.5 ns). Their sensitive area (210×80 mm^2 for $SC2$ and 200×80 mm^2 for SC4) covers the whole image plane, while the thickness (5 mm) chosen was a compromise between particle losses and scintillation signals. Moreover, the homogeneity of the detectors was measured mechanically to be better than ±18 μm, which corresponds to an energy loss difference comparable to the typical straggling in energy (~30 MeV).

The scintillation light is transported by total internal reflection, collected by light guides, and registered by means of fast photomultipliers HAMAMATSU R2083 type, which allow for counting rates up to 10^5 particles per second, and small transit-time jitters in order to preserve the good time-resolution. The positions of the ions were determined from the time difference between the signals arriving at the two photomultipliers, mounted at the left and right sides of the plastic scintillator(see figure 2.10).

The signals from each photomultiplier were filtered by constant-fraction discriminators (CFD) with a threshold of around 10 mV and a delay time of 2 ns, and then used as the start and stop signals of a time-to-amplitude-converter (TAC). The analog output of the TAC was transformed by an analog-to-digital converter (ADC) and then converted into positions by means of a linear calibration. In the case of $SC2$, the high dispersion found in the dispersive plane spread the transmitted nuclei over the whole range of the detector. Assuming a linear response of the time signals given by the TAC's with the position of the measured nuclei in the plastic scintillator, the detector signals could be calibrated by comparing the maximum and minimum signals of the TAC's, referred to as $SC2_{max}$ and $SC2_{min}$ (see figure 2.11), +with the geometrical dimension of the active area of the scintillator ($x_2(max) = 110$ mm and $x_2(min) = -110$ mm). The slope a and the offset b were given by:

$$a = -\frac{x_2(max) - x_2(min)}{SC2_{max} - SC2_{min}} \tag{2.7}$$

and

$$b = \frac{x_2(max) \cdot SC2_{max} - x_2(min) \cdot SC2_{min}}{SC2_{max} - SC2_{min}} \tag{2.8}$$

This calibration method could not be applied for $SC4$ because the traversing nuclei did not cover the whole range of the plastic scintillator in any of the mea-

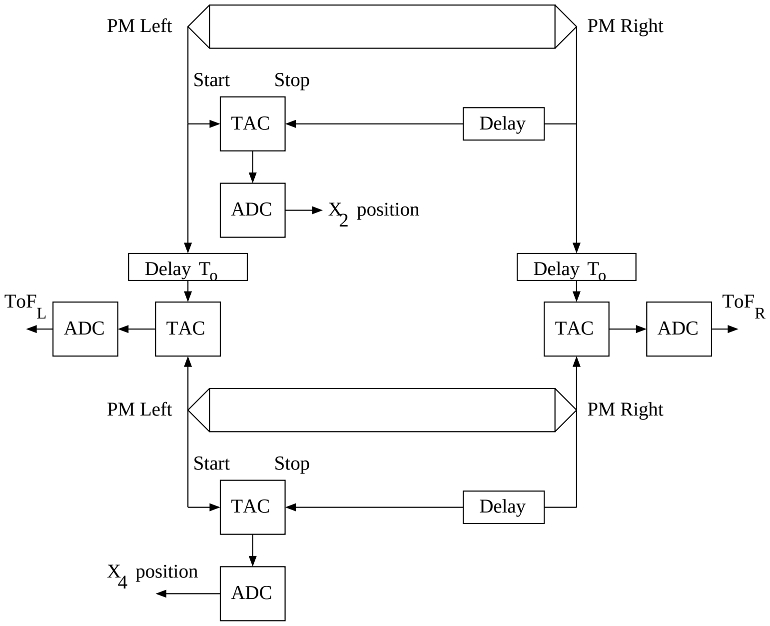

Figure 2.10: *Electronic scheme of the two plastic scintillators for the measurement of the x-positions at S2 and S4 and of the time-of-flight.*

sured magnetic settings. In that case, the calibration of the detector was done by comparing its electronic signals with the positions x_4^{MW} determined from the signals of the last two multiwires, according to:

$$x_4^{MW}(mm) = x_{MW42} + \frac{x_{MW42} - x_{MW41}}{d} \times L \tag{2.9}$$

where d and L are the distance between the two multiwires and from $MW42$ to $SC4$, respectively.

During the analysis of the experimental data, an unexpected dependence of the position signals registered by $SC2$ on the energy lost by the nuclei was observed. As shown in the left panel of figure 2.12, the maximum range of positions measured at the second image plane seems to increase as the energy loss of the nucleus decreases, while it remains rather constant for high charges. The same trend was not observed for the signals measured with $SC4$. This deficiency of the plastic $SC2$ was attributed to a failure of the constant fraction discriminators (CFD).

In order to correct the positions measured by the plastic $SC2$ we use the left panel of figure 2.12 to adjust the dependence of the borders of the spectra $SC2_{max}$ and $SC2_{min}$ on the energy lost by the nucleus in the MUSIC chamber (see next section). The resulting signals $SC2_{max}(Z)$ and $SC2_{min}(Z)$ were then introduced in equation 2.7 and 2.8 to determine the calibration parameters. This method provided a constant range of positions, as shown in the right panel of figure 2.12.

Furthermore, the two plastic scintillators were also used to determine the time-of-flight (ToF) of the traversing ions between $S2$ and $S4$. This quantity was measured

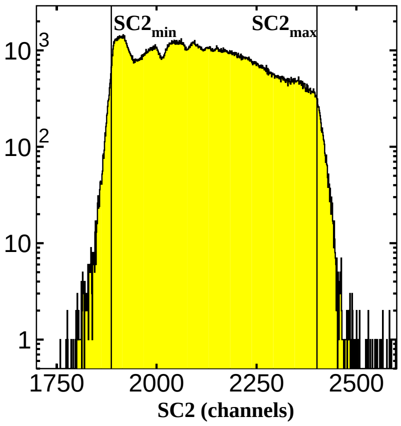

Figure 2.11: *Spectra of position signals measured by the plastic scintillator SC2. The dashed lines depict the maximum and minimum signals which correspond to the physical borders of the plastic scintillators.*

as an average of the left and right time difference between the signals of both plastics at each side:

$$ToF^* = \frac{\alpha_L \cdot ToF_L^* + \alpha_R \cdot ToF_R^*}{2} = (T_2 + T_0) - T_4 \tag{2.10}$$

where α_L and α_R are the calibration factors which were determined by means of a pulse generator of adjustable frequency. As can be seen in the scheme of figure 2.10, the signal T_2 from $S2$ was delayed a quantity T_0 in order to provide the stop signal for the TAC, while the start signal was given by T_4. The real time of flight ToF is obtained from the measured ToF^*, according to:

$$ToF = T_4 - T_2 = T_0 - ToF^* \tag{2.11}$$

The resolution attained with these detectors reach extremely good values of Δt=150 ps (FWHM), for time measurements and of (Δx=2 mm), for positions.

The ionization chambers (MUSIC)

The relation established by Bethe and Bloch, between the energy loss of an ion in a layer of matter and the square of its atomic number Z, enables the use of gaseous detectors to determine this quantity. In the present experiment, two identical multi-sampling ionization chambers (MUSIC) were placed at the end of the FRS, one after the other [Pfu94].

Figure 2.13 shows a schematic view of the MUSIC detector. The entrance and exit windows are made of 25 μm Kapton foils covered by an aluminum layer of 40 μg/cm^2. The active volume of the detector is 400 mm in beam direction and 276×150 mm^2 in x and y directions, filled with P10 gas (a mixture of 90% Ar and

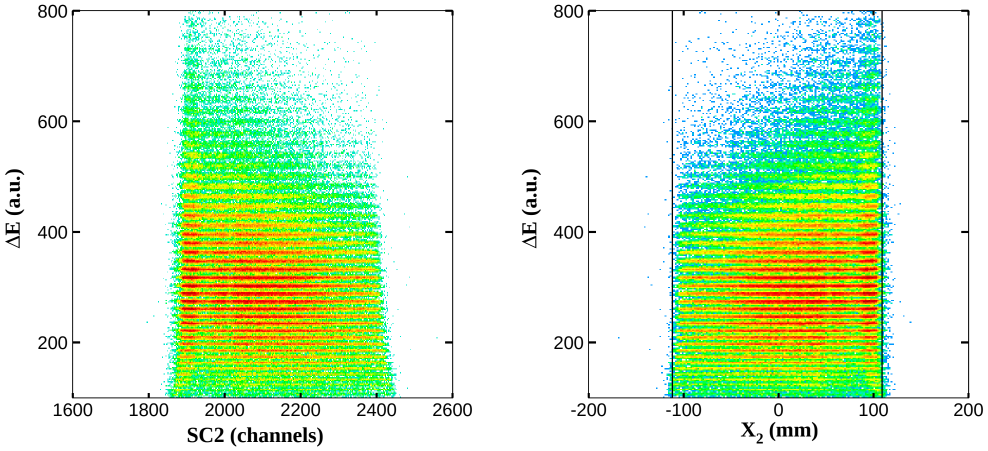

Figure 2.12: *Positions measured by the plastic scintillator SC2 for different energy loss signals* ΔE *measured with the MUSIC detectors (each horizontal line corresponds to a different charge). Left: raw signal obtained from the readout of the ADC's. Right: calibrated signal.*

10% CH_4) at atmospheric pressure and room temperature. In order to preserve the operational conditions during the experiment, the gas mixture is renewed by an external pumping circuit. Pressure and temperature of the gas were measured during the entire experiment by probes connected to the data acquisition system.

The electric field inside the chamber is generated by a high voltage supplied to the electrodes, in x direction. The anode plate, situated on one side of the detector, was divided into four sections, each coupled to a charge sensitive preamplifier. Two supplementary anodes placed at the edges are used to avoid border effects. In order to preserve the anodes from distortions of the electric field due to the presence of ions, they were shielded by a metallic grid.

The cloud of electrons generated by the passage of the nuclei through the gas was collected by the anodes, inducing a signal on the preamplifiers proportional to the energy loss. The output signals of the four preamplifiers were fed into main amplifiers whose gain was properly adjusted depending on the range of charges to be measured. The resulting signals were then digitized by an ADC and read by the DAQ system.

A fraction of the electrons can be recombined with the atoms of the gas before reaching the anodes. The probability of recombination rises as the distance between the trajectory of the nuclei and the anodes, leading to a dependence of the energy-loss signal upon the transversal position of the traversing nuclei. In addition, the energy lost in the gas detector also depends on the velocity of the traversing nuclei. The signal ΔE_m registered by the MUSIC detector is a function of the atomic number Z of the nuclei, their velocity v, and the transversal positions x. As a first approximation, these dependencies were factorized, so that the signal ΔE_m could

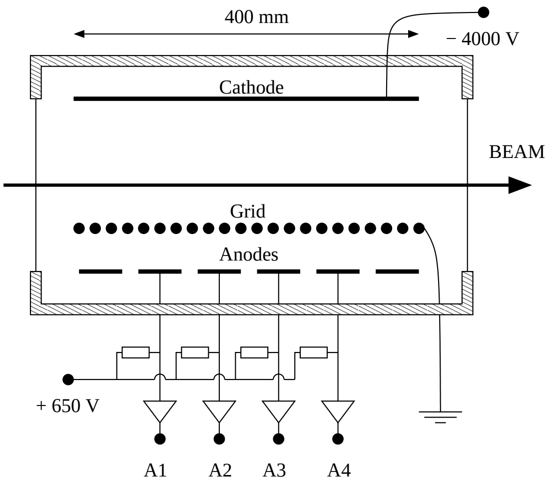

Figure 2.13: *Schematic top view of the multi-sampling ionization chamber MUSIC.*

be corrected to provide the atomic number Z:

$$Z^2 \propto \frac{\Delta E_m}{f(v) \cdot g(x)} \tag{2.12}$$

$f(v)$ was determined by analyzing the functional velocity dependence of the energy loss with the AMADEUS [Amad] code. The function $g(x)$ was determined for each anode by adjusting the dependence of the energy-loss signal ΔE_i to the transversal position x_i, with the index i denoting each anode. The values of x_i were determined from the positions x_4 measured with the plastic scintillator $SC4$ and the last two multiwires $MW41$, $MW42$:

$$x_i = x_4 - d_i \cdot \frac{x_{MW41} - x_{MW42}}{d} \tag{2.13}$$

where d_i is the distance from the plastic scintillator $SC4$ to the ith-anode and d is the distance between the two multiwires. In order to analyze the position dependence of the energy loss over a wide range of positions x we scattered the primary beam at the end of the FRS by switching off the last quadrupole. The signal ΔE_m left by the beam was then plotted as a function of x for the four anodes (see figure 2.14), and adjusted to a mathematical function which provides $g(x)$.

By including these corrections, a final charge resolution of about 0.3 (FWHM) was achieved, which is sufficient to separate atomic numbers up to 80. This is illustrated in figure 2.15 where the the raw energy-loss signals accumulated during the experiment are compared with the corrected ones.

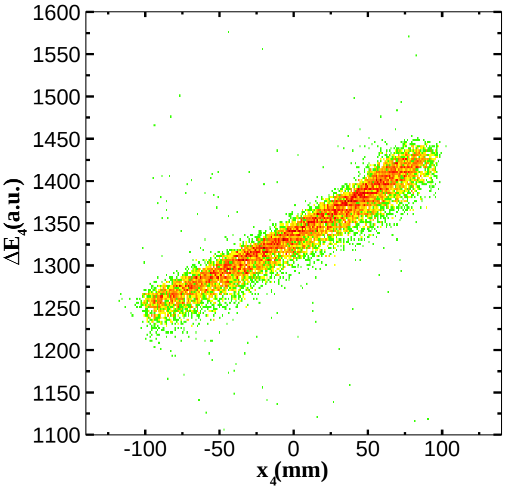

Figure 2.14: *Position dependence of the energy loss signal left by the primary beam on the first MUSIC. The figure corresponds to the fourth anode. Similar plots were obtained for the rest of the anodes.*

2.2 Selection, separation and identification of the reaction residues

The use of the Fragment Separator (FRS) at GSI constitutes the most suitable choice for analyzing the projectile-like residues produced in kinematically reversed spallation reactions. Within this device, the nuclei follow different trajectories defined by a set of phase-space variables [4]. The most important variable, related to the atomic Z and mass A numbers of each nucleus, is the magnetic rigidity $B\rho$:

$$B\rho = \left(\frac{A}{Z}\right) \cdot \frac{m_0}{e} \cdot \beta\gamma \tag{2.14}$$

where (A/Z) is the mass-to-charge ratio, m_0 is the nuclear mass unit, e is the electron charge, and $\beta\gamma$ is the relativistic reduced momentum.

By following the different trajectories across the image planes of the FRS, it is possible to separate and identify the traversing nuclei from their transversal positions. The equation of motion of the transmitted nuclei at a given image plane, with respect to the phase-space configuration at the initial position i can be written as:

$$x_s = (x|x_i)_s\, x_i + (x|x_i')_s\, x_i' + (x|y_i)_s\, y_i + (x|y_i')_s\, y_i' + (x|(\delta B\rho)_i)_s\, (\delta B\rho)_i \tag{2.15}$$

---

[4] The phase-space used in ion-optics differs from the real Liouville's phase-space in the definition of the momenta of the particle. For the former, the transversal components of the momentum are replaced by the transversal angles: $x' \simeq p_x/p_z$ and $y' \simeq p_y/p_z$, while the longitudinal component is defined by the magnetic rigidity of the particle $B\rho \sim p_z$.

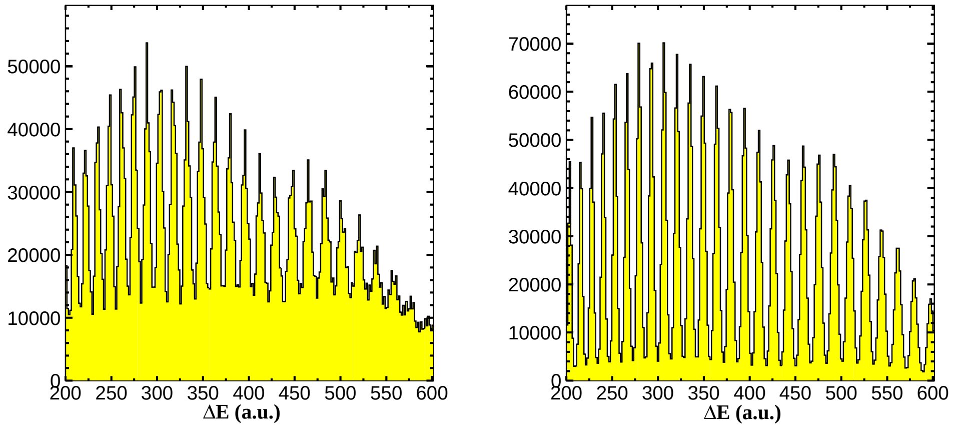

Figure 2.15: *Energy loss signal measured by the first MUSIC. Left panel: Raw spectra with no corrections. Right panel: signal including corrections on velocity and transversal positions.*

where the quantities in parenthesis are coefficients that define the ion-optics of the separator [Car87] [5] and the subscripts s refer to the values of the phase-space variables on the different FRS image planes (0 entrance, 2 second image plane and 4 fourth image plane). By definition, at these image planes there is no correlation between the transversal position x and the transversal angles x' and y', so that equation 2.15 can be simplified as:

$$x_s = (x|x_i)_s \, x_i + (x|y_i)_s \, y_i + (x|(\delta B\rho)_i)_s \, (\delta B\rho)_i \tag{2.16}$$

It is worthwhile to mention that the magnetic rigidity $(B\rho)_s$ is often described in terms of its relative deviation with respect to the value $(B\rho)_c$ for a particle following a central trajectory along the spectrometer:

$$(\delta B\rho)_s = \frac{(B\rho)_s - (B\rho)_c}{(B\rho)_c} \tag{2.17}$$

2.2.1 Selection of transmitted nuclei

The transversal dimensions of the inner tubes of the FRS and the maximum magnetic dispersions set a limit on the range of magnetic rigidities accepted by the separator. According to equations 2.16 and 2.17, the maximum accepted value of $\delta B\rho$ at the entrance of the FRS is given by:

$$(\delta B\rho)_0 = \frac{x_s}{(x \mid (\delta B\rho)_0)_s} \tag{2.18}$$

---

[5] For the present discussion the most important coefficients are the dispersion $(x|x_i)$ and the magnetic dispersion $(x|(\delta B\rho)_i)$. These and other coefficients were calculated with the GICO [Gico] code.

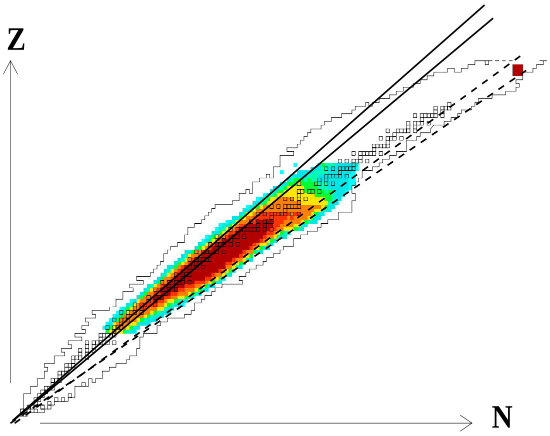

Figure 2.16: *Example of the fraction of nuclei transmitted through the FRS in one magnetic tunning, according to the acceptance in $B\rho$. The region between the two solid lines corresponds to those nuclei transmitted in one setting. The dashed lines shows a setting for which the Uranium primary beam is also transmitted (black square).*

where we have assumed that the nuclei emittance at the entrance of the FRS is very small ($x_0 \sim y_0 \sim 0$). Considering that the maximum dispersion value of -6.8 cm/% is found at the second image plane (dispersive plane), and assuming a transversal dimension at this plane of $\simeq \pm 10$ cm, we obtained a maximum $\delta B\rho$-acceptance of $\simeq \pm 1.5$ %. Those nuclei with magnetic rigidities 1.5% larger or lower than the central value $(B\rho)_c$ are deflected out to the guide line of the FRS. Following equation 2.14, the $B\rho$-acceptance leads to a limitation on the number of nuclei transmitted thought the FRS, according to their value of A/Z. Figure 2.16 shows the accepted range of A/Z on the top of the chart of nuclides for one single magnetic tunning of the magnetic dipoles.

The nuclei produced in the collision of ^{238}U at 1 A·GeV with the deuterium target are spread over a wide region of atomic and mass numbers, depending on the reaction mechanisms involved in the process. Therefore, the FRS had to be adjusted according to the magnetic rigidities of the medium-mass fission residues to be analyzed. This was done with the Lieschen code [Liesch] which includes both the kinematics of the reaction mechanism and the specific features of the FRS. From these calculated values of $B\rho$, we then selected a central value $(B\rho)_c$ for the first and second stages of the FRS by properly adjusting the magnetic fields of each dipole magnet according to its curvature radii. The tuning of the four dipole magnets established a specific magnetic setting, for which a sample of nuclei was then transmitted as shown in figure 2.16. However, the range of $B\rho$ transmitted in one setting is not sufficient to cover the whole region of interest. Thus, the measurements were repeated for different settings by scaling the magnets in increments of around 1%. For some specific settings, the ^{238}U primary beam and some very intense decay chan-

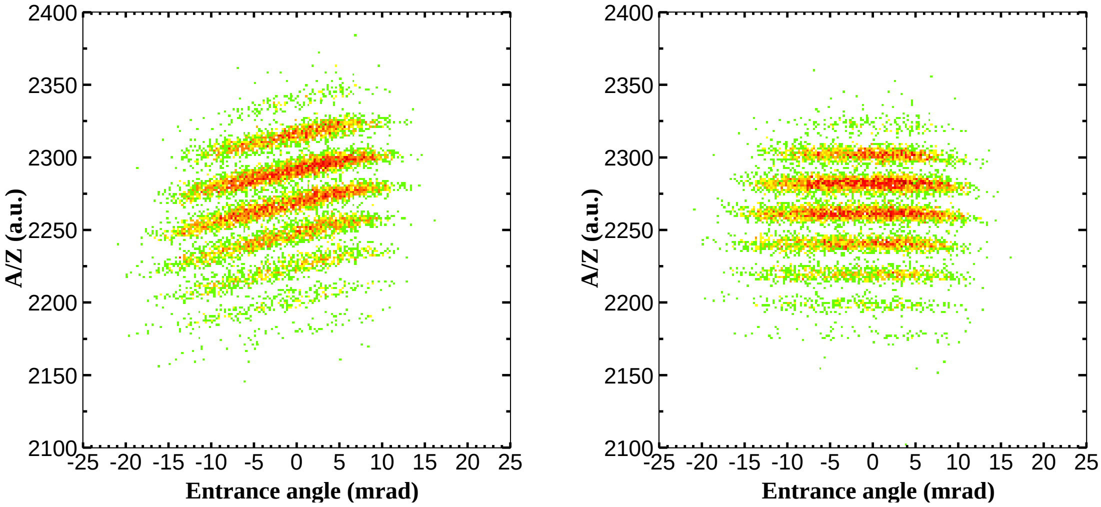

Figure 2.17: *Angular dependence of the mass-to-charge ratio. Left panel: A/Z calculated assuming a constant flight path of 37 m (coefficient $c_0 = 0$ in equation 2.24). Right panel: A/Z corrected from a linear angular dependence of the flight path ($c_0 = 0.00016$ in equation 2.24).*

nels (one-neutron removal, one-electron ionic charge state,...) were also transmitted, which would damage of detectors due to the extremely high intensities. Slits were used at $S1$ to stop these contaminants.

2.2.2 Isotope separation with the FRS

In order to analyze the nuclei selected in one setting we had to separate them according to their mass-over-charge ratio A/Z. Equation 2.14 shows the relation between the mass-over-charge ratio of one nucleus, its magnetic rigidity $B\rho$ and its reduced momentum $\beta\gamma$. These two latter quantities had to be measured in the same conditions during the experiment to separate the reaction products according to their A/Z values.

The magnetic rigidity of the transmitted nuclei at the entrance of the FRS can be calculated from equation 2.16 by assuming that their emittance is small ($x_0 \sim y_0 \sim 0$):

$$(B\rho)_0 = (B\rho)_c \cdot \left[1 - \frac{x_2}{(x \mid (\delta B\rho)_0)_2}\right] \tag{2.19}$$

where $(x \mid (\delta B\rho)_0)_2$ refers to the magnetic dispersion from the entrance to the dispersive image plane. In addition, the longitudinal velocity v of the transmitted nuclei, or equivalently the reduced momentum $\beta\gamma$ was determined by dividing the path length l covered by the ions from $S2$ to $S4$ by the time-of-flight ToF between the two plastics (equation 2.11). The path-length l differs from the central path-length l_0 according to the horizontal angle x' of the traversing ions in the second stage of the FRS. This angle is related to that determined from the positions measured by the two last multiwires (MW41 and MW42) according to:

$$x' = arctan\left(\frac{x_{MW41} - x_{MW42}}{d}\right) \tag{2.20}$$

In spite of the rather complicated trajectories of the ions along the FRS, the quantity l was assumed to depend linearly on the angle x':

$$l = l_0 \cdot (1 + c_0 \cdot x') \tag{2.21}$$

and therefore, the velocity of the nuclei could be determined according to:

$$v = \frac{l_0 \cdot (1 + c_0 \cdot x')}{T_0 - ToF^*} \tag{2.22}$$

The two constant parameters T_0 and l_0 were obtained by comparing the ToF^* signal (see equation 2.11) of the primary beam after traversing different layers of matter with the inverse of the velocities $1/v$ calculated with the AMADEUS code [Amad]. These two quantities were fit to a first degree polynomial function:

$$\frac{1}{v} = \frac{T_0}{l_0} - \frac{ToF^*}{l_0} \tag{2.23}$$

whose coefficients provided the values $T_0 = 141.3$ ns and $l_0 = 36.23$ m.

Finally the mass-over-charge ratio A/Z of each nucleus was determined from the experimental observables described above, according to the following equation:

$$\left(\frac{A}{Z}\right) = (B\rho)_c \left(1 + \frac{a \cdot SC2 + b}{(x \mid (\delta B\rho)_0)_2}\right) \cdot \left[\frac{c^2(T_0 - ToF^*)^2}{l_0^2 \cdot (1 + c_0 x')^2} - 1\right]^{-1/2} \tag{2.24}$$

This equation was obtained by combining the magnetic rigidity of the nuclei at the entrance of the FRS $(B\rho)_0$ (first stage) with their velocity behind the plastic scintillator at $S2$ (second stage). Although the energy lost by the nuclei in the plastic scintillator reduces the velocity of the nuclei with respect to their value in the first stage, the final effect will be a small shift of the values of A/Z, which could still be identified unambiguously.

An optimum resolution in the separation of A/Z relies on the correct determination of the calibration coefficients a, b, l_0, T_0, c_0 and the quantities $(B\rho)_c$ [6] and $(x \mid (\delta B\rho)_0)_2$. A wrong value of one of these parameters may lead to an unphysical dependence of the mass-over-charge ratio on the different experimental observables (x_2, ToF^* and x') used for its determination. We have systematically analyzed the possible correlations of A/Z with x_2, ToF^* and x', by means of two-dimensional spectra, in order to cross-check the parameters of equation 2.24. As an example,

---

[6] This quantity was determined for each magnetic setting by multiplying the magnetic fields of the four dipoles, measured with Hall probes, by the curvature radius of each magnet.

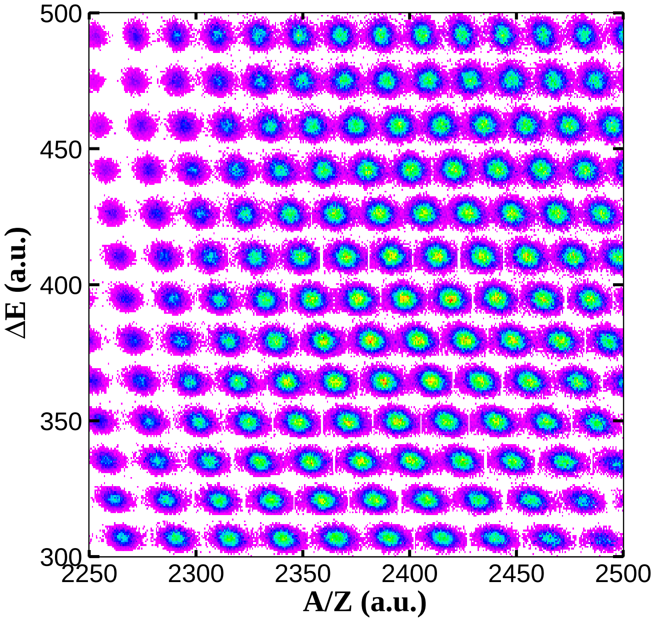

Figure 2.18: *Two dimensional cluster plot showing the corrected energy loss signal and the mass-to-charge ratio. Each spot corresponds to a different nucleus.*

figure 2.17 illustrates the influence of the coefficient c_0 on the correlation between A/Z and the transversal angle x'.

The final resolution attained in the separation of the reaction products is illustrated in figure 2.18, where the corrected energy-loss signal is plotted against the mass-over-charge ratio. The figure was obtained by summing up all the fission settings measured in the experiment.

2.2.3 Isotopic identification

The identification of the atomic number Z for each nucleus was rather simple since we could use the energy-loss signal corresponding to the projectile, for which a maximum value of the energy loss ΔE is expected. From this peak it was possible to identify all the energy-loss peaks corresponding to the different atomic numbers of the residual nuclei. Figure 2.19 shows the energy-loss peaks for three different settings centered on a sample of nuclei with very high charges. The maximum value of ΔE, marked with a vertical line, corresponds to the projectile ($Z = 92$).

In order to validate the identification, the charge spectra of fission settings centered on the most neutron-rich isotopes were analyzed. These nuclei are mainly produced by fission induced at very low excitation energy, where structural effects are easily observable (odd-even effects, low-energy asymmetric fission modes). Figure 2.20 shows the charge spectra obtained for a magnetic setting of the FRS centered

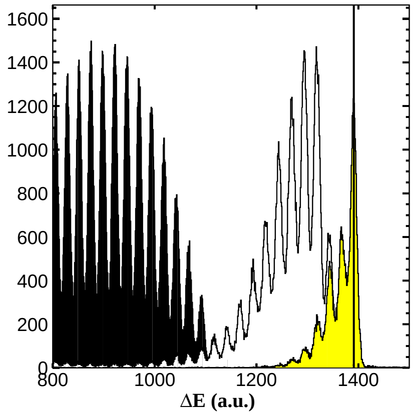

Figure 2.19: *Charge identification of the peak signals from the MUSIC. Each color represents a different setting. The vertical line corresponds to the projectile (Z=92).*

on ^{135}Cd. The highest peak for a charge $Z = 50$ (Sn) is understood in terms of shell closure: In this setting, the doubly-magic isotope ^{132}Sn $(Z = 50, N = 82)$ is fully transmitted.

The identification of masses can be obtained from the matrix $(A/Q) - Z$ (figure 2.21). In this cluster plot, each nucleus is represented by a spot. Depending on the values of the mass and charge of the nucleus, the clusters are located at different positions in this matrix. The possible combinations made between the quantities A/Z and Z, where Z and A are integer numbers, define a characteristic pattern in which the nuclei can be grouped within curved lines. The only line with no curvature corresponds to light nuclei with the same amount of protons and neutrons $(Z = N)$ $(A/Z = 2)$. The next group-line on the right corresponds to nuclei with $N = Z + 1$, which differs a bit from a perfect vertically. If one now goes n steps to the right, the line found corresponds to the group of isotopes with $N = Z + n$. Mass identification is then possible from the vertical group-line since $A = 2Z$ and the charge is well known. The same rule applies to the next lines to the right $(N = Z + 1, N = Z + 2, ...)$ in such a way that all the nuclei can be classified according to their mass A and charge Z.

As shown in figure 2.22, about 1000 fission nuclei were identified by following this procedure.

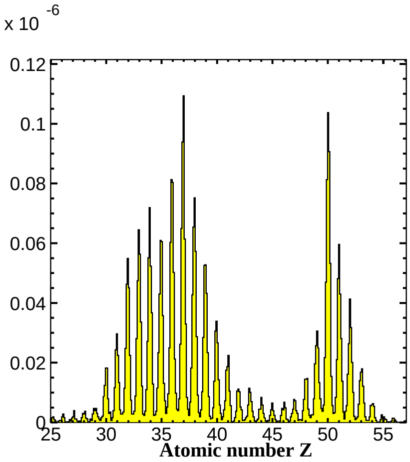

Figure 2.20: *Atomic numbers from MUSIC for a setting centered on* ^{135}Cd.

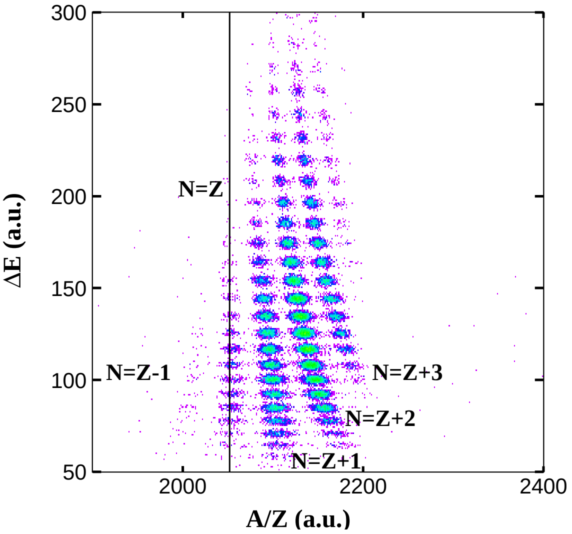

Figure 2.21: *Identification matrix showing the atomic number and the mass-over-charge ratio for the lightest residues. The vertical line corresponds to nuclei with* $N = Z$*. From this line it was possible to identify all the nuclei.*

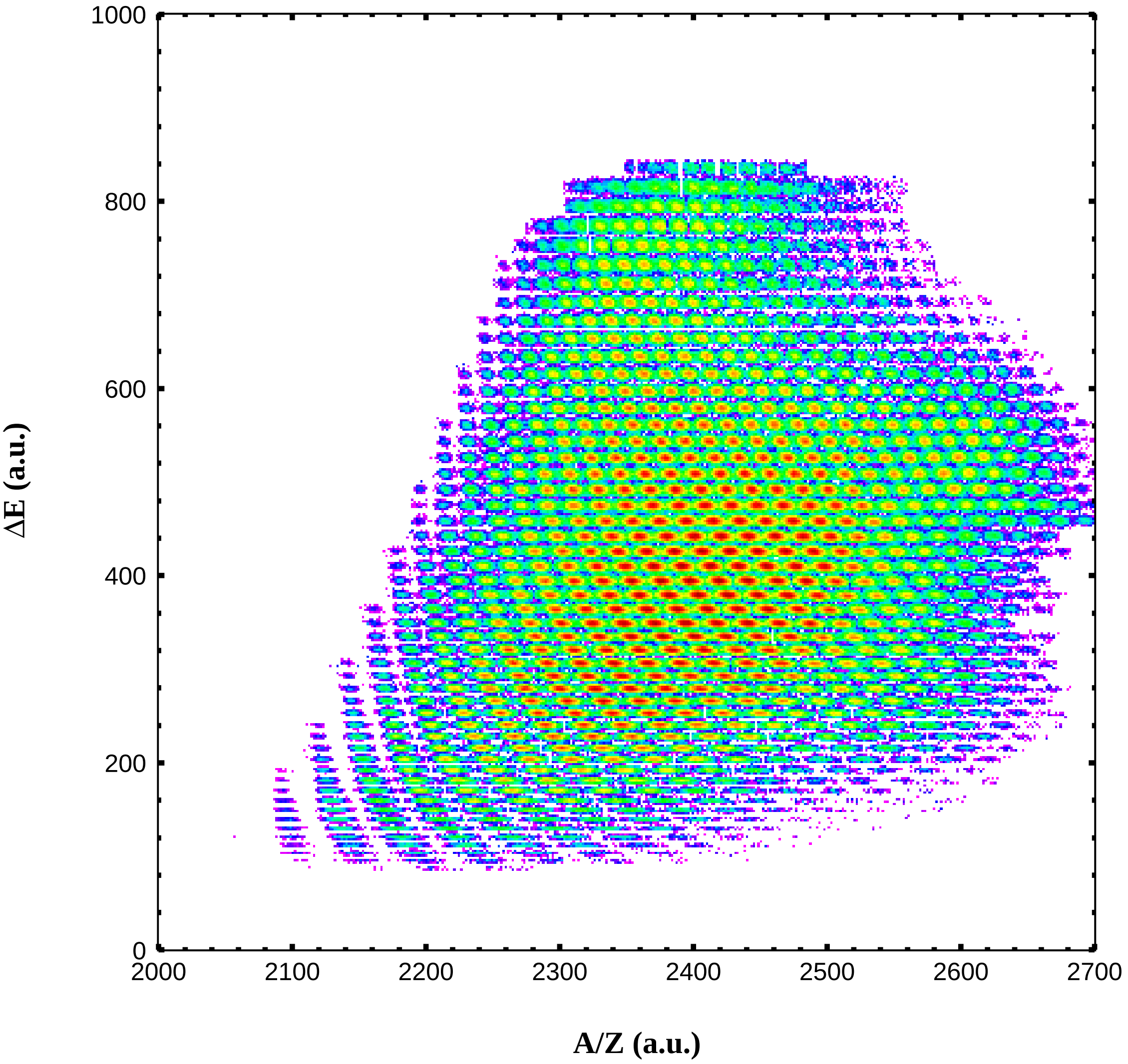

Figure 2.22: *Identification matrix showing the atomic number and the mass-over-charge ratio for almost 1000 different fission residues measured in the reaction* 238*U(1 A·GeV)+d.*

Chapter 3

Kinematics of fission residues

The present chapter is devoted to the analysis and interpretation of the kinematical properties of the residues produced in the reaction induced by ^{238}U at 1 A·GeV on the deuterium target. In particular, we have determined the velocities of the fission residues measured in this work by following an specific experimental method. The interest of such a study concerned different technical and theoretical aspects:

First, the different kinematics associated with the two dominant reaction mechanisms, namely fission and evaporation, made it possible to approximately disentangle these two processes. Secondly, the detailed analysis of the fission kinematics allowed to reconstruct the angular emittance of each fission fragment, which was necessary to determine the angular transmission through the FRS. Finally, since the fission velocities depend mainly on the configuration of the two nascent fragments in the scission point, this analysis provided valuable information on the different fission decay modes associated with specific configurations. Moreover, from these velocities it is also possible to reconstruct the mother fissioning nucleus responsible for the production of a given residue.

These different aspects are extensively discussed in the present chapter. In the first section, we briefly present the kinematics of reaction mechanisms to illustrate the limitations of the FRS in terms of angular and longitudinal velocity acceptance. In the second section we describe the sequence followed to obtain the final parameters which determine the velocity of each nucleus transmitted through the FRS. Finally, a last section is devoted to the discussion and interpretation of the results.

3.1 Kinematics of fission and evaporation residues

The spallation reactions investigated with the FRS in inverse kinematics are characterized by a high-energetic peripheral collision between the heavy projectile and the light target nucleus, followed by the deexcitation of the projectile-like fragments by fission or by evaporation of light particles. The kinematics of the final residues correspond to the convolution of the velocity distribution produced by the fast interaction of projectile and target and the subsequent deexcitation processes.

In order to illustrate the differences of the fission and evaporation reaction mechanisms, from a kinematical point of view, we depict in figure 3.1-a the contribution of each mechanism to the final velocity distribution for a given fragment, together with the contribution due to the first stage of the reaction:

According to the incoherent droplet model proposed by K.Huang [Hua66, Hua67], the velocities of the pre-fragments after the first stage of the collision follow a three-dimensional Gaussian distribution produced by the original Fermi motion of abraded nucleons [Gol74] . The subsequent deexcitation stage affects the final kinematics of the nuclear residues in a different manner: In the case of evaporation, the recoil of the fragments due to the isotropic evaporation of nucleons tends to increase the widths of the original Gaussian distribution [Mor89]. By contrast, the kinematics of the fission residues is governed by the strong Coulomb repulsion between the two nascent fragments [Wil76], leading to a spherical distribution of the velocity vectors. The diffuseness of the shell of this sphere can partly be attributed to the original Gaussian distribution of velocities of the fissioning pre-fragment.

In addition, the collision between the projectile and target induces a reduction of the mean longitudinal velocity of the projectile-like residues. This slowing down is expected to increase as the projectile-like pre-fragment mass decreases [Mor89].

In order to determine the contribution from fission and evaporation, to the production of a given nucleus, it is necessary to separate the individual components from their rather different kinematics. These two reaction mechanisms can be disentangled by measuring the longitudinal velocity parallel to the beam direction $v_{||}$, filtered by the limited angular acceptance of the FRS. As is schematically illustrated in figures 3.1-c and 3.1-d, this limitation modifies the kinematics of fission and evaporation in a different manner, leading to rather different distributions of $v_{||}$. From these new spectra it was then possible to separate these two processes.

3.2 Angular and velocity acceptances of the FRS

The phase space filled by the residues produced by fission and/or evaporation is constrained by the limited magnetic rigidity $B\rho$ and angular acceptances of the Fragment Separator (see figure 3.1-c). According to equation 2.15, for a fixed A/Z value the limited $B\rho$-acceptance of ± 1.5 % defines a longitudinal velocity window of $\sim \pm 1.5\%$ which is not sufficient to fully cover the velocity distributions of residues produced by fission ($\sim$ 10%) or evaporation ($\sim$ 3%-6%) reactions. As was discussed in section 2.2.1, this limitation is overcome by combining several magnetic settings centered at different values of $(B\rho)_c$ in such a way that the whole velocity distribution can be reconstructed. In order to cover the full velocity spectra of all the fission residues, a total number of 35 settings were measured for the reaction ^{238}U(1 A·GeV)+d. Moreover, the residue contamination produced in the titanium windows surrounding the liquid deuterium target had to be determined. Thus, another 35 settings were measured with the cryogenic target replaced by a titanium dummy target with a thickness equivalent to that of the titanium windows.

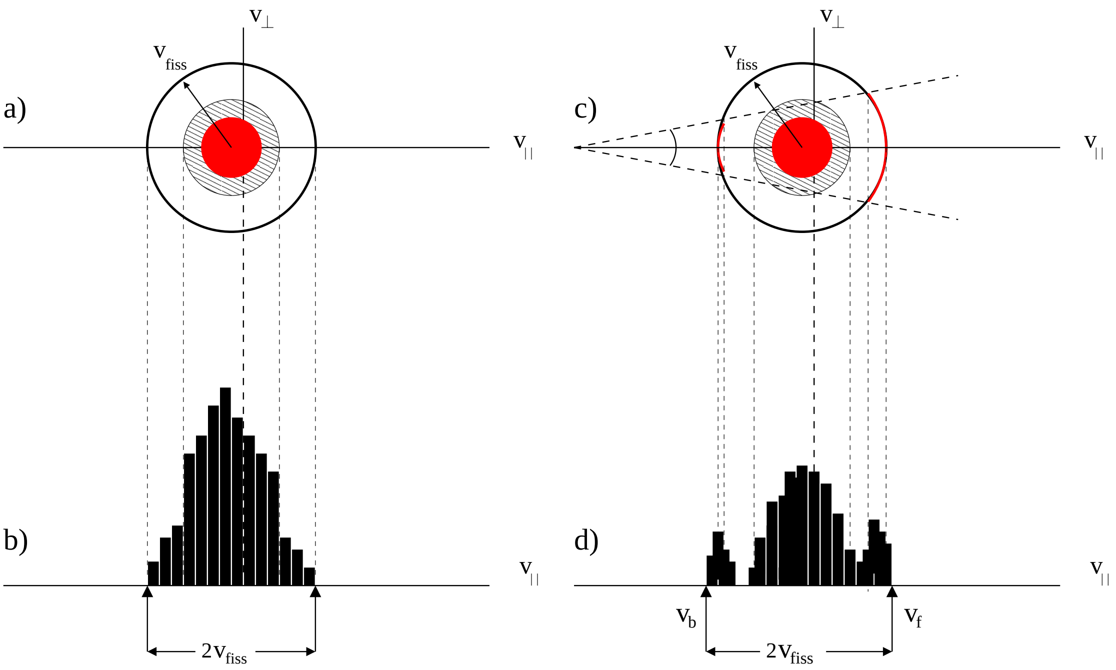

Figure 3.1: *a) Schematic representation of the velocity distributions of a projectile-like residue produced by fission and evaporation. The outer sphere corresponds to the fission contribution, the inner dashed circle represents the evaporation component and the inner black circle represents the Gaussian velocity distribution of pre-fragments produced in the first stage of the collision. b) Projection of these distributions onto the axis parallel to the beam direction (longitudinal component* $v_{||}$*). c) Same distributions constrained the limited angular acceptance of the FRS. d) Projection of transmitted fission and evaporation residues onto the axis of longitudinal velocities (see text for details).*

In contrast to the velocity acceptance, the angular acceptance of the FRS is an unavoidable intrinsic limitation of these so-called zero-degree spectrometers which must be properly calculated in order to correct the final data. A detailed analysis of this limitation is given in appendix C. The calculated value of the angular acceptance α_{eff} defines a cone in the space of velocities which truncates the velocity distributions of the reaction products as shown in figure 3.1-c. The major part of the evaporation component is transmitted due to its relatively small angular emittance, while in the case of fission, only the forward and backward emitted fragments are accepted by the spectrometer. The effect of this limitation in the measured velocities is schematically illustrated in figure 3.1-d: The spectra of longitudinal velocities show a characteristic pattern defined by a triple-humped distribution; the central peak corresponds to the transmitted evaporation residues while the external side peaks correspond to the forward and backward fission components. Thus, these two components can be well separated from the spectra of velocities filtered by the angular acceptance of the FRS.

In order to better understand the link between the angular acceptance of the FRS and the shape of the velocity spectra, we performed a Monte Carlo simulation of the transmission of a nucleus (^{104}Pd), produced by fission and evaporation.The kinematics of both reaction mechanisms were included in the calculations, as well as the geometrical constraints of the FRS. The three upper panels of figure 3.2 show the velocity spectra obtained by assuming an angular acceptance of 100% for fission (left), evaporation (center) and fission plus evaporation (right). The latter demonstrates that the longitudinal velocity distributions for these two different reaction mechanisms are almost indistinguishable. The lower panels of figure 3.2 show the effect of the limited angular acceptance of the spectrometer on the velocity distributions. The left panel was obtained with a circular angular cut of 15 mrad radius and a fission velocity determined exclusively by the Coulomb repulsion of the two fission fragments [Wil76]. The central panel shows the same distribution with a more realistic description of the angular cuts, which accounts for the shape of the inner guide-line of the spectrometer [Per99, BeP02]. Finally, the right panel depicts the fission and evaporation contributions affected by the angular cuts of the spectrometer and the velocity diffuseness due to the straggling in the target, the velocity spread of the pre-fragments and the fluctuations of the total kinetic energy released at scission [Mor75].

The comparison of this figure with the measured velocity spectrum of the same nucleus (figure 3.3) provides a better understanding of the different contributions that define the shape of the velocity spectra, namely, the kinematics of the reaction mechanism and the angular acceptance of the FRS.

3.3 Determination of fission velocities with the FRS

The determination of the velocities of the fission residues v_{fiss} from the measured values of $v_{||}$ were undertaken in three steps: First the longitudinal velocity spectra for each projectile residue were determined by accumulating the velocities $v_{||}$ measured event-by-event with the FRS. Then, the parts of the spectra measured in different settings were normalized to the corresponding beam intensities and overlapped, so that the full velocity spectra could be reconstructed. The resulting spectra of each nucleus were then fitted to determine the value of v_{fiss}. This sequence is explained in the following sections:

Measurement of the longitudinal velocity with the FRS

According to equation 2.22 and 2.24, the longitudinal velocities of the nuclei transmitted through the FRS were determined from their positions in the dispersive image plane, measured with the plastic scintillator $SC2$ (see figure 2.9):

$$v_{||} = c \cdot \left\{ \left[\frac{A/Z}{(B\rho)_c \cdot \left(1 + \frac{x_2}{D}\right)} \right]^2 + 1 \right\}^{-1/2} \tag{3.1}$$

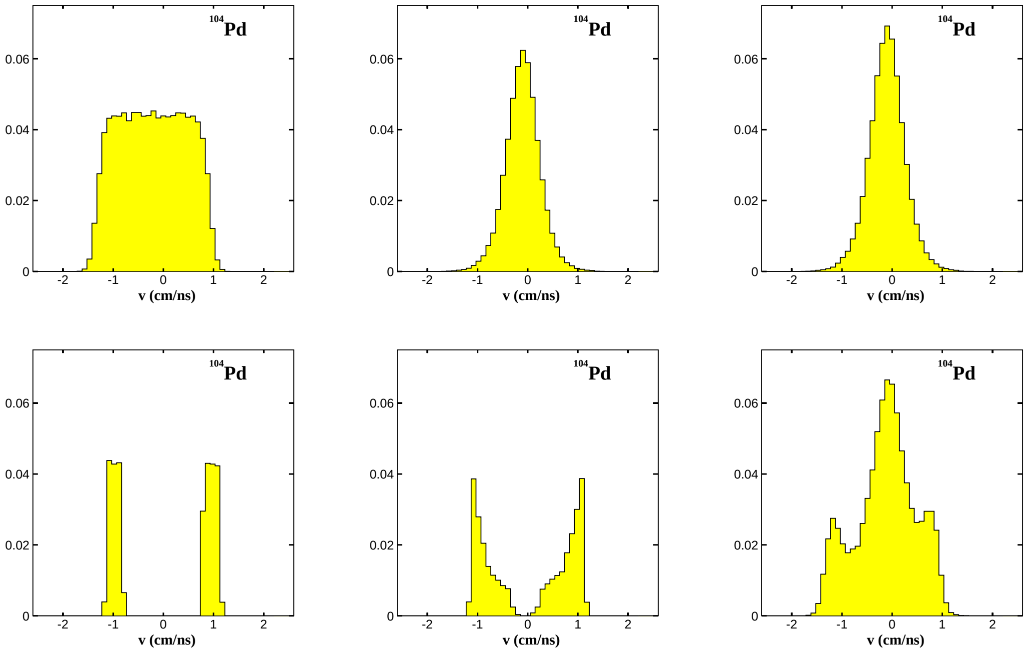

Figure 3.2: *Calculated velocity distributions of* ^{104}Pd *in the frame of the projectile. Upper part: fission (left), evaporation (center) and fission+evaporation (right) contributions calculated for an angular acceptance of 100 %. Lower part: fission contribution affected by a circular cut of* 15 *mrad radius (left), fission affected by a more realistic cut (center), fission+evaporation contributions affected by the limited angular acceptance and velocity diffuseness (right).*

In order to determine the velocities right after the reaction took place, the values obtained from equation 3.1 had to be corrected by the slowing down of the transmitted nuclei in the different layers of matter situated between the deuterium target and the plastic scintillator [1]. This correction was done by calculating the energy lost by each nucleus along its flight path from the middle of the target, where the reaction was assumed to take place on average, to the second image plane. Figure 3.4 schematically illustrates this correction for a given nucleus. Finally, these velocities were transformed into the frame of the projectile, according to the Lorentz transformation:

$$v_{\|} = \frac{v'_{\|} - v_0}{1 - \left(\frac{v'_{\|} \cdot v_0}{c^2}\right)} \tag{3.2}$$

where $v'_{\|}$ and v_0 are the velocities of the transmitted nuclei and of the primary beam in the middle of the target (see figure 3.4), determined in the laboratory frame.

The accuracy of the velocity determined from equations 3.1 and 3.2is mainly limited by the position resolution of the plastic scintillator SC2, $\Delta x_2 \simeq 2$ mm, and

---

[1] The thicknesses of the different layers of matter from the SIS vacuum window to the end of the FRS are reported in appendix D.

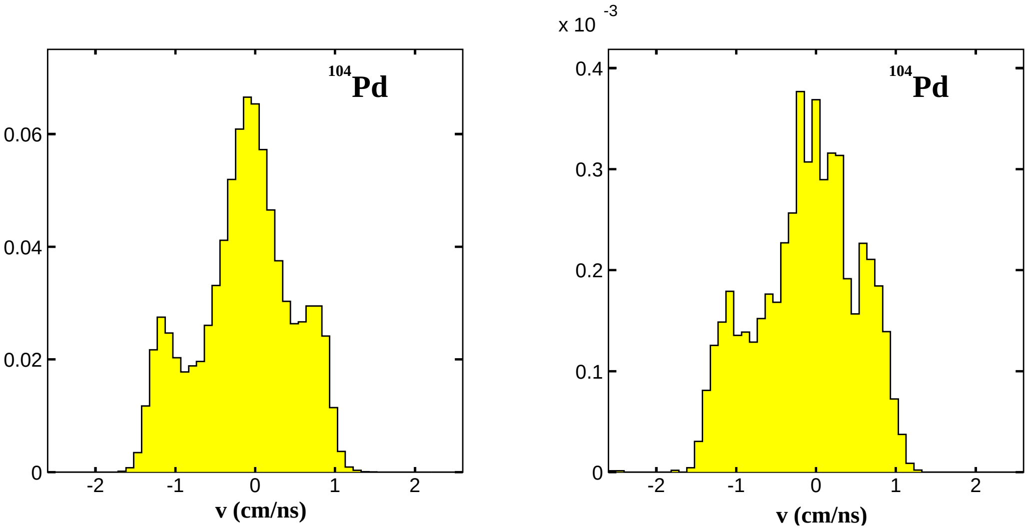

Figure 3.3: *Spectrum of longitudinal velocities of* ^{104}Pd *measured with the FRS (left) and calculated with a Monte Carlo simulation (right). Details of the simulations are given in the text.*

the relative resolution of $(B\rho)_c$ of the order of $\sim 10^{-4}$. These values lead to a final relative precision of the velocity of about $3 \cdot 10^{-4}$ which proves to be a real achievement when compared with other experimental techniques.

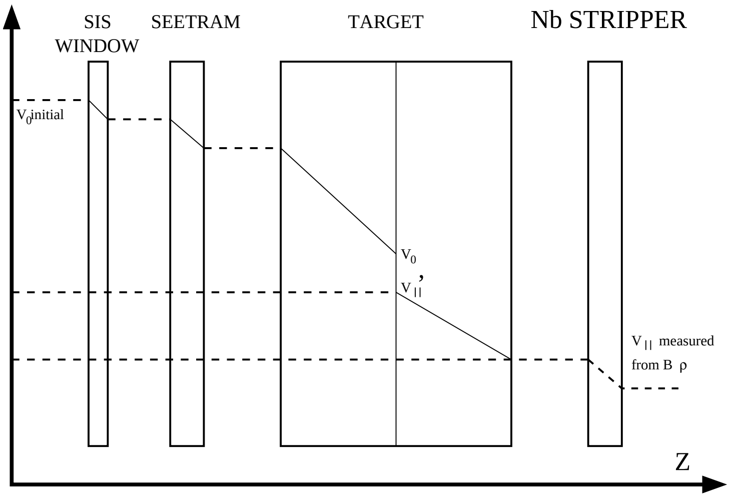

Figure 3.4: *Schematic diagram of the evolution of the velocities along the path from the SIS to the FRS. All the velocities are considered in the laboratory frame.*

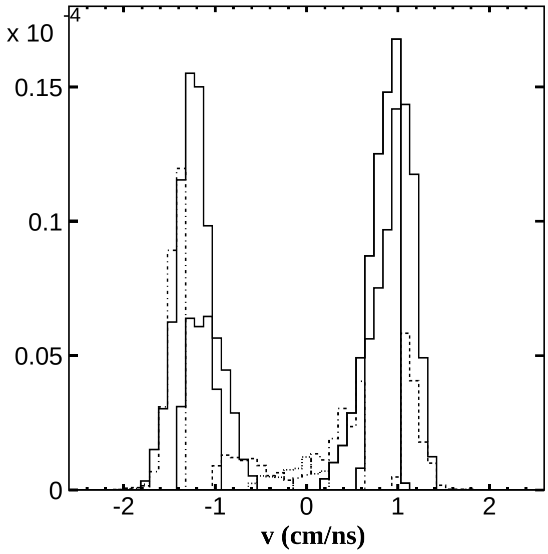

Figure 3.5: *Distribution of measured velocities for ^{77}Se, obtained by combining ten different magnetic settings. The different lines correspond to different settings.*

Reconstruction of the velocity distributions from different magnetic setting

The velocity distribution of a given nucleus was reconstructed by summing up the contributions measured in different magnetic settings of the FRS. Since each setting was measured with different beam intensities, it was necessary to normalize their contributions by a factor f given by:

$$f = \frac{1}{N_{proj} \cdot \epsilon_{\tau}} \tag{3.3}$$

where N_{proj} refers to the number of beam particles determined from equation 2.1 for each setting and ϵ_{τ} is the corresponding efficiency associated to the dead time of the data acquisition. As an example of this procedure, figure 3.5 shows the contribution of different magnetic setting to the velocity spectrum of ^{77}Se. The origin of the figure corresponds to the velocity of the primary beam in the middle of the target.

Figure 3.6 depicts a series of velocity spectra obtained for several projectile residues, which enable a preliminary discussion of the general trends of the fission and evaporation mechanisms:

As discussed above, the center of these distributions is slightly slowed down with respect to the velocity of the projectile. The two external peaks, which correspond to the forward- and backward-emitted fission fragments, approach each other as the residue charge increases. The separation between these two peaks is related to the fission velocity v_{fiss} and its reduction can be partially attributed to a decrease of the kinetic energy of the fission partners due to the weakness of their Coulomb

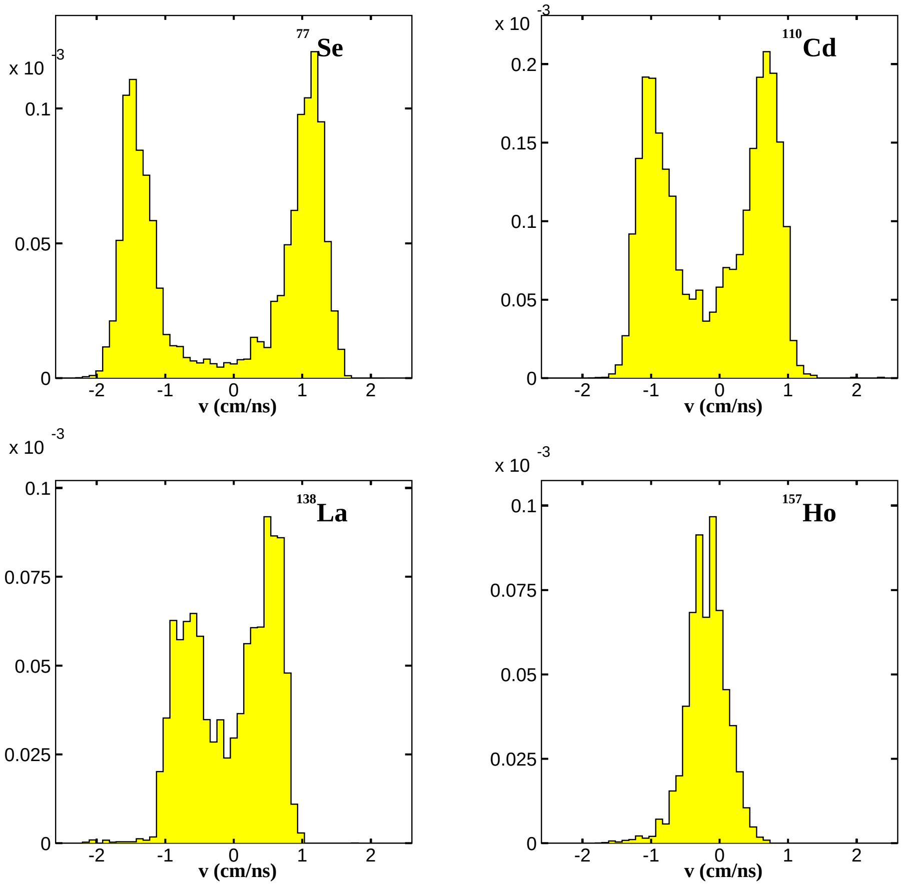

Figure 3.6: *Velocity spectra for several isotopes obtained in the reaction* ^{238}*U(1 A · GeV)+d.*

repulsion at large charge asymmetries. For a given couple of fission fragments, the light partner will acquire larger velocities than the heavy one due to momentum conservation. Finally, one observes a gradual increase of the evaporation component as the charge of the nuclei increases. In fact, this mechanism becomes dominant for ^{157}Ho.

The contributions of fission and evaporation are better illustrated in the series of cluster plots shown in figure 3.7 for different elements.

In these figures, the velocities of the different isotopes of a given element, measured in the projectile frame, are represented as a function of their mass number. The upper and lower wings correspond to the forward and backward emitted fission fragments, respectively, while the central cloud represents the contribution of evaporation. The distribution of residues produced in the two reaction mechanisms is consistent with the theoretical expectations: fission residues are mostly produced with greater neutron excess, while evaporation generally leads to nuclei along the so-called evaporation corridor, located on the neutron-deficient side of the beta-stability valley. Moreover, as the charge of the element increases, the evaporation contribution is enhanced until it becomes the dominant production mechanism.

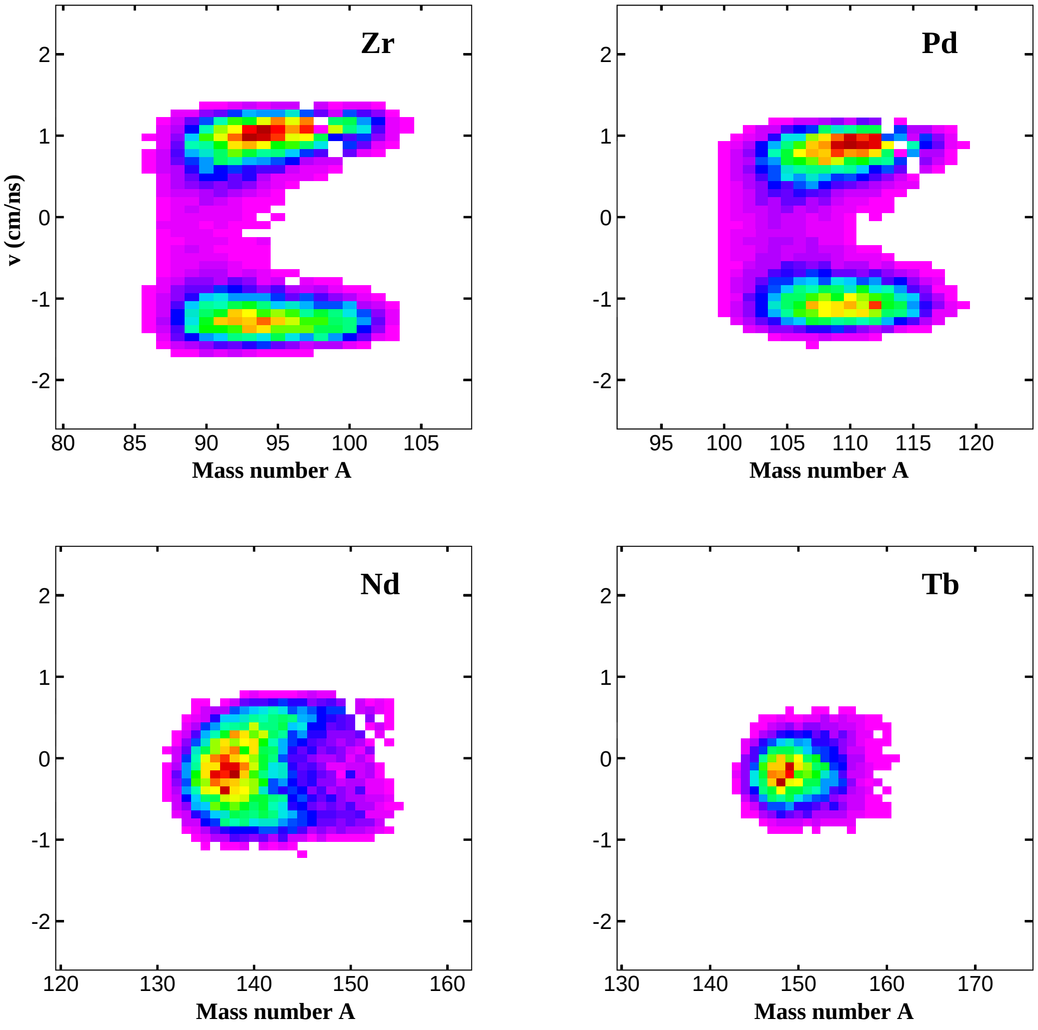

Figure 3.7: *Scatterplots of* ${}_{40}Zr$, ${}_{46}Pd$, ${}_{60}Nd$ *and* ${}_{65}Tb$ *isotopes showing the velocity distributions measured in the frame of the projectile, as a function of the mass number.*

Determination of fission velocities from the measured spectra

The mean velocities of the fission residues v_{fiss} were obtained in the projectile frame by fitting the measured spectra of velocities to specific functions which reproduce the contribution from each reaction mechanism. The central peak, originated from the evaporation component was described by a Gaussian function $f_{evap}(v_{||})$, while the forward and backward fission peaks were better reproduced by fitting functions defined by the convolution of a Gaussian and an exponential function. Each o these functions $f^f_{fiss}(v_{||})$ and $f^b_{fiss}(v_{||})$ had four free parameters each, three of which corresponded to the Gaussian component, while the fourth parameter corresponded to the skew of the inner tail. The spectra was then fitted to a global function $F(v_{||})$ with eleven parameters (three from the Gaussian evaporation component and eight from the forward and backward functions):

$$F(v_{||}) = f^b_{fiss}(v_{||}) + f_{evap}(v_{||}) + f^f_{fiss}(v_{||}) \tag{3.4}$$

The spectra of isotopes produced only by fission or evaporation were better described by fitting functions which included only the corresponding component. Figure 3.8 depicts an example of the fit obtained for ^{83}Sr.

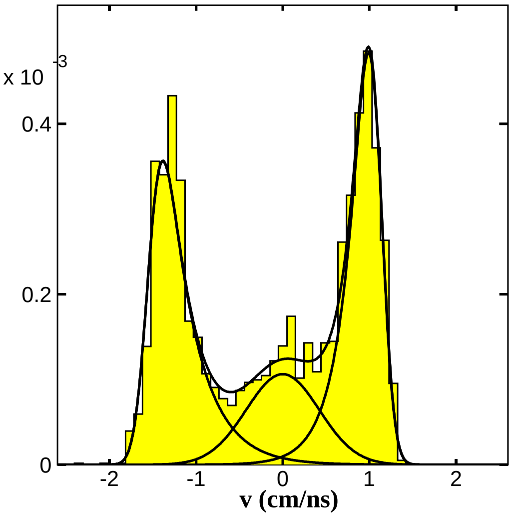

Figure 3.8: *Velocity spectrum of ^{83}Sr showing the contribution from evaporation (central Gaussian curve) and fission (external curves) to the global fit.*

As can be seen in figure 3.1-d, the radius of the spherical fission distribution corresponding to the velocity of the fission residues v_{fiss}, could be obtained by halving the distance between the external sides of the forward and backward fission peaks, given by v_f and v_b:

$$v_{fiss} = \frac{|v_f - v_b|}{2} = \frac{|v_f| + |v_b|}{2} \tag{3.5}$$

The determination of v_f and v_b from the velocity spectra was quite complicated due to the smooth side tails of the fission peaks. An alternative method based on the fitting functions discussed above is illustrated in figure 3.9: According to this figure, the values of v_f and v_b can be expressed as a function of the velocities v_f^{max} and v_b^{max} that correspond to the maximum of the forward and backward fitting functions

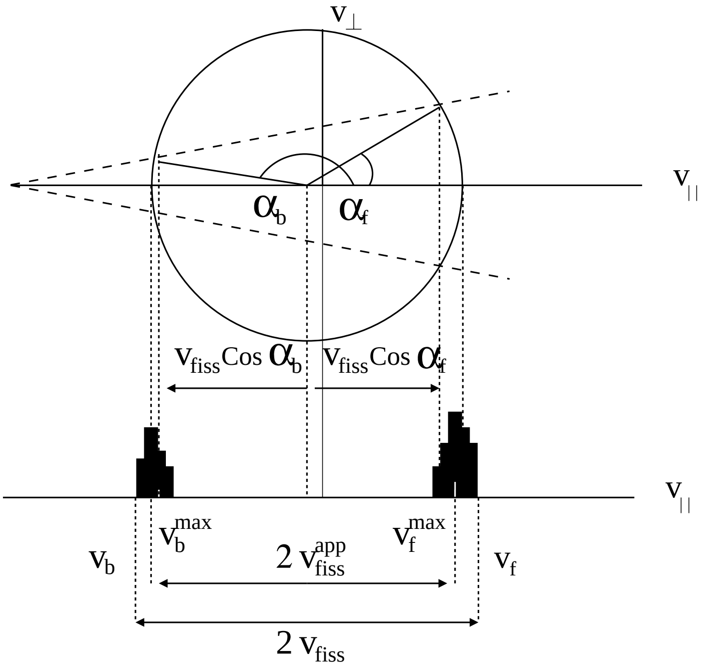

Figure 3.9: *Up: Schematic representation of the velocity distribution of fission residues affected by the cuts produced by the limited angular acceptance of the FRS. (Note the shift of the velocity distribution with respect to the velocity of the projectile, marked by the origin of the reference frame). Down: Projection of the transmitted nuclei onto the axis parallel to the beam direction (longitudinal component). The measured forward and backward fission velocities* v_f^{max} *and* v_b^{max} *are compared with the real values* v_f *and* v_b.

$f_f(v_{||})$ and $f_b(v_{||})$, according to:

$$v_f = v_f^{max} + \frac{v_{fiss} - v_{fiss}\cos\alpha_f}{2} \tag{3.6}$$

and

$$v_b = v_b^{max} + \frac{v_{fiss} + v_{fiss}\cos\alpha_b}{2} \tag{3.7}$$

where α_f and α_b are the forward and backward angles obtained by a Lorentz transformation of the angular acceptance α_{eff} of the FRS into the frame of the fissioning system (see appendix C). These two equations can be re-written as:

$$v_f = v_f^{max} + v_{fiss} \cdot T_f \tag{3.8}$$

and

$$v_b = v_b^{max} + v_{fiss} \cdot T_b \tag{3.9}$$

where T_f and T_b are the transmission of the forward- and backward-emitted fission fragments, calculated in appendix C according to:

$$T_f = \frac{\int_0^{2\pi}\int_0^{\alpha_f} \sin\theta d\theta d\phi}{4\pi} = \frac{1-\cos\alpha_f}{2} \tag{3.10}$$

$$T_b = \frac{\int_0^{2\pi}\int_{\alpha_b}^{\pi} \sin\theta d\theta d\phi}{4\pi} = \frac{1+\cos\alpha_b}{2} \tag{3.11}$$

The idea behind these equations is that the velocities v_f^{max} and v_b^{max} obtained from the fitting functions, must be corrected using the fission velocity v_{fiss} and the angular transmission in order to provide the values v_f and v_b. However, according to equation 3.5, v_{fiss} also depends on v_f and v_b and consequently we had to develop an iterative algorithm to solve the problem:

1. The fitting functions $f_f(v_{||})$ and $f_b(v_{||})$ were used to determine the values of v_f^{max} and v_f^{max}.

2. These two velocities provided the "apparent" fission velocity v_{fiss}^{app} and a first estimation of the velocity of the fissioning system in the frame of the projectile $v_0(proj)$ (see figure 3.9):

   $$v_{fiss}^{app} = \frac{|v_f^{max} - v_b^{max}|}{2} = \frac{|v_f^{max}| + |v_b^{max}|}{2} \tag{3.12}$$

   and

   $$v_0(proj) = \frac{|v_f^{max}| - |v_b^{max}|}{2} \tag{3.13}$$

3. The value of $v_0(proj)$ was then transformed into the laboratory frame, and used, together with v_{fiss}^{app}, to calculate T_f and T_b from equations 3.10 and 3.11.

4. With these values of T_f and T_b, the velocities v_f and v_b were calculated from equations 3.8 and 3.9 by replacing v_{fiss} by v_{fiss}^{app}.

5. The velocities v_f^{max} and v_b^{max} were then replaced in equations 3.12 and 3.13 by the calculated values of v_f and v_b and the sequence started again.

The iterative algorithm stops when v_{fiss}^{app} converges to a constant value which is assumed to correspond to v_{fiss}, providing in addition the value of the velocity of the fissioning system in the laboratory frame v_0 and the forward and backward transmission T_f, T_b.

Uncertainties

There are two sources of uncertainty with respect to the velocities determined using the above-described method: First is the determination of the mean values from the velocity distribution fits and second is the uncertainty of the angular acceptance value α_{eff} used to calculate T_f and T_b. The former varies a lot from one nucleus to another and depends mainly on the smoothness of the velocity spectra profile. It ranges typically from 1% to 5%, though in some particular cases it reaches maximun values of up to 20%. Concerning the uncertainty due to α_{eff}, it mainly affects the velocities of residues with rather low transmission. A deep analysis of the ion-optics and the geometry of the FRS yield a total uncertainty for α_{eff} of about

4% [Per99, BeP02], resulting in an uncertainty for the velocities of less than 5% (see also appendix C).

Finally, an additional source of error can arise from the production of secondary reactions in the deuterium target induced by a heavy primary fission fragment. Such a process would reduce the atomic and mass numbers of the fission residues, while slightly blurring its velocity spectra. As a consequence, the velocity distribution of the isotope will be partially contaminated by the velocities of the heavier fission fragments that underwent a secondary reaction, leading to a reduction of the measured values of v_f^{max} and v_b^{max}. As will be discussed in the next section, this contamination is only significant for the most neutron-deficient residues.

3.4 Kinematical analysis of fission residues

Figure 3.10 shows the velocity distributions of the fission residues measured in the reaction induced in the deuterium target surrounded by the titanium windows (left) and in the titanium dummy target (right). The distributions were obtained for each element by integrating the contributions of the whole isotopic chain. In the figure, the evaporation residues lay in a region of velocities close to that of the primary beam, while the forward- and backward-emitted fission fragments correspond to the upper and lower wings. The increase of the fission velocities as the atomic number of the residues decreases is a natural consequence of the momentum conservation between the light and heavy fission fragments in the frame of the fissioning system. Moreover, the evaporation residues produced in the reaction induced on titanium (right panel) are observed to increase their velocities at low atomic numbers. This finding is in clear contradiction to the expected reduction of evaporation velocities for decreasing projectile masses [Mor89], and was interpreted as being due to the blast of compressed nuclear matter during the first stage of the reaction [Ric03, Shi01]. Apart from this, it is noteworthy that the contribution of the evaporation component observed in the left figure for atomic numbers lower than $Z = 65$ comes almost entirely from the titanium windows, demonstrating that the fragmentation component from the deuterium target is almost negligible in this region.

The method described in the previous section was used to determine the fission velocities v_{fiss} of the projectile residues with atomic numbers ranging from $Z = 23$ to $Z = 66$. Figures 3.11-3.14 show the isotopic chains of v_{fiss} for all measured fission residues. The numerical values, with their associated uncertainties are included in appendix B. These velocities are slightly larger than the values deduced from figure 3.6 due to the influence of the limited angular acceptance of the FRS. Before entering into a detailed discussion of figures 3.11-3.14 one observes, as a general trend, a reduction of the average fission velocities with the increasing charges of the fission residue. Moreover, for a given element, the velocities decrease smoothly from their maximum value, which is always found in the neutron-rich side, to smaller values for the lighter isotopes. This reduction is more pronounced in the most neutron deficient side with an abrupt decline of v_{fiss} to values 20% below the maximun. The

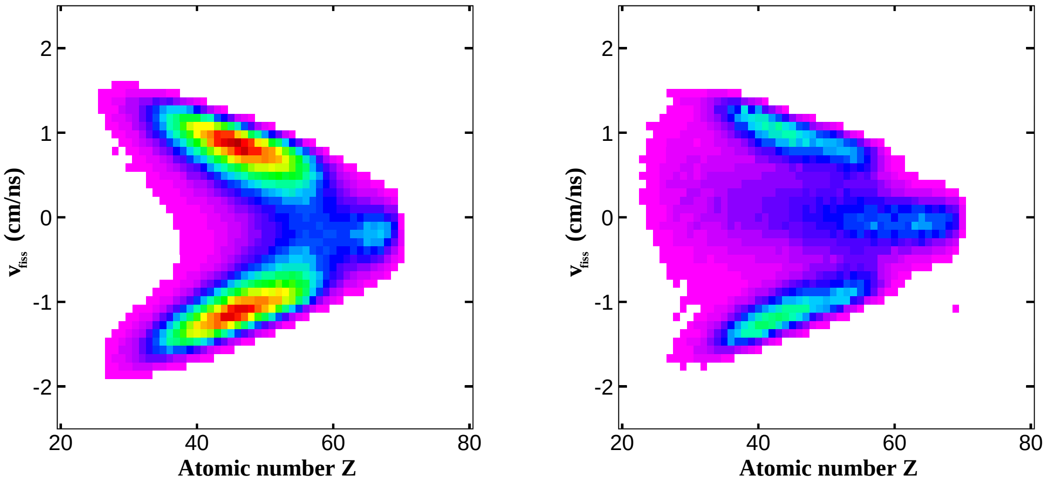

Figure 3.10: *Velocity distributions as a function of the atomic number of residues measured with the deuterium target enclosed in the titanium container (left) and with the titanium dummy target (right).*

characteristic pattern shown in these figures was already observed in the analysis of fission residues produced in the reaction ^{238}U (1 A·GeV)+p [Ber03]. According to this work, the abrupt decrease of the velocities in the neutron-deficient side can to some extent be attributed to the contamination of secondary reactions from primary fission fragments. In order to estimate such an effect, we have used a model proposed by P. Napolitani et al. [Nap03] to evaluate the rates of contaminants (see also next chapter). As expected, they correspond to the most neutron-deficient isotopes.

The measured fission velocities reflect the total kinetic energy released in the fission process itself. According to the semi-statistical scission point model of Wilkins et al. [Wil76] the main contribution to this energy comes from the Coulomb repulsion of the two nascent fragments at the scission point and depends only weakly on the dynamics of the process from saddle to scission. In a “hard” statistical version of this model, the later contribution can be neglected compared to the dominant Coulomb term and thus the total kinetic energy (TKE) is given by:

$$TKE \simeq \frac{Z_1 \cdot Z_2 \cdot e^2}{D} \tag{3.14}$$

where e is the electron charge, and Z_1 and Z_2 refer to the charge of the two fission fragments. The distance D between the two uniformly charged spheroids which constitute the fission fragments is given by:

$$D = r_0 A_1^{1/3}\left(1+\frac{2\beta_1}{3}\right) + r_0 A_2^{1/3}\left(1+\frac{2\beta_2}{3}\right) + d \tag{3.15}$$

where A_1 and A_2 are the masses of the two nuclei, d is the distance between the tips of the spheroids and β_1 and β_2 refer to their quadrupole deformations at scission. According to the scission model, at low excitation energies these two latter parameters might depend on the shell structure of the two nascent fragments, while at higher energies they can be determined on the basis of the liquid-drop model. In the present discussion we use the parameters proposed by Wilkins et al. for high energy fission: r_0=1.16 fm, d=2 fm and $\beta_1 = \beta_2 = 0.625$. These values were later confirmed by Böckstiegel et al. [Boc97] by adjusting the TKE measured on nuclear-induced fission of several actinides and pre-actinides. From these equations it is possible to determine the velocities of the fission residues v_{fiss} as a function of the charge of the fissioning nucleus ($Z_{fiss} = Z_1 + Z_2$), provided the momentum between the two fragments is conserved in the frame of the fissioning system. Furthermore, the mass of the second fission partner A_2 must be imposed by following the unchanged-charge-density (UCD) criteria which preserves the mass-to-charge ratio of the fissioning nucleus ($A_{fiss}/Z_{fiss} = A_1/Z_1 = A_2/Z_2$) in the fission process. This assumption neglects the post-scission neutron evaporation.

$$v_{fiss} = \left\{ \frac{2Z(Z_{fiss} - Z)^2 e^2}{m_0 A Z_{fiss}[r_0 A^{1/3}[1 + 2/3\beta_1 + (Z_{fiss}/Z - 1)^{1/3}(1 + 2/3\beta_2)] + d]} \right\}^{1/2} \tag{3.16}$$

being m_0 the nuclear mass unit. In this equation we used the values of the parameters r_0, d, β_1 and β_2 described above. The explicit relation between v_{fiss} and the charge of the fissioning nucleus shown in 3.16 can be used to investigate the properties of the fissioning nuclei from the measured velocities.

Figures 3.11-3.14 show the measured velocities, together with the values calculated with equation 3.16 for different Z_{fiss}. As can be seen, the different isotopes of a given element can be produced by different parent nuclei: the most neutron-rich isotopes are produced by the heaviest fissioning elements including Uranium, Protactinium and Thorium, while the neutron-deficient ones are populated by lighter fissioning systems. This trend is in agreement with the Z^2_{fiss}/A_{fiss}-dependence of the fissility: As a consequence of the low fissilities of light parent nuclei (low Z_{fiss}), only the most neutron-deficient isotopes (low A_{fiss}) have the possibility of undergoing fission due to their smaller fission barriers. The residues produced by these parent nuclei will then be neutron-deficient. On the contrary, the high facilities of heavy fissioning systems are rather insensitive to a variation of the neutron number, thus extending their productions to more neutron-rich nuclei.

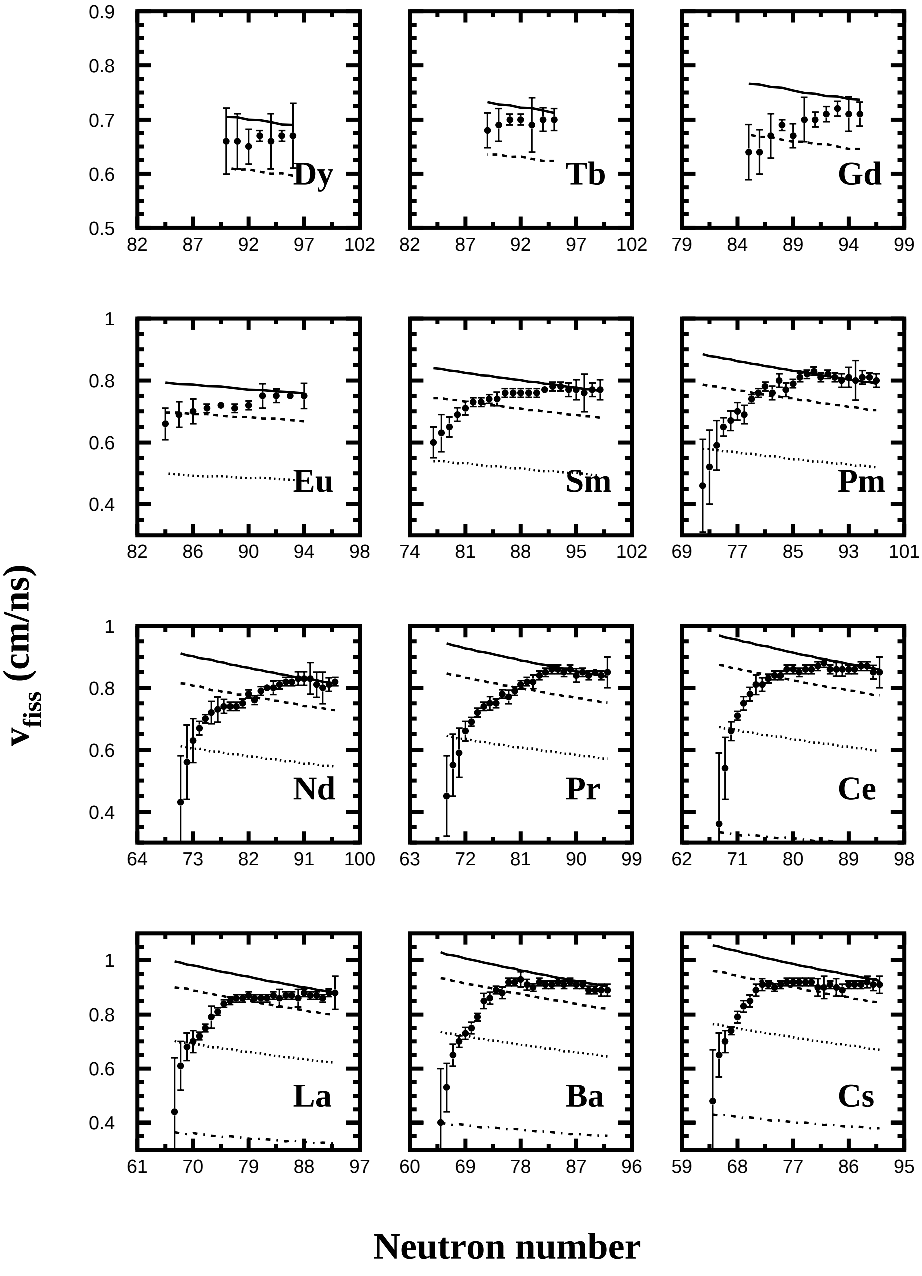

Figure 3.11: *Isotopic distribution of fission residue velocities measured in the reaction* ^{238}*U(1 A·GeV)+d compared to the values calculated from equation 3.16 (see text for details). The calculations were obtained for different fissioning systems: Uranium Z=92 (solid line), Radium Z=88 (dashed line), Mercury Z=80 (dotted line) and Rhenium Z=75 (dash-dotted line).*

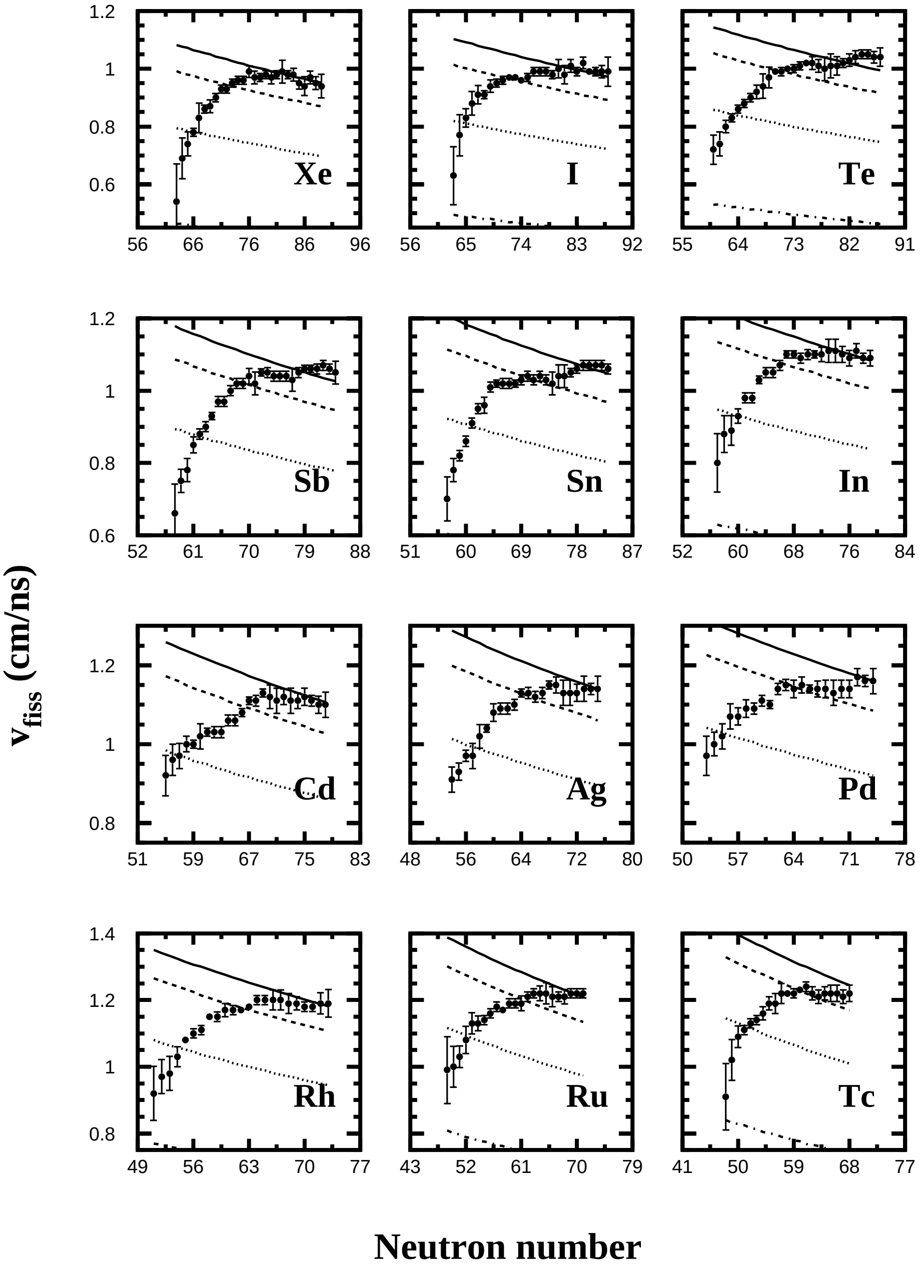

Figure 3.12: *Isotopic distribution of fission residue velocities measured in the reaction* ^{238}*U(1 A·GeV)+d compared to the values calculated from equation 3.16 (see text for details). The calculations were obtained for different fissioning systems: Uranium Z=92 (solid line), Radium Z=88 (dashed line), Mercury Z=80 (dotted line) and Rhenium Z=75 (dash-dotted line).*

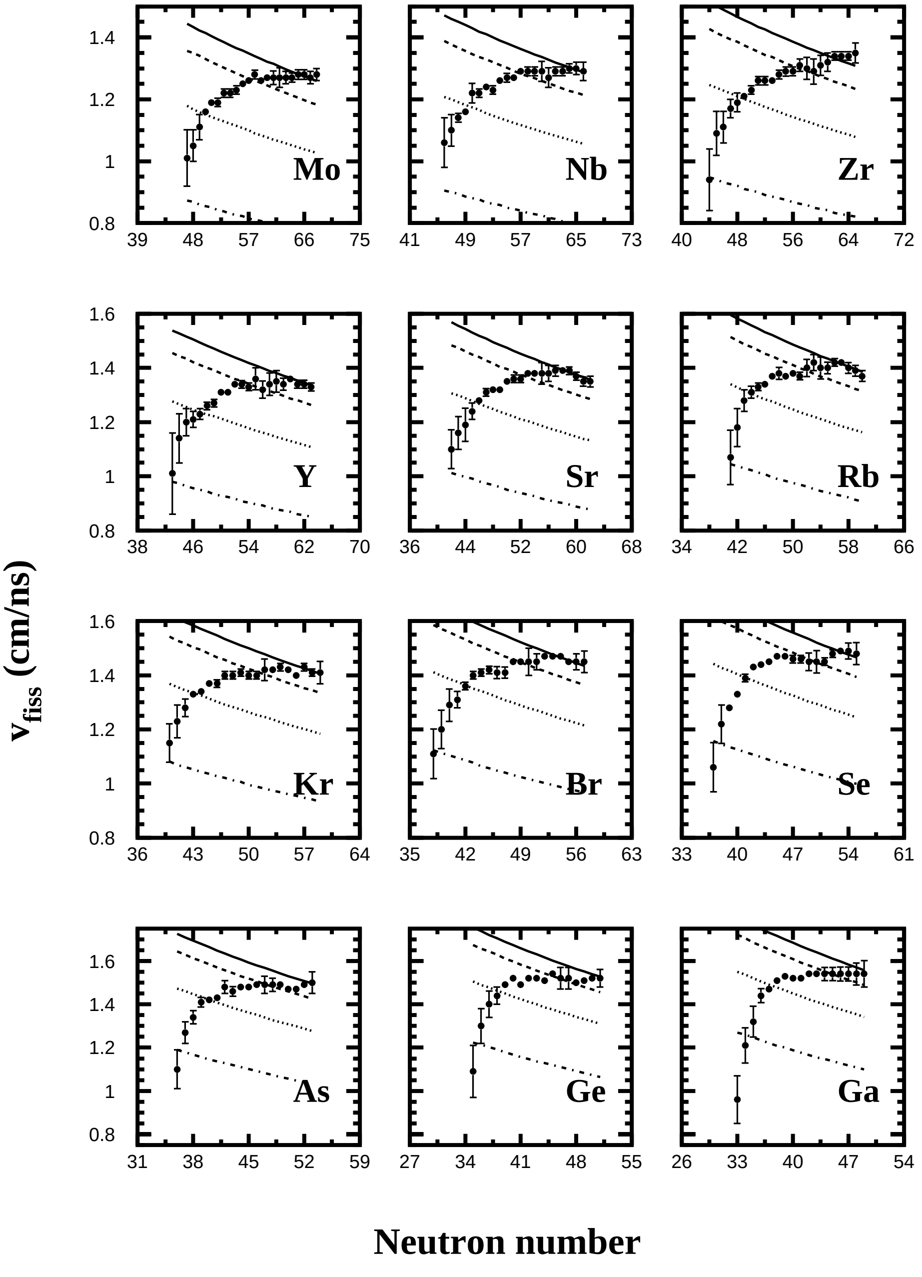

Figure 3.13: *Isotopic distribution of fission residue velocities measured in the reaction* ^{238}*U(1 A·GeV)+d compared to the values calculated from equation 3.16 (see text for details). The calculations were obtained for different fissioning systems: Uranium Z=92 (solid line), Radium Z=88 (dashed line), Mercury Z=80 (dotted line) and Rhenium Z=75 (dash-dotted line).*

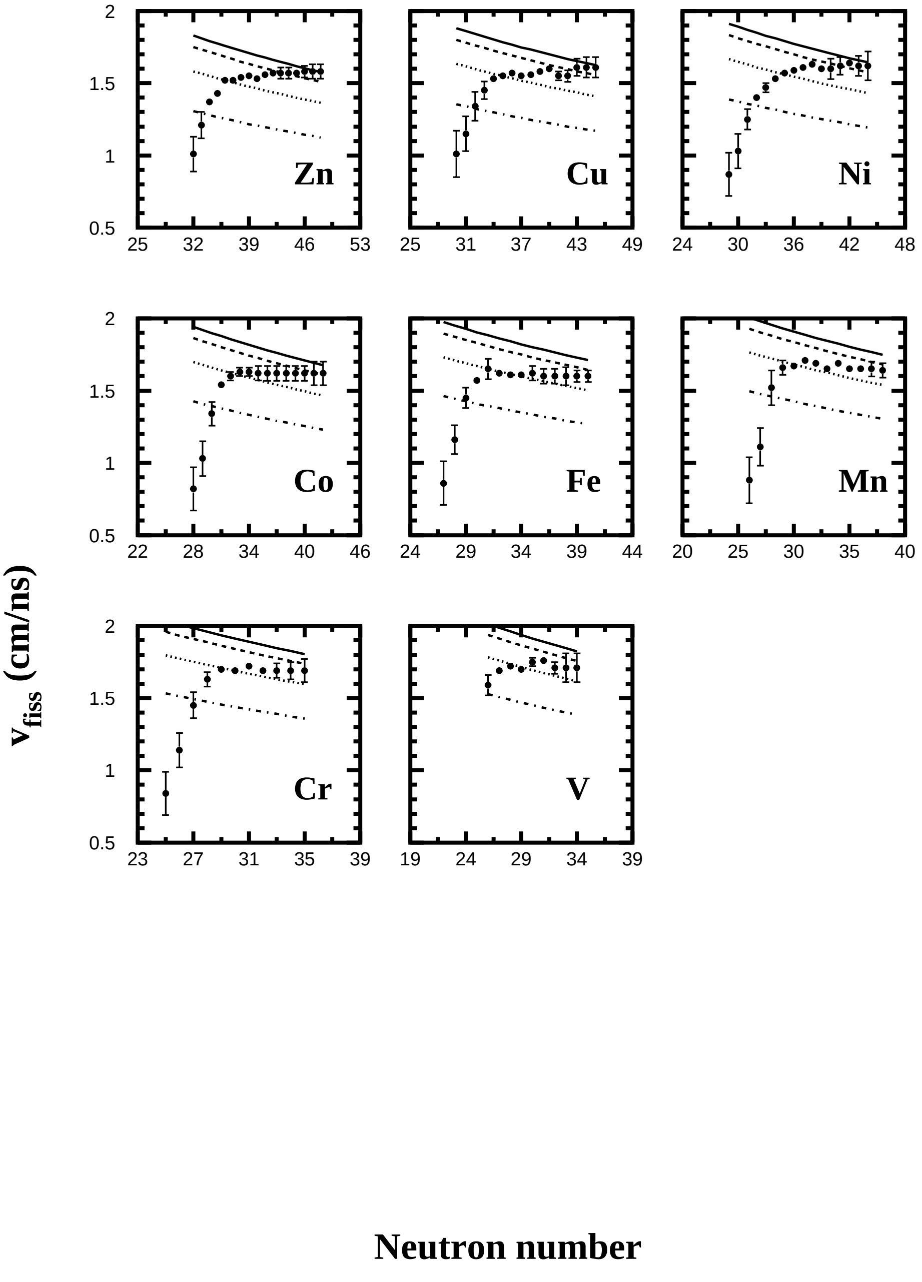

Figure 3.14: *Isotopic distribution of fission residue velocities measured in the reaction* ^{238}*U(1 A·GeV)+d compared to the values calculated from equation 3.16 (see text for details). The calculations were obtained for different fissioning systems: Uranium Z=92 (solid line), Radium Z=88 (dashed line), Mercury Z=80 (dotted line) and Rhenium Z=75 (dash-dotted line).*

Apart from the dependency with the neutron number, it is noteworthy that

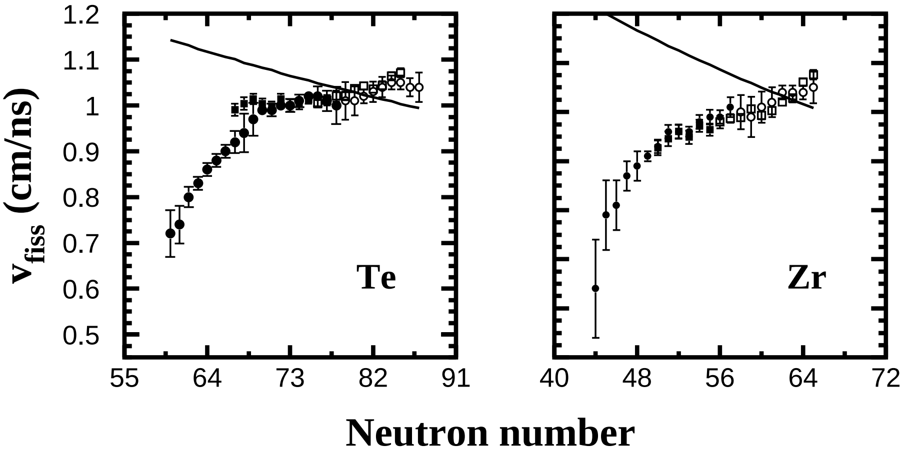

Figure 3.15: *Fission velocities of Tellurium and Zirconium isotopes measured in the reactions* ^{238}*U(1 A·GeV)+d (dots) and* ^{238}*U(1 A·GeV)+Pb [Enq99] (squares). The open symbols represent the isotopes that were mainly produced by low-energy asymmetric modes (see text for more details).*

in figures 3.11-3.14, the lightest fission elements ($Z < 28$) and the heaviest ones ($Z > 63$) are produced on average by lighter fissioning nuclei, even the most neutron-rich isotopes. Such a finding demonstrates that these nuclei were produced by high-energy fission:

The charge of the fissioning nuclei Z_{fiss} is directly linked to the number of protons abraded from the uranium projectile during the first stage of the reaction. Due to this interaction, the excitation energy of the projectile-like residue increases with the number of abraded protons. Therefore, the low values of Z_{fiss} found for parent nuclei of light and heavy fission elements correspond to high excitation energies. This finding agrees with the fact that high energy fission leads to broader symmetric charge distributions of fission residues, which enhances the production of heavy and light elements [Sch98, Don98, Enq02]. Furthermore, the same idea can also explain the rather small N/Z ratios measured for the isotopic chains of nuclei in the region $Z < 28$ and $Z > 63$ compared to medium-charge elements: The low neutron numbers of those fission residues demonstrates that they were produced by highly excited light fissioning nuclei.

The high energy symmetric fission is also responsible for the production of fission elements in the region $30 \leq Z \leq 59$, specially for isotopes with low and medium neutron numbers. On the other hand, the neutron-rich side is mainly fed by a low-energy nuclear fission component from uranium-like nuclei.

For charges in the regions $50 \leq Z \leq 52$ and $40 \leq Z \leq 42$, the velocities of these neutron-rich nuclei are even faster than the values predicted by equation 3.16. A similar trend was previously observed by Enqvist et al. [Enq99] in electromagnetic induced fission of ^{238}U on lead at 1 A·GeV. Figure 3.15 compares the measured velocities in that work for Tellurium and Zirconium with the present data (open symbols). As can be seen, both reactions show a similar trend for the velocities of these neutron-rich isotopes. According to the scission model of Wilkins et at [Wil76], the increase of fission velocities -or TKE- with respect to the values predicted by equation 3.16 might be interpreted as a signature of low-energy asymmetric fission modes, where the shell structure of the nascent fragments leads to more compact shapes with the subsequent increase of the Coulomb repulsion. According to Brosa et al. [Bro90], this low-energy asymmetric fission mode consists of two subchannels: a channel with higher kinetic energy (Standard I), corresponding to a spherical heavy fragment (N$\simeq$82) and a channel with lower kinetic energy (Standard II), that corresponds to a deformed heavy fragment (N$\simeq$88). The contribution of these two low-energy asymmetric modes to the residue production in uranium fission was investigated by Donzaud et al. [Don98] from electromagnetic-induced fission measurements on lead. According to this work, Standard I is placed around ^{134}Te/^{104}Zr and Standard II around ^{142}Xe/^{96}Sr. Thus, the large velocities observed in figures 3.11-3.14 for neutron-rich isotopes in the region $50 \leq Z \leq 52$ and $40 \leq Z \leq 42$ can be interpreted as being due to the Standard I mode. By contrast, the lower kinetic energies expected for Standard II can not be separated from the values predicted by equation 3.16 for high-energy fission.

The dependence of the velocities of the fission residues on their charge can also be illustrated by the so-called mean fission velocities $\bar{v}_{fiss}$. This quantity was calculated by averaging the fission velocities v_{fiss} over the isotopic chains of each fission element. These velocities are shown in figure 3.16, together with the results obtained by M. Bernas et al. for ^{238}U (1 A·GeV)+p [Ber03].

Here, by excluding the velocities of the most neutron-rich isotopes in the calculation of the average value, we have limited the discussion to the high-energy fission component. In figure 3.16 we also compare the elemental distribution of $\bar{v}_{fiss}$ for the two reactions with the results determined from equation 3.16, using the values of the parameters obtained in the nuclear-induced fission measurements of Böckstiegel et al. [Boc97]. The different lines correspond to the velocities of the fission residues for different charges of the fissioning element. When the calculated lines are compared with the data measured in the two reactions, several conclusions can be reached: Firstly, since none of the lines coincides exactly with the data, fissioning systems with a total charge between 75 and 92 are necessary to reproduce the data. Moreover, the lighter fission elements tend to cross the lines corresponding to lighter fissioning parent nuclei, indicating that those residues were mainly produced by rather high-energy fission. Secondly, although the two reactions investigated show very similar trends, one observes lower velocity values for the reactions induced on deuterium, indicating also the contribution from lighter fissioning systems. This becomes more evident in the region of light fission residues where the deviation of the data toward lighter fissioning elements is more pronounced in the deuterium case . Similar trends were already observed for the reactions ^{208}Pb(1 A·GeV)+p,d [Enq02] and ^{238}U(750 A·MeV)+Pb [Don98, Sch98].

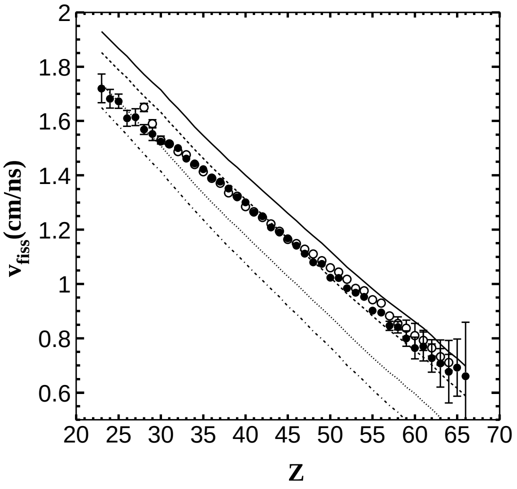

Figure 3.16: *Measured fission-fragment mean velocities as a function of their proton number for the reactions* ^{238}*U(1 A·GeV)+d (full dots) measured in the present work, and* ^{238}*U(1 A·GeV)+p (open circles) obtained from Bernas et al. [Ber03]. The lines indicate the velocities calculated from 3.16 for different fissioning elements: Uranium Z=92 (full line), Francium (dashed line), Mercury Z=80 (dotted line) and Rhenium Z=75 (dash-dotted line).*

Finally, it is worthwhile to mention that the very high precision of the measured velocities made it possible to investigate in detail the mass and charge distributions of the fissioning nucleus, as will be seen in chapters 4 and 5.

Chapter 4

Production cross sections of fission residues

The present chapter is devoted to the analysis and discussion of the production cross sections of fission residues measured in the reaction ^{238}U(1 A·GeV) on deuterium. These data will complete the previous analysis of the evaporation residues obtained in the same reaction [Cas01], providing a comprehensive survey of spallation reactions induced with Uranium beams on deuterium at 1 A·GeV.

The specific setup characteristics used in the present experiment made it possible to identify all nuclei and then determine the cross sections by measuring their productions, which were normalized to the number of beam particles and target nuclei per surface unit. The measured production cross sections had to be corrected due to some limitations intrinsic to the experimental technique and the analysis method. The first half of this chapter is devoted to the determination of the isotopic cross sections, with a detailed discussion of these corrections; while, the second half is dedicated to an extended presentation of the data and a quantitative analysis of the main characteristics of the fission process.

4.1 Evaluation of the production cross sections

The production of a given isotope $N(Z,A)$ in a reaction is related to the cross section of that reaction channel $\sigma_{prod}(Z,A)$ according to the following equation:

$$N(Z,A) = N_{proj}\sigma_{prod}(Z,A)\chi e^{-\sigma_{prod}(Z,A)\cdot\chi} \tag{4.1}$$

where N_{proj} is the number of beam particles and χ the density of deuterium nuclei integrated over the target thickness. By expanding this equation in a power series and keeping the first order term, we can deduce the production cross sections $\sigma_{prod}(Z,A)$ in a simple way, according to:

$$\sigma_{prod}(Z,A) = \frac{N(Z,A)}{N_{proj}\cdot\chi} \tag{4.2}$$

where we assumed the factor $\sigma_{prod}(Z,A) \cdot \chi$ to be small, i.e. for relatively thin targets.

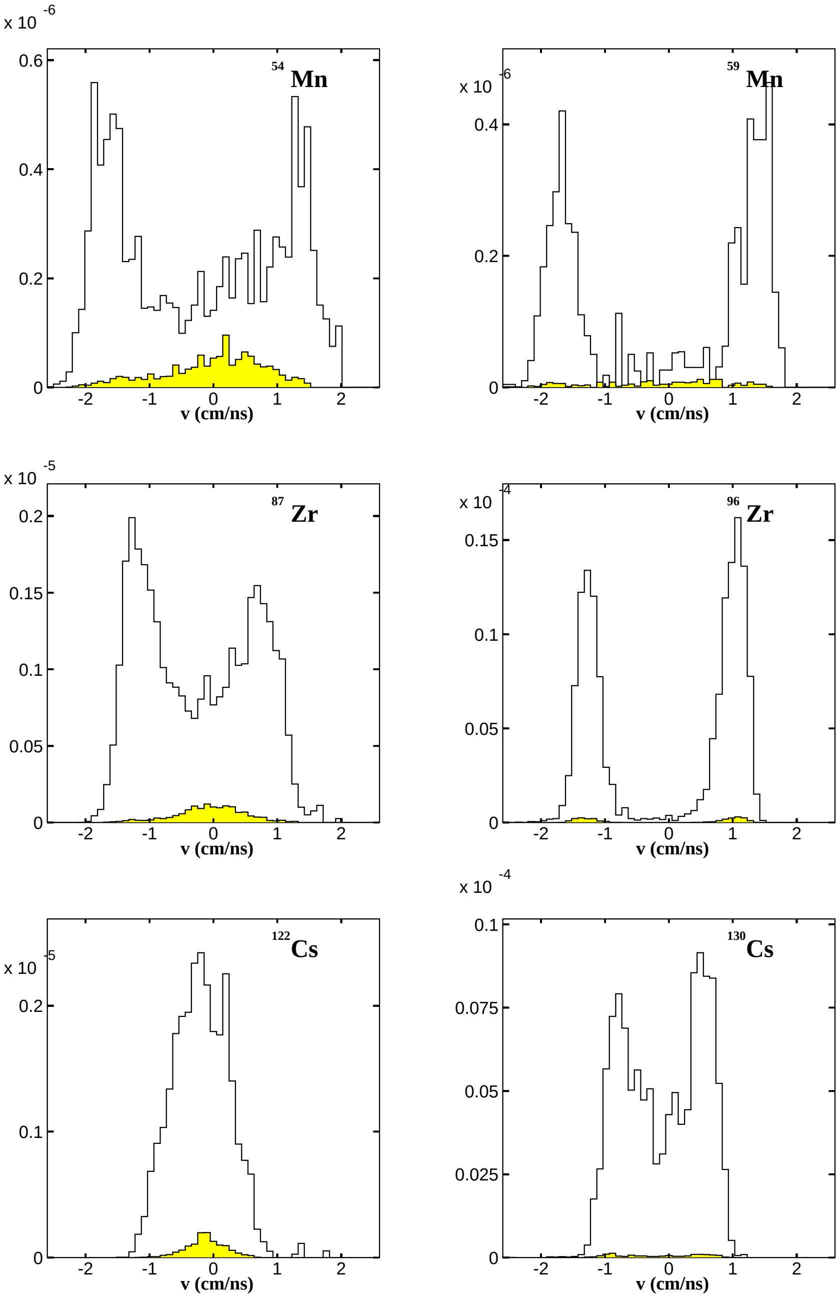

Figure 4.1: *Velocity spectra measured in the projectile frame for six different isotopes. Empty histograms show the productions from the cryogenic target, including the liquid deuterium and the Titanium windows; the contribution from the latter is represented by filled histograms.*

In the present experiment, the ratio $N(Z,A)/N_{proj}$, which corresponds to the

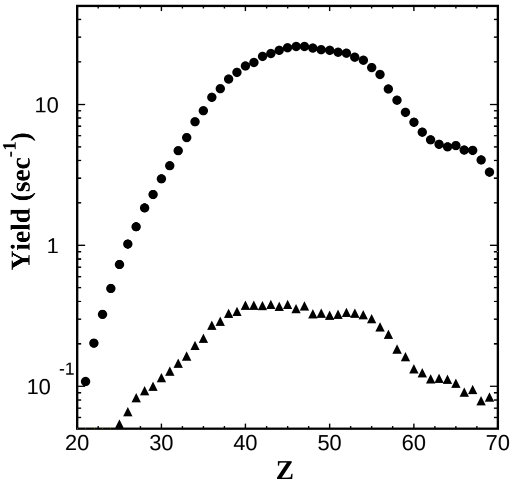

Figure 4.2: *Mass integrated total yields $Y^{tot}(Z)$ (dots) and $Y^{dummy}(Z)$ (triangles).*

total yield $Y^{tot}(Z, A)$, was obtained by integrating the measured velocity spectra for each nucleus. These spectra were partly contaminated by the residue production on the Titanium windows surrounding the cryogenic target, as shown in figure 4.1. The total yields $Y^{tot}(Z, A)$, integrated over the isotopic chains, are compared in figure 4.2 with the contribution from the Titanium windows.

From these measurements, the production cross sections for the reaction induced on deuterium could be calculated according to:

$$\sigma_{prod}^{U+d}(Z, A) = \frac{1}{\chi_d} \cdot \left[Y^{tot}(Z, A) - Y^{dummy}(Z, A)\right] \cdot F \tag{4.3}$$

being χ_d the density of deuterium target nuclei integrated over the thickness and Y^{dummy} the total yield measured when the cryogenic target was replaced by the Titanium dummy target. The factor F accounts for the different corrections that had to be applied to the measured data due to the limitations of the experimental setup. This factor was calculated according to:

$$F = f_{eff} \cdot f_{sr} \cdot f_{ch} \cdot f_{ev} \tag{4.4}$$

where f_{eff} accounts for the efficiencies of the experimental setup, f_{sr} corresponds to the corrections that were necessary due to secondary reactions, f_{ch} considers the charge-states of the measured nuclei and f_{ev} corrects the contamination from evaporation reactions. Furthermore, the dead time of the data acquisition system was corrected in the velocity spectra, according to equation 3.3.

4.1.1 Correction due to efficiencies in the experimental setup

The experimental setup used to measured the reaction products had a limited efficiency due to the limited angular transmission of the separator and the intrinsic efficiency associated with the detection system.

Angular transmission

As was discussed in the previous chapter, the limited angular acceptance of the FRS is not sufficient to cover the characteristic angular emittances of the reaction products. Since the losses induced by this limitation must be properly corrected for every nucleus, we have developed an analytical method for determining the transmission of fission residues through the FRS [Per99, BeP02]. In this method, which is described in detail in appendix C, the angular transmission is assumed to depend on two different factors: the angular distribution of each nucleus and the angular acceptance of the separator α_{eff}. While the former is given by the kinematics of the reaction mechanism, the latter depends exclusively on the ion-optic and geometrical characteristics of the FRS.

One of the most important results of this method is that the angular acceptance seen by the fission residues depends on their positions at the fourth image plane $\alpha_{eff}(x_4)$. Moreover, as already discussed in the previous chapter, the kinematics of fission reactions lead to a spherical distribution of the reaction residues in the fissioning system frame, which is truncated by the limiting value of $\alpha_{eff}(x_4)$. According to this, the forward and backward angular transmissions of the fission residues can be calculated by integrating the fraction of the spherical residue distribution within the angular acceptance:

$$T_f(x_4) = \frac{\int_0^{2\pi}\int_0^{\alpha_f(x_4)} \sin\theta d\theta d\phi}{4\pi} = \frac{1-\cos\alpha_f(x_4)}{2} \tag{4.5}$$

$$T_b(x_4) = \frac{\int_0^{2\pi}\int_{\alpha_b(x_4)}^{\pi} \sin\theta d\theta d\phi}{4\pi} = \frac{1+\cos\alpha_b(x_4)}{2} \tag{4.6}$$

In these two equations, $\alpha_f(x_4)$ and $\alpha_f(x_4)$ correspond to the forward and backward angular acceptances resulting from the transformation of $\alpha_{eff}(x_4)$ from the laboratory frame into the fissioning system frame. Their cosines can be calculated as:

$$\cos\alpha_{f,b}(x_4) = \frac{b \pm \sqrt{b^2 - 4a(v_0^2 - v_{fiss}^2)}}{2a\alpha_{eff}\gamma v_{fiss}} - \frac{v_0}{v_{fiss}} \tag{4.7}$$

where v_{fiss} is the velocity of the fission residue in the frame of the fissioning nucleus and v_0 is the velocity of this system in the laboratory frame. The coefficients a, b and α_{eff} are given in appendix C. Figure 4.3 shows the result of these corrections for the forward, backward and total angular transmissions as a function of the fission velocities. This correction, is also shown in figure 4.4 for three selected elements.

Finally, it is worthwhile to remember from the previous chapter's discussion that the fission velocities v_{fiss} needed to calculate the transmissions in equation 4.7 are affected by the transmission itself. Consequently, these two quantities had to be determined by the iterative algorithm described in section 3.3.

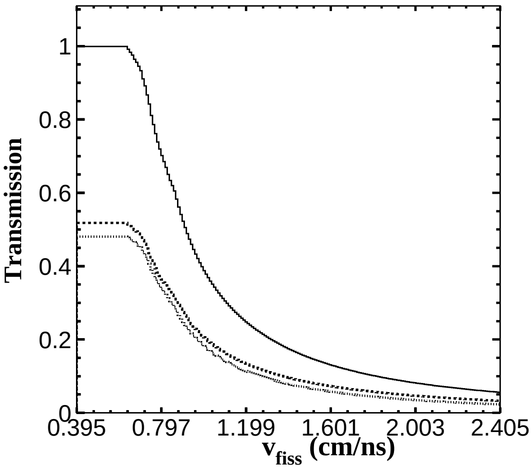

Figure 4.3: *Angular transmission as a function of the velocity of the fissioning nuclei. The total angular transmission (solid line) results from the transmission of the forward emitted fragments (dashed line) plus the backward transmission (dotted line).*

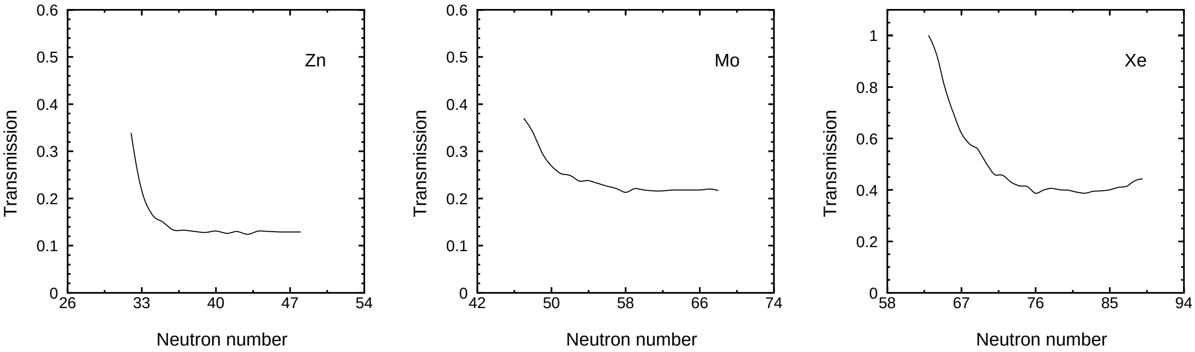

Figure 4.4: *Example of calculated angular transmission for three selected isotopic chains corresponding to $_{30}$Zn (left), $_{42}$Mo (center) and $_{54}$Xe.*

The uncertainty associated with this correction method arises from two different sources, namely the calculation of the angular acceptance $\alpha_{eff}(x_4)$ and the kinematical analysis to determine the fission velocities v_{fiss}. Whereas the former was estimated in reference [BeP02] to be approximately 3%, the latter depends on the specific uncertainties of v_{fiss}. The final transmission correction error varies significantly from about 5 % to 30 %, for some particular cases.

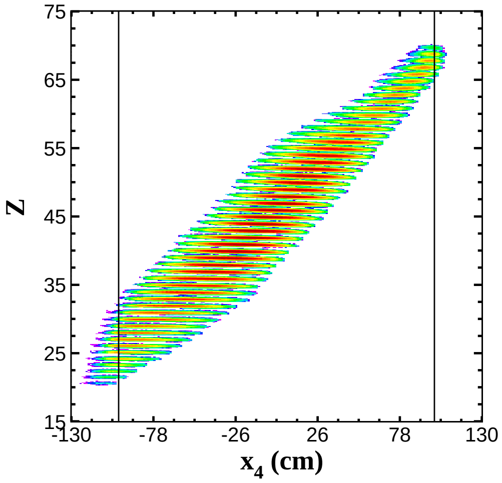

Figure 4.5: *Scatter plot showing the correlation between the charge of the measured nuclei and their transversal positions at the end of the separator. The vertical lines indicate the geometrical limits of the multiwire MW41 and MW42 of ±100 mm.*

Intrinsic detection efficiencies

The intrinsic detection efficiency is defined by the fraction of transmitted residual nuclei which were not recorded by the detection system. The detection efficiencies of the two scintillators and MUSIC detector were estimated in previous experiments to be greater than 99% (e.g. references [Enq02, Enq99, BeA01]). However, the specific characteristics of the multiwire chambers leads to slightly smaller values. As was explained in section 2.1.5, the rather constant value of the sum of the left and right time signals $x_L + x_R$ was used to discriminate good events from multi-hit events. However, it has been observed that some events produced by the passage of a nucleus at the border of the detectors can leave signals $x_L + x_R$ which may lay out of the window of accepted constant values. The rejection of these good events leads to a reduction of the detection efficiency at the borders of the chambers.

As shown in figure 4.5, the ion-optical properties of the FRS introduce a correlation between the charge of the transmitted nuclei and their transversal position at the end of the separator [Gei92]. Thus, according to the last chapter's discussion, some of the heavier and lighter elements passing near the right and left sides of the multiwires were not measured by these detectors. In order to estimate the fraction of lost events, we have compared the charge signals collected from the MUSIC, for which an efficiency of 100% was assumed, with the events detected by the two multiwire chambers.

Figure 4.6 shows the detection efficiency of the multiwire detectors as a function of the charge of the measured elements. Withing the range of elements between 34 and 62, the fraction of detected events was about 98%. For lighter and heavier ele-

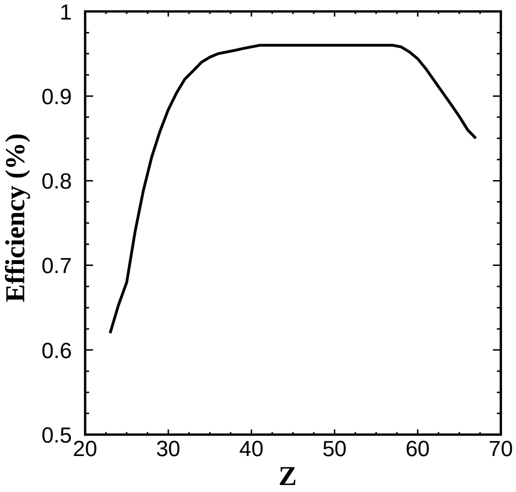

Figure 4.6: *Detection efficiency as a function of the charge of the measured residues.*

ments this value systematically drops down to values as low as 55% for Vanadium. This correction had no associated errors because it was deduced from a direct counting of the lost events.

4.1.2 Correction due to secondary reactions

Apart from the primary reactions in the production target, the beam particles and the reaction products can undergo further reactions in the different layers of matter placed along the FRS.

Reactions in the layers of matter in the target area

Together with the cryogenic deuterium target, there are other layers of matter placed at $S0$ that contribute to the residue production. The list of possible "parasitic" targets includes the accelerator window, the aluminum SEETRAM foils, the Titanium windows surrounding the cryogenic target and a niobium stripper foil, behind the target.

As was explained above, the contamination produced in the Titanium target windows was determined by measuring Y_{dummy} (see figure 4.2). Apart from this, the contamination from the other layers of matter was estimated by multiplying the production cross sections, calculated with the ABRABLA code [Gai91], by the number of impinging beam particles and the number of target nuclei of the corresponding layer. Most of the residues produced in the aluminum SEETRAM foils and the accelerator window were not transmitted through the FRS due to their distance with respect to the entrance of the separator. This effect, together with the very small thicknesses of these "parasitic" targets led to contributions to the total measured productions of about 5 %.

Multiple reactions in the target

The residual nuclei produced in the reaction ^{238}U(1 A·GeV)+d may undergo a secondary reaction before leaving the rather thick production target. These secondary products can also induce a ternary reaction resulting in a multi-step reaction chain. Since the present experiment focuses on the analysis of primary productions, the deuterium target thickness χ was optimized to minimize its multiple reaction rates, whose average contribution of about 5% is within the total experimental uncertainty. However, the multiple reaction contaminants do not spread uniformly over the total residue production but concentrates in some specific regions close to the evaporation corridor. In the case of fission residues, this contamination mainly affects the neutron-deficient isotopes, gradually increasing as the neutron number decreases. Consequently, the measured productions had to be corrected in order to extract their primary fission productions.

In the present analysis, we used the correction method proposed by P. Napolitani et al. [Nap03]. According to these authors, the measured production rates (referred to as apparent cross sections $\tilde{\sigma}$) could be formulated through a system of master equations that included the losses of residues due to their interaction in the target and the gains due to the contamination from intermediate multiple reactions:

$$\tilde{X} = G \cdot X - L \cdot X \qquad (4.8)$$

In this system of equations, G and L are matrices describing the gain and loss terms, and $\tilde{X}$ and X, are vectors with the measured apparent $\tilde{\sigma}$ and unknown primary σ cross sections, respectively. The latter were disentangled from the multiple contribution by solving the system of equations 4.8 inversely. A detailed discussion of this model and the underlying approximations used to solve the set of master equations can be found in reference [Nap03]. Here, we will limit ourselves to listing the fundamental ideas and findings of their results:

- The ternary and higher order contributions were lower than the uncertainties of the data due to the experimental procedure. Consequently, the calculation was limited to primary and secondary productions.
- Due to the very low fissility of the fission residues, the probability to undergo two consecutive fission reactions is negligible. Thus, the combinations of the two consecutive processes included in the calculation were: evaporation followed by evaporation, fission followed by evaporation and evaporation followed by fission.
- Due to the large emittances of the fission residues, angular transmissions must be included in the calculations.

Following the Napolitani's notation, the primary production cross sections of a given nucleus (Z, A) from the primary beam (Z_0, A_0) can be calculated by:

$$\begin{aligned} \sigma^{evap}_{(Z_0A_0\to ZA)} &= \tilde{\sigma}^{evap}_{(Z_0A_0\to ZA)} e^{\frac{\chi}{2}\left(\sigma^{tot}_{Z_0A_0}+\sigma^{tot}_{ZA}\right)} \\ -\frac{\chi}{2} &\sum_{A_i\geq A, Z_i\geq Z} \left[\sigma^{evap}_{(Z_0A_0\to Z_iA_i)} \cdot \sigma^{evap}_{(Z_iA_i\to ZA)} T^{evap,evap}(Z_iA_i, ZA) e^{\frac{\chi}{6}\left(\sigma^{tot}_{Z_0A_0}-2\sigma^{tot}_{Z_iA_i}+\sigma^{tot}_{ZA}\right)}\right] \end{aligned} \tag{4.9}$$

for evaporation residues, and:

$$\begin{aligned} \sigma^{fiss}_{(Z_0A_0\to ZA)} &= \tilde{\sigma}^{fiss}_{(Z_0A_0\to ZA)} e^{\frac{\chi}{2}\left(\sigma^{tot}_{Z_0A_0}+\sigma^{tot}_{ZA}\right)} \\ -\frac{\chi}{2} &\sum_{A_i\geq A, Z_i\geq Z} \left[\sigma^{fiss}_{(Z_0A_0\to Z_iA_i)} \cdot \sigma^{evap}_{(Z_iA_i\to ZA)} T^{fiss,evap}(Z_iA_i, ZA) e^{\frac{\chi}{6}\left(\sigma^{tot}_{Z_0A_0}-2\sigma^{tot}_{Z_iA_i}+\sigma^{tot}_{ZA}\right)}\right] \\ -\frac{\chi}{2} &\sum_{A_i\geq A, Z_i\geq Z} \left[\sigma^{evap}_{(Z_0A_0\to Z_iA_i)} \cdot \sigma^{fiss}_{(Z_iA_i\to ZA)} T^{evap,fiss}(Z_iA_i, ZA) e^{\frac{\chi}{6}\left(\sigma^{tot}_{Z_0A_0}-2\sigma^{tot}_{Z_iA_i}+\sigma^{tot}_{ZA}\right)}\right] \end{aligned} \tag{4.10}$$

for fission. In these two equations $\sigma^{tot}(Z, A)$ refers to the total reaction cross sections of a nucleus (Z, A) with the deuterium target, which were calculated numerically according to the model of Karol [Kar75]; while $\sigma^{evap,fiss}_{(Z_0A_0\to ZA)}$ are the evaporation and fission production cross sections of a nucleus (Z, A) from (Z_0, A_0). The terms T represents the transmission coefficients of the nuclei participating in the two consecutive reaction processes (evaporation followed by evaporation $T^{evap,evap}$, fission followed by evaporation $T^{evap,fiss}$ and evaporation followed by fission $T^{fiss,evap}$).

These two equations were solved numerically for decreasing masses of the observed residues (Z, A). Following this order, the unknown primary reaction cross section $\sigma^{evap,fiss}_{(Z_0A_0\to Z_iA_i)}$ that appears in the system had already been calculated in the previous step of the interaction. The intermediate cross sections $\sigma^{evap,fiss}_{(Z_iA_i\to ZA)}$ were calculated numerically by means of a Monte Carlo code based on the two-step model. In these calculations the BURST routine [Enq01] used to describe the nucleus-nucleus interaction of projectiles and targets, was coupled to an statistical decay code, which includes a dynamical competition between fission and evaporation, and a further multifragmentation decay process [Gai91, Jun98]. This code will be described in the next chapter.

The solution of the above mentioned system of equations provides the correction factors $f_{mr}(Z, A)$ that enable the determination of the primary production cross sections from the measured apparent values:

$$f_{mr}(Z, A) = \frac{\sigma_{Z_0A_0\to ZA}}{\tilde{\sigma}_{Z_0A_0\to ZA}} \tag{4.11}$$

These factors are depicted in figure 4.7 for some fission elements analyzed in this work. Within each isotopic chain, we observe a rather flat correction of about

5% to 7% which corresponds to the losses included in the first exponential term of equations 4.10 and 4.11. This trend, is drastically truncated when approaching the neutron-deficient side, wherein the corrections reach values close to 100 %.

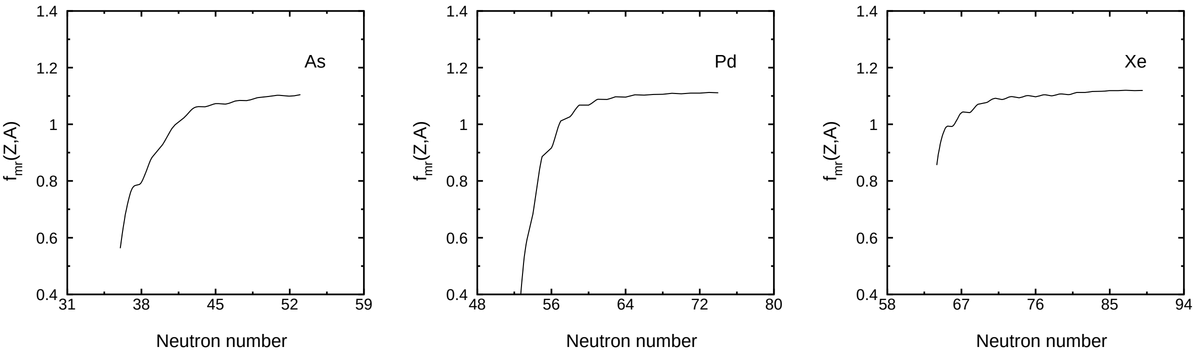

Figure 4.7: *Correction factor* $f_{mr}(Z,A)$*, calculated for some selected fission isotopes produced in the reaction* ^{238}U*(1 A·GeV) on deuterium:* $_{33}As$ *(left),* $_{46}Pd$ *(center) and* $_{54}Xe$ *(right).*

The uncertainty associated with this correction method arises from the uncertainties of the calculated values of $\sigma^{evap,fiss}_{(Z_iA_i \to ZA)}$, which were assumed to be about 30%. This error is propagated into the final results, depending on the values of the correction factors $f_{mr}(Z,A)$. Because of the accuracy requirements imposed for the present experiment, we have decided to omit those isotopes with correction factors larger than 50%. This criterion limits the experimental accessibility of the neutron-deficient fission residues.

Secondary reactions of nuclear residues at the intermediate plane

The forward-emitted residues, produced in the deuterium target, may undergo a secondary nuclear reaction in the plastic scintillator $SC2$ situated at $S2$. Since the secondary fragments have a different A/Z-ratio, they are rejected by the second magnetic selection of the separator, leading to an underestimation of the measured yield which must be corrected. The correction factor $f_{SC2}(Z,A)$ was determined for each nucleus as the inverse of its survival probability $P_{SC2}(Z,A)$ at $SC2$:

$$P_{SC2}(Z,A) = e^{-\sigma_{TOT}(Z,A)\cdot\chi_{SC2}} \tag{4.12}$$

Herein, $\sigma_{TOT}(Z,A)$ is the total reaction cross section of the nucleus in the plastic material, calculated according to the microscopic model of Karol [Kar75], and χ_{SC2} is the density of atoms of the plastic material per unit of area. This last quantity depends on the weight fraction of each chemical component of the plastic material (see appendix D). The correction factor $f_{SC2}(Z,A)$, averaged over each isotopic chain, is shown in figure 4.8 as a function of the atomic number. As can be seen, it reaches rather low values ranging from ∼10%, for the lightest elements to almost 20% for the heaviest.

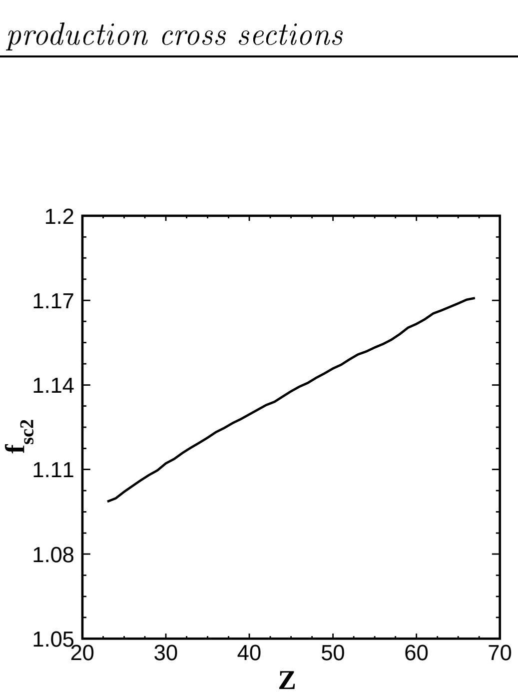

Figure 4.8: *Correction factor f_{SC2} due to secondary reactions in the plastic scintillator at $S2$.*

The uncertainties associated with the corrections obtained by this method were determined in reference [Cas01] by comparing the number of nuclei transmitted along the FRS with and without an intermediate aluminum degrader at S2 with the predictions of our calculations. The number of lost nuclei given by the code differs from the measured value by less than 10%. From this difference a maximum uncertainty of 10% was assumed for this correction.

4.1.3 Ionic charge states of the residual nuclei

The measured reaction products may carry some electrons at the target exit depending on the charge-state distribution of the incoming projectile [1], its energy and other specific characteristics of the target material. After the reaction takes place, the residual nuclei can also pick-up or strip-off some electrons due to the atomic interactions with the different layers of matte, leading to a change of the atomic charge. The variation of the A/Q value of the transmitted nuclei makes it difficult to identify them using the FRS. For this reason, we have limited our analysis to ions with no electrons (bare ions). In order to maximize the fraction of bare ions, a Niobium stripper foil was placed behind the target. Its 60 mg/cm^2 thickness was found as a compromise between a maximum number of elements reaching charge-state equilibrium [Sig91] and a secondary nuclear reactions rate below 2 %. Figure 4.9 shows the equilibrium charge-state distributions of the reaction residues after traversing this Niobium foil, for the bare P_0, hydrogen-like P_1 and helium-like

---

[1] The 73+ charge-state of the Uranium beam, defined at the exit of the SIS might be modified before impinging on the target due to the atomic interactions with the Titanium windows of the accelerator and the aluminum foils of the SEETRAM monitor.

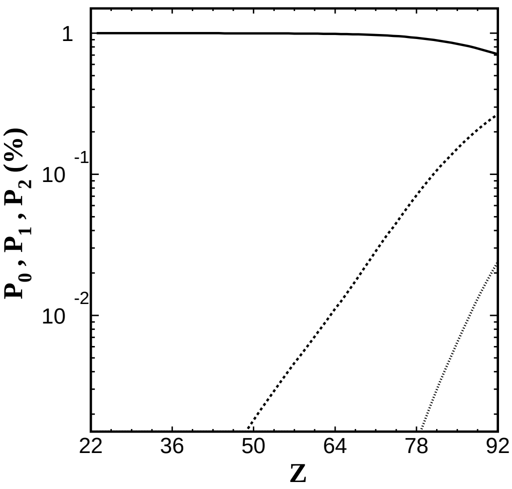

Figure 4.9: *Fraction of charge-state configurations behind the 60 mg/cm^2 niobium stripper foil as a function of the charge of the reaction product. The calculation included the most populated configurations, namely bare ions (solid line), hydrogen-like ions (dotted line), and helium-like ions (dashed line).*

P_2 ions.

The equilibrium charge-state distribution behind the stripper foil is altered from the first stage of the FRS to the second one due to the interaction with the plastic scintillator $SC2$ at S2. The strong correlation between the positions of the ions at the exit of the FRS and their ionic charge-state makes it possible to discriminate the charge-state changing from the first to the second stage of the FRS. Figure 4.10 shows the energy loss signal measured in the first MUSIC versus the positions measured by the plastic scintillator $SC4$. The three different groups of diagonal bands shown in the figure correspond to nuclei with different charge-state configurations at both stages of the FRS.

In order to obtain an unambiguous isotopic identification of the reaction products, we have restricted the analysis to ions with the same charge-state in both stages of the FRS. Apart from bare ions, this includes the contamination from hydrogen-like and helium-like ions; although the extremely low probability of the latter (less than 1%) for the range of charges covered by this analysis, did not affect appreciably the final result. According to this, the losses in the number of measured nuclei due to the fraction of incompletely stripped ions had to be corrected. The correction factor for a given nucleus is the inverse of its probability of being fully stripped along the FRS, i.e. the product of the fractions of bare ions behind the niobium stripper foil (first stage) and behind the scintillator $SC2$ (second stage), respectively. These fractions were calculated with the GLOBAL code [Sch98, Glo99] which has been extensively used in numerous applications [Sch98]. As many as 28 charge states were included in the calculation, along with a refined description of the electron

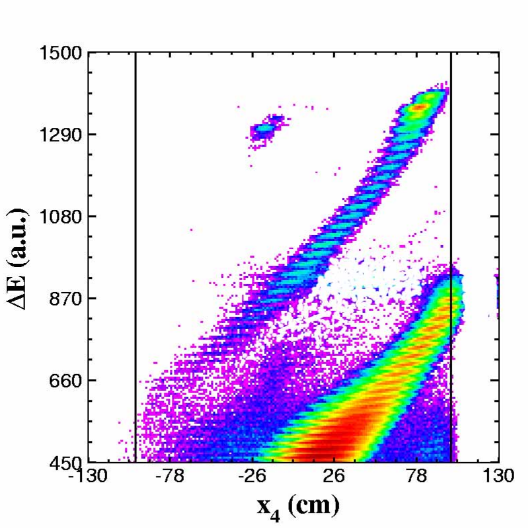

Figure 4.10: *Correlation between the energy loss measured with MUSIC 1 and the positions at the end of the FRS. The three diagonal band correspond to different combinations of charge states along the FRS (see text for details). The vertical lines indicate the geometrical limits of the multiwire detectors.*

capture and ionization cross sections for the different atomic shells and subshells. Other improvements, such as screening effects or projectile energy losses with penetration depth were included as well. The results of the calculations are depicted in figure 4.11. The correction factor to be applied to the measured yields is shown for the different elements. While always remaining below ∼10%, this correction is observed to increase with the charge of the measured nuclei.

The charge state probabilities calculated with the GLOBAL code could be compared with direct measurements for some particular cases, as described in reference [Cas01]. According to that work, the agreement between the experimental and calculated charge state ratios yields a total uncertainty correction of 5%.

4.1.4 Contamination due to the evaporation residues

Since the aim of the present work is the determination of the production cross sections of fission residues, we had to disentangle the evaporation reactions contribution to the measured residue productions. By comparing the velocity distributions of all the residues produced in the cryogenic deuterium target and the Titanium dummy target (see figure 3.10 left and right, respectively) we have demonstrated that the evaporation residues measured in the former system were mainly produced in the Titanium windows. However, after subtracting these contaminants, we still observe a small evaporation component in the reaction ^{238}U(1 A·GeV)+d for heavy neutron-deficient isotopes. In a former analysis of evaporation residues produced in this reaction [Cas01], it was found that these nuclei populate the evaporation corridor

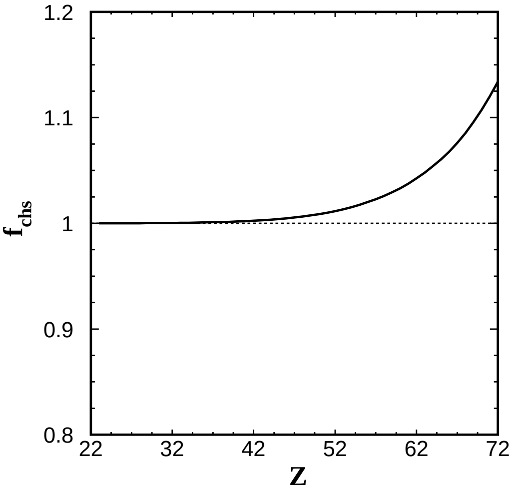

Figure 4.11: *Correction factor f_{chs} to be applied to the measured elements due to the fraction of nuclei which were not fully stripped. The dashed line shows the limit where no correction was needed.*

situated on the neutron-deficient side of the chart of the nuclides, from Uranium isotopes down to elements with atomic numbers of about 70. Below this value, the evaporation component drops quickly, though it can still contribute to the production of the most neutron-deficient isotopes. At the same time, the fission production increases very quickly in the neutron-rich side. According to this, we can expect both reaction mechanisms to coexist in the region of light evaporation residues, around $_{65}$Tb, with a transition from evaporation to fission as the neutron number increases.

Unfortunately, the separation method described in chapter 3, based on the different kinematics of each mechanism cannot be applied when the fission residues are fully transmitted through the FRS. This is the case for the neutron-deficient isotopes of heavy fission elements, ranging from Yb to Rh, which is precisely the region where the evaporation component is still present. In figure 4.12 we illustrate this problem by showing the velocity spectra of three different isotopes of $_{55}$Cs. Within the isotopic chain of this element, the lightest and heaviest isotopes are only produced by evaporation and fission, respectively, while an intermediate situation is found for ^{125}Cs, wherein a very weak evaporation component is strongly mixed with the dominant fission mechanism.

The evaporation contamination to the measured fission residues was estimated using a phenomenological model based on the two-step formalism [Ser47]. The routine BURST [Enq01] was chosen to reproduce the fast interaction between the projectile and target. The evaporation stage was simulated with the statistical deexcitation code ABLA [Gai91, Jun98] and the fission mass-distribution routine PROFI [Ben98]. The next chapter will be dedicated to a detailed survey of the underlying physical concepts contained in these codes. It is sufficient to mention

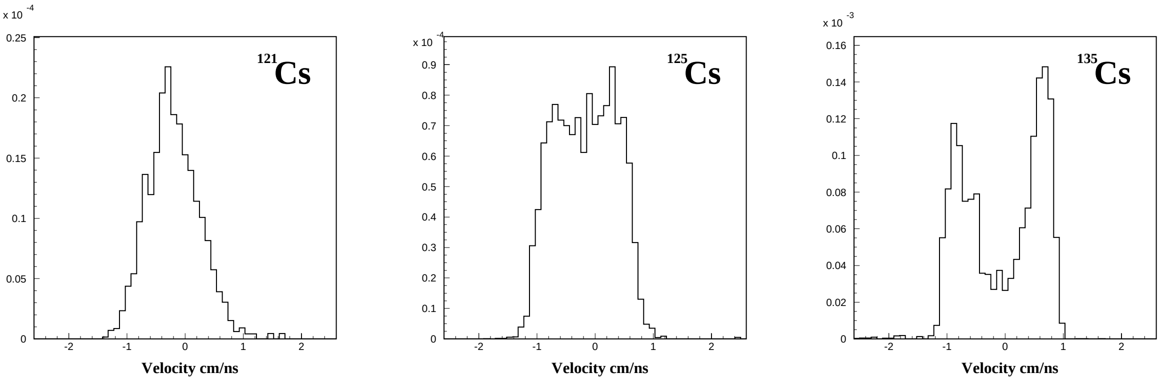

Figure 4.12: *Measured velocity spectra of three Cesium isotopes measured in the reaction* $^{238}U(1\ A{\cdot}GeV)+d$.

here that the reliability of these calculations in estimating evaporation productions in the region of neutron-deficient heavy nuclei was verified by comparing them with the evaporation cross sections measured for some nuclei. Our estimations agreed with the experimental results within an error of 50 %, which was sufficient for the precision requirements of the present analysis. According to this, the fission cross sections were determined by subtracting the evaporation contamination from the measured production cross sections. In order to avoid ambiguity in the analysis, those nuclei with evaporation contributions greater than 50% were not included in the final results.

4.2 Results and discussion

All the fission residues measured in the present work are represented at the top of the chart of the nuclides in figure 4.13. They cover a region on the neutron-rich side of the valley of stability, with elements ranging from Vanadium to Dysprosium. The most populated region corresponds to elements between Niobium and Cadmium with decreasing intensities for lower and higher atomic numbers. For most of these elements, the maximum productions span an extended flat ridge with 2-3 mass units on the right side of the valley of stability. Above the doubly closed shell Z=50 N=82, an enhanced fission residue production is observed on the neutron-rich side. Beyond Z=55, the residues move again toward the valley of stability until they cross it at around Z=58. For higher charges, fission fragments populate the neutron-deficient side of the valley of stability.

Figures 4.14-4.17 provide a more detailed survey of the fission residue production, showing the isotopic production cross sections for all measured fission residues. The measured cross sections range from about 30 mb for intermediate charges, down to values as low as 0.01 mb on the neutron-rich side. This sensitivity was not attained in the neutron-deficient side due to the corrections introduced to account for the contamination of secondary reactions in the target. Moreover, the high contami-

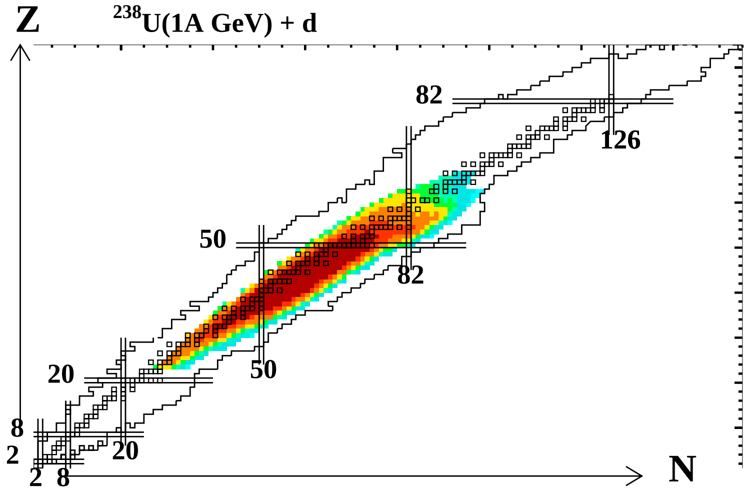

Figure 4.13: *Fission residues in the reaction ^{238}U + d at 1 A·GeV on top of the chart of the nuclides. The grey scale indicates different production cross sections.*

nation due to evaporation for elements above $_{60}Nd$ restricted the measurements of fission isotopes to those with rather high neutron numbers.

As a general trend, the isotopic chains of the fission residues follow a wide Gaussian distribution with mean neutron numbers slightly shifted toward the neutron-rich side of the valley of stability. The maximum productions cover an extended region of elements around $_{46}$Pd, which corresponds to symmetric fission. For some elements above Z=50, these Gaussian shapes display a pronounced shoulder in the neutron-rich side. This results from the low-energy asymmetric fission modes which favor the production of fission residues around N=82 (Standard I) and N=88-90 (Standard II) for some particular elements, as discussed in section 3.4. This polarization of the heavy asymmetric fission fragments toward the neutron-rich side, due to shell effects, causes the lighter asymmetric partners to move toward the valley of stability, leading to a less pronounced shoulder near the maximum of the isotopic chains, as shown for elements between $_{33}$As and $_{42}$Mo. This low-energy fission mode is not observed for elements above $_{59}$Pr and below $_{30}$Zn, demonstrating that they were mainly produced by high-energy fission processes.

4.2.1 Main features of the fission residues produced in the reaction ^{238}U at 1 A·GeV on deuterium

In this section we discuss and evaluate the general trends of the measured data on the basis of underlying features of the decaying projectile pre-fragments produced in the present reaction.

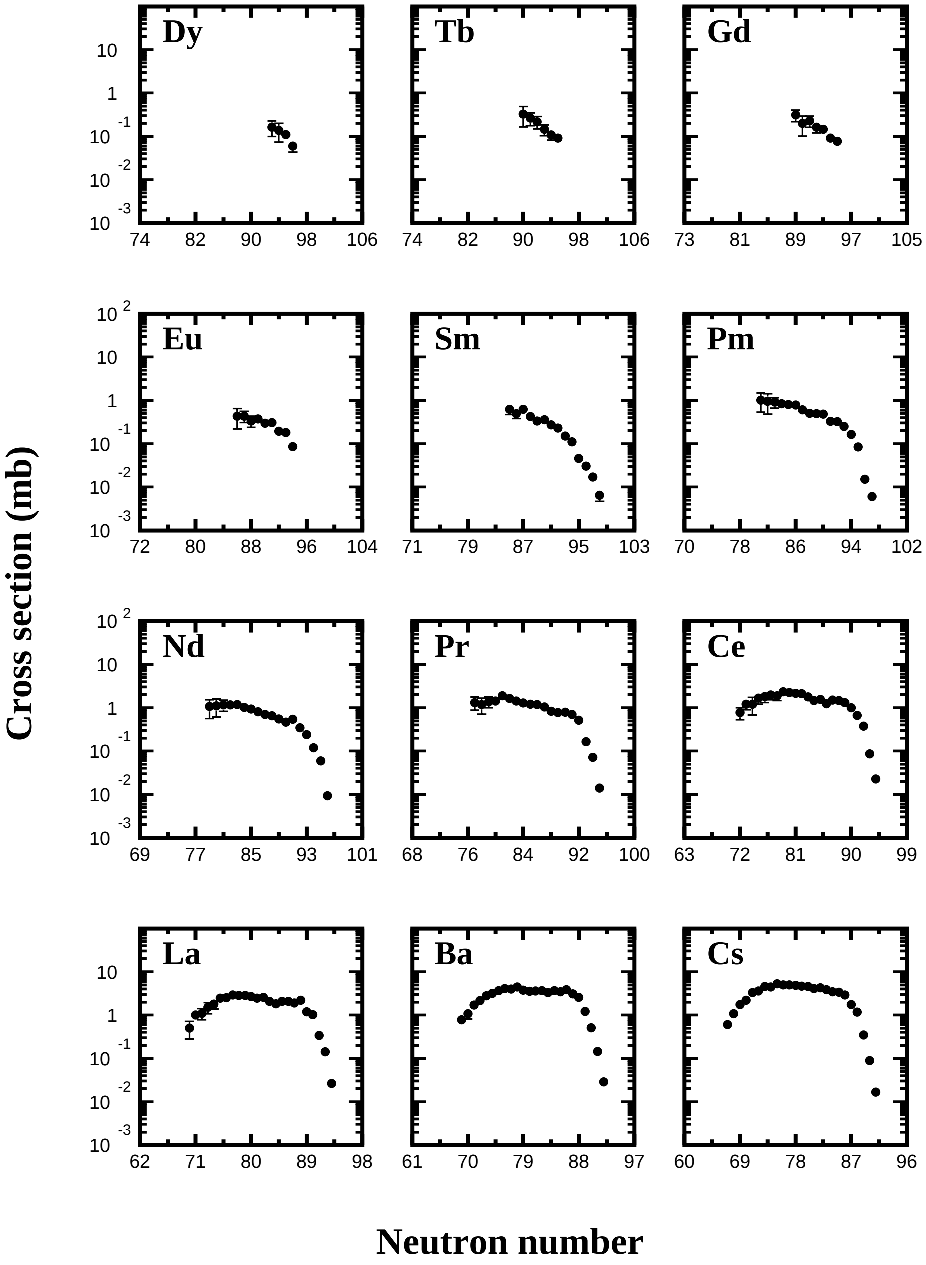

Figure 4.14: *Measured isotopic production cross sections of fission residues produced in the reaction* $^{238}U(1\ A{\cdot}GeV)+d$. *Error bars are shown if bigger than symbols.*

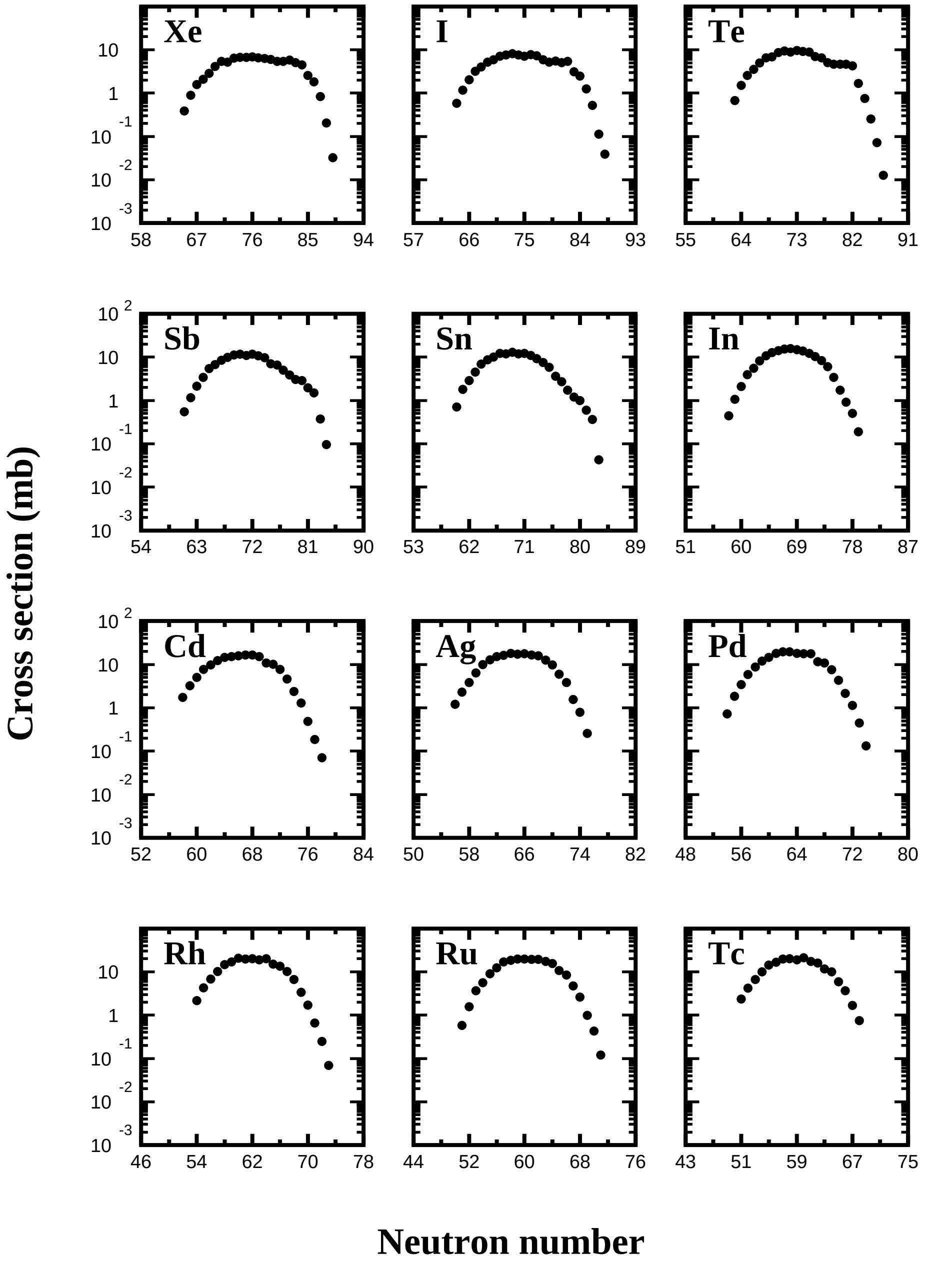

Figure 4.15: *Measured isotopic production cross sections of fission residues produced in the reaction* ^{238}*U(1 A·GeV)+d. Error bars are shown if bigger than symbols.*

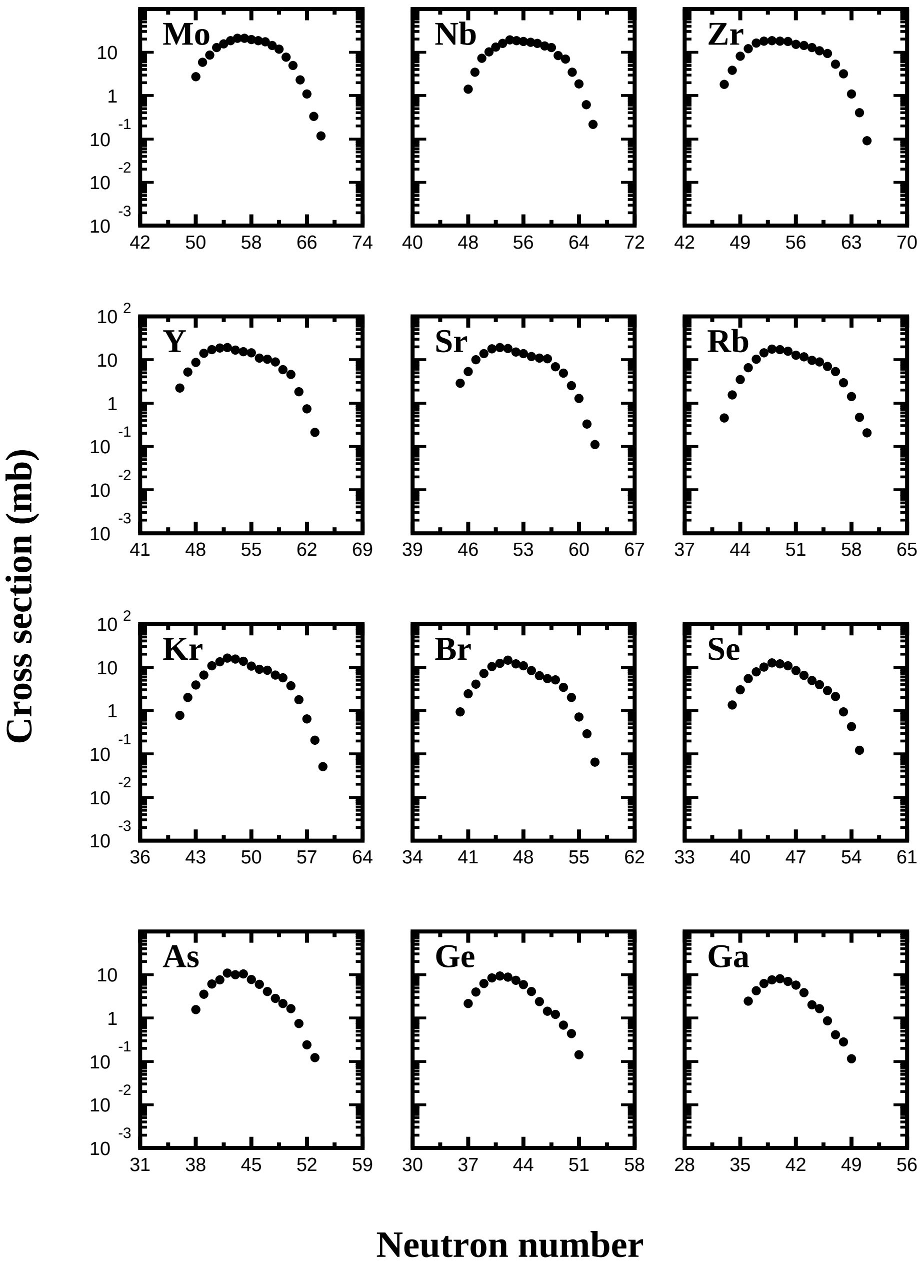

Figure 4.16: *Measured isotopic production cross sections of fission residues produced in the reaction* ^{238}*U(1 A·GeV)+d. Error bars are shown if bigger than symbols.*

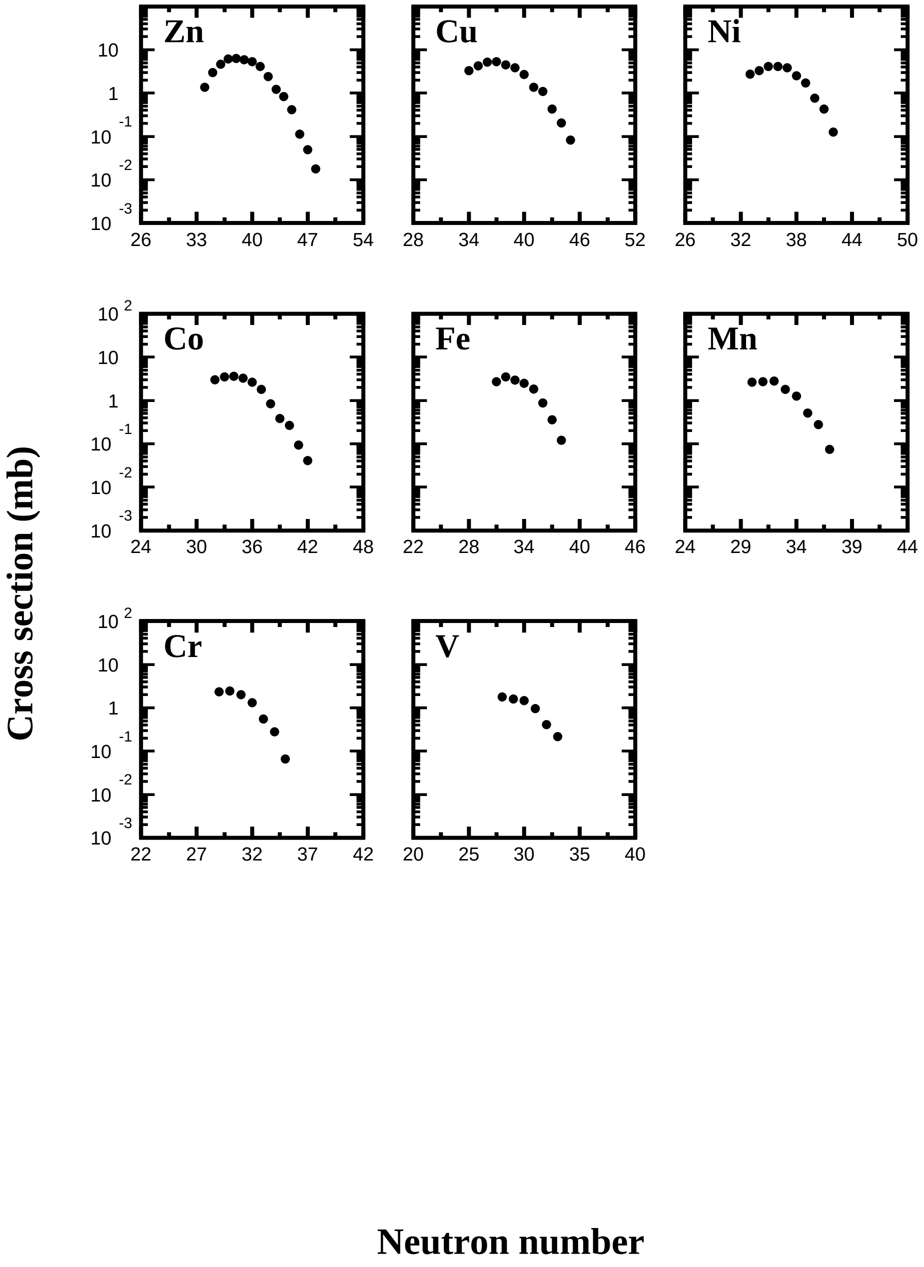

Figure 4.17: *Measured isotopic production cross sections of fission residues produced in the reaction* ^{238}*U(1 A·GeV)+d. Error bars are shown if bigger than symbols.*

Isobaric distribution of fission and evaporation residues

As a first attempt to characterize the reaction ^{238}U(1 A·GeV)+d we determined the isobaric distribution of the residual nuclei by summing up the production cross

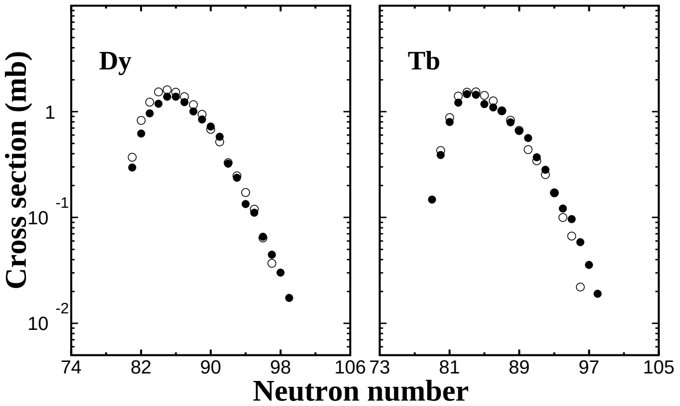

Figure 4.18: *Production cross sections of* $_{66}$*Dy (left) and* $_{65}$*Tb. The data measured in this work (dots) agree within 10% with the results obtained by E. Casarejos [Cas01] (empty dots).*

sections of all the residues (including both fission and evaporation) over each of the isobaric chains. A complete survey of the residue productions was only possible by combining the data measured in the present work with those obtained by E. Casarejos for elements above $_{65}$Tb [Cas01]. Although these two independent analysis cover different regions of the chart of nuclides, there was an overlapping region for elements between $_{65}$Tb and $_{66}$Dy which could be used to cross check the influence of possible systematic errors (see figure 4.18). The agreement between both works validates the analysis method described in the previous section.

Figure 4.19 depicts the isobaric distribution of residues produced in the reaction ^{238}U(1 A·GeV)+d as a function of the mass loss (dots). The figure also includes the isobaric distributions measured for the reaction induced with Uranium at 1 A·GeV on proton [Ber03, Tai03] (empty dots) and for the system ^{208}Pb(1 A·GeV) on deuterium [Enq02] (empty diamonds).

As far as the Lead system is concerned, the evaporation mechanism is responsible for the production of heavy residues, especially those near the projectile (corresponding to the lowest values of ΔA), and the gradual reduction of lighter fragments. Within this region, the mass of the evaporation residues reflects the initial excitation energy of the pre-fragments: high excitation energies yield longer evaporation chains and lighter evaporation residues. Consequently, the maximum available excitation energies determines the limit for the lightest masses produced by this process. Above a mass loss of 90 units the isobaric distribution increases again due to the fission mechanism, though the maximum production cross sections are far below those corresponding to evaporation. This trend is very different from that observed in the spallation of Uranium where fission turns out to be the dominant process. The production of evaporation residues in this system, specially the heaviest ones is notably lower than in the Lead case. This depopulation of the evaporation residues

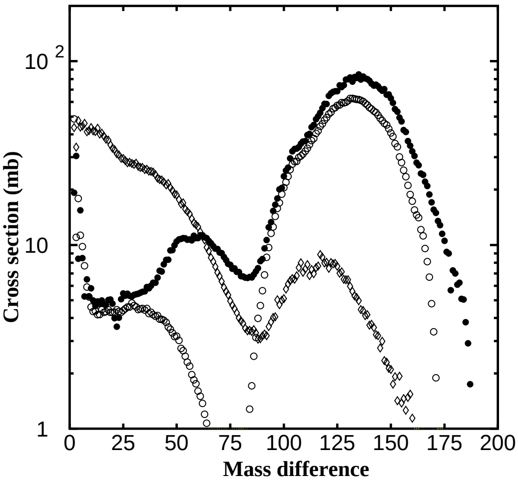

Figure 4.19: *Isobaric distribution of residual nuclei, including fission and evaporation, produced in the reactions:* ^{238}*U(1 A·GeV)+d (dots),* ^{238}*U(1 A·GeV)+p (empty dots) and* ^{208}*Pb(1 A·GeV)+d (empty diamonds)*

is explained by the higher fissilities of the actinides with respect to the rare-earths involved in the spallation of Lead. The evaporation residue productions would consequently be strongly influenced by the fission mechanism in the case of Uranium. The depletion of actinides due to fission also results in a pronounced increase of medium-mass fission fragments productions.

Comparison of the isobaric distributions of the two Uranium systems shows very similar trends, up to a mass loss about 40 units, in the region of evaporation residues. Beyond this value, the reaction induced on deuterium shows an increased production of lighter residues when compared to the proton case. The explanation of such a difference lies in the larger excitation energies in the case of deuterium, favoring the influence of transient dissipation effects, as explained in chapter 1. Since the deuterium target introduces an average of twice as much energy per collision than hydrogen, the energies spectrum includes larger values. As a consequence, the deexcitation of pre-fragments produced in this reaction is very much affected by transient effects, leading to longer evaporation chains that extends the production of evaporation residues toward lighter masses. The low fissilities of the lightest evaporation fragments produced with deuterium cause a gradual reduction of the depletion effect observed for actinides. The isobaric fission distributions are equivalent for the two systems up to a mass loss of about 100 units. Above this value, the fission contribution from the pre-actinides leads to an overproduction of light fission residues for deuterium.

Isotopic production cross sections

A deeper understanding of the fission process in Uranium-induced reactions on deuterium can be achieved by comparing the isotopic chains of fission elements measured in this work with those obtained by M. Bernas et al. [Ber03] for the reaction ^{238}U(1 A·GeV)+p (see figure 4.20).

For those elements which were partially produced by low-energy fission, the smooth hump observed in the neutron-rich side indicates identical values in both reactions. Those isotopes come from the most peripheral, or equivalently less energetic, collisions: Due to the wide spatial distribution of the deuterium, many of these collisions were induced by a single nucleon, leading to results equivalent to those obtained with protons. Apart from this, the reaction induced with deuterium shows greater neutron-deficient fission residues production than with proton. According to the Z^2/A-dependence of the fission barriers, this trend reveals an increasing light-fissioning nuclei contribution in this region, which was already observed when analyzing the velocities of the fission residues (figures 3.11-3.14): As the charge of the fissioning parent nuclei decreases, so does their neutron number, so that the production of fission fragments moves toward the neutron-deficient side. This result is also confirmed by the greater abundance of light-evaporation residues observed in figure 4.19 for the reaction induced on deuterium. The large neutron-deficient fission residue productions for this system also demonstrates the importance of the fission of light pre-actinides, in spite of their decreasing low fissilities.

Other observables characterizing the distribution of final fission residues are the mean N/Z-ratio and the widths of the isotopic distributions of fission residues. Figure 4.21 shows the results obtained in the present work, together with those analyzed by M. Bernas for the reaction induced with protons at 1 A·GeV.

The lower average values of $\bar{N}/Z$ and the broader widths of the isotopic chains σ_N observed for the deuterium system with respect to protons are the direct result of the lighter fissioning systems that contribute to the productions of these residues.

The larger excitation energies of the fissioning nuclei produced with deuterium also help to broaden the fission residue distributions [Arm70]. Apart from this, the large values of $\bar{N}/Z$ and σ_N found around $_{55}$Cs are partly due to the polarization induced by shell effects in the low-energy fission modes.

Total fission cross section

The total fission cross section, obtained by summing up all the individual isotopic production cross sections was found to be 1.97±0.21 barn. In order to account for the isotopes which were not measured, we extrapolated the isotopic chains shown in figures 4.14-4.17. The contribution from these lost residues to the total fission was 35 ±10 mb, resulting in a value of 2.00±0.22 barn. At the present moment, fission data of Uranium on deuterium are scarcely represented in the current available databases. After a systematic literature search on the EXFOR [Exf] database, the only measurements found corresponded to deuteron induced fission of Uranium at energies below 200 MeV [Ste58]. A comparison of these data with our results was pos-

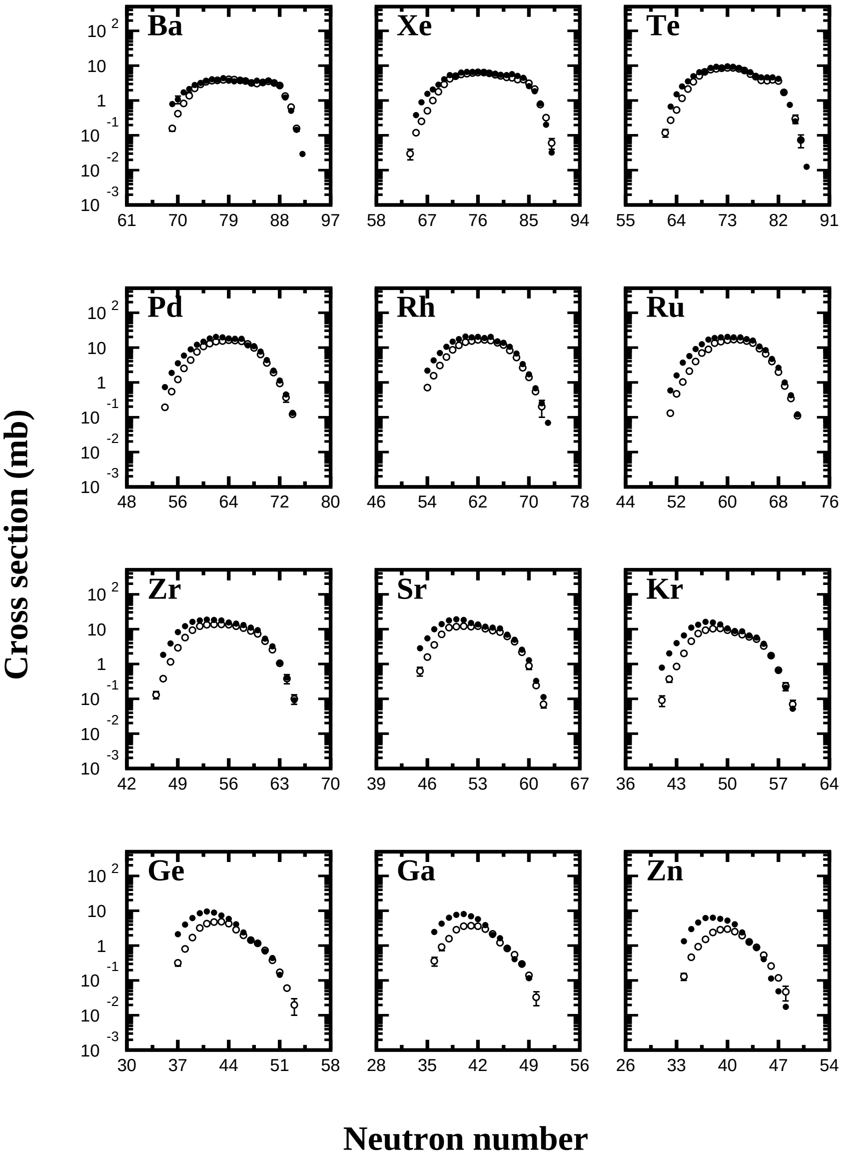

Figure 4.20: *Isotopic production cross sections of fission residues measured in the present work for the reaction* ^{238}*U(1 A·GeV)+d (full dots) and* ^{238}*U(1 A·GeV)+p [Ber03] (empty dots).*

sible by extrapolating the former according to the systematics of Prokofiev [Pro01] for proton induced fission reactions. In doing so, we had to consider the two main differences between proton and deuteron reactions at these energies, namely the average double energy introduced by deuterons, due to their additional nucleon, and the higher total reaction cross section with respect to protons. Thus, the total fission cross section measured by Stevenson et al. [Ste58] at 190 MeV for deuteron-

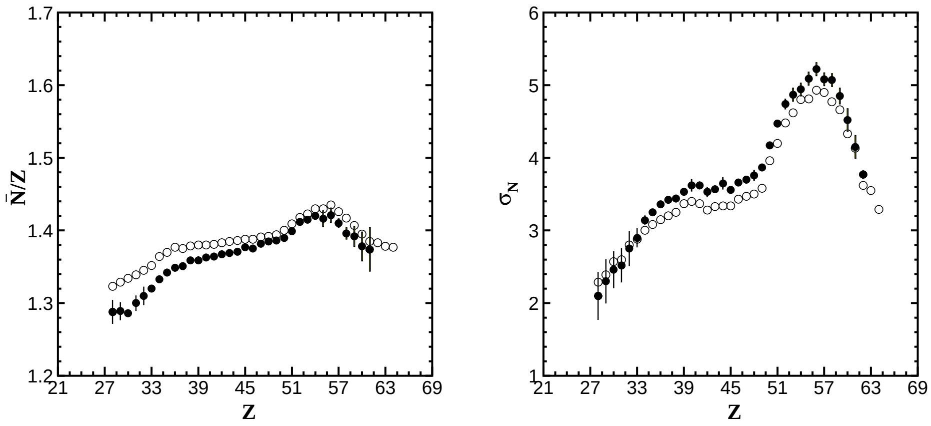

Figure 4.21: *Mean N/Z-ratio (left) and neutron widths σ_N (right) distributions of fission fragments produced by Uranium on deuterium (full dots) and Uranium on proton (empty dots) [Ber03].*

induced reactions on Uranium (2.49±0.05 barn) was compared to the value given by Prokofiev at 2×190 MeV=380 MeV for protons (1.44 barn). The differences between these data was entirely attributed to the higher total reaction cross section for deuterium, leading to a scaling factor of $S = 2.49/1.44 = 1.73$. Finally, in order to extrapolate the value of Stevenson measured at 190 MeV to 1 GeV, we multiplied the cross section calculated by Prokofiev at 2 GeV (1.18 barn) by the factor S, which yields 2.04 barn. This value compares very well with our result.

The total reaction cross sections could also be determined by adding the total the total evaporation cross section of 0.70±0.13 barn, obtained by E. Casarejos [Cas01] for the reaction ^{238}U(1 A·GeV)+d to the total fission cross section measured in the present work. The resulting value of 2.70±0.35 barn, is compatible with that of 2.51 barn calculated with the Glauber-type model of P.J. Karol [Kar75].

In contrast to other existing experimental techniques, the total fission cross section obtained in the present work was not a directly measured observable, but deduced by summing up the contributions from every fission residue. As explained in section 4.1.1, the isotopic production cross sections of the fission residues shown in figures 4.14-4.17 were obtained by applying different systematic corrections to the measured yields. Some of these corrections, like the angular transmission or the secondary reactions in the target, vary considerably as a function of the atomic and mass numbers of the final nuclei, reaching very large values in some cases. Any uncertainty in the determination of these corrections will thus affect the value of the isotopic cross sections, and consequently, the value of the total cross section. The high level of agreement between the total fission cross section obtained in the present work and that deduced by extrapolation of a directly measured value [Ste58] validates the methods used to determine these corrections. Similar conclusions are found when comparing the measured total reaction cross section with the calculated

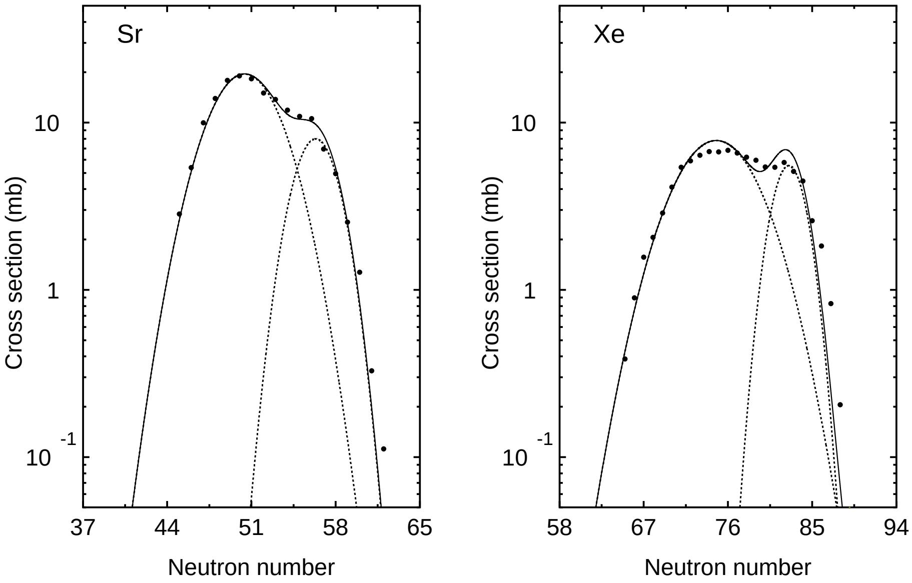

Figure 4.22: *Examples of the separation between symmetric (high-energy) and asymmetric (low-energy) fission components for two selected cases measured in the reaction* $^{238}U(1\ A{\cdot}GeV){+}d$: $_{38}Sr$ *(left),* $_{54}Xe$ *(right)*

value of J. Karol's model. However, further experiments aimed to measured the total production cross sections in this reaction are needed to confirm our results.

4.2.2 High- and low-energy fission processes

The two groups of fission residues already mentioned, from $_{50}$Sn to $_{60}$Nd and from $_{42}$Mo to $_{30}$Zn, showed a symmetric high-energy and an asymmetric low-energy fission component in the neutron-rich side. (see figures 4.14-4.17). The contribution of these two modes to the isotopic chains was obtained by fitting the data to two Gaussian functions, as shown in figure 4.22.

Post-scission neutron emission at low energies

The mean values and widths of the neutron-rich Gaussian functions were used to estimate the mean mass numbers and mass dispersions of the low-energy fission elements. The results are shown in table 4.1 together with the values obtained for asymmetric fission of ^{238}U(750 A·MeV) on lead [Don98].

The values measured in the present work differ from the so-called primary mass numbers A'_H, A'_L of the heavy and light nascent fission fragments by the number of neutrons emitted after scission. By assuming that these residues originate from the low-energy fission of Uranium isotopes, the mean total number of post-scission neutrons $\bar{\nu}_{tot}$ emitted by a given element pair can be deduced according to equation:

$$\bar{\nu}_{tot} = A_0 - \left[\bar{A}(Z_H) + \bar{A}(Z_L)\right] \tag{4.13}$$

where $\bar{A}(Z_H)$ and $\bar{A}(Z_L)$ correspond to the mean mass numbers of the heavy and light fission elements reported in table 4.1. The mean mass of the fissioning Uranium isotopes A_0 depends on the excitation energy at which fission takes place. This quantity was assumed by C. Donzaud et al. [Don98] to be equal to 237.8 and 237.2 for electromagnetic-induced fission at 12 MeV and 20 MeV, respectively. In the case of nuclear-induced reactions, the fissioning nuclei gain an average of 30 MeV per abraded nucleon. Since the structural effects that govern the low-energy fission disappear above ∼40 MeV, we have assumed $A_0 = 237$ for the present analysis. As will be seen later, the systematic error on $\bar{\nu}_{tot}$ induced by this assumption will not modify our final conclusions. Apart from this, the use of equation 4.13 implicitly neglects post-scission proton evaporation; an approximation that is justified due to the low energies available for such a process.

The results of this calculation for the different fission residue pairs are shown in figure 4.23. Despite the systematic error of $\bar{\nu}_{tot}$ induced by the assumed value A_0=237 for the mean mass of the fissioning nucleus, we observe a smooth reduction of the post-scission neutrons for the less asymmetric fission pairs ($_{50}$Sn-$_{42}$Mo, $_{51}$Sb-$_{41}$Nd,$_{52}$Te-$_{40}$Zr and $_{53}$I-$_{39}$Y). The explanation lies on the excitation energy of the two fission fragments: Using the semi-statistical scission-point model of Wilkins et al. [Wil76], the energy available for post-scission neutron emission arises from the deformation energy E_{def} of the fission fragments at the scission point and the intrinsic excitation energy E_{int}. Assuming that this latter contribution remains constant, the reduction of $\bar{\nu}_{tot}$ with the decreasing asymmetry reveals more compact scission configurations for these pairs and consequently lower deformation energy E_{def} values. By contrast, the larger $\bar{\nu}_{tot}$ values for the more asymmetric pairs corresponds to larger deformations. Within this framework, such a finding provides an interesting tool for disentangling the two asymmetric fission modes which contribute to the low-energy fission component: the compact Standard I mode, which feeds the group of elements around $_{52}$Te (and their light partners around $_{40}$Zr), and the deformed Standard II mode, producing the more asymmetric fission pairs. The neutron shells that define these two modes (Standard I, N=82 and Standard II, N=88-90) are also compatible with the primary masses A'_H, A'_L of the fission fragments deduced from the values shown in table 4.1, including the calculated post-scission neutrons. Finally, it is noteworthy that the same distribution of fission modes was deduced independently by analyzing the high velocities of the neutron-rich fission residues, as described in the previous chapter.

The mean mass numbers shown in table 4.1 for the present reaction are slightly lower than those obtained by Donzaud et al. [Don98]. This is easily explained by taking into account the intrinsic excitation energy E_{int} of the nascent fission fragments. The higher E_{int} values for low-energy nuclear-induced fission, with respect to electromagnetic-induced reactions, lead to larger post-scission neutron multiplicities.

Z	$\bar{A}$ (a)	$\bar{A}$ (b)	σ_A (a)	σ_A (b)
32	79.0±0.2		1.70±0.4	
33	82.0±0.2		1.71±0.4	
34	84.9±0.2	85.3±0.1	1.67±0.2	1.61±0.04
35	87.0±0.2	87.9±0.1	1.63±0.2	1.53±0.04
36	89.6±0.2	90.3±0.1	1.72±0.2	1.62±0.04
37	91.9±0.2	92.8±0.1	1.79±0.2	1.69±0.05
38	94.3±0.2	95.3±0.1	1.70±0.2	1.72±0.05
39	97.3±0.2	97.9±0.1	1.65±0.2	1.66±0.04
40	99.7±0.2	100.4±0.1	1.60±0.2	1.60±0.01
41	101.5±0.2	102.3±0.1	1.50±0.2	1.44±0.04
42	104.2±0.2	104.1±0.1	1.44±0.2	1.35±0.05
50	129.0±0.2	130.3±0.2	1.70±0.2	1.26±0.07
51	131.0±0.2	132.0±0.1	1.70±0.2	1.20±0.18
52	133.0±0.2	133.9±0.1	1.65±0.2	1.23±0.01
53	134.9±0.2		1.73±0.2	
54	136.5±0.2		1.70±0.2	
55	139.5±0.2		1.85±0.2	
56	142.0±0.2		1.75±0.2	
57	144.0±0.2		1.70±0.2	
58	146.4±0.2		1.70±0.2	
59	149.0±0.2		1.70±0.2	
60	150.6±0.2		1.70±0.3	

Table 4.1: Mean mass number $\bar{A}$ and mass dispersions σ_A of low-energy fission elements. The values obtained in the present work (a) are compared to those obtained in reference [Don98] for the reaction ^{238}U at 750 A·MeV on Lead (b).

Apart from this, an increase of the excitation energy E_{int} damps the shell effects and favors the liquid-drop behavior, giving rise to the high-energy symmetric fission mode. In order to characterize the residue distributions produced by this mode, figure 4.24 shows the separated contributions of the high-energy and low-energy components to the elemental distribution of $\bar{N}/Z$ and σ_N.

The values of $\bar{N}/Z$ for residues produced by the high-energy symmetric fission mode (between $_{43}$Tc and $_{49}$In) show a regular increase with the proton number that reflects a polarization effect δA of the fission fragments:

$$\delta A = \bar{A} - Z \cdot \frac{A_0}{Z_0} \tag{4.14}$$

where A_0 and Z_0 are the mass and proton numbers of the average fissioning nucleus, obtained from table 4.3. From this increase, a charge polarization of -0.04 was

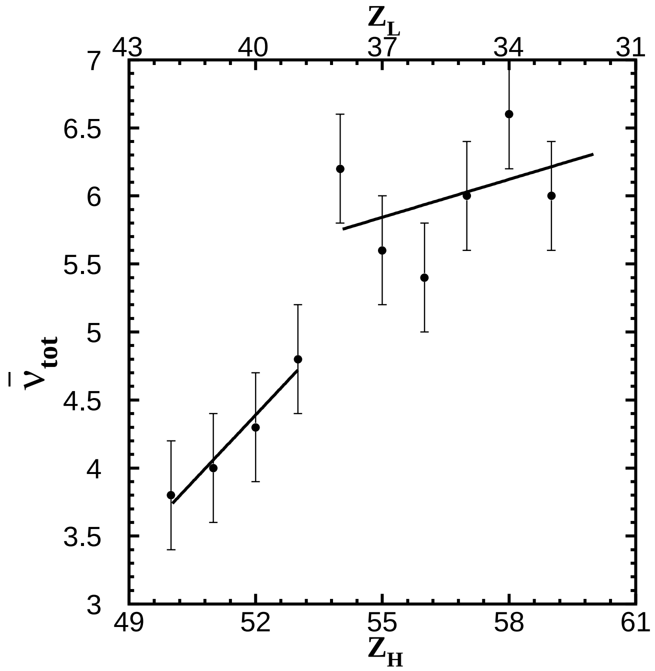

Figure 4.23: *Average total post-scission neutrons emitted from different asymmetric fission pairs. The lower and upper scales refer to the heavy and light fission partners, respectively. The two lines are fits made with fission pairs of Standard I and standard II (see text for details).*

deduced using the following equation [Ber03]:

$$P = \frac{-\delta A}{A - 0.5A_0} = -\frac{Z_0}{2} \cdot \frac{Z_0}{A_0} \cdot \frac{d(\bar{N}/Z)}{dZ} \tag{4.15}$$

This value coincides with that found by M. Bernas et al. [Ber03] for the system U+p. Such constant behavior of the charge polarization was predicted by P. Armbruster [Arm70] for the high-energy fission domain on the basis of the calculated liquid-drop energy released from saddle-to-scission configurations.

Total cross section for asymmetric and symmetric fission modes

The elemental low-energy fission component, deduced from the integrated neutron-rich Gaussian functions, was subtracted from the total elemental cross section in order to disentangle the symmetric and asymmetric fission modes. Figure 4.25 depicts the charge distribution of the symmetric (high-energy) component together with the two asymmetric (low-energy) component of fission residues. For the heavy asymmetric group, the maximum productions were found for $_{54}$Xe, coinciding with the analysis done by K.-H. Schmidt et al. [Sch01] of the mean proton number of the heavy asymmetric residues produced in low-energy electromagnetic-induced fission.

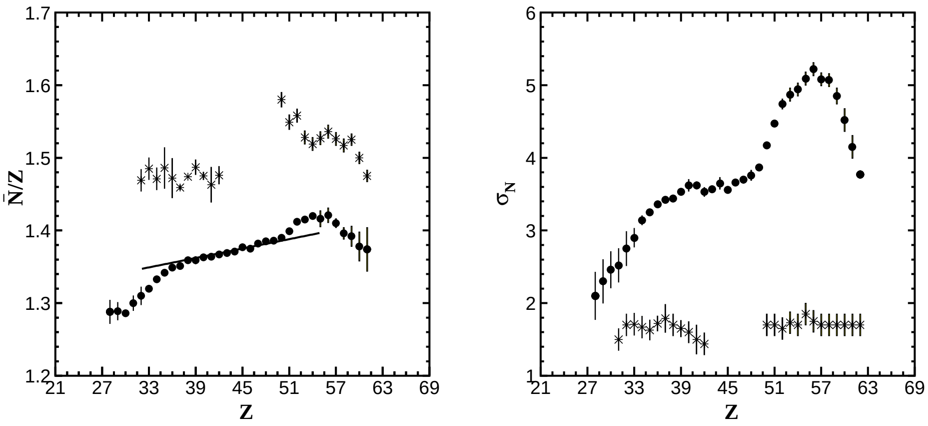

Figure 4.24: *Integrated distributions of fission fragments from Uranium on deuterium showing the contribution from total fission (dots) and low-energy asymmetric fission (asterisks). Left: Mean neutron number divided by Z as a function of Z. Right: Variance in neutron number for a given Z.*

According to these authors, the pronounced productions around Z=54 might reveal an unexpected strong contribution of proton shells in the asymmetric fission mode.

In spite of the rather high uncertainties in the separation method, the Z-integrated cross section of the two asymmetric groups were compatible with each other and equal to 92±27 mb. This cross section is slightly below the value of 105±10 mb measured for the reaction induced with Uranium on proton [Ber03], though both results are compatible within the error bars. From these measurements we see that the low-energy fission component represents less than 5% of the total fission cross section.

Table 4.2 depicts the separated contributions to the total cross section measured for the systems ^{238}U(1 A·GeV) on proton and deuterium. The references of these measurements are included in the table.

4.2.3 Distribution of fissioning nuclei at high excitation energies

The general properties of the high-energy fissioning nuclei could be determined from the fission residues distributions. From figure 4.25 a mean value of 43.7±0.2 and a total width of 7.7±0.2 charge units were deduced from the charge distribution of high-energy symmetric fission residues. These results are compared to those obtained for the reaction ^{238}U(1 A·GeV) on proton [Ber03] in table 4.3. The differences between the two systems can be understood as being due to the broader distribution of fissioning systems in the reaction induced on deuterium, and their average energies. Assuming that no protons were evaporated after scission, an average charge of 87.4±0.4 for the fissioning elements was found in the present work, to be compared

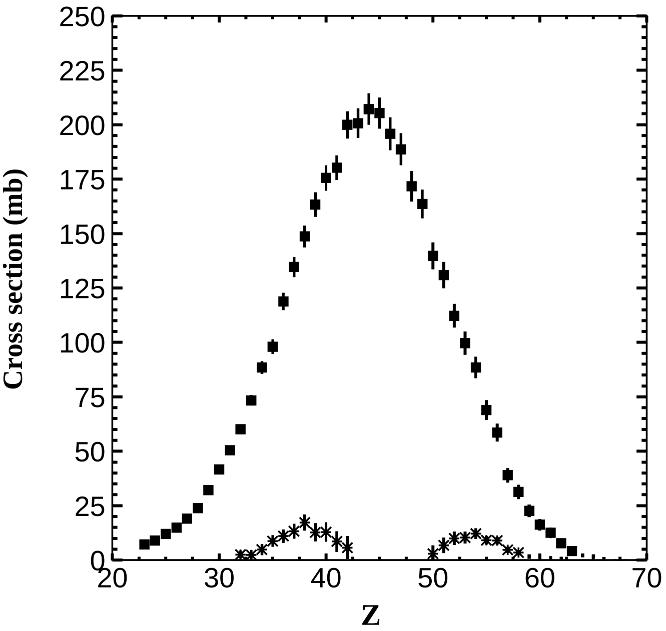

Figure 4.25: *Elemental distribution of fission cross sections showing the contribution from total fission (dots) and low-energy asymmetric fission (asterisks).*

Reaction	σ_{fiss} (mb)	σ_{fiss}^{asym} (mb)	σ_{ev} (mb)	σ_{tot} (mb)
U+d	2000±220	93±27	700±130 [Cas01]	2700±350
U+p	1530±150 [Ber03]	105±10 [Ber03]	420±20 [Tai03]	1990±170
U+Pb	3840±140 [Jur04c]	1680±140 [Jur04c]		
U+Cu	1890±60 [Jur04c]			
U+C	1300±30 [Jur04c]			

Table 4.2: Total fission cross section (σ_{fiss}), asymmetric component of fission cross section (σ_{fiss}^{asym}), evaporation cross section (σ_{ev}) and total reaction cross section (σ_{tot}) for reactions induced by ^{238}U(1 A·GeV) on different targets.

to the value of 89.8±0.2 for the proton case.

Alternatively, a deeper insight into the properties of the fissioning systems at high energies can be achieved from a kinematical analysis of the fission residues. Following the method described in section 3.3, the charges Z_{fiss} of the different fissioning nuclei could be deduced by comparing the fission velocities v_{fiss} given by equation 3.11 with the measured values shown in figure 3.11-3.14, assuming the N/Z

Reaction	$\bar{Z}$ (a.ch.u.)	$\bar{A}$ (a.m.u.)	σ_Z (a.ch.u.)	σ_A (a.m.u.)
U+d	43.7±0.2	103.0±0.2	7.7±0.2	20.0±0.5
U+p	44.9±0.1	106.8±0.25	6.4±0.2	

Table 4.3: Mean values of isotopic and isobaric distributions measured for the reactions ^{238}U(1 A·GeV)+d,p. The asymmetric contribution was suppressed in both systems.

being conserved, according to the UCD-hypothesis. The values of Z_{fiss} that better reproduced the measured v_{fiss} for each fission nucleus were weighted according to the production cross section of the corresponding fission residue. This procedure brought us to the distribution of fissioning elements Z_{fiss} shown in figure 4.26.

As can be seen, the elements that contribute to the high-energy fission process cover a rather broad region that extends to elements as light as $_{75}$Re. Moreover, if the velocities of the most neutron-deficient nuclei produced by secondary reactions in the target are omitted in the previous analysis, a mean charge of 86.8±1.0 is found from the Z_{fiss}-distribution. These results show a high level of agreement with the value 87.4±0.4 obtained by the independent measurement of the isotopic distributions shown in figure 4.25.

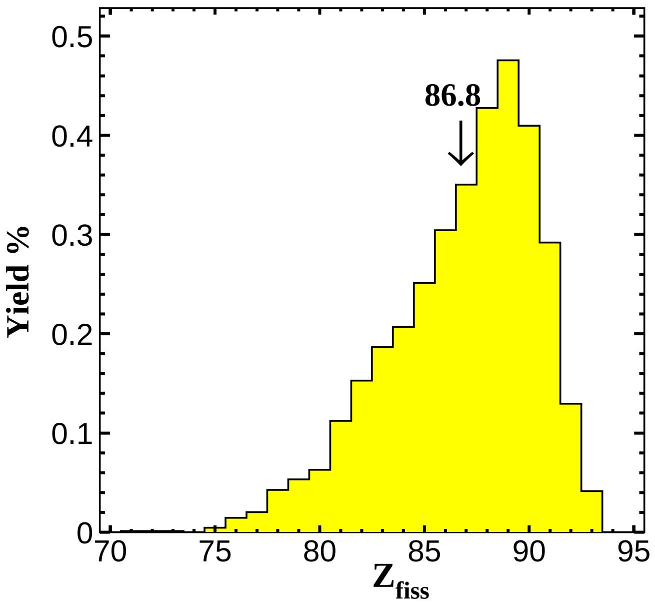

Figure 4.26: *Distribution of fissioning elements contributing to the total production of fission residues in the reaction* ^{238}*U(1 A·GeV)+d.*

Chapter 5

Analysis of collective nuclear motion in hot nuclei

The large range of mass, charge and excitation energy of the projectile pre-fragments, produced in the reaction ^{238}U at 1 A·GeV on deuterium, provided an optimum scenario to investigate collective phenomena from the competition between fission and evaporation during the deexcitation of these nuclei. In this chapter we propose to perform such an investigation from the measured fission and evaporation production cross sections, as well as the kinematical properties of the fission residues. These observables have been compared with model calculations including both the description of small- and large-amplitude collective modes. The accuracy of the data, together with the well defined initial conditions of the projectile pre-fragments produced in this reaction, will become key factors for characterizing the collective nuclear motion during the decay processes.

The chapter is organized as follows: The first section is devoted to describe the theoretical approaches used to investigate the collective motion from the measured data. This includes a discussion of the Monte Carlo codes that simulate the first stage of the collision, as well as the implementation of the collective phenomena that rule the deexcitation of these nuclei. The sensitivity of the data to small-scale collective motions is discussed in the second section. Finally, the last section concerns the analysis of the dynamics of fission at high excitation energy governed by the dissipation of nuclear matter.

5.1 Model calculations

The fission and evaporation residue productions obtained in spallation reactions are normally studied on the basis of the two-step model [Ser47]. This formalism can be implemented with Monte Carlo codes that reproduce separately each stage of the process: The first step of the reaction concerns the fast interaction between projectile and target, and the subsequent thermalization of the projectile pre-fragments. Then, the second stage corresponds to the deexcitation of these nuclei by fission or evaporation. In this section we will discuss the models used to describe each step of the reaction.

5.1.1 Initital stage of the reaction

In spallation reactions the initial stage of the collision can be described as a sequence of nucleon-nucleon interactions. In these collisions part of the initial kinetic energy of the projectile is dissipated in terms of excitation energy, while nucleons and cluster are emitted from the reaction partners. This process defines the final pre-fragments which are characterized by a given value of excitation energy E, mass A, charge Z and angular momentum J. Assuming that these pre-fragments reach thermal equilibrium, we can apply statistical methods for describing the deexcitation process leading to the final residual nuclei. Since we do not have experimental access to the pre-fragments produced in these collisions, we have to use reliable model calculations for describing the first stage of the reaction.

At present, there exist numerous models to calculate the distribution of excited pre-fragments before entering into the decay process. They differ on the accuracy, number of predicted observables and calculation times. Some examples are the pre-equilibrium model [Gri66], the intranuclear cascades [Met58a, Met58b, Ber63], the abrasion model [Gai91, Bow73, Mor78, Oli79], and the Boltzmann-Uehling-Uhlenbeck (BUU) and Vlasov-Uehling-Uhlenbeck (VUU) transport models [Aic85, Kru85]. A detailed discussion of their main considerations is well beyond the scope of this work; we will restrict ourselves to mention that for the type of reactions analyzed in this work, the so-called intranuclear cascade models (INC) represent a good compromise between accuracy, computing time and facility to be implemented with deexcitation models.

In the INC model, the thermalization of the nucleus occurs by means of sequential collisions among the excited nucleons (cascade particles) that constitute the reacting system (projectile+target). The NN-collisions are evaluated with Monte Carlo methods by considering explicitly the trajectories of the cascade particles inside the nucleus, thus neglecting the uncertainty principle. Such classical picture is expected to constitute a reasonable approximation at rather high energies (above $\simeq$100 MeV) when the wavelength of the particle is smaller than the average distance between two nucleons in the nucleus. Random numbers decide the entry point of the projectile, the collisions between the cascade particles, their nature (elastic or inelastic) and the characteristics of motion of the struck particle (energy and direction). The collision probability is evaluated on the basis of the NN-cross sections modified by the nuclear medium. Moreover, Pauli's blocking is accounted for by forbidding collisions leading to scattered particles that populate a filled region of phase-space. The calculation follows all the nucleons excited in the course of the reaction, including those that are emitted when they reach the nuclear surface and are not reflected. After each emission, the mass, charge, energy and angular momentum of the pre-fragment must be properly adjusted.

In the present work we have used two different versions of intranuclear cascades:

the ISABEL [Yar79, Yar81] code and the INCL [Cug87, Cug97, Bou02] code. Their major differences concern the treatment of the nuclear medium and the criterion used to stop the calculation:

In the case of ISABEL, the nucleus is considered as a Fermi sea of nucleons that can interact with the excited particles producing new cascade particles. After each interaction the nuclear density is readjusted and the trajectory of the new excited particle is computed. The cascade stops when the energy of every cascade particle falls below a pre-defined cut-off energy given by Coulomb barrier plus two times the binding energy. Thereafter, the energy of all the excited particles that remain bound in the nucleus is assumed to be distributed among all the nucleons of the nucleus leading to a thermalized pre-fragment .

By contrast, in the INCL code the nucleus is considered as a sample of compact balls (nucleons) whose trajectories are followed at any moment during the intranuclear cascade. At each time step, a collision between two nucleons can occur if the distance between their associated trajectories falls below a pre-defined minimum distance. The calculation continues until the computed time reaches a given value τ_{eq} which determines the end of the pre-equilibrium stage. This parameter is defined from the analysis of the time evolution of the excitation energy of the system: during the thermalization process, the kinetic energies of the emitted pre-equilibrium particles causes an abrupt reduction of the excitation energy of the nucleus. Then, as soon as thermal equilibrium is approaching, the excitation energy decrease becomes smoother. The parameter τ_{eq} can thus be defined by the transition between these two regimes. At the end of the calculation, the energy of the nucleus is calculated as the difference between the sum of the kinetic energies of all the excited nucleons and that of the ground state in a Fermi gas, both referred to the bottom of the potential well.

5.1.2 Projectile pre-fragment deexcitation

To describe the deexcitation of the thermalized projectile pre-fragments we have used the most recent version of the statistical Monte Carlo ABLA code [Gai91, Jun98, Ben98]. According to this model, right after the thermalization stage, the highly excited nucleus can break-up into clusters of different size due to thermal instabilities that might occur at very high excitation energies. This simultaneous decay, often referred to as multifragmentation [Bon95], was implemented according to the work of Ricciardi et al. [Ric02, Sch02] for those systems with temperatures exceeding the so-called break-up temperature, which was estimated to be about 5.5 MeV. After this stage, or at lower excitation energies, the deexcitation of the nucleus proceeds by a sequential decay governed by fission and evaporation decay channels. The statistical competition of these two processes was calculated at each sequential step according to equation 1.1. Assuming that the excited pre-fragments have rather low angular momenta [Jon97] and that the excitation energy E is high enough, the evaporation width of a particle j can be simplified by making use of the sharp cutoff approximation as [Mor73]:

$$\Gamma_j^{ev} = \frac{1}{2\pi\rho_c(E)} \frac{4m_j R^2}{\hbar^2} T_j^2 \rho_j(E - S_j - B_j) \tag{5.1}$$

where E is the excitation energy of the system, m_j is the mass of the emitted particle, S_j its separation energy, B_j the effective Coulomb barrier for charged particles which accounts for the transmission coefficient not considered in this equation, R is the radius of the nucleus and T_j the temperature of the residual nucleus after particle emission. The statistical weights of the initial and final states are given by the level densities of the compound ρ_c and exit channel ρ_j.

The fission width calculated according to the transition-state model of Bohr and Wheeler [Boh39] can be written as [Mor73]:

$$\Gamma_f^{BW} = \frac{1}{2\pi\rho_c(E)} T_{sad}\rho_{sad}(E - B_f) \tag{5.2}$$

being ρ_{sad} the level density of transition states of the fissioning nucleus in the saddle-point configuration, T_{sad} the corresponding nuclear temperature at saddle. The fission barriers B_f were calculated from the macroscopic rotating finite-range liquid-drop model [Sie86] including the microscopic contribution from ground-state shell structure [Mol95]. Contributions of these effects at the saddle point were disregarded since they are assumed to be small compared to those at the ground-state. The level density $\rho(E)$ included in equations 5.1 and 5.2 can be calculated from equation 1.4, including shell and pairing corrections following reference [Jun98]:

$$\rho(E) = \frac{\pi}{12} \frac{e^S}{\tilde{a}^{1/4} E^{5/4}} \tag{5.3}$$

where:

$$S = 2\sqrt{\tilde{a}(E' + k(E') \cdot \delta U + h(E') \cdot \delta P)} \tag{5.4}$$

and the asymptotic level-density parameter $\tilde{a}$ is calculated according to reference [Ign75b]:

$$\tilde{a} = 0.073A + 0.095 B_s A^{2/3} \tag{5.5}$$

being B_s a correction factor that accounts for the surface area of the deformed nucleus [Mye74].

Following the back-shifted Fermi-gas formalism, δU is the shell correction calculated according to reference [Mol95] and $k(E')$ is a function that describes the damping of this correction with excitation energy [Ign75a, Sch82]. Furthermore, pairing correlations due to two-body residual interactions can be described by an additional energy shift given by:

$$\delta P = -\frac{1}{4}\Delta^2 g + 2\Delta \tag{5.6}$$

where $\Delta = 12/\sqrt{A}$ is the average pairing gap and $g = 6\tilde{a}/\pi^2$ is the single-particle level density at the Fermi energy. Finally, the function:

$$h(E') = \begin{cases} 1 - \left(1 - \frac{E'}{E_{crit}}\right)^2 & , E' < E_{crit} \\ 1 & , E' \geq E_{crit} \end{cases}$$

parameterizes the washing out of pairing correlations due to the superfluid phase transition [Ign79b] at $E_{crit} = 10$ MeV [Ign77]. In this approach, the effective energy E' has to be modified respect to the ground-state energy E in order to reproduce the odd-even effects:

$$E' = \begin{cases} E & , for\ even - even\ nuclei \\ E + \Delta & , for\ odd - mass\ nuclei \\ E + 2\Delta & , for\ odd - odd\ nuclei \end{cases}$$

In addition, the enhancement of the level density induced by collective excitations, was described according to the adiabatic formalism. In this picture, internal and collective degrees of freedom are completely decoupled to each other, and the total level density $\rho(E)$ can be expressed as:

$$\rho(E) = K_{coll} \cdot \rho_{int}(E) \tag{5.7}$$

where $\rho_{int}(E)$ is given by equation 5.3 and K_{coll} represents the collective enhancement factor that will be described in detail in the following sections.

As discussed in chapter 1, a realistic description of fission should consider the dynamics of this process governed by dissipation. In this picture, the fission probability calculated from equation 5.2 corrected by the Kramers factor (equation 1.15). Moreover, the dynamical description of the coupling between the collective and internal degrees of freedom through dissipation causes an initial suppression of the fission probability [Gra80, Gra83]. The ABLA code includes a time dependent fission width derived by Jurado et al. [Jur04a] on the basis of an approximated solution of the Fokker-Planck equation for a parabolic nuclear potential:

$$\Gamma_f^{fpe}(t) \approx \frac{W^{par}(X = X_b, t)}{W^{par}(X = X_b, t \to \infty)} \Gamma_f^K \tag{5.8}$$

where Γ_f^K is the Bohr-Wheeler fission width, multiplied by the Kramers factor and $W^{par}(X = X_b, t)$ is the probability distribution at the saddle point X_b calculated by solving the Fokker-Planck equation for a parabolic potential [Cha43]:

$$W^{par}(X = X_b, t) = \frac{1}{\sqrt{2\pi}\sigma} e^{-\frac{X_b^2}{2\sigma^2}} \tag{5.9}$$

with σ^2 given by:

$$\sigma^2 = \frac{kT}{\mu\omega_g^2} \left\{ 1 - e^{-\beta \cdot t} \cdot \left[\frac{2\beta^2}{\beta_g^2} Sinh^2\left(\frac{\beta_g t}{2}\right) + \frac{\beta}{\beta_g} Sinh\left(\beta_g\right) + 1 \right] \right\} \tag{5.10}$$

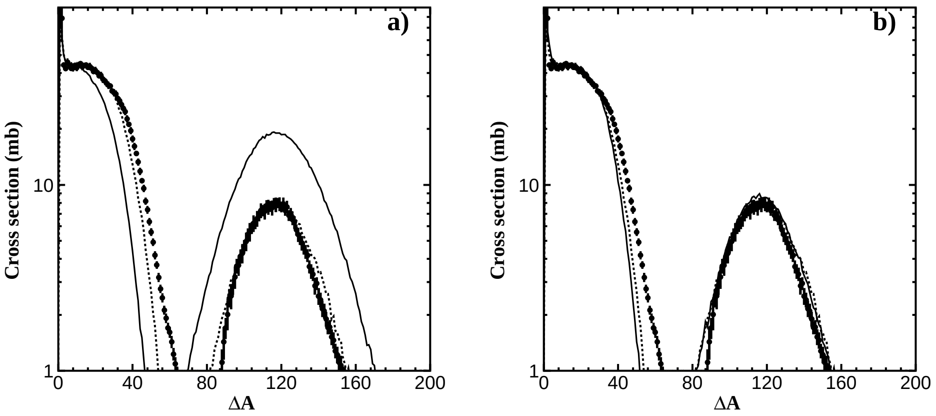

Figure 5.1: *Isobaric distribution of residues obtained in the reaction ^{208}Pb(1 A·GeV)+p (dots) compared to calculations based on the two-step model using different prescriptions for the fission probability. a): ISABEL+ABLA with the transition state fission width given by equation 5.2 (solid line) and the time-dependent $\Gamma_f^{fpe}(t)$ of reference [Jur04a] with $\beta = 2\ Zs^{-1}$ (dashed line). b): INCL+ABLA (solid line) and ISABEL+ABLA (dashed line) both with a time-dependent fission width $\Gamma_f^{fpe}(t)$ and $\beta = 2\ Zs^{-1}$.*

being β the reduced dissipation coefficient, k the Boltzmann's constant, T the nuclear temperature, μ the reduced mass associated to the fission degree of freedom X, ω_g the curvature of the potential at the ground state and $\beta_g = \sqrt{\beta^2 - 4\omega_g^2}$.

Finally, when fission occurs, the mass and charge distributions of the fission residues are calculated using to the PROFI subroutine [Ben98]. This semi-empirical model assumes that fission is decided as soon as the decaying nucleus surmounts the saddle point deformation. Then, the mass partition of the two nascent fission fragments is determined from the dependence of the nuclear potential at saddle on a mass-asymmetry coordinate. In accordance with experimental results, three main components of this potential were considered [Wil76, Bro90]: A symmetric component calculated from the liquid-drop surface potential [Itk88] (superdeformed fission mode SD) and two asymmetric components originated from the shell structure of the nascent fragments (Standard I, centered on N=82 and Standard II on N=88). Further details of the model are discussed in reference [Ben98].

5.1.3 Benchmark of INC models

The INC models used to describe the first stage of the reaction have been benchmarked with some of the simplest spallation reactions investigated at GSI. In particular, the system ^{208}Pb at 1 A·GeV on proton [Enq01] represents an optimum case. In this reaction, fission will happen at relatively high excitation energies, where shell effects and collective excitations can be neglected. At the same time, these excita-

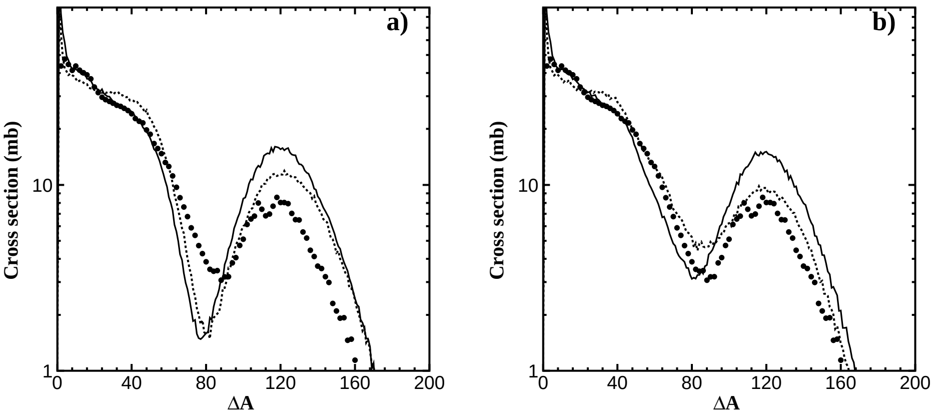

Figure 5.2: *Isobaric distribution of residues obtained in the reaction* ^{208}*Pb(1 A·GeV)+d (dots) compared with ISABEL+ABLA (dashed line) and INCL+ABLA (solid line) calculations using different description of the deexcitation process. a) Fission described by the time-dependent fission width* $\Gamma_f^{fpe}(t)$ *of reference [Jur04a] with* $\beta = 2$ *Zs*$^{-1}$*; b) An additional break-up stage is considered for temperatures above 5 MeV according to the formalism of reference [Sch02].*

tion energies are not sufficient to open the multifragmentation channel. However, when we couple any of the INC models considered in this work (ISABEL and INCL) to the pure statistical version of the ABLA code (neglecting the role of dissipation in fission), none of the calculations are able to reproduce the observed fission production cross sections, as shown in figure 5.1-a (solid line). On the contrary, a dynamical description of the fission process, formulated by the time-dependent fission width $\Gamma_f^{fpe}(t)$ proposed by Jurado et al. [Jur04a] with a dissipation coefficient $\beta = 2$ Zs^{-1} (1 Zs^{-1}=1 × 10^{21} s^{-1}) provides a good agreement with the data (figure 5.1-b).

In spite of this success, the same model calculation applied to the more energetic reaction ^{208}Pb(1 A·GeV)+d [Enq02] provides a general overestimation of the fission residue productions and the subsequent underestimation of evaporation fragments, as shown in figure 5.2-a. The same result was found independently of the intranuclear cascade employed to describe the first stage of the reaction.

Compared to the proton case, the reaction induced by ^{208}Pb at 1 A·GeV on deuteron leads to a broader distribution of projectile pre-fragments with higher excitation energies. If the temperatures associated to these energies exceed a given threshold, the thermal instabilities can produce a simultaneous break up of the excited nucleus into clusters of different size. The onset of this new decay mechanism might then be responsible for the large productions of light evaporation residues (with ΔA ~80) and the corresponding reduction of fission. Calculations performed with the code ISABEL, coupled to a break-up stage subroutine [Sch02, Ric02] prior to the statistical deexcitation ABLA model, provide a fair agreement with the experimental data (see dashed line in figure 5.2-b). This calculation also includes

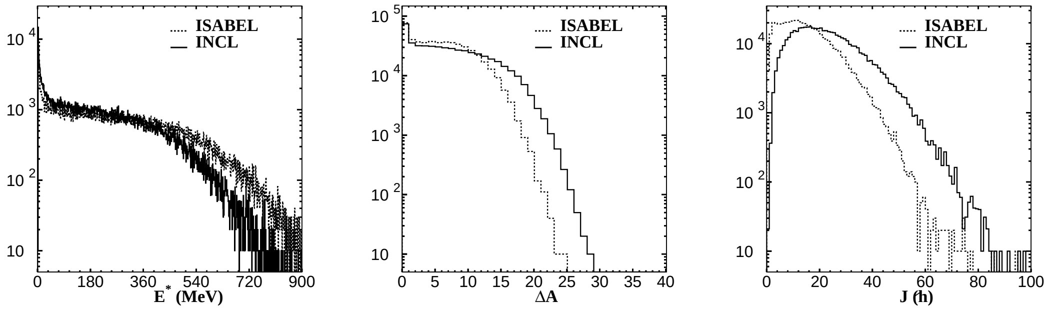

Figure 5.3: *Output parameters provided by INCL (solid line) and ISABEL (dotted line); Excitation energy (left), mass distribution (middle) and angular momentum (right).*

the time-dependent fission width given by equation 5.13 with $\beta = 2$ Zs^{-1}. On the contrary, the same calculation made with INCL still overestimates the fission productions (solid line in figure 5.2).

In order to better understand the differences between the two cascades, we have analyzed the variables which define the distribution of pre-fragments right after the thermalization stage. Figure 5.3 shows the excitation energy, mass lost and angular momentum distributions of the projectile pre-fragments calculated with INCL (solid line) and ISABEL (dotted line) codes for the reaction ^{208}Pb(1 A·GeV)+d. As can be seen, the difference between these two models can be explained in terms of the calculated angular momentum J of the pre-fragments: INCL predicts a mean J_{INCL} value about 24$\hbar$, which is twice greater than the value calculated by ISABEL J_{ISA}=12$\hbar$. The centrifugal force of a rotating nucleus with angular momentum J causes a reduction of the height of the fission barrier and a subsequent increase of the fission probability. Because this force is directly related to the angular momentum, the fission probability is expected to increase with the angular momentum. Consequently, the overproductions of fission residues obtained with INCL may be due to an overestimation of the angular momentum.

The conclusions obtained from this analysis can be summarized as follows:

1. The overestimation of the fission productions obtained in the calculation using INCL seems to be caused by an overestimation of the angular momentum in this code, rather than by an incomplete description of the deexcitation process, as claimed by Boudard et al. [Bou02].

2. At temperatures above ∼5 MeV, the onset of a break-up stage is responsible for the production of intermediate-mass fragments accompanied by a reduction of the fission productions.

Therefore, we conclude that the ISABEL intranuclear cascade is better suited to reproduce the distribution of pre-fragments in reactions induced with deuterium.

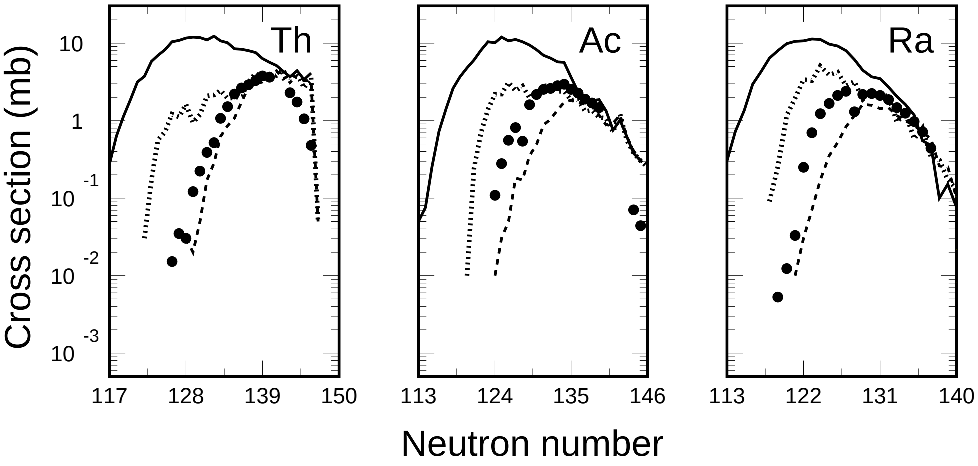

Figure 5.4: *Isotopic production cross sections of $_{90}$Th, $_{89}$Ac and $_{88}$Ra measured in the reaction ^{238}U(1 A·GeV)+d compared with calculations where fission is supressed (solid line), including fission (dashed line) and including both fission and shell effects (dotted line).*

5.2 Analysis of small-amplitude collective motion in hot fissile nuclei

The particular features of the pre-fragments produced in the spallation of Uranium on deuterium provide an optimum scenario to investigate the small-scale collective motions of the decaying systems. Contrary to the reactions induced with ^{208}Pb, the very low fission barriers of Uranium-like pre-fragments reduce drastically the survival probability against fission of these nuclei. As a consequence, the final productions of heavy-mass evaporation residues provide paradoxically valuable information on the fission decay channel and the role of small-amplitude collective motion in this process. As explained in section 5.1.2, rotations and vibrations modify the level densities and consequently the relative probability for fission and evaporation. Since the distribution of pre-fragments produced in the reaction ^{238}U(1 A·GeV)+d covers a large range of isotopes where vibrations and rotations are dominant, the transition between these two small-amplitude collective motions can be investigated from the measured residue productions.

The role of shell effects and collective excitations in the decay of fissile nuclei is illustrated in figure 5.4. In this picture we compare the isotopic production cross sections of few selected heavy elements (Thorium, Actinium and Radium), produced in the reaction ^{238}U(1 A·GeV)+d, with a calculation where fission was suppressed (solid line). The drastic overestimation of the data demonstrates the influence of the fission probability -or complementary, the survival probability against fission- in the final production cross sections. In fact, when this channel is included with the time-

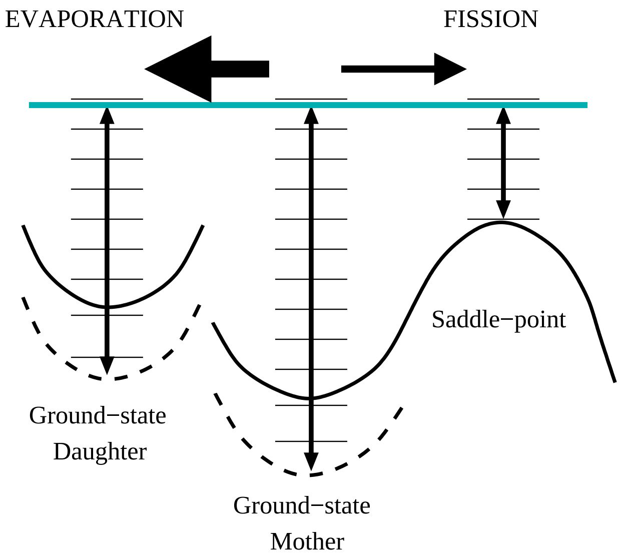

Figure 5.5: *Schematic representation of fission and evaporation decay processes. The dashed lines represent the descent of the potential due to shell effects.*

dependent fission width $\Gamma(t)_f^{fpe}$ given by equation 5.3 and $\beta = 2$ Zs^{-1} (dashed line), a general better agreement is found ; though the more neutron deficient residues are systematically underestimated.

In the previous calculations, the shell structure of the decaying nuclei was included neither in the level densities $\rho(E)$ nor in the fission barriers. Thus, the underestimated productions of isotopes near the closed shell N=126, by the calculation which included fission (dashed line), could be interpreted as a signature of shell stabilization against fission. As illustrated in figure 5.5, the increase of the binding energy due to the shell closure of an excited compound nuclei leads to a lower value of its ground-state mass energy. The energy gained by this effect causes an increase of the level density of the magic (or near magic) compound nucleus $\rho_c(E)$ and of the daughter evaporation residue $\rho_n(E - S_n)$ in equations 5.1 and 5.2. On the contrary, the shell structure of the levels above the saddle point is washed out by the large deformation at this configuration, so that the level density $\rho_{sad}(E - B_f)$ does not differ very much from that calculated from the Fermi-gas expression. As a consequence, the survival probability against fission, calculated as the inverse of the ratio ρ_{sad}/ρ_c in equation 5.2, will be increased by this effect. Likewise, the neutron evaporation width is expected to increase with respect to the fission width, as predicted by the ratio ρ_n/ρ_{sad} obtained from reference [Mor73]:

$$\frac{\Gamma_j^{ev}}{\Gamma_f} = \frac{4m_nR^2}{\hbar^2} \cdot \frac{T^2}{T_{sad}^2} \cdot \frac{\rho_n(E - S_n)}{\rho_{sad}(E - B_f)} \tag{5.11}$$

In order to include these effects in the deexcitation of the projectile pre-fragments produced in the reaction ^{238}U(1 A·GeV)+d, we repeated the previous calculation with a version of the ABLA code that included the shell and pairing corrections of

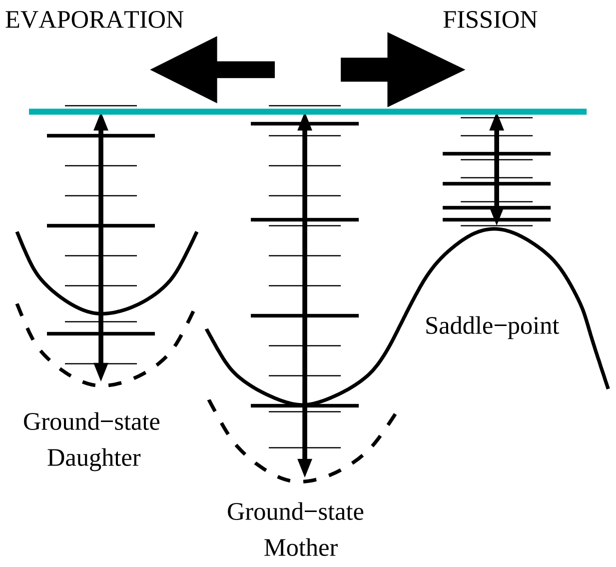

Figure 5.6: *Schematic representation of fission and evaporation decay processes. The level density results from the contribution of the microscopic levels (short horizontal lines) and the macroscopic levels (longer horizontal lines). The later include vibrations at ground-state deformations and rotational bands at saddle-point deformation.*

the level density $\rho(E)$ (equation 5.3); furthermore, the fission barriers were corrected by the ground-state shell effects as formulated in reference [Mol95]. As expected, the calculations made with this version of the code predict a pronounced enhancement of the production cross sections for nuclei near N=126 (see dotted line of figure 5.4). However, this effect leads to a general underestimation of the fission probabilities for these nuclei, as can be deduced from their larger productions with respect to the experimental data.

The astonishing lack of stabilization against fission for magic and near magic nuclei was interpreted as a signature of the level-density enhancement due to the presence of rotational collective excitations [Jun98, Hei03]: The large deformations of the mother nucleus at the saddle point favor the appearance of rotational bands above the barrier. These collective levels are then summed up to the intrinsic levels of the nucleus, leading to an increase of $\rho_{sad}(E-B_f)$ in equation 5.11 that favors the decay of the nucleus by fission. This effect can compensate the shell stabilization against fission.

In order to account for the role of collective motion in the decay of the excited compound nuclei, the ABLA code was modified according to the phenomenological formulation of the collective enhancement of the level density proposed by A. Junghans et al. [Jun98]. These authors calculated the rotational enhancement factor in terms of the spin-cutoff parameter $\sigma_{\perp}^2$ [Bjo73, Hui74a] by making use of the rigid-rotor moment of inertia $\Im_\perp$:

$$\sigma_\perp^2(rot) = \frac{\Im_\perp T}{\hbar^2} = \frac{2T}{5\hbar^2} m_0 A R^2 \left(1 + \frac{\beta_2}{3}\right) \tag{5.12}$$

where T is the nuclear temperature, $m_0 A$ is the mass of the nucleus in mass units and $R = 1.2A^{1/3}$ fm is the nuclear radius.

Furthermore, the enhancement of the level density induced by vibrational excitations was also calculated with a new formulation that avoids the inconsistencies of the adiabatic approach discussed in chapter 1 (equation 1.9). By following the functional dependence of $\sigma_\perp^2(rot)$, the vibrational enhancement factor was calculated in terms of a virtual "spin-cutoff" vibrational parameter, according to:

$$\sigma_\perp^2(vib) = S\beta_{eff}^2 \sigma_\perp^2(rot) \tag{5.13}$$

where $S = 25$ is a free parameter chosen by Junghans et al. to fit their experimental data, and β_{eff} is given by:

$$\beta_{eff} = 0.022 + 0.003\Delta N + 0.005\Delta Z \tag{5.14}$$

being $\Delta N(\Delta Z)$ the absolute values of the number of neutrons (protons) out of the nearest closed shell. The coefficient β_{eff} is a dynamical deformation parameter that somehow accounts for the variation of the excitation energies of the vibrational levels as a function of the distance from the closed shell. This new approach takes into account the disappearance of equidistant level spacing assumed in the adiabatic expression 1.9 and provides a vibrational enhancement factor that extends smoothly around the closed shells. Equation 5.14 implies that the rigid-rotor moment of inertia $\Im_\perp$, that describes the rotational motion of deformed nuclei, is merged into a irrotational flow moment of inertia ($\Im_{irr} = \beta_{eff}^2 \Im_\perp$) more appropriate to describe vibrations.

The collective character of the nuclear motion was parameterized as a function of the quadrupole deformation coefficient β_2 of the nuclear shape: Rotations govern the collective motion of nuclei with $|\beta_2| > 0.15$, while vibrations appear for $|\beta_2| \leq 0.15$. Therefore, the collective enhancement factor of the level density, described by the spin cut-off parameters of equation 5.12 or 5.13, is defined according to the quadrupole deformation of the compound nucleus.

Figure 5.6 provides an illustrative representation of the combined effects of rotations and vibrations upon the decay of a near magic nucleus:

As already mentioned, the competition between the fission and evaporation processes is governed by the level density ratio between the daughter evaporation nucleus at the ground-state configuration (ρ_n) and the mother nucleus at the saddle point (ρ_{sad}). According to the formulation described above, the increase of ρ_{sad} due to the presence of rotational bands at the saddle point ($\beta_2 > 0.15$) can be partly compensated by the collective enhancement of ρ_n. This effect will depend on the deformation of the evaporation daughter nucleus in its ground-state configuration:

If this nucleus is near a closed shell, then its small deformation ($\beta_2 \leq 0.15$) will favor the appearance of vibrational excitations. Since the factor $\sigma_\perp^2(vib)$, calculated with equation 5.13, is about one order of magnitude smaller than $\sigma_\perp^2(rot)$ (equation 5.12), the combined effect of these two collective enhancements results in an overall increase of the fission probability. On the other hand, if the ground-state configuration of the evaporation daughter nucleus is deformed ($\beta_2 > 0.15$), then the collective enhancement of ρ_{sad} is canceled by the similar increase of ρ_n due to the presence of rotational bands in the ground-state.

This example serves to illustrate the importance of the nuclear shape deformation upon the character of the collective motion. According to the previous discussion, the ground-state excitations of nuclei lying in the region of deformed ground-state shapes will be influenced by the presence of rotational band, while those with near spherical ground-state shapes will show vibrational motion. This latter group will thus present an enhancement of the fission probability.

Finally, the damping of the collective motions with excitation energy was described by A. Junghans et al. according to a Fermi function given by:

$$f(E) = \frac{1}{1 + e^{-\frac{E - E_{cr}}{d_{cr}}}} \tag{5.15}$$

where $E_{cr} = 40$ and $d_{cr} = 10$ are the critical energy and the width parameter, which contrary to references [Bjo73, Han83] do not depend on deformation.

The collective enhancement of the level densities was included in our model calculations by means of the factor $K_{coll}(E)$ [Jun98]:

$$K_{coll}(E) = \begin{cases} (\sigma_\perp^2 - 1) \cdot f(E) + 1 & , for\ \sigma_\perp^2 > 1 \\ 1 & , for\ \sigma_\perp^2 \leq 1 \end{cases}$$

where $\sigma_\perp^2$ is calculated from equation 5.12 for $|\beta_2| > 0.15$ and from 5.13 for $|\beta_2| \leq 0.15$. As an example, we show in figure 5.7 the rotational factor $K_{rot}(E)$ of the magic nucleus ^{216}Th (N=126) calculated at the saddle-point deformation (thick lines) and the vibrational factor $K_{vib}(E)$ of the daughter nucleus ^{215}Th at the ground-state deformation (thin lines).

The results of this version of the ABLA code are compared in figure 5.8 and 5.9 (dashed line) with the evaporation residue productions obtained in the reaction ^{238}U(1 A·GeV)+d (dots). As expected, the overall effect of these small-amplitude collective motions leads to an increase of the fission probability that compensates the pronounced shell stabilization of actinides near the neutron shell N=126 (dotted line). However, in spite of this improved result, the increase of the fission probability due to collective enhancement seems to be overestimated, as deduced from the low productions of these residues with respect to the experimental data. Since these nuclei are near the closed shell N=126, their ground-state configuration have rather small deformations ($\beta_2 \leq 0.15$). Thus, the low stabilization against fission, predicted by the calculation (dashed line), can be interpreted as due to an underestimation of the vibrational enhancement of the level density for these nuclei. According to this,

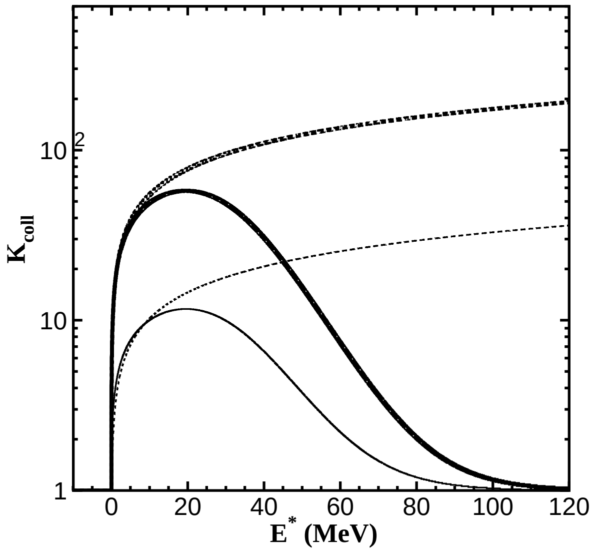

Figure 5.7: *Collective enhancement factor K_{coll} for ^{216}Th at saddle-point deformation (solid thick line) and at ground-state deformation (solid thin line). Calculations done without energy damping are also shown (dashed lines).*

we have modified the prescription of $\sigma_{\perp}^{2}(vib)$ proposed by Junghans (equation 5.13) by replacing the coefficient $S = 25$ by $S = 75$. This modification improves significantly the description of the residue productions (solid line), specially in the region around N=126, where vibrations dominate the collective motion of nuclei in the ground-state configurations.

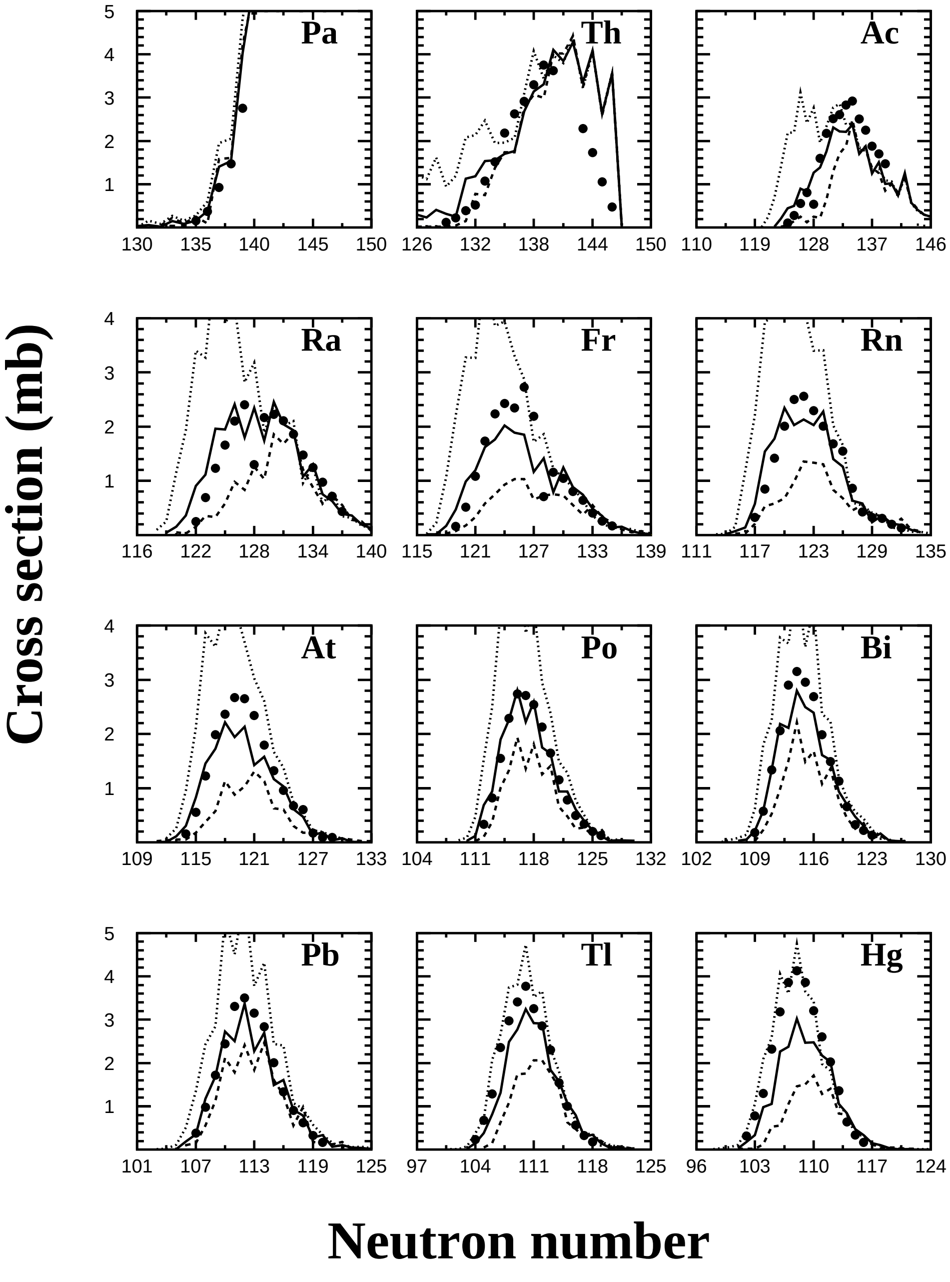

Figure 5.8: *Isotopic production cross sections of evaporation residues measured in* ^{238}*U(1 A·GeV)+d (full dots) compared with three calculations made with different versions of the ABLA code. Dashed line: calculation including both shell effects and collective enhancement with S=20. Solid line: the same calculation with S=75. Dotted line: calculation disregarding the collective enhancement of the level densities.*

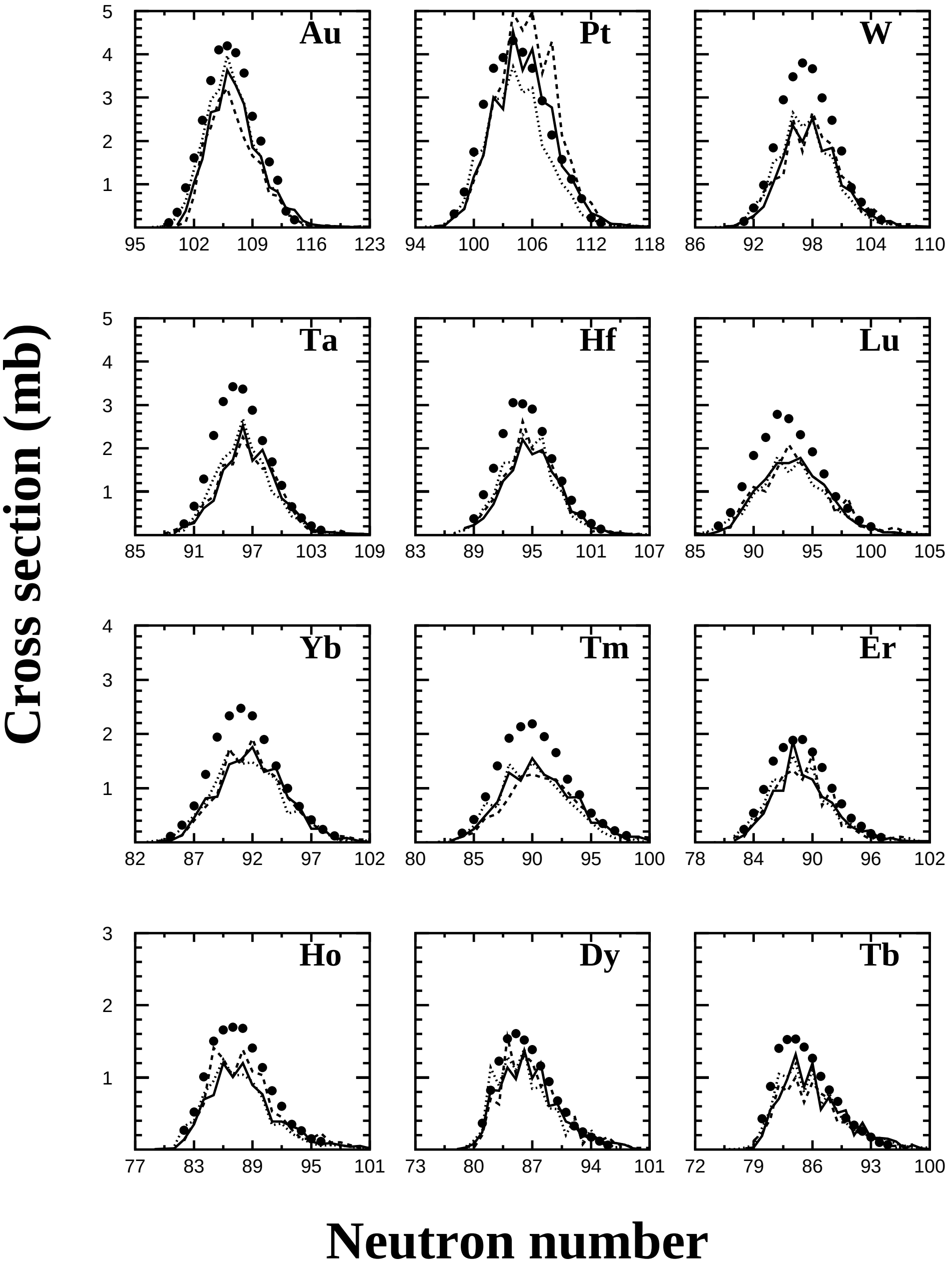

Figure 5.9: *Isotopic production cross sections of evaporation residues measured in* ^{238}*U(1 A·GeV)+d (full dots) compared with three calculations made with different versions of the ABLA code. Dashed line: calculation including both shell effects and collective enhancement with S=25. Solid line: the same calculation with S=75. Dotted line: calculation disregarding the collective enhancement of the level densities.*

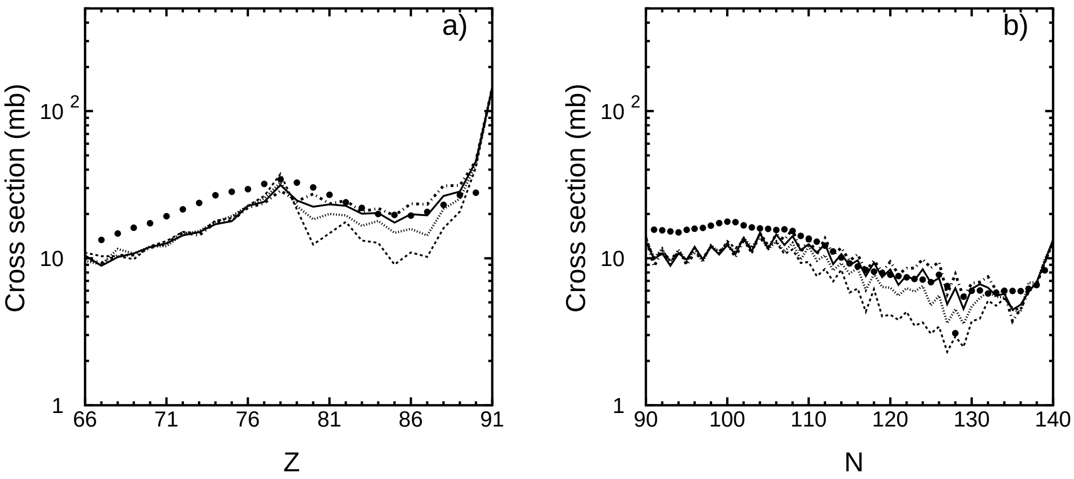

Figure 5.10: *Isotopic (a) and isotonic (b) distributions of evaporation residues in the reaction* ^{238}*U(1 A·GeV)+d (dots) compared to calculations made with the ABLA code using different factors S for the vibrational enhancement of the level density. S=25 (dashed line); S=50 (dotted line); S=75 (solid line) and S=100 (dash-dotted line).*

In order to better illustrate the role of the vibrational motion in the deexcitation of the pre-fragments produced in the present reaction, we compare in figure 5.10 the measured isotopic (Z-integrated) and isotonic (N-integrated) distributions of evaporation residues (dots) with several ABLA calculations made with different values of S (equation 5.13). In this figure, we observe a clear odd-even structure in the calculated results, especially in the isotonic distribution, due to the fact that we did not consider the deexcitation of these nuclei by gamma-emission [Ric04]. The inclusion of this process, would lead to a washing out of this structure, which would not affect the calculated absolute productions.

Despite this artificial odd-even structure, we clearly observe that the sensitivity of the calculations to the value of S is limited to a region defined by $78<Z<89$ and $110<N<134$ (around the shells $Z=82$ and $N=126$) dominated by vibrational excitations above the near spherical ground-state. The good results obtained with the factor S=75, in comparison with S=25 or S=50 suggested by Junghans, demonstrate the importance of vibrational motion upon the decay of nuclei with small deformations. In fact, only with this new factor we were able to reproduce the productions of evaporation residues in this region of the chart of the nuclides.

Apart from this success, it is of particular interest the underestimated productions of Mercury isotopes compared to other pre-actinides (see also figure 5.8). The ground-state shape of Hg isotopes is assumed to be weakly deformed, resulting in small collective enhancement factors. However, for some of these isotopes, it has been observed a coexistence of different shapes at low excitation energies caused by the appearance of deformed intruder low-lying states in the region of nearly spherical states [Woo92]. For instance, the weakly oblate ground-state band of neutron-deficient even-mass *Hg* isotopes is crossed by an intruder deformed band associated with a prolate-deformed state for ^{188}Hg. The presence of these deformed intruder states may lead to the appearance of rotational bands, which would then increase the level density. As a consequence, some of these *Hg* isotopes would be more stable against fission.

Beyond the region of small deformations, the calculated productions of lighter (Z< 78 and N< 110) and heavier (Z> 89 and N> 134) evaporation residues are insensitive to the different S factors used by the ABLA code. This trend has its explanation on the large deformations of these nuclei, which are responsible for the onset of rotational motion at the ground-state configuration: The stability of these nuclei against fission depends on the rotational enhancement factor of the ground-state level density, calculated with equation 5.12, which does not depend on the factor S. According to this, the regions around $Z \simeq 78$-$N \simeq 110$ and $Z \simeq 86$-$N \simeq 134$ correspond to the transitions from vibrational to rotational character of the collective nuclear motion. Furthermore, in spite of the increased stability of deformed nuclei against fission due to the onset of rotational motion, this decay channel seems to be overestimated in the region of light evaporation residues. In fact, these light evaporation residues are better reproduced when fission is suppressed in the ABLA code, specially below $_{73}$Ta, as shown in figure 5.11. To our understanding, the reason of these overestimated fission probabilities lays beyond the collective enhancement of the level density, because the high excitation energies of these nuclei lead to a complete damping of the collective motion. A possible explanation of this disagreement with the data might arise for instance from the long tails of the excitation energies calculated by ISABEL or from the the formulation of the multifragmentation channel. Anyhow, these possibilities demand further investigations that are beyond the scope of the present work.

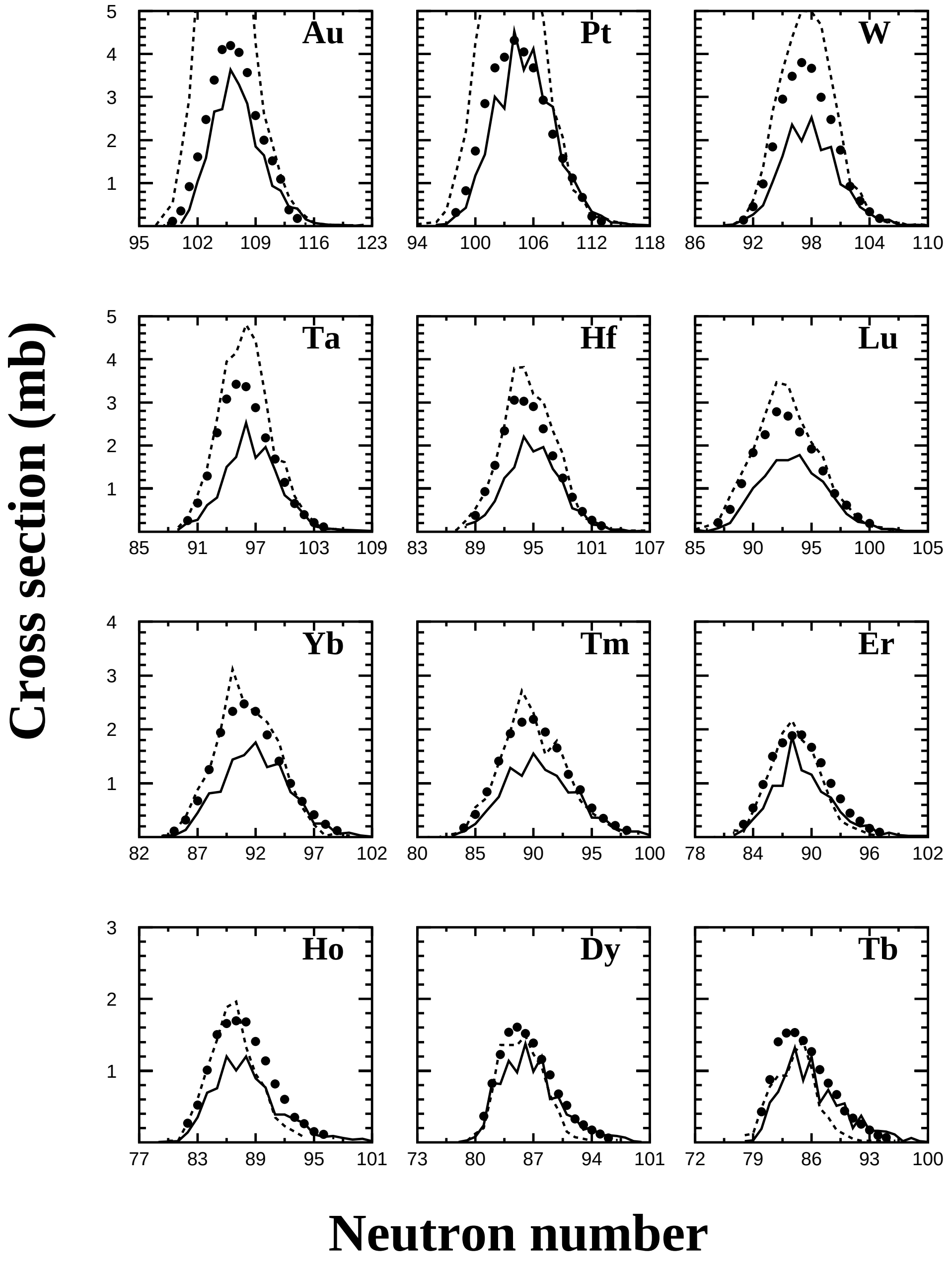

Figure 5.11: *Isotopic production cross sections of evaporation residues measured in* ^{238}*U(1 A·GeV)+d (full dots) compared with two versions of the ABLA code. Solid line: calculation including both shell effects and collective enhancement with S=75. Dashed line: calculation where fission was suppressed.*

5.3 Dynamics of excited fissioning nuclei

So far, we have analyzed the presence and nature of small-amplitude collective motion in actinides and heavy pre-actinides produced in the spallation reaction of ^{238}U at 1 A·GeV on deuteron. Other collective phenomenon associated with the deexcitation of these pre-fragments is the large-amplitude fission motion. As discussed in chapter 1, the viscosity of nuclear matter affects this process in three different aspects: First, it reduces the statistical Bohr-Wheeler decay width Γ_f^{BW}, according to the Kramers factor; second, it introduces a transient delay time τ_{tr} needed by the system to build up the quasiestationary probability flow across the saddle point; third, after fission is decided, the descent time from saddle to scission τ_{ssc} is also increased by the damping of the fission motion beyond the saddle point. Whereas the two first points concern the fission motion between the ground-state configuration and the saddle point, the latter involves dissipation at rather large deformations, when the necking of the nuclear shape starts to set in. Consequently, the analysis of these three effects make it possible to investigate dissipation at different deformations.

5.3.1 Dissipation at small deformations

As was discussed in chapter 1, dissipation at small deformations affects the production of fission residues or complementary, evaporation residues, in two different ways depending on the excitation energy of the decaying system: Low energy pre-fragments are sensitive to the reduction of the statistical fission width by the Kramers factor, while those with energies above ~150 MeV are mainly affected by the total suppression of the fission process during the transient time [Jur04b, Jur04c]. Figure 5.12-a shows the calculated initial excitation energies of the final fission and evaporation residues produced in the reaction ^{238}U(1 A·GeV)+d, as a function of their mass (in mass-lost units $\Delta A = 238 - A$). The calculation was done with the ISABEL coupled to the standard version of ABLA, which includes $\beta = 2$ Zs^{-1} and $\Gamma_f^{fpe}(t)$. As can be seen, evaporation residues exhibit a clear correlation between their final masses and the initial excitation energies of the decaying pre-fragments, which is not observed in the case of fission. According to this, the production of these heavy nuclei is affected by the two effects of dissipation at small deformations, depending on their final masses: while actinides and heavy pre-actinides are influenced by the Kramers factor, the lighter evaporation nuclei are also sensitive to transient effects. This provides a preliminary understanding of the production of evaporation nuclei ($\Delta A < 85$) shown in figure 5.12-b:

The region of actinides and heavy pre-actinides were produced at rather low energies, where fission is simply hindered by the Kramers factor. This effect was compensated by the high fissilities of these nuclei which were responsible for the pronounced depletion of the evaporation residue productions in the region $\Delta A < 20$. At higher energies, like those involved in the deexcitation of lighter evaporation nuclei, the low fissilities and the total suppression of fission during the transient

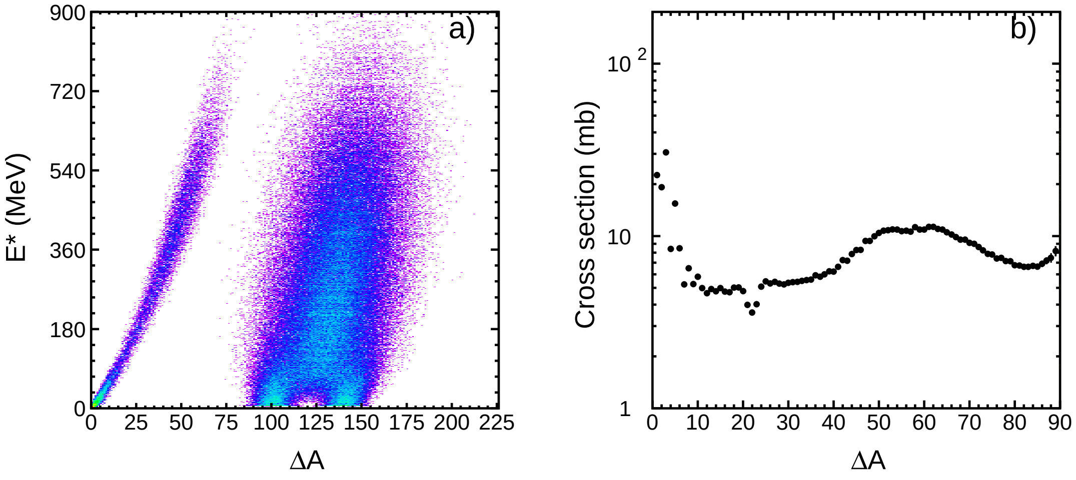

Figure 5.12: *Left: correlation between initial energies and final masses of the residues produced in the reaction* ^{238}*U(1 A·GeV)+d, calculated with ISABEL coupled to the standard version of the ABLA code (section 5.1.3), which includes* $\beta = 2$ *Zs*$^{-1}$ *and the time-dependent fission width* $\Gamma_f^{fpe}(t)$ *(equation 5.3). Right: measured isobaric distribution of evaporation residues, produced in the same reaction [Cas01].*

time led to longer evaporation chains that cool down the decaying nucleus. For the lightest pre-fragments, these chains could occasionally terminate in a region of rather light evaporation residues, with very high fission barriers. Consequently, the depletion effects observed for actinides and heavy pre-actinides disappear gradually as the mass loss increases, leading to an enhanced production of residues with ΔA around 40-80.

Figure 5.13 compares the isobaric distributions of evaporation residues produced in the reaction ^{238}U at 1 A·GeV on deuterium [Cas01] with two calculations made with ISABEL coupled to different versions of the ABLA code, both with a reduced dissipation coefficient $\beta = 2$ Zs^{-1}. One of the calculations (solid line) accounted for the two effects induced by dissipation at small deformation, namely the transient effects described by the time-dependent fission width $\Gamma_f^{fpe}(t)$ and the hindrance of fission due to the Kramers factor. The second one (dashed line) only included the latter effect, while disregarded the delay of the fission process during the transient time. As expected, there are no major differences between both calculations in the region of actinides and heavy pre-actinides ($\Delta A < 20$), demonstrating that these nuclei are not sensitive to the delay of the fission process induced by the transient effects. By contrast, this effect plays a dominant role in the production of light evaporation residues. In fact, a much better agreement between experimental data and calculations in the region $40 < \Delta A < 80$ is found when including the time-dependent fission width $\Gamma_f^{fpe}(t)$.

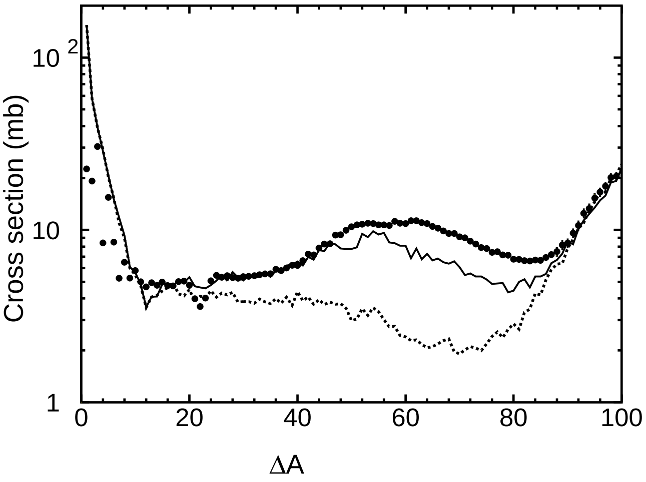

Figure 5.13: *Isobaric distribution of evaporation residues obtained in the reaction* ^{238}*U(1 A·GeV)+d [Cas01] compared with model calculations using different description for the fission probability: Fission width given by the Kramers solution* Γ_f^K *(dashed line) and the time-dependent solution of reference [Jur02] with* $\beta = 2$ *Zs*$^{-1}$ *(solid line).*

Determination of β from the Kramers factor

The productions of actinides and heavy pre-actinides could then be used to analyze the value of β responsible for the hindrance of fission at low excitation energies. Figure 5.14-a compares the measured isobaric distribution of evaporation residues with different calculations made with the time-dependent fission width of equation 5.3 using three different values of the dissipation coefficient. As can be seen, the value that better reproduced the productions of evaporation residues in the region $\Delta A < 40$ was β =2 Zs^{-1}, which corresponds to a critical damping of the fission motion. On the other hand, as expected by the β-dependence of the Kramers factor (equation **??**), the underdamped (β =1 Zs^{-1}) and overdamped (β =3 Zs^{-1}) coefficients led to an underestimation and an overestimation of the hindrance of fission, respectively.

Analysis of the time dependence of the fission width

At higher energies, or equivalently for lighter masses ($\Delta A > 50$), the sensitivity of the data to the differences on β decreases; in fact this region is almost equally well reproduced with any of the three values of β. Such a behavior is a direct consequence of the onset of transient-effects which occurs at energies above ∼150 MeV, as discussed in section 1.2. The influence of dissipation upon the productions of light evaporation residues arises from the combined actions of the Kramers factor and transient effects, so that the relation between β and the fission probability is more complicated than at lower energies.

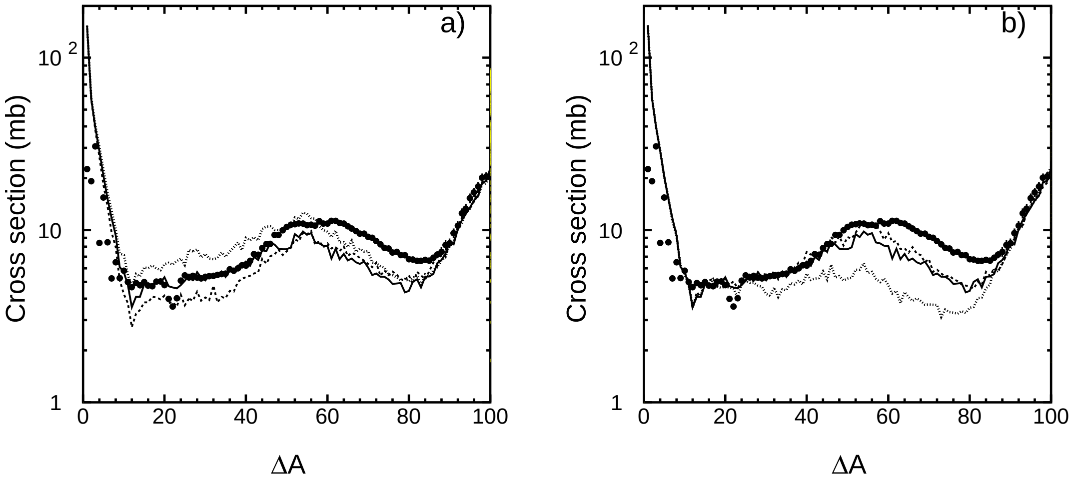

Figure 5.14: *Isobaric distribution of evaporation residues produced in the reaction* $^{238}U(1\ A\cdot GeV)+d$ *[Cas01] compared with model calculations using different description for the fission probability. (a) Fission width given by* $\Gamma_f^{fpe}(t)$ *with* $\beta = 1\ Zs^{-1}$ *(dashed line),* $\beta = 2\ Zs^{-1}$ *(solid line) and* $\beta = 3\ Zs^{-1}$ *(dotted line). (b) Fission widths calculated with* $\beta = 2\ Zs^{-1}$ *and the approximated solution of the Fokker-Planck equation* $\Gamma_f^{fpe}(t)$ *(solid line), the step function* $\Gamma_f^{ste}(t)$ *(dashed line) and the exponential in-growth function* $\Gamma_f^{exp}(t)$ *(dotted line).*

The sensitivity of the lightest evaporation residues to the transient times, which was illustrated in figure 5.13, could be used to test the validity of other time-dependent formulations of the fission width. Figure 5.14-b compares the results obtained with the fission width of B. Jurado et al. [Jur04a] (equation 5.3), with two alternative formulations that have been largely used in the past, namely the step function $\Gamma_f^{ste}(t)$:

$$\Gamma_f^{ste}(t) = \begin{cases} 0 & , t < \tau_{tr} \\ 1 & , t \geq \tau_{tr} \end{cases}$$

and the exponential in-growth function $\Gamma_f^{exp}(t)$:

$$\Gamma_f^{exp}(t) = \Gamma_f^K \cdot \left(1 - e^{-\frac{t}{\tau}}\right)$$

where τ_{tr} is the transient time, calculated according to reference [Bha86] with $\beta = 2\ \mathrm{Zs}^{-1}$; $\tau = \tau_{tr}/2.3$ and Γ_f^K is the Bohr and Wheeler fission width multiplied by the Kramers factor.

The fast increase of the $\Gamma_f^{exp}(t)$ compared to the other two formulations enables fission to occur at very earlier. As a consequence, the production of low-fissile evaporation residues in the region $40 < \Delta A < 80$ is depleted due to the underestimated transient effects, in clear contradiction with the experimental data. This result demonstrates the disability of $\Gamma_f^{exp}(t)$ to describe the fission process at high energies, as was already demonstrated in the analysis of Jurado et al. [Jur04b]. A much better agreement is obtained with the two other formulations, $\Gamma_f^{fpe}(t)$ and $\Gamma_f^{ste}(t)$ which provide equivalent results; though the formulation based on the approximated solution of the Fokker-Planck equation has a major physical consistency.

Transient effects on the total fission cross section

Transient effects can also been experimentally investigated by analyzing the total nuclear fission cross sections σ_{fiss} of spallation reactions induced with Uranium on different targets [Jur04c]. For a given reaction, the total fission cross section can be calculated according to:

$$\sigma_{fiss} = \sigma_R \cdot P_{fiss} \tag{5.16}$$

where σ_R is the total reaction cross section and P_{fiss} is the fission decay probability for the excited compound nuclei. Whereas σ_R increases with the mass of the target nuclei, the value of P_{fiss} depends very much on the distribution of decaying compound nuclei and their excitation energies. Figure 5.15 shows the calculated distribution of the fission probability as a function of the charge of the fissioning compound nuclei for some reactions investigated in reference [Jur04c], together with the present reaction. The value of P_{fiss} for each reaction corresponds to the integral of the respective curves.

According to B. Jurado et al. [Jur04c], the reduction of the fission probability for heavier targets has its explanation on dissipation: As the mass of the target increases, the pre-fragment productions extend to lighter nuclei with higher excitation energies and higher fission barriers. Due to the increasing energies, the fission decay is affected by transient effects, leading to a systematic reduction of P_{fiss}.

As far as the total fission cross section is concerned, the decrease of the fission probability is partly compensated by the increase of σ_R with the mass of the target nuclei. These two opposite trends lead to the characteristic behavior of σ_{fiss} with the target mass, shown in figure 5.16. The figure compares the values of σ_{fiss}, measured in reference [Jur04c] and in the present work, with different model calculations. Since the ISABEL code (solid line) can not describe heavy nucleus-nucleus collisions, we used the abrasion code of J.-J. Gaimard and K.-H. Schmidt [Gai91] (dashed line) to calculate the first step of the reactions induced on the heaviest targets (Copper and Lead). The second stage was calculated with two different versions of the ABLA deexcitation code: one with $\beta = 2$ Zs^{-1} and Γ_f^{fpe}, and the other one without dissipation. In this sense, it is noteworthy the very good agreement between the calculations made with ISABEL and the abrasion codes for an intermediate target nucleus like Carbon.

As can be seen, the inclusion of dissipation (thick solid and dashed lines) leads to a general good quantitative agreement with the experimental data. In particular, the dependence of σ_{fiss} on the mass of the target nuclei, including the local maximum found for the reaction induced on deuterium, is only reproduced when dissipation is included. By contrast, the experimental cross sections of the heaviest targets

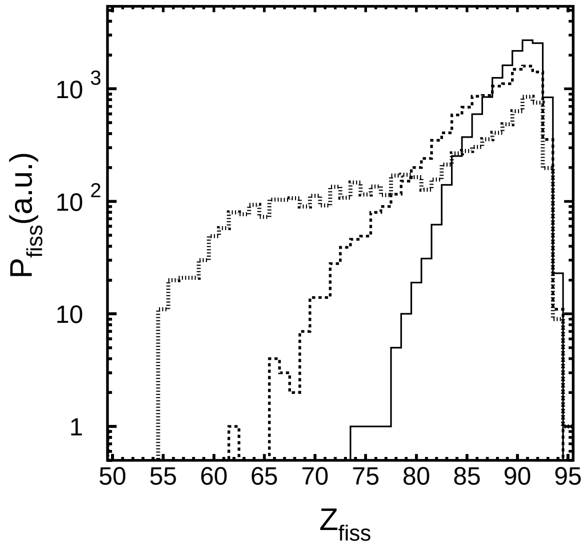

Figure 5.15: *Calculated fission probability P_{fiss} as a function of the charge of the fissioning compound nuclei Z_{fiss} produced in three spallation reaction: ^{238}U at 1 A·GeV on proton [Jur04c] (solid line), ^{238}U at 1 A·GeV on deuteron (dashed histogram) and ^{238}U at 1 A·GeV on carbon [Jur04c] (dotted histogram). The calculation was done with the standard version of our code, which included $\beta = 2\ Zs^{-1}$ and $\Gamma_f^{fpe}(t)$.*

(between Carbon and Lead) are drastically overestimated by the calculation that considered the statistical Bohr-Wheeler fission width (thin solid and dashed lines). On the other hand, the value of σ_{fiss} measured in the present work for the deuterium target turns out to be insensitive to dissipation, or in other words, the total fission cross section could be equally well reproduced with the calculation with and without dissipation. The underestimated value of the calculated σ_{fiss} in the deuterium case could come from the total reaction cross section σ_R used to normalize the fission cross sections: This quantity, which was calculated according to the Karol's model[Kar75], was slightly underestimated with respect to the measured value of 2.70±0.35 barn, as was discussed in the previous chapter. The use of this latter value would improve the results of the calculation with dissipation.

According to the work of B. Jurado et al. [Jur04c], the increasing excitation energies of the reactions induced with the heavier targets lead to a systematic decrease of σ_{fiss}, from a maximum value for the proton case to a minimum value found for the Carbon target. Our result, however, demonstrates that although dissipation reduces the value of P_{fiss} for the increasing target masses, the opposite trend of σ_R leads to a more complicated behavior of σ_{fiss} in the region of light targets (between proton and Carbon) that is responsible for the local maximum observed for the deuterium case.

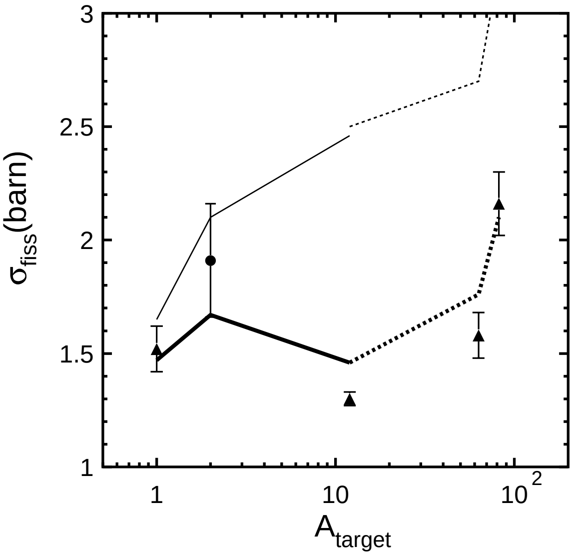

Figure 5.16: *Total nuclear fission cross section of* ^{238}*U(1 A·GeV) as a function of the target mass. Experimental data obtained in reference [Jur04c] are represented by triangles, while that measured in the present work corresponds to the full dot. The calculations were done with ISABEL (solid line) and ABRA (dashed line), both coupled to the deexcitation subroutine that includes dissipation. The calculations were made with* $\beta = 2$ *Zs*$^{-1}$ *and* $\Gamma_f^{fpe}(t)$ *(thick lines) and without including dissipation (thin lines). Note that the horizontal axis is in logarithmic scale.*

Effects of dissipation at small deformation on the fission residue productions

As discussed in above, the lack of correlation between the mass of the fission fragments and their initial energy (see figure 5.12) makes it impossible to separate the two effects of dissipation at small from the measured masses of these residues. However, the conclusions extracted from the analysis of the evaporation residues can be used to calculate the fission production cross sections.

Figure 5.17 compares the measured isotopic fission cross sections of some selected elements with a calculation made with the standard version of the ISABEL+ABLA code, which uses $\beta = 2$ Zs^{-1} and $\Gamma_f^{fpe}(t)$ given by equation 5.3. As can be seen, the fair agreement between the experimental data and the calculation validates the results obtained from the previous analysis of evaporation residues.

Apart from this, the maximum of these isotopic chains are sensitive to the number of neutrons evaporated beyond the saddle point, which depends on the excitation energy of the nucleus at the saddle point. Since this energy is very much affected by the transient effect discussed above, the good agreement between the calculated and measured isotopic fission cross sections demonstrates that the excitation energies at saddle are well described when dissipation is included.

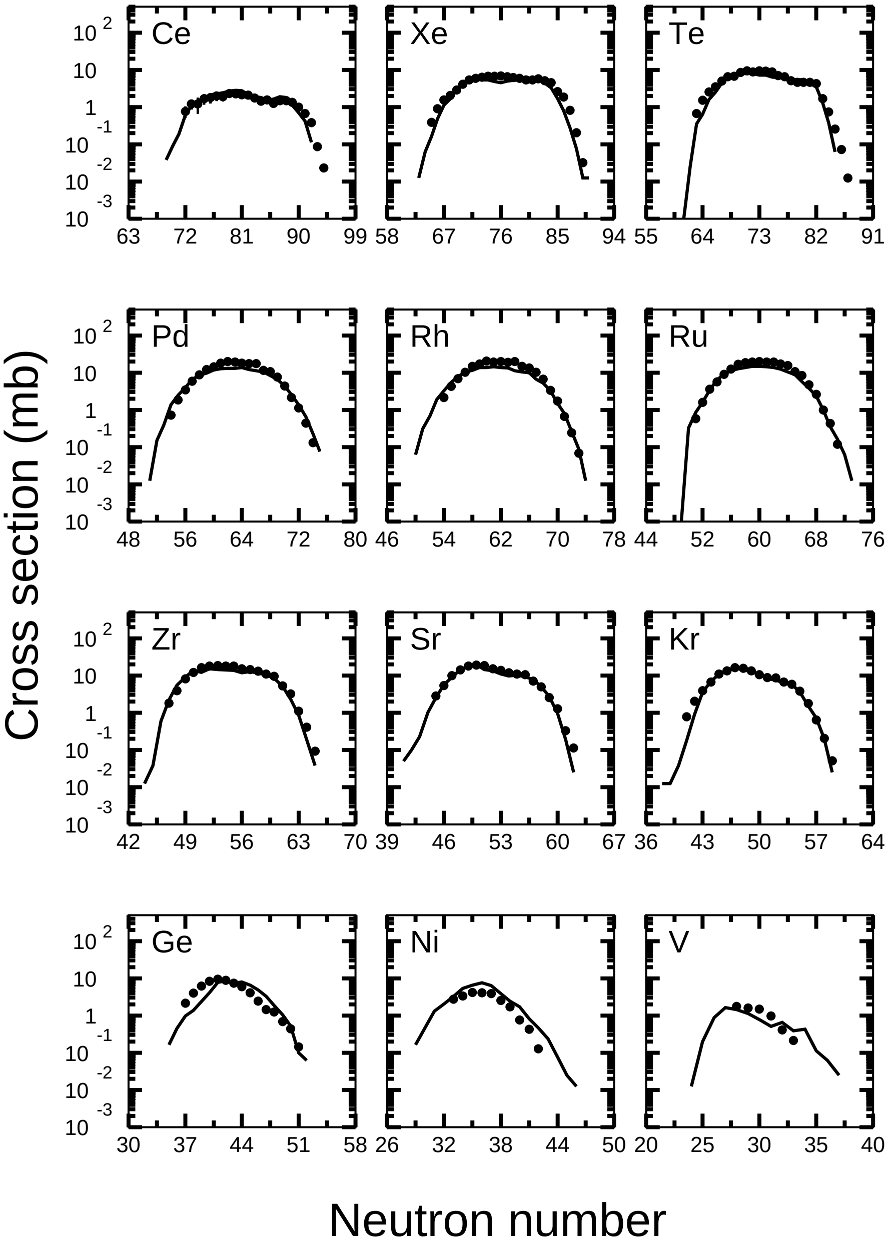

Figure 5.17: *Isotopic production cross sections of fission residues measured in the present work for the reaction* ^{238}*U(1 A·GeV)+d (full dots) compared with calculations made with ISABEL coupled to the ABLA code using* $\beta = 2\ Zs^{-1}$ *and* $\Gamma_f^{fpe}(t)$ *(solid line).*

Finally, from the results discussed above, we conclude that the production cross sections of evaporation residues, measured in the reaction ^{238}U(1 A·GeV)+d, are better suited to investigate dissipation at small deformations than fission. The wide mass ranges covered by those residues offer an optimum tool to analyze the damping of the fission motion as a function of excitation energy: Firstly, the productions of actinides and heavy pre-actinides at low energies were very sensitive to the Kramers factor. Then, these residues provided information on the value of β. Secondly, at higher excitation energies, the strong dependence of the production of light evaporation residues on the transient effects enabled to investigate the formulation of $\Gamma_f(t)$. The value of $\beta = 2$ Zs^{-1} obtained in the present analysis coincides with the results obtained from previous measurements of spallation residues of ^{197}Au at 1 A·GeV on proton [Ben02]. Moreover, the conclusions regarding the formulation of the time-dependent fission width validate the analysis of Jurado et al. [Jur04b].

5.3.2 Dissipation at large deformations

As already mentioned above, the time required for a fissioning nucleus to descent from the saddle to the scission points, i.e. the saddle-to-scission time τ_{ssc}, can be affected by dissipation. Since the nuclear deformations involved in this process are much larger than those near the ground-state configuration, the dissipation coefficient may vary significantly with respect to the value at small deformations. In this section we propose to investigate this issue by estimating the average saddle-to-scission neutron multiplicities of the decaying compound nuclei produced in the present reaction. This analysis was possible by combining the measured velocities of fission residues, shown in chapter 3, with their production cross sections, described in chapter 4:

Post-scission neutron multiplicities

The method used in chapter 4 to determine the charge distribution of the fissioning nuclei from the measured velocities v_{fiss} (figure 4.26) could also be used to reconstruct the masses of these parent nuclei. According to equation 3.16, based on the scission model [Wil76], the measured fission velocity v_{fiss} of a given nucleus (Z_1, A_1) can be used to deduce the charge of the fissioning system $Z_{fiss} = Z_1 + Z_2$ (with the indexes 1 and 2 referring to the two fragments that define a fission pair). From this quantity is then possible to determine the mass of the corresponding fissioning nucleus $A_{fiss}(Z_{fiss})$, by making use of the unchanged-charge-density hypothesis (UCD):

$$A_{fiss}(Z_{fiss}) = Z_{fiss}\frac{A_1}{Z_1} = Z_{fiss}\frac{A_2}{Z_2} \tag{5.17}$$

For each fission residue, the values of Z_{fiss} and A_{fiss} that better reproduced the measured velocity were weighted according to its production cross sections. By following this procedure we obtained a distribution of fissioning nuclei.

It is important to note that the UCD-hypothesis, used to determine mass A_{fiss} in equation 5.17, implicitly neglects the neutrons evaporated from the two fission fragments (post-scission neutron emission). As a consequence, the A_{fiss}-distribution obtained by this method is shifted toward the neutron deficient side with respect to the actual masses of the fissioning systems at the scission point (referred to as A^0_{fiss}). Let's define Z^0_1, Z^0_2, A^0_1 and A^0_2 as the atomic and mass numbers of the two fission fragments at scission (note that $A^0_1 + A^0_2 = A^0_{fiss}$). Since we can assume that no protons are evaporated post-scission, then $Z_1 = Z^0_1$ and $Z_2 = Z^0_2$. On the other hand, the final masses of the measured fission residues (A_1, A_2) are related to their original values at scission according to:

$$A_1 = A^0_1 - \nu_{sc,1} \tag{5.18}$$

$$A_2 = A^0_2 - \nu_{sc,2} \tag{5.19}$$

where $\nu_{sc,1}$ and $\nu_{sc,2}$ are the post-scission neutrons emitted from the two fragments. For a given value of Z_{fiss}, the mass deduced from the measured values Z_1, A_1, using equation 5.17 is equal to:

$$A_{fiss,1} = Z_{fiss}\frac{A_1}{Z_1} = Z_{fiss}\left(\frac{A^0_1}{Z_1} - \frac{\nu_{sc,1}}{Z_1}\right) = A^0_{fiss} - \frac{Z_{fiss}}{Z_1}\cdot\nu_{sc,1} \tag{5.20}$$

where the subindex $fiss,1$ refers to the fissioning system calculated from the measured fission fragment Z_1, A_1. If we assume for simplicity that $Z_1 \simeq Z_{fiss}/2$, then this equation becomes:

$$A_{fiss,1} = Z_{fiss}\frac{A_1}{Z_1} \simeq A^0_{fiss} - 2\cdot\nu_{sc,1} \tag{5.21}$$

Likewise, for the other fission fragment Z_2, A_2:

$$A_{fiss,2} = Z_{fiss}\frac{A_2}{Z_2} \simeq A^0_{fiss} - 2\cdot\nu_{sc,2} \tag{5.22}$$

by summing these two equations we get:

$$\nu_{sc,1} + \nu_{sc,2} \simeq A^0_{fiss} - \frac{A_{fiss,1} + A_{fiss,2}}{2} \tag{5.23}$$

Thus, for a given Z_{fiss}, the average number of post-scission neutrons could be determined from the difference between the mean value of the A_{fiss}-distribution, deduced from the measured v_{fiss}, neglecting post-scission neutron evaporation, and the actual mass of the fissioning isotopes A^0_{fiss}. This latter quantity was estimated with the version of the ISABEL+ABLA code used in the previous section to describe both the evaporation and fission production cross sections. The results of these calculations are compared in figure 5.18 with the measured evaporation cross sections (dots) for some selected elements. The solid line represents the distributions of residues obtained with the version of the code that included dissipation, while the dashed line corresponds to a calculation where fission was switched off. The latter is the result of two different contribution: The first one comes from those nuclei

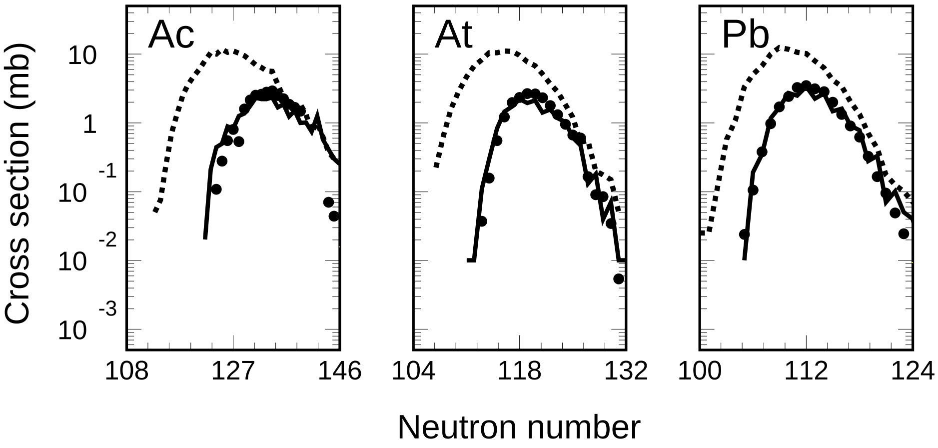

Figure 5.18: *Three examples of the method used to determine the actual distribution of fissioning nuclei (A^0_{fiss}). The dots represent the isotopic cross sections of evaporation residues [Cas01], which are very well reproduced by the standard version of the ISABEL+ABLA code (solid line). The dashed line represents the results obtained when fission was suppressed in the calculation.*

that will not fission, even when this process is switched on in the calculation (it corresponds to the region where the dashed and solid lines coincide). The second one corresponds to the evaporation residues that result from the deexcitation of the nuclei that would fission at scission if this decay channel was switched on. Since the fissioning nuclei at scission lay somewhere in the region delimited by these distributions, we choose as a first approximation of A^0_{fiss} the mean value of these isotopic curves.

The mean mass of the fissioning nuclei (A^0_{fiss}), corresponding to a given element, was compared with the value obtained from the analysis of the velocities of the fission residues. The differences between these two masses provided an estimation of the average post-scission neutron multiplicities for that element. An example of this method is illustrated in figure 5.19 for two selected elements. The resulting post-scission neutron multiplicities $\bar{\nu}_{ssc}$ are shown in figure 5.20 as a function of Z_{fiss}. The large error bars associated with these method arise from the uncertainties in determining the mean values A_{fiss} and A^0_{fiss}. In particular, the estimation of A^0_{fiss} from the distributions calculated with the version of ABLA that neglected fission, became more inaccurate as we approach the Uranium isotopes, due to the increasing asymmetry of these distributions. Moreover, the increasing contribution of the low-energy fission component for charges close to the Uranium projectile precludes the application of the Wilkins formula (equation 3.16) in our analysis.

In figure 5.20, we compared the post-scission multiplicities obtained in the present work (dots), with the systematics proposed by D. Hilscher and H. Rossner [Hil92] (thick dashed line), which provides these post-scission multiplicities for different

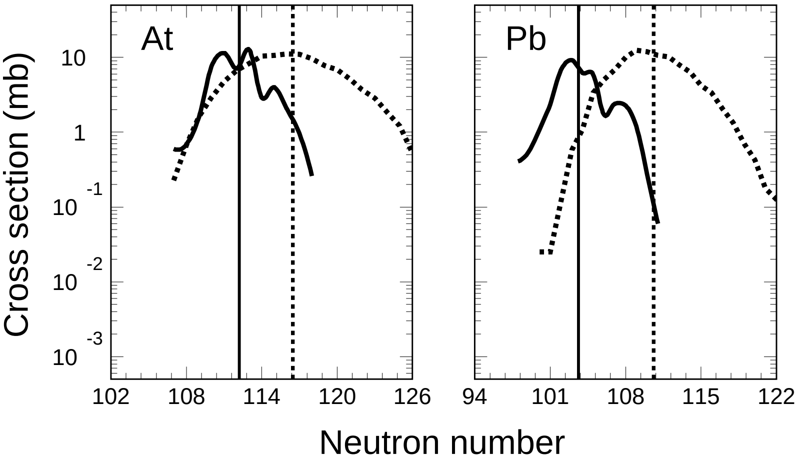

Figure 5.19: *Two examples of the method used to determine* $\bar{\nu}_{sc}$ *for* $_{85}At$ *and* $_{82}Pb$. *The dashed line represents the calculated* A^0_{fiss}*-distributions. The solid line corresponds to the* A_{fiss}*-distribution obtained from the measured fission velocities* v_{fiss}. *The vertical solid and dashed lines represent the mean values of these two distributions (see texts for details).*

elements as a function of their excitation energy. In order to make this comparison feasible, we had to estimate the average excitation energy of the pre-fragments produced in the reaction ^{238}U(1 A·GeV)+d with the standard version of the ISABEL+ABLA code. The uncertainty in this latter quantity induced an error of ±0.5 in the evaluated post-scission multiplicities from the Hilscher's systematics. As can be seen, these latter results are compatible with the our estimated values. This validates the method described above to determine the post-scission neutron multiplicities.

Finally, in order to analyze the influence of dissipation, we calculated the post-scission neutron multiplicities with a version of the ABLA code that disregarded viscosity from the ground-state configuration to the scission point. According to this code, the number of neutrons emitted after fission depends on the excitation energy transferred from the fissioning nucleus at the saddle point to the nascent fragments at the scission point. Note that in doing so, we are not explicitly considering the neutrons evaporated from the compound nucleus during the descent from saddle-to-scission. In fact, the energy that would be released in this process is directly transferred to the nascent fission fragments, or in other words, the saddle-to-scission emission is implicitly included in the calculated post-scission emission. For this reason, the calculated "post-scission" neutrons correspond actually to the post-saddle emissions $\bar{\nu}_{sad}$. In order to determine the actual value of post-scission neutrons, when dissipation is neglected, we have estimated the saddle-to-scission contributions ν_{ssc}

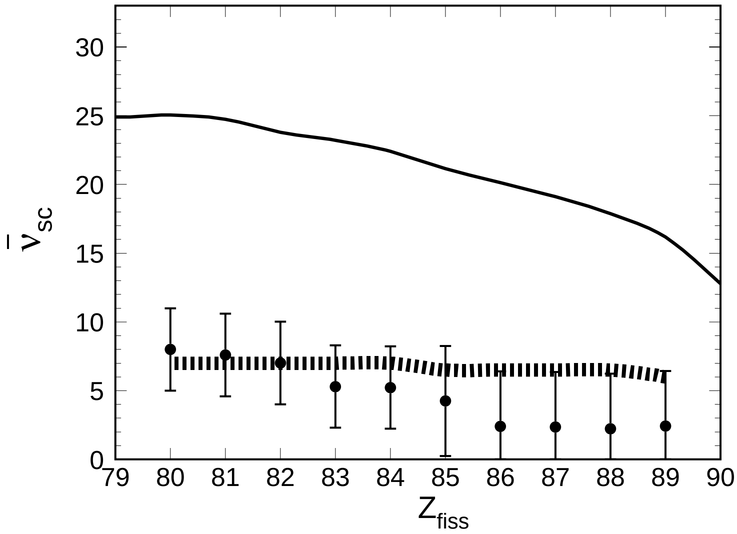

Figure 5.20: *Post-scission neutron multiplicities for the fissioning nuclei produced in the reaction* $^{238}U(1\ A{\cdot}GeV)+d$. *The results obtained in the present work (dots) are compared with Hilsher's systematics, represented by the thick dotted line. Solid line corresponds post-scission multiplicities calculated with a version of our code that disregards dissipation.*

according to:

$$\tau^0_{ssc} \equiv \sum_{i=1}^{\bar{\nu}_{ssc}} \frac{\hbar}{\Gamma_i} \tag{5.24}$$

where τ^0_{ssc} is the non-dissipative saddle-to-scission time (see appendix E) and Γ_i are the neutron evaporation widths, which were determined from the calculated charge, mass, energy and angular momentum of the compound nuclei at saddle. By following this procedure, we obtained an average saddle-to-scission multiplicity of $\bar{\nu}_{ssc} \simeq 4$, which was then subtracted to the calculated average "post-saddle" neutron. The resulting post-scission multiplicities as a function of Z_{fiss} are represented in figure 5.20 by a solid line. As can be seen, the calculated values are far above the experimental results obtained in the present work and in reference [Hil92]. To our understanding, this finding reflects an overestimation of the calculated excitation energy at scission: If dissipation is neglected, fission can occur at earlier times, when the compound nucleus is highly excited. These high excitation energies are then transferred into the nascent fission fragments, leading to overestimated post-scission multiplicities. By contrast, if dissipation is included, then the neutrons evaporated during the transient time of the fission motion might cool down the nucleus before fission occurs.

Saddle-to-scission multiplicities

As was mentioned in the beginning of this section, the saddle-to-scission neutron multiplicities $\bar{\nu}_{ssc}$ can provide valuable information on dissipation at large deformations. This quantity ($\bar{\nu}_{ssc}$) could be estimated by comparing the post-scission multiplicities $\bar{\nu}_{sc}$ obtained in the present work (figure 5.20) with the post-saddle emissions $\bar{\nu}_{sad}$, deduced from the standard version of the ABLA code (see section 5.3.1). It is worthwhile to remember that the value of $\beta = 2$ Zs^{-1} used in our calculations involves deformations up to the saddle-point. The use of this coefficient was justified by the fair agreement between the calculated and the measured productions of fission and evaporation residues. Since the shapes of the isotopic distributions of these residues are sensitive to the pre-saddle and post-saddle neutron emission, we assume that the calculated values of $\bar{\nu}_{sad}$ are correct within an error of about ±0.2.

These values were then used to determine the saddle-to-scission multiplicities $\bar{\nu}_{ssc}$ from the estimated values of $\bar{\nu}_{sc}$ shown in figure 5.20. The resulting values are shown in figure 5.21 for the different values of Z_{fiss}.

Dissipation beyond the saddle point

The values saddle-to-scission neutron multiplicities shown in figure 5.21 correspond to the average number of neutrons emitted by the fissioning nuclei during the time time τ_{ssc} (appendix E). Following the H. Hofmann and J. Nix formalism [Hof83], this parameter can be calculated according to:

$$\tau_{ssc} = \left[\left(1+\gamma^2\right)^{1/2} + \gamma\right] \tau^0_{ssc} \tag{5.25}$$

where γ is related to the reduced dissipation coefficient β according to equation 1.16, and the time τ^0_{ssc} is determined in appendix E. By making use of equation 5.25, we calculated τ_{ssc} for different dissipation coefficients γ. The resulting values of τ_{ssc} were then used to calculate the saddle-to-scission multiplicities, according to:

$$\tau_{ssc} = \sum_{i=1}^{\bar{\nu}_{ssc}} \frac{\hbar}{\Gamma_i} \tag{5.26}$$

The mass, charge, excitation energy and angular momentum required to determine the values of Γ_i and τ^0_{ssc} were provided by the standard version of the ABLA code (that included $\beta = 2$ Zs^{-1} up to the saddle point). Figure 5.21 shows the saddle-to-scission multiplicities, calculated for different dissipation coefficients, compared to the value of $\bar{\nu}_{ssc}$ obtained from the analysis described in the previous section [1].

As can be seen, the value $\gamma = 1$, which approximately corresponds to $\beta = 2$ Zs^{-1}, does not reproduce the deduced saddle-to-scission neutron multiplicities. By contrast, the larger dissipation coefficients $\gamma > 3$ provide a general better agreement

---

[1] By assuming $\omega_0 \simeq 1$ Zs^{-1}, we could relate the values of γ with the reduced dissipation coefficient β according to $\beta = 2\gamma$ Zs^{-1}

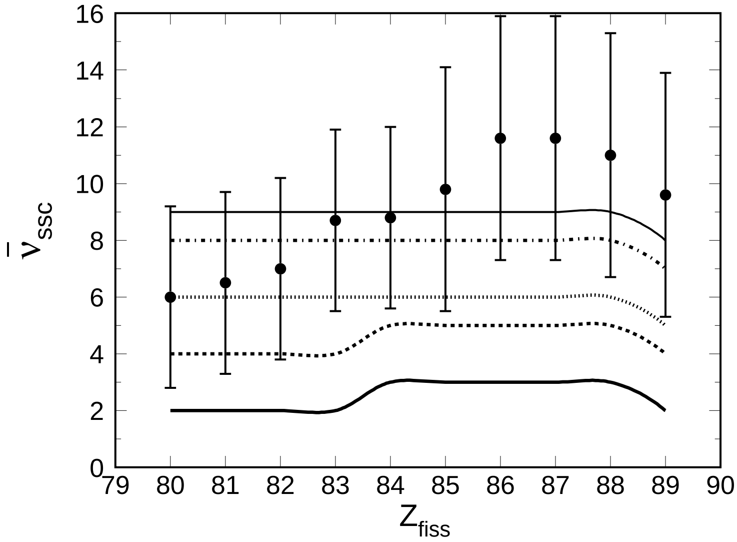

Figure 5.21: *Saddle-to-scission neutron multiplicities for the fissioning nuclei produced in the reaction* ^{238}*U(1 A·GeV)+d. The results obtained in the present work (dots) are compared with calculations made with equation 5.25 for different values of* γ*:* $\gamma = 1$ *(thick solid line),* $\gamma = 3$ *(thick dashed line),* $\gamma = 5$ *(dotted line),* $\gamma = 12$ *(dash-dotted line) and* $\gamma = 24$ *(solid line).*

with the data. This trend was also observed when the post-scission neutron multiplicities determined from Hilscher's systematics were used to estimate $\bar{\nu}_{ssc}$. In that case, the values of the dissipation coefficient that better described the data corresponded to value about $\gamma = 5 - 10$.

According to this result, the dissipation coefficient varies with deformation, from a constant value of $\beta = 2$ Zs^{-1} (between the ground-state configuration and the saddle point) to values $\beta > 6$ Zs $^{-1}$. It is noteworthy that these increase of β at large deformations suggests a deformation-dependent dissipation coefficient. In fact, such an increase was already proposed by Fröbrich et al. [Fro93] to explain the large pre- and post-scission multiplicities observed in fusion-fission reactions. It is worthwhile to insist on the fact that our method is not sensitive to the exact value of γ but rather to its increase with deformations. Such dependency might be interpreted as a signature of one-body dissipation mechanisms.

Finally, we conclude that the present experiment made it possible to investigate the role of dissipation at different excitation energies and different deformations. From the analysis of the evaporation cross sections we could investigate separately the absolute value of the reduced dissipation coefficient β and the time-dependence of the fission width at higher excitation energies. This results confirmed the conclusions of previous works aimed to analyze dissipation from the productions of fission residues in spallation reactions.

In addition, the productions cross sections and kinematical properties of fission residues were used to deduce an approximated value of post-scission multiplicities. The validity of this method was partly justified by the good agreement between our results and the values deduced from experimental systematics. Apar from this, by comparing these post-scission multiplicities with model calculations we could investigate the role of dissipation at large deformations. From this analysis we observed an increase of dissipation with respect to the value $\beta = 2\ \mathrm{Zs}^{-1}$ at small deformations. The validity of this result might be experimentally confirmed by analyzing the reaction ^{238}U(1 A·GeV)+d with an improved experimental setup that provide a complete kinematical analysis of the two fission fragments, together with the number of pre-scission and post-scission neutron multiplicities.

Conclusions

In the present work, the collective nature of excited nuclei was investigated by analyzing the collective motion associated to the fission process and its competition to the evaporation of light particles. From a comparative study of the residue productions originated from these two processes, we could get insight into the dynamical coupling of collective and internal degrees of freedom through viscosity, as well as the presence of collective rotational and vibrational motions.

The hot fissioning nuclei produced by the spallation of Uranium at 1 A·GeV on deuterium were characterized by small shape deformations, low angular momentum and wide ranges of excitation energy [Ser47]. These initial conditions provide an optimum scenario to investigate the phenomena associated to the subsequent deexcitation processes. The high fissilities of Uranium-like pre-fragments enable to investigate the damping of the fission motion at rather low excitation energies, as well as the role of rotations and vibrations on the competition between fission and evaporation during the deexcitation process. Moreover, at higher energies, the excited fissioning nuclei are expected to be very sensitive to transient effects.

The precisions required to investigate the fission residues produced in the reaction ^{238}U(1 A·GeV)+d were only attainable with the heavy-ion experimental facility at GSI (Germany). The Uranium beam, accelerated in the SIS up to 1 A·GeV, was focused onto the deuterium target sited at the entrance of the FRagment Separator (FRS). The high resolutions of this device enabled to separate and identify the reaction products according to their atomic Z and mass A numbers. Furthermore, the kinematical properties and production yields of each nucleus were measured very precisely. A total amount of about 1000 fission residues were analyzed by following this procedure. These data, together with the previously analyzed evaporation contribution [Cas01] provide a complete experimental survey on the production of residual nuclei in the reaction ^{238}U(1 A·GeV)+d.

As far as the kinematical analysis is concerned, it consisted on the measurement of the absolute velocities of the fission residues in the frame of the fissioning system. By comparing these velocities with the predictions of the quasiestatistical prescission model of Wilkins et al. [Wil76], applied to high-energy fission [Boc97], the distribution of fissioning elements contributing to the final residue productions could be inferred. Within a given isotopic chain, the most neutron-deficient nuclei were produced by rather light fissioning elements, while the opposite trend was observed with approaching the neutron-rich side. The distribution of fissioning elements was estimated to range from about charge Z=70, for the lightest fission fragments to

Z=92, for the most neutron-rich isotopes. Moreover, the larger velocities of the most neutron-rich isotopes of Sn,Sb and Te respect to the theoretical predictions of the Wilkins model were interpreted as a signature of low-energy fission. According to the Wilkins model, the low-energy fission mode Standard I [Bro90], associated to the closed shell N=82, is characterized by rather compact shapes. The observed increase of the fission velocity with respect to the Wilkins model was then produced by the increased Coulomb repulsion. This result is in agreement with previous measurements of low-energy induced fission of Uranium systems [Don98, Enq99].

The production cross sections of fission residues were measured for each nucleus with precisions of the order of 10% to 30%, down to values of 10 μb. The comparison of these measurements with the results obtained for the reaction ^{238}U(1 A·GeV)+p [Ber03] revealed an enhanced production of neutron-deficient isotopes arising from the lightest fissioning systems. On the other hand, the enhanced productions of neutron-rich isotopes observed in both reactions for some elements were interpreted as originated from the low-energy fission component. By adjusting each isotopic chain to two Gaussian functions we could determine the contribution of the high- and low-energy components to the total isotopic productions of some elements. The Z-integrated cross section of the low-energy component was 92±27 mb, which represents a very small fraction of the total fission cross section of 2.00±0.22 barn. In addition, the mean values and widths of these Gaussian functions also provided the mean mass numbers and mass dispersions of the high- and low-energy fission component. From these values, the average post-scission neutron multiplicity could be estimated for the different low-energy fission element pairs. These multiplicities were found to decrease sharply from a constant value about 6, for the more asymmetric element pairs, to ∼4 for the less asymmetric pairs $Te - Zr$, $Sb - Nb$ and $Sn - Mo$. This result indicates a reduction of the deformation energy of these nuclei, which is compatible with the compact shapes expected from the Standard I asymmetric fission mode, already deduced from the analysis of the fission velocities.

Concerning the high-energy component, the combination of the isotopic production cross sections and the analysis of the fission velocities with the Wilkins formula enabled to deduce the distribution of fissioning elements for the first time. This distribution showed a considerable contribution from the light fissioning systems which reflects the delay of the fission process at high energies due to transient effects.

Finally, the fission and evaporation residue productions measured in the reaction ^{238}U(1 A·GeV)+d were compared with the predictions of model calculations in order to get insight into the collective motions manifested during the deexcitation process.

From the isobaric distributions of actinides and heavy pre-actinides we could investigate the presence of collective rotational and vibrational excitations. These two modes are known to affect the competition between fission and evaporation by increasing the statistical weight associated to each decay process. According to our calculations, the large contribution of rotational states at saddle-point deformations compensate the shell stabilization against fission of actinide isotopes near N=126, confirming the results of A. Junghans et al. [Jun98]. However, we have shown that the description of the level density enhancement due to vibrational modes, introduced by these authors, led to an understimation of the measured evaporation cross sections around the closed shells Z=82 and N=126. The accuracy of the new data has allowed to improve this prescription.

The underestimated productions of Hg isotopes seems to indicate the necessity of including additional collective modes at the ground-state to increase the stability against fission. This phenomenon might be explained as due to the coexistence of different intruder low-lying deformed states near the ground-state, that would enhance the level density. These results demonstrates the sensitivity of the residual nuclei produced after long evaporation chains to collective excitations and their damping with excitation energy. Furthermore, this new observable provides a complentary approach to the spectroscopic techniques.

We also demonstrated that the isobaric distributions of evaporation residues are sensitive to the damping of fission due to dissipation at small deformations. In particular, the large range of excitation energies covered by these data allowed to dissentangle the two main manifestations of dissipation in fission: the reduction of the statistical fission width and the delay of fission due to transient effects. We have shown that the productions of actinides and heavy pre-actinides $\Delta A < 20$ at low energies were very much affected by the absolute value of the reduced dissipation coefficient, which was established to be $\beta = 2$ Zs^{-1}. This finding confims the results obtained in previous experiments [Ben02, Jur04c]. Moreover, lighter evaporation residues produced at higher excitation energies turned out to be very sensitive to transient effects. Systematic comparisons of the production cross sections of these nuclei with model calculations have allowed to investigate the time dependence of the fission width. Our data confirm the validity of the time-dependent fission width proposed by Jurado et al. [Jur04a], based on an approximated solution of the Fokker-Planck equation. In addition, this analysis allowed to reject some unrealistic time-dependent fission widths that have been largely used in the past.

The two additional observables provided by this experiment -the production cross sections and kinematic properties of the fission residues-, together with the model calculations were used to investigate the dissipation in fission at large deformation. A new method has been proposed to estimate the post-scission neutron evaporation from these two observables. Although these neutron multiplicities were deduced following an indirect method, the final values were validated by the systematics of Hilscher [Hil92]. The comparison of these results with reliable model calculations allowed to estimate the saddle-to-scission neutron multiplicities. Following the formalism of H. Hofmann and J. Nix [Hof83], to describe the dynamics from saddle to scission, we showed that the deduced neutron multiplicities were compatible with a dissipation coefficient γ larger than 5. The confirmation of these results would demonstrate a dependence of the nuclear viscosity with deformation.

Appendix A

Fission cross sections

Z	A	σ_{fiss}	$\delta\sigma_{fiss}$	Z	A	σ_{fiss}	$\delta\sigma_{fiss}$	Z	A	σ_{fiss}	$\delta\sigma_{fiss}$
23	51	1.757	0.039	27	60	3.454	0.114	29	73	0.205	0.003
23	52	1.583	0.013	27	61	3.651	0.101	29	74	0.082	0.002
23	53	1.462	0.010	27	62	3.248	0.080	30	64	1.344	0.049
23	54	0.962	0.018	27	63	2.629	0.058	30	65	3.004	0.089
23	55	0.406	0.013	27	64	1.794	0.038	30	66	4.622	0.128
23	56	0.216	0.009	27	65	0.841	0.023	30	67	6.168	0.151
24	53	2.335	0.047	27	66	0.382	0.008	30	68	6.336	0.185
24	54	2.449	0.048	27	67	0.264	0.007	30	69	5.941	0.145
24	55	2.024	0.037	27	68	0.094	0.002	30	70	5.262	0.126
24	56	1.315	0.025	27	69	0.041	0.001	30	71	4.067	0.098
24	57	0.546	0.007	28	61	2.747	0.130	30	72	2.424	0.061
24	58	0.277	0.004	28	62	3.334	0.144	30	73	1.209	0.018
24	59	0.066	0.003	28	63	4.142	0.119	30	74	0.837	0.011
25	55	2.666	0.062	28	64	4.071	0.121	30	75	0.414	0.010
25	56	2.688	0.070	28	65	3.872	0.077	30	76	0.114	0.004
25	57	2.807	0.058	28	66	2.530	0.060	30	77	0.049	0.002
25	58	1.792	0.034	28	67	1.727	0.041	30	78	0.018	0.001
25	59	1.254	0.027	28	68	0.757	0.014	31	67	2.439	0.117
25	60	0.509	0.014	28	69	0.431	0.016	31	68	4.275	0.117
25	61	0.278	0.006	28	70	0.126	0.002	31	69	6.287	0.149
25	62	0.074	0.002	29	63	3.283	0.098	31	70	7.644	0.204
26	57	2.725	0.061	29	64	4.264	0.116	31	71	8.136	0.207
26	58	3.505	0.089	29	65	5.239	0.144	31	72	6.944	0.176
26	59	2.921	0.063	29	66	5.253	0.146	31	73	5.689	0.132
26	60	2.501	0.060	29	67	4.444	0.130	31	74	3.872	0.092
26	61	1.849	0.042	29	68	3.868	0.094	31	75	2.023	0.061
26	62	0.865	0.022	29	69	2.682	0.064	31	76	1.631	0.024
26	63	0.358	0.012	29	70	1.366	0.037	31	77	0.860	0.035
26	64	0.121	0.003	29	71	1.087	0.015	31	78	0.410	0.012
27	59	3.031	0.123	29	72	0.430	0.011	31	79	0.283	0.007

Table A.1: Fission production cross sections (in mb) measured in the reaction ^{238}U(1·GeV+d)

Z	A	σ_{fiss}	$\delta\sigma_{fiss}$	Z	A	σ_{fiss}	$\delta\sigma_{fiss}$	Z	A	σ_{fiss}	$\delta\sigma_{fiss}$
31	80	0.115	0.002	33	85	0.241	0.007	35	86	5.501	0.084
32	69	2.143	0.141	33	86	0.122	0.003	35	87	5.173	0.062
32	70	3.972	0.186	34	73	1.351	0.057	35	88	3.420	0.095
32	71	6.200	0.176	34	74	3.023	0.141	35	89	1.995	0.057
32	72	8.405	0.241	34	75	5.450	0.191	35	90	0.717	0.023
32	73	9.442	0.234	34	76	7.865	0.272	35	91	0.289	0.006
32	74	8.833	0.232	34	77	10.170	0.247	35	92	0.065	0.003
32	75	7.365	0.190	34	78	12.445	0.314	36	77	0.776	0.064
32	76	5.839	0.155	34	79	11.989	0.313	36	78	2.028	0.145
32	77	4.113	0.103	34	80	10.706	0.279	36	79	3.922	0.173
32	78	2.420	0.045	34	81	8.465	0.224	36	80	6.639	0.255
32	79	1.442	0.032	34	82	6.439	0.171	36	81	10.859	0.276
32	80	1.227	0.030	34	83	4.873	0.076	36	82	13.445	0.352
32	81	0.686	0.017	34	84	3.944	0.068	36	83	16.237	0.456
32	82	0.435	0.011	34	85	2.918	0.080	36	84	15.452	0.425
32	83	0.143	0.003	34	86	2.087	0.060	36	85	13.534	0.349
33	71	1.576	0.081	34	87	0.947	0.028	36	86	10.497	0.298
33	72	3.543	0.126	34	88	0.429	0.008	36	87	8.853	0.249
33	73	6.148	0.178	34	89	0.122	0.003	36	88	8.605	0.142
33	74	7.647	0.185	35	75	0.947	0.080	36	89	6.673	0.090
33	75	10.800	0.278	35	76	2.462	0.123	36	90	5.700	0.157
33	76	10.033	0.253	35	77	4.085	0.207	36	91	3.757	0.112
33	77	10.395	0.263	35	78	7.266	0.256	36	92	1.762	0.054
33	78	7.746	0.201	35	79	10.410	0.294	36	93	0.636	0.020
33	79	6.031	0.169	35	80	12.277	0.329	36	94	0.206	0.003
33	80	4.134	0.071	35	81	14.477	0.396	36	95	0.051	0.002
33	81	2.833	0.042	35	82	12.034	0.336	37	79	0.451	0.049
33	82	2.174	0.026	35	83	10.729	0.278	37	80	1.555	0.120
33	83	1.630	0.046	35	84	8.378	0.222	37	81	3.458	0.198
33	84	0.742	0.011	35	85	6.352	0.127	37	82	6.602	0.233

Table A.2: Fission production cross sections (in mb) measured in the reaction ^{238}U(1·GeV+d)

Z	A	σ_{fiss}	$\delta\sigma_{fiss}$	Z	A	σ_{fiss}	$\delta\sigma_{fiss}$	Z	A	σ_{fiss}	$\delta\sigma_{fiss}$
37	83	10.261	0.296	38	98	1.275	0.040	40	96	15.263	0.455
37	84	14.378	0.415	38	99	0.328	0.007	40	97	14.350	0.404
37	85	17.444	0.522	38	100	0.112	0.003	40	98	13.049	0.251
37	86	17.226	0.512	39	85	2.247	0.240	40	99	10.936	0.265
37	87	15.872	0.431	39	86	5.223	0.211	40	100	9.351	0.194
37	88	12.705	0.384	39	87	8.701	0.305	40	101	5.241	0.075
37	89	11.588	0.325	39	88	14.159	0.418	40	102	3.164	0.098
37	90	9.734	0.174	39	89	17.276	0.498	40	103	1.106	0.035
37	91	8.797	0.150	39	90	18.738	0.543	40	104	0.404	0.012
37	92	7.013	0.104	39	91	19.183	0.530	40	105	0.091	0.003
37	93	5.321	0.156	39	92	16.944	0.499	41	89	1.417	0.102
37	94	2.947	0.088	39	93	15.390	0.458	41	90	3.460	0.168
37	95	1.430	0.043	39	94	14.376	0.442	41	91	7.274	0.274
37	96	0.477	0.013	39	95	11.090	0.152	41	92	10.229	0.321
37	97	0.208	0.004	39	96	10.308	0.342	41	93	13.084	0.383
38	83	2.846	0.175	39	97	8.842	0.206	41	94	15.866	0.487
38	84	5.381	0.259	39	98	5.901	0.185	41	95	19.250	0.597
38	85	9.981	0.297	39	99	4.548	0.141	41	96	18.502	0.571
38	86	13.925	0.348	39	100	1.836	0.055	41	97	17.906	0.530
38	87	17.869	0.471	39	101	0.739	0.021	41	98	16.938	0.507
38	88	19.018	0.553	39	102	0.211	0.004	41	99	16.042	0.487
38	89	18.304	0.524	40	87	1.822	0.131	41	100	14.040	0.212
38	90	15.040	0.414	40	88	3.885	0.249	41	101	12.824	0.244
38	91	13.769	0.398	40	89	8.157	0.287	41	102	8.442	0.195
38	92	11.890	0.344	40	90	12.208	0.351	41	103	6.987	0.104
38	93	10.881	0.198	40	91	16.198	0.473	41	104	3.477	0.054
38	94	10.548	0.153	40	92	17.984	0.520	41	105	1.861	0.031
38	95	6.948	0.223	40	93	18.480	0.575	41	106	0.615	0.011
38	96	4.940	0.147	40	94	18.166	0.528	41	107	0.220	0.005
38	97	2.544	0.080	40	95	17.853	0.527	42	92	2.721	0.184

Table A.3: Fission production cross sections (in mb) measured in the reaction ^{238}U(1·GeV+d)

Z	A	σ_{fiss}	$\delta\sigma_{fiss}$	Z	A	σ_{fiss}	$\delta\sigma_{fiss}$	Z	A	σ_{fiss}	$\delta\sigma_{fiss}$
42	93	5.849	0.203	43	106	11.666	0.305	45	102	10.272	0.370
42	94	8.622	0.264	43	107	10.069	0.225	45	103	14.721	0.512
42	95	12.800	0.406	43	108	5.814	0.088	45	104	17.142	0.594
42	96	15.766	0.486	43	109	3.640	0.056	45	105	20.420	0.767
42	97	18.507	0.577	43	110	1.690	0.031	45	106	19.594	0.659
42	98	20.939	0.647	43	111	0.739	0.014	45	107	20.122	0.692
42	99	20.982	0.650	44	95	0.575	0.064	45	108	18.779	0.627
42	100	19.981	0.582	44	96	1.578	0.161	45	109	20.145	0.659
42	101	18.425	0.580	44	97	3.640	0.189	45	110	14.947	0.228
42	102	17.537	0.578	44	98	5.642	0.248	45	111	13.436	0.395
42	103	14.423	0.233	44	99	8.913	0.303	45	112	10.303	0.313
42	104	11.960	0.249	44	100	12.303	0.410	45	113	6.632	0.201
42	105	7.753	0.122	44	101	16.932	0.552	45	114	3.348	0.056
42	106	4.991	0.073	44	102	18.404	0.617	45	115	1.701	0.034
42	107	2.312	0.077	44	103	19.600	0.661	45	116	0.663	0.012
42	108	1.105	0.035	44	104	19.927	0.734	45	117	0.245	0.007
42	109	0.335	0.006	44	105	19.449	0.754	45	118	0.069	0.002
42	110	0.117	0.002	44	106	19.338	0.649	46	100	0.720	0.094
43	94	2.367	0.126	44	107	17.254	0.568	46	101	1.845	0.171
43	95	4.171	0.177	44	108	15.628	0.318	46	102	3.459	0.231
43	96	6.669	0.236	44	109	10.663	0.267	46	103	5.858	0.243
43	97	9.910	0.364	44	110	8.354	0.221	46	104	8.825	0.393
43	98	14.288	0.516	44	111	4.700	0.069	46	105	12.061	0.478
43	99	16.626	0.635	44	112	2.638	0.055	46	106	14.557	0.521
43	100	19.604	0.670	44	113	0.988	0.018	46	107	18.040	0.667
43	101	20.118	0.651	44	114	0.427	0.007	46	108	19.743	0.675
43	102	18.732	0.622	44	115	0.119	0.002	46	109	19.409	0.702
43	103	20.974	0.687	45	99	2.152	0.196	46	110	18.083	0.642
43	104	17.298	0.538	45	100	4.250	0.161	46	111	17.749	0.629
43	105	15.980	0.503	45	101	6.877	0.231	46	112	17.604	0.590

Table A.4: Fission production cross sections (in mb) measured in the reaction ^{238}U(1·GeV+d)

Z	A	σ_{fiss}	$\delta\sigma_{fiss}$	Z	A	σ_{fiss}	$\delta\sigma_{fiss}$	Z	A	σ_{fiss}	$\delta\sigma_{fiss}$
46	113	11.482	0.470	48	108	5.044	0.350	49	118	14.722	0.566
46	114	10.812	0.230	48	109	7.763	0.330	49	119	13.809	0.515
46	115	7.563	0.233	48	110	9.819	0.431	49	120	12.179	0.458
46	116	4.365	0.113	48	111	12.300	0.529	49	121	10.230	0.197
46	117	2.131	0.036	48	112	14.424	0.564	49	122	8.325	0.209
46	118	1.127	0.019	48	113	15.134	0.584	49	123	6.093	0.153
46	119	0.443	0.009	48	114	15.828	0.612	49	124	3.439	0.070
46	120	0.132	0.004	48	115	16.485	0.608	49	125	1.741	0.031
47	103	1.213	0.084	48	116	16.647	0.597	49	126	0.922	0.018
47	104	2.310	0.168	48	117	15.088	0.534	49	127	0.501	0.010
47	105	3.836	0.269	48	118	10.863	0.477	49	128	0.188	0.006
47	106	6.401	0.258	48	119	10.242	0.227	50	110	0.712	0.092
47	107	9.952	0.481	48	120	7.618	0.127	50	111	1.815	0.116
47	108	12.777	0.484	48	121	4.572	0.153	50	112	2.903	0.210
47	109	15.198	0.573	48	122	2.410	0.042	50	113	4.509	0.256
47	110	16.356	0.611	48	123	1.291	0.026	50	114	6.881	0.368
47	111	18.052	0.681	48	124	0.489	0.010	50	115	8.710	0.454
47	112	17.428	0.619	48	125	0.187	0.005	50	116	9.990	0.501
47	113	17.728	0.649	48	126	0.071	0.003	50	117	12.106	0.525
47	114	16.546	0.597	49	107	0.442	0.081	50	118	11.851	0.531
47	115	15.716	0.547	49	108	1.070	0.102	50	119	12.941	0.578
47	116	12.653	0.363	49	109	2.081	0.144	50	120	11.991	0.484
47	117	9.656	0.316	49	110	3.974	0.215	50	121	12.179	0.496
47	118	6.012	0.156	49	111	5.592	0.323	50	122	11.003	0.467
47	119	3.810	0.067	49	112	8.198	0.434	50	123	9.303	0.176
47	120	1.569	0.032	49	113	10.713	0.477	50	124	7.518	0.211
47	121	0.783	0.015	49	114	12.735	0.518	50	125	5.832	0.169
47	122	0.255	0.007	49	115	14.057	0.594	50	126	3.630	0.095
48	106	1.745	0.213	49	116	15.501	0.579	50	127	2.708	0.051
48	107	3.206	0.190	49	117	15.724	0.585	50	128	1.725	0.033

Table A.5: Fission production cross sections (in mb) measured in the reaction ^{238}U(1·GeV+d)

Z	A	σ_{fiss}	$\delta\sigma_{fiss}$	Z	A	σ_{fiss}	$\delta\sigma_{fiss}$	Z	A	σ_{fiss}	$\delta\sigma_{fiss}$
50	129	1.204	0.029	52	116	1.525	0.128	53	123	5.849	0.455
50	130	0.989	0.024	52	117	2.554	0.168	53	124	7.057	0.385
50	131	0.600	0.016	52	118	3.555	0.292	53	125	7.615	0.423
50	132	0.367	0.010	52	119	4.967	0.369	53	126	8.125	0.395
50	133	0.042	0.002	52	120	6.517	0.457	53	127	7.650	0.379
51	112	0.553	0.050	52	121	6.780	0.442	53	128	7.179	0.321
51	113	1.165	0.101	52	122	8.601	0.464	53	129	7.708	0.345
51	114	2.121	0.125	52	123	9.390	0.435	53	130	7.221	0.313
51	115	3.392	0.222	52	124	8.817	0.435	53	131	5.927	0.125
51	116	5.438	0.333	52	125	9.522	0.431	53	132	5.229	0.120
51	117	6.666	0.408	52	126	9.273	0.390	53	133	5.582	0.157
51	118	8.519	0.475	52	127	8.750	0.369	53	134	5.038	0.132
51	119	9.896	0.465	52	128	7.016	0.142	53	135	5.435	0.111
51	120	11.110	0.496	52	129	6.527	0.146	53	136	3.138	0.070
51	121	11.769	0.493	52	130	5.119	0.108	53	137	2.471	0.060
51	122	11.068	0.478	52	131	4.670	0.143	53	138	1.255	0.034
51	123	11.601	0.471	52	132	4.618	0.123	53	139	0.516	0.015
51	124	10.768	0.425	52	133	4.615	0.092	53	140	0.113	0.004
51	125	9.630	0.381	52	134	4.245	0.099	53	141	0.039	0.002
51	126	7.065	0.287	52	135	1.667	0.047	54	119	0.386	0.045
51	127	6.598	0.130	52	136	0.747	0.022	54	120	0.895	0.078
51	128	5.039	0.138	52	137	0.253	0.009	54	121	1.566	0.218
51	129	3.853	0.078	52	138	0.072	0.003	54	122	2.058	0.261
51	130	3.089	0.059	52	139	0.013	0.001	54	123	2.882	0.350
51	131	2.870	0.120	53	117	0.583	0.044	54	124	4.124	0.364
51	132	1.971	0.047	53	118	1.181	0.121	54	125	5.409	0.381
51	133	1.477	0.036	53	119	2.036	0.200	54	126	5.188	0.463
51	134	0.374	0.011	53	120	3.171	0.268	54	127	6.380	0.380
51	135	0.097	0.005	53	121	4.059	0.296	54	128	6.714	0.374
52	115	0.673	0.046	53	122	5.231	0.412	54	129	6.674	0.346

Table A.6: Fission production cross sections (in mb) measured in the reaction ^{238}U(1·GeV+d)

Z	A	σ_{fiss}	$\delta\sigma_{fiss}$	Z	A	σ_{fiss}	$\delta\sigma_{fiss}$	Z	A	σ_{fiss}	$\delta\sigma_{fiss}$
54	130	6.844	0.338	55	138	3.807	0.099	56	146	0.513	0.019
54	131	6.574	0.329	55	139	3.434	0.117	56	147	0.146	0.008
54	132	6.212	0.276	55	140	3.385	0.086	56	148	0.029	0.002
54	133	5.952	0.127	55	141	2.914	0.073	57	127	0.500	0.120
54	134	5.422	0.132	55	142	1.731	0.047	57	128	1.007	0.154
54	135	5.414	0.134	55	143	1.158	0.032	57	129	1.099	0.326
54	136	5.791	0.185	55	144	0.350	0.015	57	130	1.515	0.433
54	137	5.106	0.109	55	145	0.089	0.005	57	131	1.795	0.400
54	138	4.468	0.094	55	146	0.017	0.001	57	132	2.480	0.373
54	139	2.590	0.064	56	125	0.787	0.133	57	133	2.521	0.355
54	140	1.831	0.053	56	126	1.082	0.268	57	134	2.937	0.350
54	141	0.827	0.027	56	127	1.729	0.306	57	135	2.828	0.288
54	142	0.206	0.008	56	128	2.144	0.428	57	136	2.843	0.207
54	143	0.032	0.003	56	129	2.813	0.474	57	137	2.659	0.173
55	122	0.607	0.062	56	130	3.186	0.479	57	138	2.445	0.152
55	123	1.080	0.131	56	131	3.696	0.374	57	139	2.569	0.152
55	124	1.750	0.204	56	132	4.116	0.336	57	140	2.058	0.119
55	125	2.207	0.332	56	133	3.994	0.259	57	141	1.823	0.052
55	126	3.333	0.409	56	134	4.409	0.272	57	142	2.092	0.062
55	127	3.606	0.455	56	135	3.742	0.210	57	143	2.076	0.057
55	128	4.560	0.391	56	136	3.525	0.201	57	144	1.885	0.063
55	129	4.493	0.410	56	137	3.628	0.186	57	145	2.204	0.060
55	130	5.228	0.323	56	138	3.712	0.190	57	146	1.192	0.035
55	131	4.984	0.299	56	139	3.331	0.082	57	147	1.028	0.035
55	132	4.979	0.271	56	140	3.712	0.088	57	148	0.341	0.014
55	133	4.885	0.252	56	141	3.468	0.083	57	149	0.142	0.006
55	134	4.633	0.229	56	142	3.825	0.095	57	150	0.027	0.003
55	135	4.528	0.225	56	143	3.089	0.078	58	130	0.767	0.236
55	136	4.090	0.114	56	144	2.574	0.066	58	131	1.206	0.303
55	137	4.305	0.149	56	145	1.215	0.040	58	132	1.205	0.520

Table A.7: Fission production cross sections (in mb) measured in the reaction ^{238}U(1·GeV+d)

Z	A	σ_{fiss}	$\delta\sigma_{fiss}$	Z	A	σ_{fiss}	$\delta\sigma_{fiss}$	Z	A	σ_{fiss}	$\delta\sigma_{fiss}$
58	133	1.671	0.452	59	146	1.037	0.030	61	147	0.781	0.079
58	134	1.800	0.479	59	147	0.820	0.026	61	148	0.609	0.055
58	135	1.990	0.458	59	148	0.775	0.024	61	149	0.507	0.039
58	136	1.896	0.422	59	149	0.796	0.026	61	150	0.492	0.035
58	137	2.333	0.245	59	150	0.690	0.022	61	151	0.478	0.036
58	138	2.244	0.213	59	151	0.519	0.017	61	152	0.329	0.024
58	139	2.136	0.161	59	152	0.165	0.006	61	153	0.319	0.013
58	140	2.112	0.144	59	153	0.072	0.003	61	154	0.248	0.009
58	141	1.759	0.107	59	154	0.014	0.002	61	155	0.164	0.005
58	142	1.457	0.084	60	139	1.054	0.487	61	156	0.085	0.003
58	143	1.554	0.088	60	141	1.151	0.334	61	157	0.015	0.001
58	144	1.233	0.036	60	142	1.166	0.236	61	158	0.006	0.001
58	145	1.485	0.048	60	143	1.184	0.149	62	147	0.622	0.146
58	146	1.467	0.046	60	144	1.028	0.094	62	148	0.495	0.115
58	147	1.328	0.040	60	145	0.945	0.079	62	149	0.619	0.070
58	148	1.002	0.031	60	146	0.808	0.071	62	150	0.421	0.064
58	149	0.666	0.021	60	147	0.690	0.065	62	151	0.334	0.045
58	150	0.375	0.014	60	148	0.658	0.060	62	152	0.358	0.044
58	151	0.087	0.005	60	149	0.555	0.044	62	153	0.271	0.033
58	152	0.023	0.003	60	150	0.470	0.017	62	154	0.229	0.022
59	136	1.325	0.450	60	151	0.537	0.016	62	155	0.149	0.015
59	137	1.180	0.469	60	152	0.343	0.011	62	156	0.111	0.010
59	138	1.384	0.395	60	153	0.240	0.009	62	157	0.046	0.005
59	139	1.449	0.302	60	154	0.119	0.008	62	158	0.030	0.004
59	140	1.884	0.209	60	155	0.059	0.004	62	159	0.017	0.003
59	141	1.627	0.143	60	156	0.009	0.001	62	160	0.006	0.002
59	142	1.447	0.110	61	142	1.011	0.472	63	149	0.431	0.213
59	143	1.289	0.097	61	144	0.905	0.247	63	150	0.432	0.123
59	144	1.199	0.078	61	145	0.840	0.152	63	151	0.335	0.097
59	145	1.180	0.073	61	146	0.802	0.121	63	152	0.370	0.077

Table A.8: Fission production cross sections (in mb) measured in the reaction ^{238}U(1·GeV+d)

Z	A	σ_{fiss}	$\delta\sigma_{fiss}$	Z	A	σ_{fiss}	$\delta\sigma_{fiss}$	Z	A	σ_{fiss}	$\delta\sigma_{fiss}$
63	153	0.299	0.055	0	0	0.000	0.000	0	0	0.000	0.000
63	154	0.310	0.037	0	0	0.000	0.000	0	0	0.000	0.000
63	155	0.191	0.024	0	0	0.000	0.000	0	0	0.000	0.000
63	156	0.182	0.023	0	0	0.000	0.000	0	0	0.000	0.000
63	157	0.085	0.010	0	0	0.000	0.000	0	0	0.000	0.000
64	153	0.312	0.093	0	0	0.000	0.000	0	0	0.000	0.000
64	154	0.199	0.097	0	0	0.000	0.000	0	0	0.000	0.000
64	155	0.229	0.067	0	0	0.000	0.000	0	0	0.000	0.000
64	156	0.162	0.041	0	0	0.000	0.000	0	0	0.000	0.000
64	157	0.147	0.019	0	0	0.000	0.000	0	0	0.000	0.000
64	158	0.090	0.014	0	0	0.000	0.000	0	0	0.000	0.000
64	159	0.076	0.011	0	0	0.000	0.000	0	0	0.000	0.000
65	155	0.326	0.162	0	0	0.000	0.000	0	0	0.000	0.000
65	156	0.263	0.086	0	0	0.000	0.000	0	0	0.000	0.000
65	157	0.218	0.070	0	0	0.000	0.000	0	0	0.000	0.000
65	158	0.144	0.041	0	0	0.000	0.000	0	0	0.000	0.000
65	159	0.108	0.026	0	0	0.000	0.000	0	0	0.000	0.000
65	160	0.090	0.017	0	0	0.000	0.000	0	0	0.000	0.000
66	159	0.164	0.064	0	0	0.000	0.000	0	0	0.000	0.000
66	161	0.111	0.019	0	0	0.000	0.000	0	0	0.000	0.000
66	162	0.060	0.016	0	0	0.000	0.000	0	0	0.000	0.000

Table A.9: Fission production cross sections (in mb) measured in the reaction ^{238}U(1·GeV+d)

Appendix B

Velocities of fission residues

Z	A	v_{fiss}	δv_{fiss}	Z	A	v_{fiss}	δv_{fiss}	Z	A	v_{fiss}	δv_{fiss}
23	49	1.590	0.070	25	61	1.650	0.022	27	68	1.620	0.081
23	50	1.690	0.020	25	62	1.650	0.051	27	69	1.620	0.081
23	51	1.720	0.022	25	63	1.640	0.051	28	57	0.870	0.150
23	52	1.700	0.010	26	53	0.860	0.150	28	58	1.030	0.120
23	53	1.750	0.030	26	54	1.160	0.100	28	59	1.250	0.071
23	54	1.760	0.010	26	55	1.450	0.070	28	60	1.400	0.020
23	55	1.710	0.040	26	56	1.570	0.022	28	61	1.470	0.032
23	56	1.710	0.100	26	57	1.650	0.070	28	62	1.530	0.010
23	57	1.710	0.100	26	58	1.620	0.010	28	63	1.570	0.014
24	49	0.840	0.150	26	59	1.610	0.010	28	64	1.590	0.010
24	50	1.140	0.120	26	60	1.610	0.020	28	65	1.610	0.010
24	51	1.450	0.090	26	61	1.620	0.050	28	66	1.630	0.010
24	52	1.630	0.050	26	62	1.600	0.051	28	67	1.600	0.014
24	53	1.700	0.010	26	63	1.600	0.051	28	68	1.600	0.071
24	54	1.690	0.010	26	64	1.600	0.061	28	69	1.620	0.060
24	55	1.720	0.010	26	65	1.600	0.041	28	70	1.640	0.022
24	56	1.690	0.010	26	66	1.600	0.041	28	71	1.620	0.070
24	57	1.690	0.050	27	55	0.820	0.150	28	72	1.620	0.100
24	58	1.690	0.060	27	56	1.030	0.120	29	59	1.010	0.160
24	59	1.690	0.080	27	57	1.340	0.081	29	60	1.150	0.120
25	51	0.880	0.160	27	58	1.540	0.010	29	61	1.340	0.100
25	52	1.110	0.130	27	59	1.600	0.030	29	62	1.450	0.061
25	53	1.520	0.120	27	60	1.630	0.030	29	63	1.530	0.022
25	54	1.660	0.050	27	61	1.630	0.030	29	64	1.550	0.014
25	55	1.670	0.010	27	62	1.620	0.050	29	65	1.570	0.014
25	56	1.710	0.022	27	63	1.620	0.051	29	66	1.550	0.014
25	57	1.690	0.014	27	64	1.620	0.051	29	67	1.560	0.010
25	58	1.650	0.010	27	65	1.620	0.051	29	68	1.580	0.014
25	59	1.690	0.010	27	66	1.620	0.051	29	69	1.600	0.010
25	60	1.650	0.014	27	67	1.620	0.051	29	70	1.550	0.030

Table B.1: Velocities of fission residues (in cm/ns) measured in the frame of the fissioning system for the reaction ^{238}U(1·GeV+d)

Z	A	v_{fiss}	δv_{fiss}	Z	A	v_{fiss}	δv_{fiss}	Z	A	v_{fiss}	δv_{fiss}
29	71	1.550	0.040	31	73	1.540	0.014	33	74	1.430	0.014
29	72	1.610	0.060	31	74	1.540	0.014	33	75	1.480	0.030
29	73	1.610	0.070	31	75	1.540	0.030	33	76	1.460	0.022
29	74	1.610	0.071	31	76	1.540	0.030	33	77	1.480	0.010
30	62	1.010	0.120	31	77	1.540	0.032	33	78	1.480	0.010
30	63	1.210	0.091	31	78	1.540	0.032	33	79	1.490	0.010
30	64	1.370	0.022	31	79	1.540	0.051	33	80	1.490	0.040
30	65	1.430	0.014	31	80	1.540	0.061	33	81	1.490	0.030
30	66	1.520	0.010	32	67	1.090	0.120	33	82	1.490	0.010
30	67	1.520	0.014	32	68	1.300	0.080	33	83	1.470	0.010
30	68	1.540	0.010	32	69	1.400	0.061	33	84	1.470	0.010
30	69	1.550	0.010	32	70	1.440	0.040	33	85	1.490	0.014
30	70	1.530	0.010	32	71	1.490	0.010	33	86	1.500	0.050
30	71	1.560	0.010	32	72	1.520	0.010	34	71	1.060	0.091
30	72	1.570	0.020	32	73	1.490	0.014	34	72	1.220	0.071
30	73	1.570	0.040	32	74	1.520	0.014	34	73	1.280	0.010
30	74	1.570	0.040	32	75	1.520	0.014	34	74	1.330	0.010
30	75	1.570	0.014	32	76	1.510	0.010	34	75	1.390	0.014
30	76	1.580	0.040	32	77	1.540	0.010	34	76	1.430	0.010
30	77	1.580	0.050	32	78	1.520	0.050	34	77	1.440	0.010
30	78	1.580	0.050	32	79	1.520	0.050	34	78	1.450	0.010
31	64	0.960	0.110	32	80	1.500	0.014	34	79	1.470	0.010
31	65	1.210	0.081	32	81	1.510	0.014	34	80	1.470	0.010
31	66	1.320	0.071	32	82	1.520	0.014	34	81	1.460	0.014
31	67	1.440	0.032	32	83	1.520	0.041	34	82	1.460	0.014
31	68	1.470	0.010	33	69	1.100	0.090	34	83	1.450	0.032
31	69	1.510	0.010	33	70	1.270	0.050	34	84	1.450	0.041
31	70	1.530	0.014	33	71	1.340	0.030	34	85	1.450	0.014
31	71	1.520	0.014	33	72	1.410	0.022	34	86	1.480	0.014
31	72	1.520	0.014	33	73	1.420	0.014	34	87	1.490	0.010

Table B.2: Velocities of fission residues (in cm/ns) measured in the frame of the fissioning system for the reaction ^{238}U(1·GeV+d)

Z	A	v_{fiss}	δv_{fiss}	Z	A	v_{fiss}	δv_{fiss}	Z	A	v_{fiss}	δv_{fiss}
34	88	1.490	0.030	36	84	1.400	0.014	37	96	1.390	0.020
34	89	1.480	0.041	36	85	1.410	0.014	37	97	1.370	0.020
35	73	1.110	0.091	36	86	1.400	0.014	38	80	1.100	0.071
35	74	1.200	0.071	36	87	1.400	0.014	38	81	1.160	0.061
35	75	1.290	0.060	36	88	1.420	0.040	38	82	1.190	0.061
35	76	1.310	0.030	36	89	1.420	0.010	38	83	1.240	0.030
35	77	1.360	0.014	36	90	1.430	0.014	38	84	1.280	0.010
35	78	1.400	0.014	36	91	1.420	0.010	38	85	1.310	0.014
35	79	1.410	0.014	36	92	1.400	0.010	38	86	1.320	0.010
35	80	1.420	0.014	36	93	1.430	0.014	38	87	1.320	0.010
35	81	1.410	0.022	36	94	1.410	0.014	38	88	1.350	0.010
35	82	1.410	0.020	36	95	1.410	0.041	38	89	1.360	0.014
35	83	1.450	0.010	37	78	1.070	0.100	38	90	1.360	0.014
35	84	1.450	0.010	37	79	1.180	0.070	38	91	1.380	0.010
35	85	1.450	0.050	37	80	1.280	0.040	38	92	1.380	0.010
35	86	1.450	0.030	37	81	1.310	0.022	38	93	1.380	0.040
35	87	1.470	0.010	37	82	1.330	0.014	38	94	1.380	0.030
35	88	1.470	0.010	37	83	1.340	0.010	38	95	1.390	0.020
35	89	1.470	0.010	37	84	1.370	0.010	38	96	1.390	0.010
35	90	1.450	0.010	37	85	1.380	0.022	38	97	1.390	0.014
35	91	1.450	0.030	37	86	1.370	0.010	38	98	1.370	0.015
35	92	1.450	0.040	37	87	1.380	0.010	38	99	1.350	0.017
36	76	1.150	0.071	37	88	1.370	0.014	38	100	1.350	0.020
36	77	1.230	0.061	37	89	1.400	0.032	39	82	1.010	0.150
36	78	1.280	0.032	37	90	1.420	0.030	39	83	1.140	0.091
36	79	1.330	0.010	37	91	1.400	0.041	39	84	1.200	0.050
36	80	1.340	0.010	37	92	1.400	0.022	39	85	1.210	0.030
36	81	1.370	0.010	37	93	1.420	0.014	39	86	1.230	0.020
36	82	1.370	0.014	37	94	1.420	0.010	39	87	1.260	0.014
36	83	1.400	0.014	37	95	1.400	0.020	39	88	1.270	0.014

Table B.3: Velocities of fission residues (in cm/ns) measured in the frame of the fissioning system for the reaction ^{238}U(1·GeV+d)

Z	A	v_{fiss}	δv_{fiss}	Z	A	v_{fiss}	δv_{fiss}	Z	A	v_{fiss}	δv_{fiss}
39	89	1.310	0.010	40	100	1.310	0.032	42	92	1.160	0.010
39	90	1.310	0.010	40	101	1.320	0.030	42	93	1.190	0.010
39	91	1.340	0.010	40	102	1.340	0.014	42	94	1.190	0.014
39	92	1.340	0.014	40	103	1.340	0.014	42	95	1.220	0.014
39	93	1.330	0.014	40	104	1.340	0.014	42	96	1.220	0.014
39	94	1.360	0.041	40	105	1.350	0.032	42	97	1.230	0.014
39	95	1.320	0.032	41	87	1.060	0.080	42	98	1.250	0.010
39	96	1.340	0.041	41	88	1.100	0.051	42	99	1.260	0.010
39	97	1.350	0.040	41	89	1.140	0.014	42	100	1.280	0.014
39	98	1.340	0.022	41	90	1.160	0.010	42	101	1.260	0.010
39	99	1.360	0.010	41	91	1.220	0.032	42	102	1.270	0.010
39	100	1.340	0.015	41	92	1.220	0.014	42	103	1.270	0.022
39	101	1.340	0.015	41	93	1.240	0.010	42	104	1.270	0.032
39	102	1.330	0.015	41	94	1.230	0.014	42	105	1.270	0.020
40	84	0.940	0.100	41	95	1.260	0.010	42	106	1.270	0.015
40	85	1.090	0.071	41	96	1.270	0.014	42	107	1.280	0.015
40	86	1.110	0.051	41	97	1.270	0.010	42	108	1.280	0.015
40	87	1.170	0.030	41	98	1.290	0.010	42	109	1.270	0.020
40	88	1.190	0.030	41	99	1.290	0.014	42	110	1.280	0.020
40	89	1.210	0.010	41	100	1.290	0.014	43	91	0.910	0.100
40	90	1.230	0.014	41	101	1.290	0.032	43	92	1.020	0.061
40	91	1.260	0.014	41	102	1.270	0.032	43	93	1.090	0.032
40	92	1.260	0.014	41	103	1.290	0.014	43	94	1.110	0.014
40	93	1.260	0.010	41	104	1.290	0.014	43	95	1.130	0.014
40	94	1.280	0.014	41	105	1.300	0.015	43	96	1.140	0.014
40	95	1.290	0.015	41	106	1.300	0.020	43	97	1.160	0.020
40	96	1.290	0.014	41	107	1.290	0.030	43	98	1.190	0.020
40	97	1.310	0.020	42	89	1.010	0.091	43	99	1.190	0.030
40	98	1.300	0.035	42	90	1.050	0.051	43	100	1.220	0.030
40	99	1.290	0.041	42	91	1.110	0.041	43	101	1.220	0.010

Table B.4: Velocities of fission residues (in cm/ns) measured in the frame of the fissioning system for the reaction ^{238}U(1·GeV+d)

Z	A	v_{fiss}	δv_{fiss}	Z	A	v_{fiss}	δv_{fiss}	Z	A	v_{fiss}	δv_{fiss}
43	102	1.220	0.014	44	113	1.220	0.014	46	103	1.070	0.022
43	103	1.230	0.010	44	114	1.220	0.014	46	104	1.090	0.022
43	104	1.240	0.014	44	115	1.220	0.014	46	105	1.090	0.014
43	105	1.220	0.020	45	96	0.920	0.081	46	106	1.110	0.014
43	106	1.210	0.020	45	97	0.970	0.051	46	107	1.100	0.010
43	107	1.220	0.020	45	98	0.980	0.051	46	108	1.140	0.014
43	108	1.220	0.025	45	99	1.030	0.030	46	109	1.150	0.014
43	109	1.220	0.025	45	100	1.080	0.010	46	110	1.140	0.022
43	110	1.210	0.020	45	101	1.100	0.014	46	111	1.150	0.020
43	111	1.220	0.025	45	102	1.110	0.014	46	112	1.140	0.010
44	93	0.990	0.100	45	103	1.150	0.010	46	113	1.140	0.020
44	94	1.000	0.061	45	104	1.150	0.014	46	114	1.140	0.022
44	95	1.030	0.032	45	105	1.170	0.020	46	115	1.130	0.032
44	96	1.080	0.041	45	106	1.170	0.014	46	116	1.140	0.022
44	97	1.130	0.032	45	107	1.170	0.010	46	117	1.140	0.022
44	98	1.130	0.022	45	108	1.180	0.010	46	118	1.170	0.022
44	99	1.140	0.014	45	109	1.200	0.014	46	119	1.160	0.014
44	100	1.160	0.014	45	110	1.200	0.014	46	120	1.160	0.032
44	101	1.180	0.014	45	111	1.200	0.030	47	101	0.910	0.032
44	102	1.170	0.010	45	112	1.200	0.030	47	102	0.930	0.022
44	103	1.190	0.014	45	113	1.190	0.030	47	103	0.970	0.014
44	104	1.190	0.014	45	114	1.190	0.020	47	104	0.970	0.032
44	105	1.190	0.022	45	115	1.180	0.014	47	105	1.020	0.030
44	106	1.210	0.014	45	116	1.180	0.014	47	106	1.040	0.010
44	107	1.220	0.014	45	117	1.190	0.032	47	107	1.080	0.022
44	108	1.220	0.022	45	118	1.190	0.041	47	108	1.090	0.014
44	109	1.220	0.032	46	99	0.970	0.050	47	109	1.090	0.014
44	110	1.210	0.030	46	100	1.000	0.030	47	110	1.100	0.014
44	111	1.210	0.014	46	101	1.020	0.032	47	111	1.130	0.010
44	112	1.210	0.022	46	102	1.070	0.032	47	112	1.130	0.014

Table B.5: Velocities of fission residues (in cm/ns) measured in the frame of the fissioning system or the reaction ^{238}U(1·GeV+d)

Z	A	v_{fiss}	δv_{fiss}	Z	A	v_{fiss}	δv_{fiss}	Z	A	v_{fiss}	δv_{fiss}
47	113	1.120	0.014	48	123	1.120	0.022	50	110	0.860	0.014
47	114	1.130	0.014	48	124	1.110	0.014	50	111	0.910	0.014
47	115	1.150	0.010	48	125	1.100	0.022	50	112	0.950	0.014
47	116	1.150	0.020	48	126	1.100	0.032	50	113	0.960	0.022
47	117	1.130	0.032	49	106	0.800	0.081	50	114	1.010	0.014
47	118	1.130	0.032	49	107	0.880	0.051	50	115	1.020	0.010
47	119	1.130	0.022	49	108	0.890	0.041	50	116	1.020	0.014
47	120	1.140	0.032	49	109	0.930	0.020	50	117	1.020	0.014
47	121	1.140	0.014	49	110	0.980	0.014	50	118	1.020	0.010
47	122	1.140	0.032	49	111	0.980	0.014	50	119	1.030	0.014
48	103	0.920	0.051	49	112	1.030	0.010	50	120	1.040	0.014
48	104	0.960	0.040	49	113	1.050	0.014	50	121	1.030	0.014
48	105	0.970	0.032	49	114	1.050	0.014	50	122	1.040	0.014
48	106	1.000	0.020	49	115	1.070	0.014	50	123	1.030	0.014
48	107	1.000	0.010	49	116	1.100	0.010	50	124	1.020	0.032
48	108	1.020	0.032	49	117	1.100	0.010	50	125	1.040	0.032
48	109	1.030	0.010	49	118	1.090	0.014	50	126	1.040	0.032
48	110	1.030	0.014	49	119	1.100	0.014	50	127	1.050	0.012
48	111	1.030	0.014	49	120	1.100	0.010	50	128	1.060	0.012
48	112	1.060	0.014	49	121	1.100	0.020	50	129	1.070	0.014
48	113	1.060	0.014	49	122	1.110	0.032	50	130	1.070	0.014
48	114	1.080	0.010	49	123	1.110	0.032	50	131	1.070	0.014
48	115	1.110	0.010	49	124	1.100	0.022	50	132	1.070	0.014
48	116	1.110	0.014	49	125	1.090	0.022	50	133	1.060	0.014
48	117	1.130	0.010	49	126	1.110	0.020	51	109	0.660	0.081
48	118	1.120	0.030	49	127	1.090	0.014	51	110	0.750	0.032
48	119	1.110	0.032	49	128	1.090	0.022	51	111	0.780	0.032
48	120	1.120	0.020	50	107	0.700	0.061	51	112	0.850	0.022
48	121	1.110	0.032	50	108	0.780	0.032	51	113	0.880	0.014
48	122	1.110	0.020	50	109	0.820	0.014	51	114	0.900	0.014

Table B.6: Velocities of fission residues (in cm/ns) measured in the frame of the fissioning system for the reaction ^{238}U(1·GeV+d)

Z	A	v_{fiss}	δv_{fiss}	Z	A	v_{fiss}	δv_{fiss}	Z	A	v_{fiss}	δv_{fiss}
51	115	0.930	0.010	52	121	0.970	0.036	53	127	0.960	0.010
51	116	0.970	0.014	52	122	0.990	0.010	53	128	0.970	0.014
51	117	0.970	0.014	52	123	0.990	0.014	53	129	0.990	0.014
51	118	1.000	0.014	52	124	1.000	0.010	53	130	0.990	0.014
51	119	1.020	0.014	52	125	1.000	0.014	53	131	0.990	0.014
51	120	1.020	0.014	52	126	1.010	0.014	53	132	0.980	0.014
51	121	1.040	0.022	52	127	1.020	0.010	53	133	1.000	0.032
51	122	1.020	0.032	52	128	1.020	0.022	53	134	0.980	0.032
51	123	1.050	0.010	52	129	1.010	0.022	53	135	1.010	0.022
51	124	1.050	0.014	52	130	1.000	0.041	53	136	0.990	0.014
51	125	1.040	0.014	52	131	1.010	0.041	53	137	1.020	0.020
51	126	1.040	0.014	52	132	1.010	0.032	53	138	0.990	0.010
51	127	1.040	0.014	52	133	1.020	0.015	53	139	0.990	0.014
51	128	1.030	0.032	52	134	1.030	0.022	53	140	0.990	0.022
51	129	1.050	0.014	52	135	1.040	0.022	53	141	0.990	0.051
51	130	1.060	0.010	52	136	1.050	0.015	54	117	0.540	0.130
51	131	1.060	0.010	52	137	1.050	0.015	54	118	0.690	0.071
51	132	1.060	0.014	52	138	1.040	0.020	54	119	0.740	0.041
51	133	1.070	0.014	52	139	1.040	0.032	54	120	0.780	0.014
51	134	1.060	0.014	53	116	0.630	0.100	54	121	0.830	0.051
51	135	1.050	0.032	53	117	0.770	0.071	54	122	0.860	0.014
52	112	0.720	0.051	53	118	0.830	0.032	54	123	0.870	0.022
52	113	0.740	0.041	53	119	0.880	0.041	54	124	0.900	0.014
52	114	0.800	0.022	53	120	0.910	0.032	54	125	0.930	0.014
52	115	0.830	0.014	53	121	0.910	0.014	54	126	0.930	0.014
52	116	0.860	0.014	53	122	0.940	0.022	54	127	0.950	0.014
52	117	0.880	0.014	53	123	0.950	0.014	54	128	0.960	0.014
52	118	0.900	0.014	53	124	0.960	0.014	54	129	0.960	0.014
52	119	0.920	0.024	53	125	0.970	0.010	54	130	0.990	0.020
52	120	0.940	0.042	53	126	0.970	0.010	54	131	0.970	0.022

Table B.7: Velocities of fission residues (in cm/ns) measured in the frame of the fissioning system for the reaction ^{238}U(1·GeV+d)

Z	A	v_{fiss}	δv_{fiss}	Z	A	v_{fiss}	δv_{fiss}	Z	A	v_{fiss}	δv_{fiss}
54	132	0.970	0.014	55	137	0.900	0.041	56	141	0.910	0.014
54	133	0.980	0.014	55	138	0.910	0.014	56	142	0.920	0.014
54	134	0.970	0.022	55	139	0.900	0.032	56	143	0.910	0.014
54	135	0.980	0.014	55	140	0.890	0.022	56	144	0.910	0.014
54	136	0.990	0.040	55	141	0.910	0.014	56	145	0.890	0.014
54	137	0.980	0.014	55	142	0.910	0.014	56	146	0.890	0.014
54	138	0.980	0.022	55	143	0.910	0.014	56	147	0.890	0.022
54	139	0.950	0.020	55	144	0.920	0.022	56	148	0.890	0.022
54	140	0.940	0.032	55	145	0.910	0.022	57	124	0.440	0.200
54	141	0.970	0.022	55	146	0.910	0.032	57	125	0.610	0.090
54	142	0.950	0.022	56	121	0.400	0.200	57	126	0.680	0.051
54	143	0.940	0.041	56	122	0.530	0.090	57	127	0.700	0.041
55	119	0.480	0.190	56	123	0.650	0.041	57	128	0.720	0.014
55	120	0.650	0.081	56	124	0.700	0.022	57	129	0.750	0.014
55	121	0.700	0.041	56	125	0.730	0.022	57	130	0.790	0.041
55	122	0.740	0.014	56	126	0.750	0.022	57	131	0.810	0.014
55	123	0.790	0.022	56	127	0.790	0.014	57	132	0.840	0.014
55	124	0.830	0.022	56	128	0.850	0.028	57	133	0.850	0.014
55	125	0.850	0.022	56	129	0.860	0.022	57	134	0.860	0.014
55	126	0.890	0.022	56	130	0.890	0.014	57	135	0.860	0.014
55	127	0.910	0.022	56	131	0.880	0.022	57	136	0.870	0.014
55	128	0.910	0.014	56	132	0.920	0.014	57	137	0.860	0.014
55	129	0.900	0.014	56	133	0.920	0.014	57	138	0.860	0.014
55	130	0.910	0.014	56	134	0.930	0.028	57	139	0.860	0.014
55	131	0.920	0.014	56	135	0.910	0.020	57	140	0.870	0.014
55	132	0.920	0.014	56	136	0.900	0.014	57	141	0.860	0.032
55	133	0.920	0.014	56	137	0.920	0.014	57	142	0.870	0.014
55	134	0.920	0.014	56	138	0.910	0.014	57	143	0.870	0.014
55	135	0.920	0.014	56	139	0.910	0.014	57	144	0.860	0.032
55	136	0.900	0.032	56	140	0.920	0.014	57	145	0.880	0.014

Table B.8: Velocities of fission residues (in cm/ns) measured in the frame of the fissioning system for the reaction ^{238}U(1·GeV+d)

Z	A	v_{fiss}	δv_{fiss}	Z	A	v_{fiss}	δv_{fiss}	Z	A	v_{fiss}	δv_{fiss}
57	146	0.870	0.014	58	151	0.850	0.022	60	132	0.560	0.120
57	147	0.870	0.014	58	152	0.850	0.050	60	133	0.630	0.071
57	148	0.860	0.014	59	128	0.450	0.130	60	134	0.670	0.022
57	149	0.880	0.014	59	129	0.550	0.100	60	135	0.700	0.014
57	150	0.880	0.061	59	130	0.590	0.080	60	136	0.720	0.036
58	126	0.360	0.230	59	131	0.660	0.032	60	137	0.730	0.041
58	127	0.540	0.100	59	132	0.690	0.014	60	138	0.740	0.022
58	128	0.660	0.030	59	133	0.720	0.014	60	139	0.740	0.014
58	129	0.710	0.014	59	134	0.740	0.014	60	140	0.740	0.014
58	130	0.750	0.022	59	135	0.750	0.022	60	141	0.750	0.014
58	131	0.780	0.022	59	136	0.750	0.014	60	142	0.780	0.014
58	132	0.810	0.032	59	137	0.780	0.014	60	142	0.780	0.014
58	133	0.810	0.022	59	138	0.770	0.022	60	143	0.760	0.014
58	134	0.830	0.014	59	139	0.790	0.014	60	144	0.790	0.014
58	135	0.840	0.014	59	140	0.810	0.014	60	145	0.800	0.010
58	136	0.840	0.014	59	141	0.820	0.014	60	146	0.800	0.022
58	137	0.860	0.014	59	142	0.820	0.022	60	147	0.810	0.014
58	138	0.860	0.014	59	143	0.840	0.014	60	148	0.820	0.014
58	139	0.850	0.014	59	144	0.850	0.014	60	149	0.820	0.014
58	140	0.860	0.014	59	145	0.860	0.014	60	150	0.830	0.022
58	141	0.860	0.014	59	146	0.860	0.014	60	151	0.830	0.022
58	142	0.870	0.014	59	147	0.850	0.014	60	152	0.830	0.051
58	143	0.880	0.014	59	148	0.860	0.014	60	153	0.810	0.041
58	144	0.860	0.014	59	149	0.840	0.022	60	154	0.800	0.051
58	145	0.860	0.022	59	150	0.850	0.014	60	155	0.810	0.022
58	146	0.860	0.022	59	151	0.840	0.014	60	156	0.820	0.014
58	147	0.860	0.014	59	152	0.850	0.010	61	133	0.460	0.150
58	148	0.860	0.014	59	153	0.840	0.014	61	134	0.520	0.120
58	149	0.870	0.014	59	154	0.850	0.050	61	135	0.590	0.080
58	150	0.870	0.014	60	131	0.430	0.150	61	136	0.650	0.030

Table B.9: Velocities of fission residues (in cm/ns) measured in the frame of the fissioning system for the reaction ^{238}U(1·GeV+d)

Z	A	v_{fiss}	δv_{fiss}	Z	A	v_{fiss}	δv_{fiss}	Z	A	v_{fiss}	δv_{fiss}
61	137	0.670	0.032	62	147	0.740	0.022	64	154	0.700	0.041
61	138	0.700	0.028	62	148	0.760	0.014	64	155	0.700	0.014
61	139	0.690	0.030	62	149	0.760	0.014	64	156	0.710	0.014
61	140	0.740	0.014	62	150	0.760	0.014	64	157	0.720	0.014
61	141	0.760	0.014	62	151	0.760	0.014	64	158	0.710	0.032
61	142	0.780	0.014	62	152	0.760	0.014	64	159	0.710	0.022
61	143	0.760	0.022	62	153	0.770	0.010	65	154	0.680	0.032
61	144	0.800	0.022	62	154	0.780	0.014	65	155	0.690	0.030
61	145	0.770	0.022	62	155	0.780	0.014	65	156	0.700	0.010
61	146	0.790	0.014	62	156	0.770	0.022	65	157	0.700	0.010
61	147	0.810	0.014	62	157	0.770	0.032	65	158	0.690	0.050
61	148	0.820	0.014	62	158	0.760	0.061	65	159	0.700	0.022
61	149	0.830	0.014	62	159	0.770	0.022	65	160	0.700	0.020
61	150	0.810	0.014	62	160	0.770	0.032	66	156	0.660	0.061
61	151	0.820	0.014	63	147	0.660	0.051	66	157	0.660	0.051
61	152	0.810	0.014	63	148	0.690	0.041	66	158	0.650	0.032
61	153	0.800	0.022	63	149	0.700	0.040	66	159	0.670	0.010
61	154	0.810	0.032	63	150	0.710	0.014	66	160	0.660	0.051
61	155	0.800	0.064	63	151	0.720	0.010	66	161	0.670	0.010
61	156	0.810	0.022	63	152	0.710	0.014	66	162	0.670	0.060
61	157	0.810	0.014	63	153	0.720	0.014	0	0	0.000	0.000
61	158	0.800	0.022	63	154	0.750	0.040	0	0	0.000	0.000
62	139	0.600	0.050	63	155	0.750	0.022	0	0	0.000	0.000
62	140	0.630	0.060	63	156	0.750	0.010	0	0	0.000	0.000
62	141	0.650	0.032	63	157	0.750	0.041	0	0	0.000	0.000
62	142	0.690	0.022	64	149	0.640	0.051	0	0	0.000	0.000
62	143	0.710	0.022	64	150	0.640	0.041	0	0	0.000	0.000
62	144	0.730	0.014	64	151	0.670	0.041	0	0	0.000	0.000
62	145	0.730	0.014	64	152	0.690	0.010	0	0	0.000	0.000
62	146	0.740	0.014	64	153	0.670	0.022	0	0	0.000	0.000

Table B.10: Velocities of fission residues (in cm/ns) measured in the frame of the fissioning system for the reaction ^{238}U(1·GeV+d)

Appendix C

Calculation of the angular transmission

The specific geometrical and ion-optical characteristics of the Fragment separator introduced a limitation in the maximun angles of the transmitted nuclei to be accepted by the apparatus. The large angular emittances originated from the fission process can exceed largely this angular acceptance, leading to losses of the transmitted nuclei, which must then be properly accounted for. The importance of this correction motivated the developement of a new method to determine the angular transmission in zero-degree in-flight separators. In the present appendix we included a publication wherein this method is explained in detail.

Appendix D

List of layers in the experiment

The nuclei produced in the target are kinematically focused onto the entrance of the FRS. The trajectories followed by these nuclei crosses different layers of matter, which correspond to the different detectors and stripper foils placed along the FRS. The exact location of these detectors at the intermediate $S1$ and final $S4$ areas are shown in figures D.1 and D.2, respectively.

The thicknesses of the layers of matter that define the different detectors, targets and strippers of the FRS are listed in table D.1. The numbers on the last column correspond to the different elements: 1) Vacuum window; 2) SEETRAM; 3) Cryogenic container of the deuterium target; 4) Target; 5) Niobium stripper; 6) Plastic scintillators ($SC2$ at $S2$ and $SC4$ at $S4$; 7) MUSIC ionization chambers; 8) Air gap.

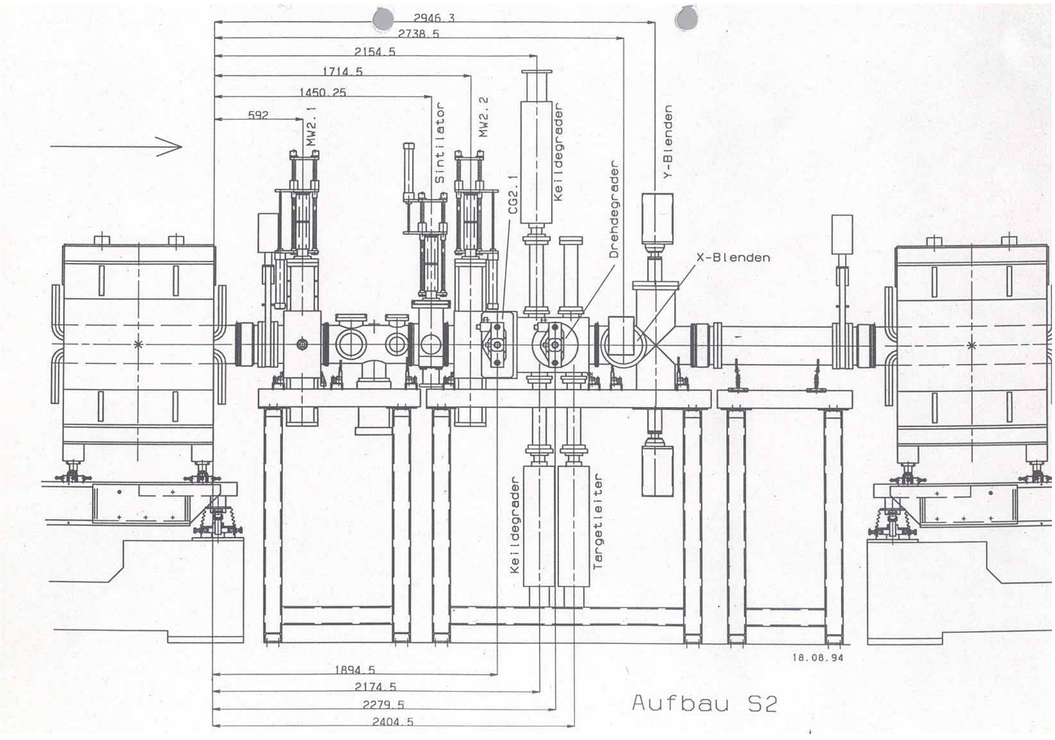

Figure D.1: *Schematic view of the detection setup placed at the intermediate area S2 of the FRS. The arrows indicate the relative distances (in milimeters) between the different detectors.*

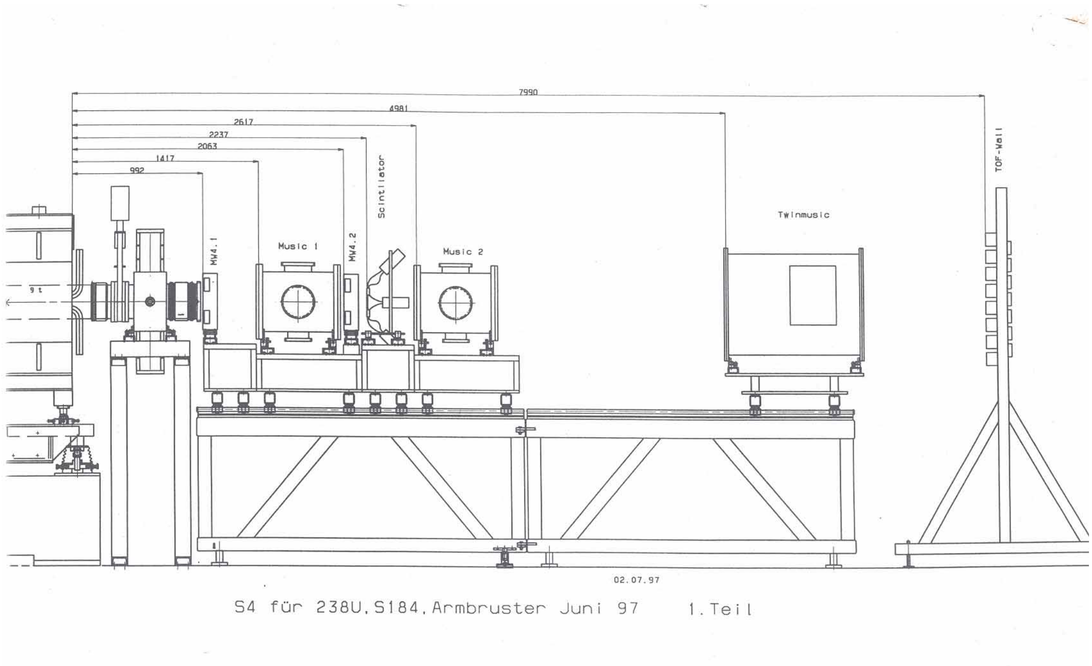

Figure D.2: *Schematic view of the detection setup placed at final area S4 of the FRS. The arrows indicate the relative distances (in milimeters) between the different detectors.*

Area	Material	Thickness (mg/cm^2)	Element
S0	Al	4.07	(1)
	Al	8.90	(2)
	Ti	18.16	(3)
	deuterium	201.00	(4)
	Al	9.70	(3)
	Ti	18.16	(3)
	Nb	60.00	(5)
S2	H	49.30	(6)
	C	532.50	(6)
S4	Al	4.07	(1)
	N	50.00	(8)
	O	15.00	(8)
	Ar	107.00	(7)
	Nb	230.00	(5)
	H	26.40	(6)
	C	285.30	(6)
	N	39.00	(8)
	O	12.00	(8)
	Ar	107.00	(7)

Table D.1: *Thicknesses of the layers of matter that constitute the different elements placed along the FRS.*

Appendix E

Calculation of the saddle-to-scission time τ_{ssc}

The time needed by a compound fissioning nucleus to evolve from the saddle to the scission points τ_{ssc} was firstly calculated by H. Hofmann and J. Nix [Hof83]. According to these authors, the time required for the system to move from the saddle point X_{sad} to the scission point X_{sc} can be written as:

$$\tau_{ssc} = \int_{X_{sad}}^{X_{sc}} dX \frac{n(X)}{j(X)} \tag{E.1}$$

where X is the fission (deformation) degree of freedom, defined by the specific coordinate system; $n(X)$ is the probability density of the nucleus to be at a given deformation and $j(X)$ is the current probability across the point X.

By making use of the Kramer's stationary solution W_{sta} of the Fokker-Planck equation [Kra40], $n(X)$ and $j(X)$ can be calcualted according to the following equations:

$$\begin{aligned} n(X) \;&=\; \int_{-\infty}^{\infty} W_{sta}(X,\dot{X})d\dot{X} = \qquad\qquad (E.2) \\ &\frac{\omega_g}{2}\sqrt{\frac{M}{2\pi T}}\, exp\left[\frac{-B_f + 1/2M\omega_0^2X^2}{T}\right] \cdot erfc\left[\sqrt{\frac{1/2M\omega_0^2X^2}{T}}\right] \end{aligned}$$

and

$$j(X) = \int_{-\infty}^{\infty} \dot{X} W_{sta}(X,\dot{X})d\dot{X} = \frac{\omega_g}{2\pi}\left[\left(1+\gamma^2\right)^{1/2} - \gamma\right] exp\left[-\frac{B_f}{T}\right] \tag{E.3}$$

where ω_g and ω_0 are the frequencies of two potential oscillators that simulated the shape of the nuclear potential at the ground state and at the fission barrier, respectively; T is the temperature; B_f the fission barrier at saddle; M is the inertia and γ corresponds to the dissipation coefficient.

By inserting these two expressions into equation E.1, one obtains:

$$\tau_{ssc} = \left[\left(1+\gamma^2\right)^{1/2} + \gamma\right] \tau_{ssc}^0 \tag{E.4}$$

where τ_{ssc}^{0} is the non-dissipative saddle-to-scission time. In the last section of chapter 5, we have derived the saddle-to-scission time τ_{ssc} using this equation with different values for the dissipation coefficient γ. In these calcualtions, the value of τ_{ssc}^{0} was deduced according to:

$$\tau_{ssc}^{0} = \frac{2}{\omega_0} R\left[\left(\frac{\Delta V}{T}\right)^{1/2}\right] \tag{E.5}$$

where:

$$R(z) = \int_0^z e^{y^2} dy \int_y^{\infty} e^{-x^2} dx \tag{E.6}$$

is a function studied and tabulated by Rosser [Ros48] and ΔV is the potential energy difference between the saddle point and the scission point, which can be calculated by approximating the potential around the saddle point by an inverted oscillator of frequency ω_0:

$$\Delta V = \frac{1}{2} M \omega_0^2 X'^2 \tag{E.7}$$

X' represents the deformation of the nucleus at the scission point with respect to that at saddle.

In order to determine the time τ_{ssc}^{0} of a given nucleus (Z, A) from equation E.5, it was necessary to calculate the mass inertia M of the nucleus, the nuclear temperature T, the deformations X' and the frequency ω_0:

The mass inertia was derived as suggested by J.P. Lestone [Les95]:

$$M \simeq \frac{m}{4}\left\{1 + \frac{17}{15}\, exp\left[-\frac{128}{51}\left(\frac{r}{R_0} - \frac{3}{4}\right)\right]\right\} \tag{E.8}$$

where $m = r_0 A^{1/3}$ is the nuclear mass (with $r_0 = 1.16$ fm) and r/R_0 represents the deformation of the nucleus in terms of its quadrupole shape parameter β_q:

$$\frac{r}{R_0} = 1 + \frac{2}{3}\beta_q \tag{E.9}$$

The nuclear temperature was calculated from the excitation energy of the nucleus E^*, by making use of the Fermi-gas model:

$$T = \sqrt{\frac{E^*}{\tilde{a}}} \tag{E.10}$$

where $\tilde{a}$ is the asymptotic level-density parameter, given by [Ign75b]:

$$\tilde{a} = 0.073A + 0.095 B_s A^{2/3} \tag{E.11}$$

being B_s a correction factor that accounts for the surface area of the deformed nucleus [Mye74].

The difference between the deformation of the nucleus at saddle and at scission was calculated as:

$$X' = X_{ssc} - X_{sad} \tag{E.12}$$

where X_{sad} is related to the quadrupole deformation of the nucleus at saddle [Mye74], according to:

$$X_{sad} = r_0 A^{1/3} \left(1 + \frac{2}{3}\beta_{sad}\right) \tag{E.13}$$

and X_{sc} was deduced on the basis of the distance between the two spheroids that define the nascent fission fragments at scission [Wil76]:

$$X_{sc} = r_0 A_1^{1/3} \left(1 + \frac{2}{3}\beta_1\right) + r_0 A_2^{1/3} \left(1 + \frac{2}{3}\beta_2\right) + d \tag{E.14}$$

being A_1 and A_2 the masses of the two nascent fragments, d the distance between the tips of the two spheroids and β_1 and β_2 the quadrupole deformations at scission. In the present analysis we used the parameters proposed by Wilkins et al. for high energy fission: r_0=1.16 fm, d=2 fm and $\beta_1 = \beta_2 = 0.625$. Thus, equation E.12 was approximated to:

$$X' \simeq d + r_0 A^{1/3} \left[0.587 + \frac{2}{3}\left(1 - \beta_{sad}\right)\right] \tag{E.15}$$

Finally, the frequency ω_0 was approximated to 1×10 s^{-21}.

The approximation made in deriving these quantities, specially in the coordinate X' induced a final error on τ^0_{ssc} of $\sim$ 30%, which is propagated to the saddle-to-scission time τ_{ssc}, according to equation E.4. The influence of this uncertainty in the derivation of the saddle-to-scission multiplicities, discussed in chapter 5, was found to be negligible.

Bibliography

[Abe96] Y. Abe, S. Ayik, P.-G. Reinhard and E. Suraud, Phys. Rep. 275 (1996) 49

[Acc95] htt+://www-wnt.gsi.de

[Aic85] J. Aichelin and G. Bertsch, Phys. Rev. C13 (1985) 1730

[Ald56] K. Alder, A. Bohr, T. Huus, B. Mottelson and A. Winther, Rev. Mod. Phys. 28 (1956) 432

[Amad] The Amadeus code is available from http://www-wnt.gsi.de/kschmidt/amadeus.htm

[Ann85] R. Anne, A. Lefol, G. Milleret and R. Perret, Nucl. Instr. and Meth. 152 (1985) 395

[Arm70] P. Armbruster, Nucl. Phys. A140 (1970) 385

[Bab70] H. Baba, Nucl. Phys. A159 (1970) 625

[BeA01] J. Benlliure, P. Armbruster, M. Bernas, A. Boudard, J.P. Dufour, T. Enqvist, R. Legrain, S. Leray, B. Mustapha, F. Rejmund, K.-H. Schmidt, C. Stéphan, L. Tassan-Got and C. Volant Nucl. Phys. A683 (2001) 513

[Ben98] J. Benlliure, A. Grewe, M. de Jong, K.-H. Schmidt and S. Zhdanov Nucl. Phys. A 628 (1998) 458

[Ben02] J. Benlliure, P. Armbruster, M. Bernas, A. Boudard, T. Enqvist, R. Legrain, S. Leray, F. Rejmund, K.-H. Schmidt, C. Stéphan, L. Tassan-Got and C. Volant, Nucl. Phys. A700 (2002) 469

[BeP02] J. Benlliure, J. Pereira-Conca and K.-H. Scmidt, Nucl. Instr. Meth. A478 (2002) 493

[Ber63] H.W. Bertini, Phys. Rev. 131 (1963) 1801

[Ber03] M. Bernas, P. Armbruster, J. Benlliure, A. Boudard, E. Casarejos, S. Czajkowski, T. Enqvist, R. Legrain, S. Leray, B. Mustapha, P. Napolitani, J. Pereira, F. Rejmund, M. V. Ricciardi, K.-H. Schmidt, C. Stéphan, J. Taieb, L. Tassan-Got and C. Volant, Nucl. Phys. A725 (2003) 213

[Bet36] H. Bethe, Phys. Rev. 50 (1936) 332

[Bha86] K.-H. Bhatt, P. Grangé and B. Hiller, Phys. Rev. C33 (1986) 954

[Bjo73] S. Bjornholm, A. Bohr and B.R. Mottelson, Proc. third IAEA Symp. on the physics, chemistry of fission, Roechester, NY, 13-17 August 1973, vol. 1 (IAEA, Vienna, 1974) p.367

[Blo78] J. Blocki, Y. Boneh, J.R. Nix, J. Randrup, M. Robel, A.J. Sierk and W.J. Swiatecki, Ann. Phys. (N.Y.) 113 (1978) 330

[Boc97] C. Böckstiegel, S. Steinhaeuser, J. Benlliure, H.-G. Clerc, A. Grewe, A. Heinz, M. de Jong, A.R. Junghans, J. Mueller and K.-H. Schmidt, Phys. Lett. B398 (1997) 259

[Boh39] N. Bohr and J.A. Wheeler, Phys. Rev. 56 (1939) 426

[Boh98] A. Bohr and B.R. Mottelson, Nuclear Structure, World Scientific, London (1998)

[Bon95] J.P. Bondorf, A.S. Botvina, A.S. Iljinov, I.N. Mishustin and K. Sneppen Phys. Rep. 257 (1995) 133

[Bou02] A. Boudard, J. Cugnon, S. Leray, C. Volant, Phys. Rev. C 66 (2002) 044615

[Bow73] J.D. Bowman, W.J. Swiatecki and C.E. Tsang, Lawrence Berkeley Laboratory report LBL-2908 (1973)

[Bro70] K.L. Brown, SLAC-Report No 91, Stanford (1970)

[Bro90] U. Brosa, S. Grossmann and A. Müller, Phys. Rep. 197, 4 (1990) 167

[But91] R. Butsch, D.J. Hofman, C.P. Montoya, P. Paul and M. Thoennessen, Phys. Rev. C44 (1991) 1515

[Car86] N. Carjan, A.J. Sierk and J.R. Nix, Nucl. Phys. A452 (1986) 381

[Car87] David C. Carey, The Optics of the Charged Particle Beams, Harwood Academic Publishers, Switzerland (1987)

[Cas01] E. Casarejos, PhD. Thesis, Universidad de Santiago de Compostela (USC) (2001)

[Cha43] S. Chandrasekhar, Rev. Mod. Phys. 15 (1943) 1

[Che96] Ph. Chesny, A. Forgeas, J.M. Gheller, G. Guiller, P. Pariset, L. Tassan-Got, P. Armbruster, K.-H. Behr, J. Benlliure, K. Burkard, A. Brünle, T. Enqvist, F. Farget, K.-H. Schmidt, GSI-reports LNS/SSGD/93-73

[ChP01] G. Chaudhuri and S. Pal, Phys. Rev. C63 (2001) 064603

[ChP02] G. Chaudhuri and S. Pal, Phys. Rev. C65 (2002) 054612

[Cle95] H.-G. Clerc, M. de Jong, T. Brohm, M. Dornik, A. Grewe, E. Hanelt, A. Heinz, A. Junghans, C. Roehl, S. Steinhäuser, B. Voss, C. Ziegler, K.-H. Schmidt, S. Czajkowski, H. Geissel, H. Irnich, A. Magel, G. ünzenberg, F. Nickel, A. Piechaczek, C. Scheidenberger, W. Schwab, K. Sümmerer, W. Trinder, M. Pfützner, B. Blank, A. Ignatyuk and G. Kudyaev Nucl. Phys. A590 (1995) 785

[Coh63] S. Cohen, F. Plasil and W.J. Swiatecki, Proc. Third Conf. on reactions between complex nuclei, ed. A. Ghiorso, R.M. Diamond and H.E. Conzett (University of California Press, 1963) p.325 University of California Radiation Laboratory report UCRL-10775 (1963)

[Coh72] S. Cohen, F. Plasil and W.J. Swiatecki, University of California Berkeley Radiation Laboratory report LBL-1502 (1972)

[CoS63] S. Cohen and W.J. Swiatecki, Ann. Phys. 22 (1963) 406

[Cug87] J. Cugnon, Nucl. Phys. A 462 (1987) 751

[Cug97] J. Cugnon, C. Volant, S. Vuillier, Nucl. Phys. A 620 (1997) 475

[Dav76] K.T. Davis, A.J. Sierk and J.R. Nix, Phys. Rev. C13 (1976) 2385

[Dio00] I. Diószegi, N.P. Shaw, I. Mazumdar, A. Hatzikoutelis and P. Paul, Phys. Rev. C61 (2000) 024613

[Dio01] I. Diószegi, N.P. Shaw, A. Bracco, F. Camera, S. Tettoni, M. Mattiuzzi and P. Paul, Phys. Rev. C63 (2001) 014611

[Don98] C. Donzaud, S. Czajkowski, P. Armbruster, M. Bernas, C. Böckstiegel, Ph. Dessagne, H. Geissel, E. Hanelt, A. Heinz, C. Kozhuharov, Ch. Miehé, G. Münzenberg, M. Pfützner, W. Schwab, C. Stéphan, K. Sümmerer, L. Tassan-Got and B. Voss, Eur. Phys. Jour. A1 (1998) 407

[Eis88] J.M. Eisenberg and W. Greiner, Nuclear Models: Collective and Single-Particle Phenomena, Elsevier Science Ltd. (1988) Ch. 2

[Enq99] T. Enqvist, J. Benlliure, F. Farget, K.-H. Schmidt, P. Armbruster, M. Bernas, L. Tassan-Got, A. Boudard, R. Legrain, C. Volant, C. Böeckstiegel, M. de Jong and J.P. Dufour, Nucl. Phys. A658 (1999) 47

[Enq01] T. Enqvist, W. Wlazlo, P. Armbruster, J. Benlliure, M. Bernas, A. Boudard, S. Czajkowski, R. Legrain, S. Leray, B. Mustapha, M. Pravikoff, F. Rejmund, K.-H. Schmidt, C. Stéphan, J. Taieb, L. Tassan-Got and C. Volant Nucl. Phys. A 686 (2001) 481

[Enq02] T. Enqvist, P. Armbruster, J. Benlliure, M. Bernas, A. Boudard, S. Czajkowski, R. Legrain, S. Leray, B. Mustapha, M. Pravikoff, F. Rejmund, K.-H. Schmidt, C. Stéphan, J. Taieb, L. Tassan-Got, F. Vivès, C. Volant and W. Wlazlo, Nucl. Phys. A 703 (2002) 435

[Eri60] T. Ericson, Advan. Phys. 9 (1960) 425

[Exf] The EXFOR entries are available at the OECD NEA Data Bank, http://www.nea.fr/html/dbdata

[Fel87] H. Feldmeier, Rep. Prog. Phys. 50 (1987) 915

[Fer74] E. Fermi, Nuclear Physics, University of Chicago Press, midway reprint (1974)

[Fro93] P. Fröbrich, I.I. Gontchar and N.D. Mavlitov, Nucl. Phys. A556 (1993) 281

[Fro98] P. Fröbrich and I.I. Gontchar, Phys. Rep. 292 (1998) 131

[Gad92] E. Gadioli and P. Hodgson, Pre-equilibrium Nuclear Reactions, Clarendon Press, Oxford (1992)

[Gai91] J.-J. Gaimard, K.-H. Schmidt Nucl. Phys. A531 (1991) 709

[Gav81] A. Gavron, J.R. Beene, B. Cheynis, R.L. Ferguson, F.E. Obenshain, F. Plasil, G.R. Young, G.A. Petitt, M. Jääskeläinen, D.G. Sarantites and C.F. Maguire, Phys. Rev. Lett. 57 (1981) 1255; erratum 48 (1982) 835

[Gei92] H. Geissel et al., P. Armbruster, K.H. Behr, A. Brünle, K. Burkard, M. Chen, H. Folger, B. Franczak, H. Keller, O. Klepper, B. Langenbeck, F. Nickel, E. Pfeng, M. Pfützner, E. Roeckl, K. Rykaczewski, I. Schall, D. Schardt, C. Scheidenberger, K.H. Schmidt, A. Schröter, T. Schwab, K. Sümmerer, M. Weber, G. Münzenberg, T. Brohm, H.-G. Clerc, M. Fauerbach, J.-J. Gaimard, A. Grewe, E. Hanelt, B. Knödler, M. Steiner, B. Voss, J. Weckenmann, C. Ziegler, A. Magel, H. Wollnik, J.P. Dufour, Y. Fujita, D.J. Vieira and B. Sherrill, Nucl. Instr. and Meth. B70 (1992) 286

[Gico] An extended description of the Gico code is can be found in http://www-linux.gsi.de/ weick/gico

[Glo99] The GLOBAL program is available via anonymous ftp from borsu8.in2p3.fr in the directory */pub/nex/global/pc* and $/pub/nex/global/vms_unix$ for PCs and workstations, respectively

[Gol74] A.S. Goldhaber, Phys. Lett. B53 (1974) 30

[Gon91] F. Gönnenwein, Mass, charge and kinetic energy of fission fragments. C. Wagemans (Ed.), The Nuclear Fission Process, CRC Press, London (1991) p.409

[Gra80] P. Grangé and H.A. Weidenmüller, Phys. Lett. B96 (1980) 26

[Gra83] P. Grangé, L. Jun-Qing and H.A. Weidenmüller, Phys. Rev. C27 (1983) 2063

[Gra86] P. Grangé, S. Hassani, H.A. Weidenmüller, A. Gavron, J.R. Nix and A.J. Sierk, Phys. Rev. C34 (1986) 209

[Gri66] J.J. Griffin, Phys. Rev. Lett. 17 (1966) 478

[Han83] G. Hansen and A.S. Jensen, Nucl. Phys. A406 (1983) 236

[Hau52] W. Hauser and H. Feshbach, Phys. Rev. 87 (1952) 366

[Hei03] A. Heinz, K.-H. Schmidt, A.R. Junghans, P. Armbruster, J. Benlliure, C. Böckstiegel, H.-G. Clerc, A. Grewe, M. de Jong, J. Müller, M. Pfützner, S. Steinhäuser and B. Voss, Nucl. Phys. A 713 (2003) 3

[HiH92] D.J. Hinde, D. Hilscher, H. Rossner, B. Gebauer, M. Lehmann and M. Wilpert, Phys. Rev. C45 (1992) 1229

[Hil81] D. Hilsher, E. Holub, U. Jahnke, H. Orf and H. Rossner, Proc. 3rd adriatic Europhysics Conf. on dynamics of heavy-ion collistions, Hvar, Yugoslavia, North-Holland, Amsterdam, 1981, p. 225

[Hil92] D. Hilsher and H. Rossner, Ann. Phys. Fr. 17 (1992) 471

[Hin92] D.J. Hinde, D. Hilscher and H. Rossner, Nucl. Phys. A538 (1992) 243

[Hui72] J.R. Huizenga and L.G. Moretto, Ann. Rev. Nucl. Part. Sci. 22 (1972) 427

[Hui74a] J.R. Huizenga, A.N. Behkami, R.W. Atcher, J.S. Sventek, H.C. Britt and H. Freiesleben, Nucl. Phys. A223 (1974) 589

[Hui74b] J.R. Huizenga, A.N. Behkami, R.W. Atcher, J.S. Sventek, H.C. Britt and H. Freiesleben, Nucl. Phys. A223 (1974) 577

[Hof83] H. Hofmann and J.R. Nix, Phys. Lett. B122 (1983) 117

[Hof94] D.J. Hofman, B.B. Back, I. Diószegi, S. Schadmand, R. Varma and P. Paul, Phys. Rev. Lett. 72 (1994) 470

[Hua66] K. Huang, Phys. Rev. 146 (1966) 1075

[Hua67] K. Huang, Phys. Rev. 156 (1967) 1555

[Ign75a] A.V. Ignatyuk, G.N. Smirenkin and A.S. Tishin, Yad. Fiz. 21 (1975) 485 (Sov. J. Nucl. Phys. 21 (1975) 255)

[Ign75b] A.V. Ignatyuk, M.G. Itkis, V.N. Okolovich, G.N. Smirenkin and A.S. Tishin, Yad. Fiz. 21 (1975) 1185 (Sov. J. Nucl. Phys. 21 (1975) 612)

[Ign77] A.V. Ignatyuk, M.G. Itkis, V.N. Okolovich, G.R. Rus'kina, G.N. Smirenkin and A.S. Tishin, Yad. Fiz. 25 (1977) 25 (Sov. J. Nucl. Phys. 27 (1977) 13)

[Ign79a] A.V. Ignatyuk, K.K. Istekov and G.N. Smirenkin, Yad. Fiz. 30 (1979) 1205 (Sov. J. Nucl. Phys. 30 (1979) 626)

[Ign79b] A.V. Ignatyuk, K.K. Istekov and G.N. Smirenkin, Yad. Fiz. 29 (1979) 875 (Sov. J. Nucl. Phys. 29 (1979) 450)

[Ign83] A.V. Ignatyuk, K.K. Istekov and G.N. Smirenkin, Yad. Fiz. 37 (1983) 831 (Sov. J. Nucl. Phys. 37 (1983) 495)

[Ign85] A.V. Ignatyuk, G.N. Smirenkin, M.G. Itkins, S.I. Mulgin and V.N. Okolovich, Fiz. Elem. Chastits At. Yadra 16 (1985) 709 (Sov. J. Part. Nucl. 16 (1985) 307)

[Ign95] A.V. Ignatyuk, G.A. Kudyaev, A. Junghans, M. de Jong, H.-G. Clerc and K.-H. Schmidt, Nucl. Phys. A593 (1995) 519

[Ilj92] A.S. Iljinov, M.V. Mebel, N. Bianchi, E. De Sanctis, C. Cuaraldo, V. Lucherini, V. Muccifora, E. Polli, A.R. Reolon and P. Rossi, Nucl. Phys. A543 (1992) 517

[Itk88] M.G. Itkis, V.N. Okolovich, A.Ya. Rusanov and G.N. Smirekin, Fiz. Elem. Chastits At. Yadra 19 (1988) 701 (Sov. J. Part. Nucl. 19 (1988) 301)

[Iwa97] N. Iwasa, H. Geissel, G. Münzenberg, C. Scheidenberger, Th. Schwab and H. Wollnik., Nucl. Instr. and Meth. B126 (1997) 284

[Jon97] M. de Jong, A.V. Ignatyuk and K.-H. Schmidt, Nucl. Phys. A613 (1997) 435

[Jun98] A.R. Junghans, M. de Jong, H.-G. Clerc, A.V. Ignatyuk, G.A. Kudyaev and K.-H. Schmidt, Nucl. Phys. A629 (1998) 635

[Jur02] B. Jurado, PhD. Thesis, Universidad de Santiago de Compostela (USC) (2002)

[Jur03] B. Jurado, K.-H. Schmidt and J. Benlliure, Phys. Lett. B 533 (2003) 186

[Jur04a] B. Jurado, C. Schmitt, K.-H. Schmidt, J. Benlliure and A.R. Junghans, arXiv nucl-ex/0302003, submitted to Nucl. Phys. A

[Jur04b] B. Jurado, C. Schmitt, K.-H. Schmidt, J. Benlliure and A.R. Junghans, arXiv nucl-ex/0403004, submitted to Nucl. Phys. A

[Jur04c] B. Jurado, C. Schmitt, K.-H. Schmidt, J. Benlliure, T. Enqvist, A.R. Junghans, A. Kelic and F. Rejmund, arXiv nucl-ex/0403006, submitted to Nucl. Phys. A

[JuS02] B. Jurado, K.-H. Schmidt and K.-H. Behr, Nucl. Instr. and Meth. A483 (2002) 603

[Kar75] P. Karol, Phys. Rev. C11, 4 (1975) 1203

[Kat78] S.K. Kataria, V.S. Ramamurthy and S.S. Kapoor, Phys. Rev. C18 (1978) 549

[Kra40] H.A. Kramers, Physika VII 4 (1940) 284

[Kru85] H. Kruse, B.V. Jacak and H. Stöcker, Phys. Rev. Lett. 54 (1985) 289

[Lan65] D.W. Lang, Nucl. Phys. 77 (1965) 545

[Les95] J.P. Lestone, Phys. Rev. C51 (1995) 580

[Lev85] S. Levit and P. Bonche, Nucl. Phys. A437 (1985) 426

[Liesch] The Lieschen code is available from http://www-wnt.gsi.de/kschmidt/lieschen.htm

[Met58a] N. Metropolis, R. Bivins, M. Storm, A. Turkevich, J.M. Miller and G. Friendlander, Phys. Rev. 110 (1958) 185

[Met58b] N. Metropolis, R. Bivins, M. Storm, A. Turkevich, J.M. Miller and G. Friendlander, Phys. Rev. 110 (1958) 204

[Mol95] P. Möller, J.R. Nix, W.D. Myers and W.J. Sciatecki, At. Data Nucl. Data Tables 59 (1995) 185

[Mor72] L.G. Moretto, Nucl. Phys. A185 (1972) 145

[Mor73] L.G. Moretto, Proc. third IAEA Symp. on the physics, chemistry of fission, Roechester, NY, 13-17 August 1973, vol. 1 (IAEA, Vienna, 1974) p.329

[Mor75] L.G. Moretto, Nucl. Phys. A247 (1975) 211

[Mor78] D.J. Morrissey, W.R. Marsh, R.J. Otto, W. Loveland and G.T. Seaborg, Phys. Rev. C18 (1978) 1267

[Mor89] D.J. Morrisey, Phys. Rev. C39 (1989) 460

[Mor91] J. Moreau and K. Heyde, Theoretical Models of Mass Distributions, C. Wagemans (Ed.), The Nuclear Fission Process, CRC Press, London (1991) p.231

[Mor95] L.G. Moretto, K.X. Jing, R. Gatti, G.J. Wozniak and R.P. Schmitt, Phys. Rev. Lett. 75 (1995) 4186

[Mul98] S.I. Mulgin, K.-H. Schmidt, A. Grewe and S.V. Zhdanov, Nucl. Phys. A640 (1998) 375

[Mus99] B. Mustapha, Ph.D. Thesis, University of Paris XI, October 1999

[Mye74] W.D. Myers and W.J. Swiatecki, Ann. Phys. 84 (1974) 186

[Nap03] P. Napolitani, L. Tassan-Got, P. Armbruster and M. Bernas, Nucl. Phys. A727 (2003) 120

[Neg78] J.W. Negele, S.E. Koonin, P. Möller, J.R. Nix and A.J. Sierk, Phys. Rev. C17 (1978) 1098

[Nix65] J.R. Nix and W.J. Swiatecki, Nucl. Phys. 71 (1965) 1

[Oli79] L.F. Oliveira, R. Donangelo and J.O. Rasmussen, Phys. Rev. C19 (1979) 826

[Pau94] P. Paul and M. Thoennessen, Ann. Rev. Nucl. Part. Sci. 44 (1994) 65

[Per99] J. Pereira, Diploma Thesis, Universidad de Santiago de Compostela (USC) (1999)

[Pfu94] M. Pfützner, H. Geissel, G. Münzenberg, F. Nickel, C. Scheidenberger, K.-H. Schmidt, K. Sümmerer, T. Brohm, B. Voss and H. Bichsel, Nucl. Instr. and Meth. B86 (1994) 213

[Pro01] A.V. Prokofiev, Nucl. Instr. and Meth. A463 (2001) 557

[Ree90] H. Reeg, N. Schneider and S. Steinhäuser, GSI Scientific Report (1990) 392

[Rej00] F. Rejmund, A.V. Ignatyuk, A.R. Junghans and K.-H. Schmidt, Nucl. Phys. A678 (2000) 215

[Ric02] M.V. Ricciardi, PhD. Thesis, Universidad de Santiago de Composelta (USC), in preparation

[Ric03] M.V. Ricciardi, T. Enqvist, J. Pereira, J. Benlliure, M. Bernas, E. Casarejos, V. Henzl, A. Kelić, J. Taieb and K.-H. Schmidt, Phys. Rev. Lett. 90 (2003) 212302

[Ric04] M.V. Ricciardi, A.V. Ignatyuk, A. Kelić, P. Napolitani, , F. Rejmund, K.-H. Schmidt, O. Yordanov, Nucl. Phys. A733 (2004) 299

[Ros48] J.B. Rosser, Theory and application of $\int_0^z e^{-x^2}dx$ and $\int_0^z e^{-p^2y^2}dx \int_0^y e^{-x^2}dx$, Mapleton House, New York (1948) pp. 102-191

[Sah85] C.C. Sahm, H.-G. Clerc, K.-H. Schmidt, W. Resdorf, P. Armbruster, F.P. Hessberger, J.G. Keller, G. Münzenberg and D. Vermeulen, Nucl. Phys. A441 (1985) 316

[Sch82] K.-H. Schmidt, H. Delagrange, J.P. Dufour, N. Cârjan and A. Fleury, Z.Phys. A308 (1982) 215

[Sch84] K.-H. Schmidt, J.G. Keller and D. Vermeulen, Z. Phys. A315 (1984) 159

[Sch98] W. Schwab, M. Bernas, P. Armbruster, S. Czajkowski, P. Dessagne, C. Donzaud, H. Geissel, A. Heinz, C. Kozhuharov, C. Miehe, G. Muenzenberg, M. Pfuetzner, C. Stephan, K.-H. Schmidt, K. Süemmerer, L. Tassan-Got and B. Voss, Eur. Phys. J. A2 (1998) 179

[Sch00] K.-H. Schmidt, S. Steinhäuser, C. Böckstiegel, A. Grewe, A. Heinz, A.R. Junghans, J. Benlliure, H.-G. Clerc, M. de Jong, J.Müller, M. Pfützner and B. Voss, Nucl. Phys. A665 (2000) 221

[Sch01] K.-H. Schmidt, J. Benlliure and A.R. Junghans, Nucl. Phys. A693 (2001) 169

[Sch02] K.-H. Schmidt, M.V. Ricciardi, A. Botvina and T. Enqvist, Nucl. Phys. A710 (2002) 157

[ScS98] C. Scheidenberger, Th. Stoehlker, W.E. Meyerhof, H. Geissel, P.H. Mokler and B. Blank Nucl. Instr. Methods B142 (1998) 441

[Ser47] R. Serber, Phys. Rev. 72 (1947) 1114

[Sha00] N.P. Shaw, I. Diószegi, I. Mazumdar, A. Buda, C.R. Morton, J. Velkovska, J.R. Beene, D.W. Stracener, R.L. Varner, M. Thoennessen and P. Paul, Phys. Rev. C61 (2000) 044612

[Shi01] L. Shi, P. Danielewicz and R. Lacey, Phys. Rev. C64 (2001) 034601

[Sie86] A.J. Sierk, Phys. Rev. C33 (1986) 2039

[Sig91] P. Sigmund, Interaction of Charged Particles with Solids and Surfaces, Eddited by A. Gras-Marti et al., NATO ASI Series B, vol. 271, Plenum Press, New York (1991) p.73

[Son91] H.Q. Song and R.K. Su, Phys. Rev. C44 (1991) 2505

[Ste58] P.C. Stevenson, H.G. Hicks, W.E. Nervik and D.R. Nethaway, Phys. Rev. 111 (1958) 886

[Ste91] H. Stelzer, Nucl. Instr. and Meth. A310 (1991) 103

[Ste92] M. Steiner et al., M. Blasche, H.-G. Clerc, H. Eickhoff, B. Franczak, H. Geissel, G. Münzenberg, K.-H. Schmidt, H. Stelzer and K. Sümmerer, Nucl. Instr. and Meth. A312 (1992) 420

[Swi83] W.J. Swiatecki, Aust. J. Phys. 36 (1983) 641

[Tai03] J. Taieb, K.-H. Schmidt, L. Tassan-Got, P. Armbruster, J. Benlliure, M. Bernas, A. Boudard, E. Casarejos, S. Czajkowski, T. Enqvist, R. Legrain, S. Leray, B. Mustapha, M. Pravikoff, F. Rejmund, C. Stephan, C. Volant and W. Wlazlo, Nucl. Phys. A724 (2003) 213

[Ver84] D. Vermeulen, H.-G. Clerc, C.C. Sahm, K.-H. Schmidt, J.G. Keller, G. Münzenberg and W. Resdorf, Z. Phys. A318 (1984) 157

[Vos95] B. Voss, T. Brohm, H.-G. Clerc, A. Grewe, E. Hanelt, A. Heinz, M. de Jong, A. Junhans, W. Morawek, C. Röhl, S. Steinhäuser, C. Ziegler, K.-H. Schmidt, K.-H. Behr, H. Geissel, G. Münzenberg, F. Nickel, C. Scheidenberger, K. Sümmerer, A. Magel and M. Pfützner Nucl. Instr. and Meth. A364 (1995) 150.

[Wei30] V. Weisskopf and E. Wigner, Z. Physik 63 (1930) 54

[Wei37] V.F. Weisskopf, Phys. Rev. 52 (1937) 295

[Wei50] V.F. Weisskopf, Helv. Phys. Acta 23 (1950) 187

[Wei80] H.A. Widenmüller, Progress in particle and Nuclear Physics, Pergamon, Oxford, Vol.3 (1980) 49

[Wer81] E. Werner, H.S. Wio, H. Hofmann and K. Pomorski, Z. Phys. A299 (1981) 231

[Wil76] B.D. Wilkins, E.P. Steinberg and R.R. Chasman., Phys. Rev. C14 (1976) 1832

[Woo92] J.L. Wood et al. Phys. Rep. 215 (1992) 101

[Yar79] Y. Yariv and Z. Fraenkel, Phys. Rev. C20 (1979) 2227

[Yar81] Y. Yariv and Z. Fraenkel, Phys. Rev. C24 (1981) 448

[Zub02] A.S. Zubov, G.G. Adamian, N.V. Antonenko, S.P. Ivanova and W. Scheid, Phys. Rev. C65 (2002) 024308